

# Theory of the Structural Glass Transition: A Pedagogical Review

Vassiliy Lubchenko\*

*Department of Chemistry, University of Houston, Houston, TX 77204-5003 and*

*Department of Physics, University of Houston, Houston, TX 77204-5005*

(Dated: February 22, 2022)

## Abstract

The random first-order transition (RFOT) theory of the structural glass transition is reviewed in a pedagogical fashion. The rigidity that emerges in crystals and glassy liquids is of the same fundamental origin. In both cases, it corresponds with a breaking of the translational symmetry; analogies with freezing transitions in spin systems can also be made. The common aspect of these seemingly distinct phenomena is a spontaneous emergence of the molecular field, a venerable and well-understood concept. In crucial distinction from periodic crystallisation, the free energy landscape of a glassy liquid is vastly degenerate, which gives rise to new length and time scales while rendering the emergence of rigidity gradual. We obviate the standard notion that to be mechanically stable a structure must be essentially unique; instead, we show that bulk degeneracy is perfectly allowed but should not exceed a certain value. The present microscopic description thus explains both crystallisation and the emergence of the landscape regime followed by vitrification in a unified, thermodynamics-rooted fashion. The article contains a self-contained exposition of the basics of the classical density functional theory and liquid theory, which are subsequently used to quantitatively estimate, without using adjustable parameters, the key attributes of glassy liquids, viz., the relaxation barriers, glass transition temperature, and cooperativity size. These results are then used to quantitatively discuss many diverse glassy phenomena, including: the intrinsic connection between the excess liquid entropy and relaxation rates, the non-Arrhenius temperature dependence of  $\alpha$ -relaxation, the dynamic heterogeneity, violations of the fluctuation-dissipation theorem, glass ageing and rejuvenation, rheological and mechanical anomalies, super-stable glasses, enhanced crystallisation near the glass transition, the excess heat capacity and phonon scattering at cryogenic temperatures, the Boson peak and plateau in thermal conductivity, and the puzzling midgap electronic states in amorphous chalcogenides.

**PACS:** 64.70.Q-Theory and modeling of the glass transition; 64.70.kj Glasses; 65.60.+a Thermal properties of amorphous solids and glasses: heat capacity, thermal expansion, etc.; 71.55.Jv Disordered structures, amorphous and glassy solids; 83.80.Ab Solids: e.g., composites, glasses, semicrystalline polymers; 63.50.Lm Glasses and amorphous solids

**Keywords:** glass transition; supercooled liquids; random first order transition; rheology; midgap electronic states; two-level systems

---

\* vas@uh.edu

## CONTENTS

|  |     |
|--|-----|
| I. Motivation  | 3   |
| II. Placing the Glass Transition on the Map, Thermodynamics-wise: The Microcanonical Spectrum of Liquid, Supercooled-Liquid, and Crystal States. The Definition of the Glass Transition and Ageing   | 7   |
| III. Liquid-to-crystal transition as a breaking of translational symmetry. Review of the Theory of Liquids and Liquid-to-Solid Transition.   | 11  |
| A. What drives crystallisation, why it is a discontinuous transition, and why the entropy of fusion is modest  | 11  |
| B. Emergence of the Molecular Field  | 24  |
| C. Transferability of DFT results from model liquids to actual compounds   | 36  |
| IV. Emergence of Aperiodic Crystal and Activated Transport, as a Breaking of Translational Symmetry  | 40  |
| A. The Random First Order Transition (RFOT)  | 40  |
| B. Configurational Entropy   | 49  |
| C. Qualitative discussion of the transition at $T_A$ as a kinetic arrest, by way of mode-mode coupling. Connection between kinetic and thermodynamic views on the transition at $T_A$ . Short discussion on colloids, binary and metallic mixtures, and ionic liquids. | 55  |
| D. Connection with spin models   | 58  |
| V. Quantitative Theory of Activated transport in Glassy Liquids  | 64  |
| A. Glassy liquid as a mosaic of entropic droplets  | 64  |
| B. Mismatch Penalty between Dissimilar Aperiodic Structures: Renormalisation of the surface tension coefficient  | 73  |
| C. Quantitative estimates of the surface tension, the activation barrier for liquid transport, and the cooperativity size  | 78  |
| VI. Dynamic heterogeneity  | 94  |
| A. Correlation between non-exponentiality of liquid relaxation and fragility   | 95  |
| B. Violation of the Stokes-Einstein relation and decoupling of various processes   | 97  |
| VII. At the crossover from collisional to activated transport  | 101 |
| VIII. Relaxations far from equilibrium: glass ageing and rejuvenation  | 109 |
| A. Ageing  | 110 |
| B. Rejuvenation  | 113 |
| IX. Rheological and Mechanical Anomalies   | 115 |
| A. Shear thinning  | 115 |
| B. Mechanical Strength   | 118 |
| X. Ultra-Stable Glasses  | 119 |
| XI. Ultimate Fate of Supercooled Liquids   | 122 |
| XII. Quantum Anomalies   | 124 |
| A. Two-Level Systems and the Boson Peak  | 125 |
| B. The midgap electronic states  | 133 |

|  |     |
|--|-----|
| XIII. Summary and Connection with Jammed and Other Types of Aperiodic Solids | 141 |
| A. Volume mismatch during ageing   | 148 |
| References   | 150 |

## I. MOTIVATION

Practical use of structural glasses by early hominins—in the form of tools and weapons—likely goes back to about 2 million years ago [1] and thus well predates the appearance of the anatomically modern human. The lack of crystallite boundaries, which helped our forefathers to impart sharp and smooth edges to obsidian rocks, still underlies many uses of structural glasses. For instance, it results in optical transparency and mechanical sturdiness of amorphous silicates; the combination of the two makes glasses uniquely useful in construction and in information technology. Metallic glasses are exceptionally rigid at room temperature while being soft and malleable over a rather broad temperature range near the glass transition [2]. In contrast, polycrystalline metals liquefy almost instantly near their melting temperature and thus have a much narrower processing window. Some of the applications of glasses are thoroughly modern: The reflectivity and electrical conductance of chalcogenide alloys depend on whether the material is in a crystalline or amorphous form, a property currently utilised in optical drives. In some of these alloys, crystal-to-glass transition can be induced by electric current or irradiation, which can be exploited to make non-volatile computer memory and for other useful applications [3–9].

The relatively gradual onset of rigidity in structural glassformers—viewed alternatively as a rapid, super-Arrhenius slowing down of molecular motions with increasing density or lowering temperature—is as useful to the industrial designer as it is interesting to the physicist and chemist. For basic symmetry reasons, liquids freeze into *periodic* crystals in a discontinuous fashion so that shear resistance emerges within a narrow temperature interval. The mechanical stability of a periodic array of atoms is intuitive to those familiar with the Debye theory: The positive-definiteness of the force-constant matrix for a periodic lattice can be readily shown for a variety of generic force laws between individual atoms [10]. Even in those difficult cases where the individual interactions balance each other out in a delicate fashion—such situations often arise in applications such as multiferroics—the stability analysis of a *periodic* crystal usually reduces to that for a very small number of normal modes. In contrast, the structure and rigidity change continuously on approach to vitrification, while there is no obvious way to diagonalise the force-constant matrix for an aperiodic lattice. Another way to look at this distinction is that glassy liquid and the corresponding crystal, if any, occupy distinct regions in the phase space that are separated by a substantial barrier. The glass transition itself is not even a phase transition but, rather, signifies that the supercooled liquid falls out of equilibrium, an expressly kinetic phenomenon. Glasses are typically only *metastable* with respect to crystallisation.

Given the above notions, it appears reasonable to question whether the underlying causes of rigidity in periodic crystals and glasses are related even as the local interactions in the two types of solids are very similar, aside from subtle differences in bond lengths and angles. In such a view, the roles of the cohesive forces and the thermodynamic driving force for solidification are essentially gratuitous; the cohesive forces simply prevent the particles from flying apart and/or fix local coordination on average. To avoid confusion, we note that in liquids made of rigid particles, there is no actual bonding and so one speaks of contacts or collisions. Nevertheless, the thermodynamics of packing-driven solidification can be put in correspondence with that of chemically-bonded solids, as will be discussed.

As surprising and unpalatable it may feel, the view of a gratuitous role of thermodynamics

in glassy phenomena would seem to be suggested by a number of theoretical developments. For instance, one of the earliest methodologies that yielded an emergence of rigidity in aperiodic systems was the mode-coupling theory (MCT) [11, 12]. Hereby the rigidity arises for expressly kinetic reasons: At sufficiently high densities, a particle can not keep up with the feedback it receives from the surrounding particles in response to its own motions. To reduce the feedback, the particle is forced to slow down. In the mean-field limit of the MCT, in which equations become tractable, the slowing down is nothing short of catastrophic; it leads to a complete kinetic arrest and, hence, freezing. A thermodynamic signature of this type of freezing, if any, does not readily transpire in this framework. A variety of models characterised by complicated kinetic constraints have been conceived in the past few years [13, 14], motivated by Palmer et al.’s work on hierarchically constrained dynamics [15]. The latter models, like the MCT, were advanced in the early 80s. These kinetics-based models exhibit a slowing down of cooperative nature, and so does the MCT. Complicated kinetic phenomena, which are at least superficially similar to the non-Arrhenius and non-exponential relaxations observed in actual glass-formers, can emerge in kinetically constrained models even if the thermodynamics of the model are trivial [16].

A distinct set of models suggesting a somewhat gratuitous role of thermodynamics in the structural glass transition focus on the phenomenon of jamming [17–20]. During jamming, as epitomised by sand dunes, the thermal motions are negligible because temperature is effectively zero compared to the energies involved. In apparent similarity to glasses, the rigidity of jammed systems appears to form gradually. Flow occurs through the proliferation of soft, harmonic modes that arise when particle contacts are removed. Such soft modes also emerge in random matrix theories [21] and have been implicated as giving rise to the so called Boson Peak. The Boson Peak is a set of vibrational-like states in glasses at frequencies of 1 THz or so, which reveals itself as a “bump” in the heat capacity and excess phonon scattering at the corresponding temperatures, i.e., near  $10^1$  K [22, 23].

Yet we shall see in the following that one is, in fact, correct in expectating that thermodynamics are not simply a spectator of the slowing down that takes place in supercooled liquids when they are cooled or compressed toward the glass transition. Until vitrification has taken place, the liquid is in fact equilibrated and thus should obey detailed balance [24, 25]. (The liquid is equilibrated conditionally in that there is a lower free energy state, viz., the crystal. The latter, however, is behind a barrier and is not accessed.) By detailed balance, cooperative motions that give rise to the non-trivial kinetics observed in supercooled liquids must correspond to a specific set of microstates. Such states necessarily have a thermodynamic signature in the form of additional entropy and heat capacity. For instance, the critical slowing down during a second order transition corresponds to a non-analyticity in the free energy [26], thus leading to a singularity in the temperature dependence of the heat capacity. Detailed balance dictates that a complete theory of the slowing down in supercooled liquids must describe both the thermodynamics and kinetics in an internally consistent, unified fashion. The present review is intended as a pedagogical exposition of a theory that delivers exactly that: a unified, quantitative description of thermodynamic and kinetic phenomena in supercooled liquids and glasses. This theory is called the random first order transition (RFOT) theory and has been developed since the early-mid 80s, earlier reviews can be found in Refs. [23, 27, 28]. The theory has provided a microscopic framework that allows one to understand the emergence of rigidity in aperiodic systems in thermodynamic terms and thus connect the structural glass transition to a better understood—at least conceptually—fields of the liquid-to-crystal transition and the theory of chemical bonding in solids [29].

Despite showing basic similarity in bonding, supercooled liquids and glasses differ fundamentally from periodic crystals in that they are vastly structurally *degenerate*, that is, their free energy exhibits exponentially many minima at a specific value of the free energy. The thermodynamic signature of the degeneracy is the excess liquid entropy of the supercooled

liquid relative to the corresponding crystal. Upon vitrification, this excess entropy ceases to change as the temperature lowers, thus leading to a discontinuity in the measured heat capacity. The remarkable variety of relaxations unique to glassy systems can all be traced to transitions between the distinct free energy minima. This microscopic picture gives rise to quantitative predictions for many signature phenomena that accompany the structural glass transition and their quantitative characteristics, without using adjustable parameters. These cardinal predictions of the theory include the activation barriers for  $\alpha$ -relaxation and their relation to the excess liquid entropy [30, 31] and elastic constants [32–34], details of the deviations from Arrhenius behaviour [31, 35, 36] and the pressure dependence of the barriers. [37] In addition, the theory predicts correlations of thermodynamics with non-exponential relaxations [38], the cooperativity length [31, 33], deviations from the Stokes-Einstein relation [39], ageing dynamics in the glassy state [40], crossover between activated and collisional transport in glass-forming liquids [35, 41, 42], decoupling between various types of relaxation [43], beta-relaxation [44], shear thinning [45], dynamics near the surface of glasses [46], mechanical strength [47], rejuvenation and front propagation in ultrastable glasses [48, 49], and re-entrant  $T$ -dependence of the crystallisation rate [50].

The RFOT theory is a *microscopic* theory: For simple liquids, such as hard spheres or Lennard-Jones particles, the theory starts from the functional form of the interaction and provides a detailed approach to compute every quantity of interest from scratch. For the more complicated glass-forming materials of technology, the interactions must be evaluated by quantum-chemical means. Owing to the computational complexity of the quantum-chemical problem, detailed results cannot be expressed in closed form. In these cases, the microscopic analysis of the RFOT theory delineates a small sufficient set of system-specific quantities—structural and thermodynamic—that represent the microscopic input for computations of the dynamics. These quantities can be extracted by measurement, such as X-ray scattering, the Brillouin scattering, and the calorimetry of the liquid-to-crystal transition, while no phenomenological assumptions are made. The ensuing computations do not involve adjustable parameters, consistent of course with the microscopic nature of the description. Importantly, none of those listed measurements have to do directly with the glass transition per se or use any kind of dynamic assumptions.

Likewise, the RFOT theory has elucidated in a microscopic fashion several *quantum* phenomena, [28] which play a role at cryogenic temperatures. Somewhat surprisingly, the low temperature physics turns out to be intrinsically related to the molecular motions that froze in at the much higher, glass transition temperature. The theory ineluctably leads to the result that an equilibrated liquid must have a specific, rather universal concentration of configurations that originate from the transition state configurations for transport. In the equilibrated liquid, these special configurations are “domain walls” of high free energy density separating compact regions characterised by relatively low free energy density. The domain walls quantitatively account for the excess structural states in cryogenic glasses responsible for the mysterious two-level systems and the Boson Peak [22, 23, 51, 52]. More recently, it has been established that the domain walls have a topological signature in chalcogenide alloys and host very special midgap electronic states, responsible for light-induced midgap absorption and ESR signal [53, 54]. These quantum phenomena underscore the danger of thinking of crystals merely as some kind of disordered analogue of periodic crystals. Again, we shall use thermodynamics as our guiding light in elucidating this important feature of structural glasses.

Consistent with its being firmly rooted in thermodynamics, the RFOT theory highlights the symmetry aspects of the structural glass transition. The basic symmetry that becomes broken en route to the glass transition is the translational symmetry intrinsic to liquids and gases. As a result of this symmetry breaking, the one-particle density profile (gradually) switches from being, in time average, spatially uniform to a sensibly fixed collection of

disparate, sharp peaks. Similarly to periodic crystals, these peaks indicate the particles organise themselves into structures that live much longer than the vibrations. In contrast with periodic crystals, however, the structures are not infinitely long-lived but eventually reconfigure, thus leading to a liquid flow on long times that eventually restores the translational symmetry. Only when the activated reconfigurations become slower than the quenching rate, which depends on glass preparation, does the system fall out of equilibrium completely. Importantly, translational symmetry being broken does *not* imply there is another symmetry, like periodic ordering, that replaces it. The symmetry perspective furnishes the requisite completeness we have come to associate with established physical theories, such as the theory of second order transitions, which was originally built on a symmetry-based coarse-grained functional [55] and was later complemented by the discovery of anomalous scaling. The latter is fully determined by the symmetry and range of the molecular interaction but not its detailed form [26]. Likewise, the presence of an underlying symmetry breaking makes the RFOT description of the structural glass transition robust with respect to possible ambiguities that inevitably arise from approximations and incomplete knowledge of detailed particle-particle interactions; it thus undergirds the applicability of the theory to rigid particles and chemically-bonded liquids alike. The symmetry perspective will also allow us to connect the glass transition with the phenomenon of jamming.

The RFOT theory definitively answers the aforementioned basic question as to the mechanical stability of an aperiodic array of particles: To achieve macroscopic mechanical stability on a finite time scale, the structure does not have to be unique; indeed, even a thermodynamic degeneracy is perfectly allowed so long as it does not exceed a certain value. In turn this guarantees that the transitions between alternative free energy minima are sufficiently slow. Relics of *locally* metastable configurations are present in the frozen glass and persist down to the lowest temperatures measured but do not affect the *macroscopic* stability.

The article is intended to be a rather self-contained source on the foundations of the RFOT theory and on how to obtain its main results with a minimum of technical complexity. The narrative is organised as follows: Section II describes what the glass transition is from the viewpoint of macroscopic thermodynamics and explains the relation between the supercooled-liquid/glass states and the thermodynamically stable liquid and crystal states. Section III explains the thermodynamics of the ordinary liquid-to-periodic-crystal transition and, along the way, introduces the basic machinery of the classical density theory and the theory of liquids, which will be our main tools in discussing things glassy. These tools no longer seem to be part of standard courses in statistical mechanics; it is hoped that the present text covers the necessary minimum in a sufficiently self-contained manner. Section IV uses the machinery from Section III to understand the emergence of *aperiodic* solids, from both the thermodynamic and kinetic perspectives. There we also briefly discuss the connections with several spin models; these connections have proved to be a source of both insight and some confusion to many over the years. In Section V, we establish in a self-contained manner both the qualitative and quantitative features of activated transport and the intrinsic, testable predictions that connect the thermodynamics and kinetics of glassy liquids. These results will be used in Sections VI-XII to review quantitative predictions made by the RFOT theory on a great variety of glassy phenomena mentioned above. In Section XIII, we summarise, briefly review the formal status of the theory and establish an intrinsic connection and, at the same time, basic distinction between the glass transition and jamming.

Last but not least, let us settle a semantic issue that can be confusing to physicists and chemists alike, in the author’s experience: We will often use the words “aperiodic crystal” and “aperiodic lattice”—or simply “lattice”—when referring to the infinite aperiodic array of particles that a glass or a snapshot of a liquid is. The purpose is to avoid the repeated use



states belonging to this special spectral region are *bypassed* during crystallisation and may thus be said to comprise an enthalpy or energy “gap” because they are inaccessible in true equilibrium. For an enthalpy value falling within the gap, the system is phase-separated into liquid and crystal, while the total entropy is a linear function of the enthalpy and simply reflects the partial quantity of the liquid and crystal, an instance of the lever rule [56]:  $S(H) = xS_{\text{liq}} + (1-x)S_{\text{Xtal}}$ , where  $H = xH_{\text{liq}} + (1-x)H_{\text{Xtal}}$  and  $x$  is the mole fraction of the liquid. The quantities  $S_{\text{liq}}$  and  $S_{\text{Xtal}}$  are the entropies at the edges of the enthalpy gap, viz.,  $H_{\text{liq}}$  and  $H_{\text{Xtal}}$  respectively. The numerical value of the width of the gap,  $(H_{\text{liq}} - H_{\text{Xtal}})$ , which is equal to the latent heat, can be divided by the melting temperature  $T_m$  to obtain the entropy of fusion  $S_m = S_{\text{liq}} - S_{\text{Xtal}}$ . The latter is generically about  $1.5k_B$  per particle for ionic compounds [57]; it is somewhat larger for Lennard-Jones-like substances ( $1.68k_B$  for Ar [56]) but often less than  $k_B$  for covalently bonded liquids, such as  $\text{SiO}_2$  [57]. The corresponding enthalpy of fusion is thus comparable to the kinetic energy of the atoms.

If, however, the cooling rate is finite, the liquid must be supercooled somewhat before it can crystallise, because the nucleation barrier for crystallisation is infinite strictly at the melting temperature. Consequently, the liquid states on the right flank of the enthalpy gap are sampled. These states correspond to a *supercooled liquid*. Note the higher the viscosity, the larger the width of the sampled region, because the prefactor of the nucleation rate scales roughly inversely with the viscosity.

Now, it is often the case that the viscosity and, thus, the relaxation times grow rapidly with lowering the temperature, see Fig. 2; the details of the viscosity growth and the relation between viscosity and relaxation rates will be discussed in detail shortly. Given such an increase in the relaxation time, a liquid is often easy to bring to and maintain in a supercooled state. A familiar household example of such a supercooled liquid is glycerol, which is rather difficult to crystallise, as it turns out. (See, however, Onsager’s anecdote about a glycerol factory in Canada [58].) One can continue to cool down such a deeply supercooled liquid at a slow rate, with little risk of crystallisation. Eventually, a liquid cooled at a *steady* rate will fail to reach equilibrium—owing to the rapidly growing relaxation times. This statement applies at least to the slow rates realistically achievable in the laboratory; Stevenson and Wolynes have argued given a slow enough cooling rate, a (periodic-crystal-forming) liquid will actually crystallise [50]. The re-entrant behaviour the glass-to-crystal nucleation, which has been recently observed in some organic liquids, [59, 60] seems to be consistent with this prediction, see Section XI.

The structural relaxation responsible for the viscous flow can be readily witnessed in the form of a low-frequency peak in the dielectric loss spectrum  $\epsilon''(\omega)$ . This relatively slow process is traditionally called  $\alpha$ -relaxation. Other, faster processes can be argued to take place in addition to main  $\alpha$ -relaxation; these faster processes are often non-Arrhenius as well, see Fig. 3.

Once the liquid that is being cooled fails to equilibrate, we say that the *glass transition*, or *vitrification*, has taken place, at a temperature  $T_g$ . Although the system is no longer equilibrated, the particles continue to move and the material still relaxes partially, which is called “ageing.” These relaxational motions are even slower than the motions above the glass transition, whose sluggishness caused the falling out of equilibrium in the first place; the deeper the quench below the glass transition, the slower the ageing.

The non-equilibrium, glassy states are no longer identifiable on the equilibrium spectrum in Fig. 1. Rather, they are a complicated mixture of configurations that are similar to structures equilibrated in a continuous *range* of temperatures; these are sometimes called “fictive” temperatures. Still, before significant ageing has taken place, the structure of the glass is very close to that of the supercooled liquid just above the glass transition, save for the somewhat reduced magnitude of vibrational motions. Hereby, the fictive temperature is only weakly distributed and approximately equal to the glass transition temperature itself.



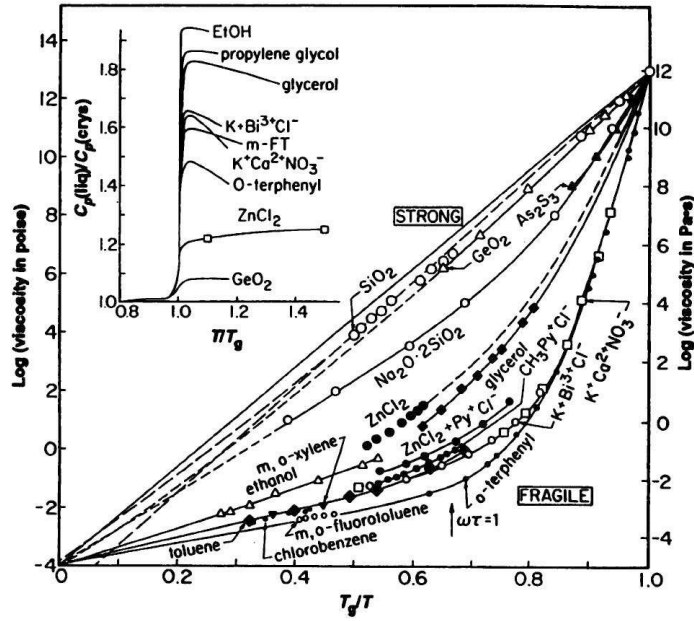


FIG. 2. The viscosities of several substances plotted as functions of the inverse temperature, the compilation and figure due to C. A. Angell [61]. The temperature is scaled by the glass transition temperature for each substance. The most notable feature of the curves is the deviation from the Arrhenius law  $e^{\text{const}/T}$ . Liquids that deviate much or little from the Arrhenius law are often called “fragile” and “strong” respectively. The inset shows the temperature dependence of the excess liquid heat capacity, relative to the corresponding crystal, additionally normalised by the crystal heat capacity. There appears to be a correlation between the magnitude of the jump in the heat capacity and the liquid’s fragility.

The system is essentially arrested in the free energy minimum it was occupying during the glass transition.

The glass transition is not a phase transition, but, instead, is an instance of kinetic arrest. Still, it can be imparted certain features of a second order phase transition with enough effort. By employing a rapid enough quench, one may make ageing largely negligible. Under these circumstances, the entropy will experience a discontinuity in its temperature derivative, because the component of the heat capacity that has to do with the reconfigurational motions of the particles is zero after the quench. (The vibrational component of the entropy will also show a small discontinuity in the temperature derivative because the  $(\partial V/\partial T)_p$  derivative will experience a jump.) As a result, the heat capacity will exhibit a jump at  $T_g$ . In actuality, the quench rate is always finite, implying the discontinuity in the heat capacity is partially smeared out, see the inset of Fig. 2.

The crystal states within the enthalpy gap are quite distinct from the supercooled-liquid states. On the left flank, they simply correspond to vibrational motions of the lattice. However, if one were to extrapolate the crystal branch toward high enthalpies so that it overlaps in enthalpy with the liquid branch, things may become more interesting: Various defect states may now become possible that are associated with what is called “mechanical melting.” Mechanical melting was proposed early on by Born and others as the cause of the melting of crystals [63]. In this mechanism, the lattice becomes soft through the proliferation of defects—such as dislocations—and melts in a relatively smooth fashion, possibly continuously. A more extreme version of such a defect-based picture of melting was proposed by Mott and Gurney [64], who visualised a liquid as a polycrystal in a very small crystallite limit. Such mechanical melting is hard to observe experimentally, however,

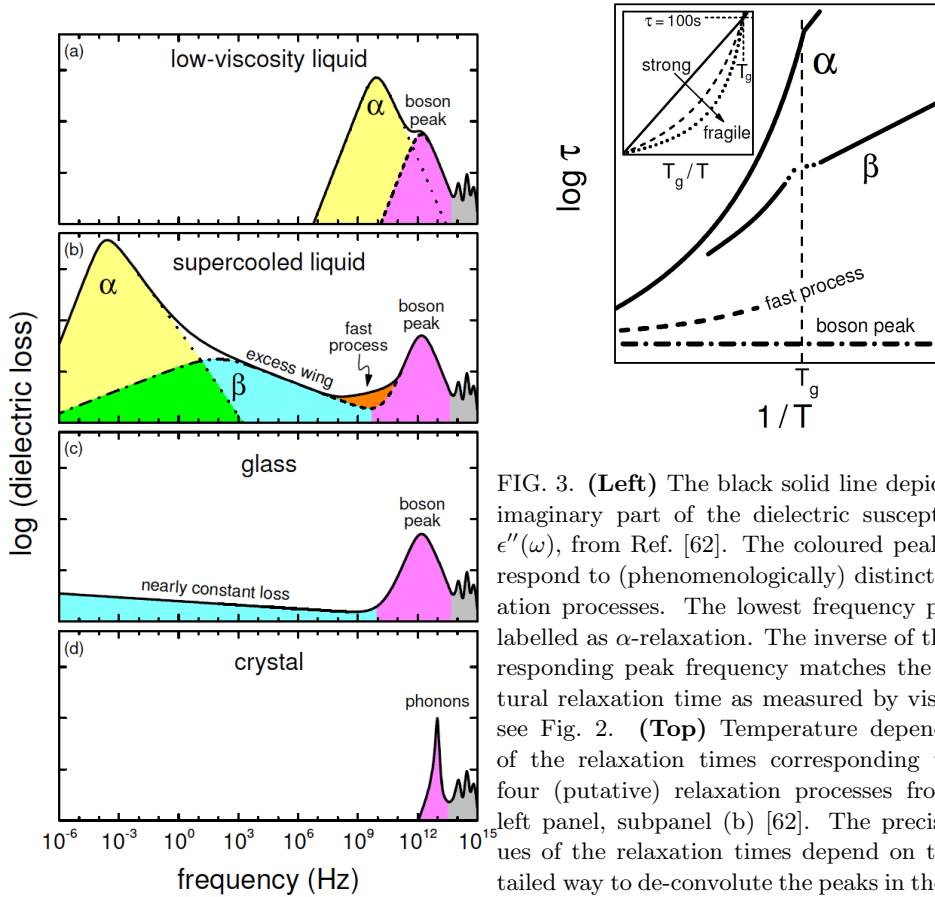


FIG. 3. **(Left)** The black solid line depicts the imaginary part of the dielectric susceptibility  $\epsilon''(\omega)$ , from Ref. [62]. The coloured peaks correspond to (phenomenologically) distinct relaxation processes. The lowest frequency peak is labelled as  $\alpha$ -relaxation. The inverse of the corresponding peak frequency matches the structural relaxation time as measured by viscosity, see Fig. 2. **(Top)** Temperature dependences of the relaxation times corresponding to the four (putative) relaxation processes from the left panel, subpanel (b) [62]. The precise values of the relaxation times depend on the detailed way to de-convolute the peaks in the overall spectrum.

because crystals melt at the surface well before they soften in the bulk. Since the barrier for surface melting is very low,  $k_B T$  or so [65], it is very hard to overheat a crystalline sample unless its sides are “clamped” using a material with a higher melting point [66, 67]. For these reasons, melting is usually “thermodynamic,” not mechanical, as it takes place near the temperature  $T_m$ , where the chemical potentials of the two phases are equal. Both experiment [66] and simulation [68] suggest that mechanical melting would take place at tens to hundreds of degrees above the melting temperature  $T_m$ .

It is not particularly conventional to employ the tangent construction using the enthalpy as the variable and the entropy as the thermodynamic potential. Yet this is completely analogous to the tangent construction used to discuss first order transitions accompanied by volume change in terms of the Helmholtz free energy as the thermodynamical potential and the specific volume as the variable, see Fig. 1(b). The common tangent in this picture reflects the mechanical equilibrium between the liquid and crystal during phase coexistence, analogously to the way the common tangent in panel (a) reflects the thermal equilibrium between the two phases. Fig. 1(b) also shows that such mechanical equilibrium can not be achieved in the isochoric ensemble without compensating externally for the difference in pressures between the liquid and crystal, by a mechanical partition for instance. The main drawback of the canonical ensemble exemplified in Fig. 1(b), where one would control the temperature not enthalpy, is that this ensemble completely misses the supercooled states, which can be seen explicitly only in a microcanonical construction, such as in Fig. 1(a).

The basic thermodynamic notions discussed above demonstrate that supercooled liquids and glasses are quite different from the corresponding crystal in that they belong to a

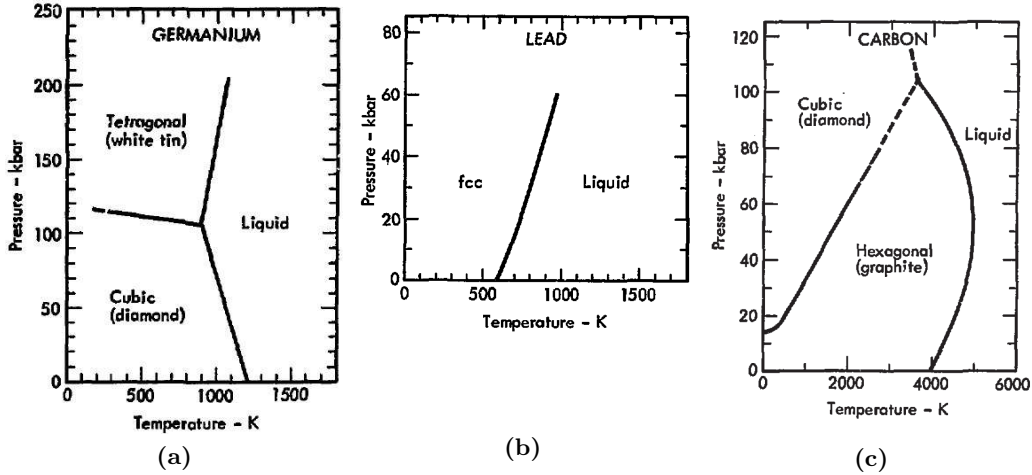


FIG. 4. Pressure-temperature phase diagrams for (a) germanium, (b) lead, and (c) carbon, from Ref. [69]. Note all three elements represent closed-shell configurations plus four valence electrons.

disparate, disconnected portion of the phase space and so at least some differences in how rigidity emerges in crystalline and glassy solids may be expected. We also directly see that the view of a glass as a defected crystal, which is often adopted in analyses of cryogenic and optoelectronic anomalies in glasses, misses the important point that the crystalline arrangement is not accessible to the atoms and so using it as a reference state for defect formation is meaningless. (Note the overlap between the wave-functions of the crystal and glass is negligible.) Instead, we shall see that one can define such reference states using mean-field aperiodic free energy minima, while the “defect” configurations correspond to interfaces between the minima and are intrinsic to an equilibrated supercooled liquid; the concentration of these high free-energy, defective regions depends only logarithmically on the speed of quenching. In contrast, the quantity of defects in crystals, such as vacancies, dislocations, twins, etc., is generally determined by the precise crystal growth setup and the interplay between heterogeneous and homogeneous nucleation, in addition to a sensitive dependence on the thermal history of the sample.

### III. LIQUID-TO-CRYSTAL TRANSITION AS A BREAKING OF TRANSLATIONAL SYMMETRY. REVIEW OF THE THEORY OF LIQUIDS AND LIQUID-TO-SOLID TRANSITION.

Before we can discuss the thermodynamics of the glass transition, it is necessary to discuss what drives the *ordinary* liquid-to-periodic-crystal transition. In addition to establishing commonalities and distinctions between periodic and aperiodic crystals, this will provide us with a practical reference point in gauging the quality of our “understanding” of the glass transition.

#### A. What drives crystallisation, why it is a discontinuous transition, and why the entropy of fusion is modest

In an extreme view of solids as very large molecules, it is tempting to think that crystallisation is driven, thermodynamically, by bond formation between the atoms. This notion seems to apply particularly well to crystals with open structures and directional bonding,

such as Si, Ge, and H<sub>2</sub>O. In the (low pressure) solids of these substances, atoms are less coordinated than in the corresponding liquids above melting, as witnessed by a positive volume change following crystallisation:  $\Delta V > 0$ , see the phase diagram of germanium in Fig. 4(a). One expects that at higher pressures, the bonding anisotropy becomes progressively subdominant to the steric repulsion, leading to the more conventional reduction in volume upon freezing,  $\Delta V < 0$ , as is the case for lead or high-pressure germanium, see Fig. 4. Yet there is generally no simple correlation between the pressure and the sign of  $\Delta V$ , as is exemplified by the phase diagram of carbon shown in Fig. 4(c). Although all three elements in Fig. 4 represent closed-shell configurations plus four valence electrons, they show very different phase behaviours. Clearly, bonding changes play a significant role in the liquid-to-crystal transition and exhibit remarkable variety even for seemingly similar electronic configurations.

Yet, while partially correct, the notion of the bonding-driven crystallisation is potentially misleading. The majority of enthalpy change due to bonding in the condensed phase occurs already during the vapour-to-liquid transition, whose latent heat is typically an order of magnitude greater than that for the liquid-to-crystal transition. This fact is reflected in the venerable Trouton’s rule [56], by which the entropy of condensation at normal pressure is numerically close to  $10^1 k_B$  per particle, compared with the fusion entropy of about  $10^0 k_B$  mentioned earlier. Indeed, the fusion enthalpy is comparable to the kinetic energy and thus is much lower than the bond enthalpy, suggesting the crystal stability is of somewhat subtle origin.

The relatively small entropy change upon freezing can be understood using the following qualitative, mean-field argument [64, 70, 71]: Neglecting correlation between particles’ movements, the partition function for the liquid can be roughly estimated as

$$Z_{\text{liquid}} \sim \frac{1}{N!} \left( \frac{V_f}{\Lambda^3} \right)^N, \quad (1)$$

where  $\Lambda \equiv (2\pi\hbar^2/mk_B T)^{1/2}$  is the de Broglie thermal wavelength. The quantity  $V_f$  is the total “free” volume, i.e., the total volume of the system minus the combined volume of the molecules which we approximate here as relatively rigid, compact objects. The combinatorial factor  $1/N!$  reflects that the particles are indistinguishable (Ref. [55], Chapter 41). The symmetry of the Hamiltonian with respect to particle identity is physically realised by the particles exchanging locations: The defining feature of an equilibrium liquid/gas is the uniform distribution of a particle’s density on any meaningful time scale. This is just a technical way to say that the liquid assumes the shape of its container. In contrast, particles comprising a solid are confined to “cages” with specific locations in space, which enables one to actually *label* the particles, even if they are indistinguishable otherwise. To estimate the partition function for the corresponding solid, let us use the Einstein approximation—which *also* neglects particle-particle correlations. Here we simply multiply the partition functions for individual particles each rattling within its own cage. The cage volume is the free volume per particle:  $V_f/N$ , thus yielding:

$$Z_{\text{solid}} \sim \frac{1}{N^N} \left( \frac{V_f}{\Lambda^3} \right)^N \quad (2)$$

The  $N!$  factor is now absent because particles in a solid can be labelled (according to which lattice sites they are nearest to) and thus may be regarded as distinguishable, as just mentioned. Consequently, the excess entropy of the liquid relative to the corresponding crystal is about  $k_B \ln(N^N/N!) \simeq Nk_B$ , roughly consistent with observation. We thus tentatively conclude that the entropy of fusion is relatively small because the translational (or “mixing”) entropy in the uniform liquid only modestly exceeds the vibrational entropy

of particle motions within assigned cages in the corresponding solid; the interactions enter the analysis through the free volume and cage shape and contribute toward system-specific corrections to the simple result  $Nk_B$ . Note that the modest value of the translational entropy in gases/liquids is a consequence of an interaction that is of statistical origin. This interaction is present even if the particles do not interact in energetic terms: Because two configurations in which two identical particles are interchanged are not distinct, the volume statistically available to an individual particle is not the total free volume  $V_f$ , but only a tiny portion of it, i.e.,  $eV_f/N$  or so, see Eq. (1).

But, in the first place, why should the liquid-to-crystal transition ordinarily be first order? This is not an entirely trivial question. For instance, early computer simulations [72], which employed small system-sizes, were ambiguous as to the discontinuous nature of the transition for hard spheres; particles had to be confined to individual cells in space to minimise effects of fluctuations, see discussion in Ref. [73]. An early constructive argument in favour of a discontinuous nature of the liquid-to-solid transition is contained in a prescient paper published by Bernal in 1937 [74], to which we shall return in due time. Of the most general applicability is Landau’s symmetry-based argument [75, 76], whose publication also dates to 1937 and *also* significantly predates the aforementioned liquid simulations. The main tool in the argument is what is now known as the Landau-Ginzburg functional [26, 55],

$$F = \int d^3\mathbf{r} [\kappa(\nabla\phi)^2/2 + V(\phi)]. \quad (3)$$

We begin from the simplest non-trivial approximation for the bulk free energy term, viz., in terms of a 4th order polynomial:

$$V(\phi) \equiv \frac{A}{2}\phi^2 + \frac{B}{3}\phi^3 + \frac{C}{4}\phi^4. \quad (4)$$

In the Landau-Ginzburg approach one makes a non-obvious assumption that both the bulk term and the  $(\nabla\phi)$ -dependent term—which we have truncated at the second order—are well-behaved, i.e., analytic.

To make analysis constructive, the terms in the expansion (4) must be traced to physical interactions. Let us do this first for a familiar system, namely, the Ising spin model with the energy function

$$\mathcal{H} = - \sum_{i<j} J_{ij} \sigma_i \sigma_j, \quad \sigma_i = \pm 1. \quad (5)$$

One can formally write down the Helmholtz free energy of the magnet as a sum of two contributions, both of which are uniquely determined by the average magnetisation on individual sites:

$$F(\{m_i\}) = F_{\text{id}}(\{m_i\}) + F_{\text{ex}}(\{m_i\}) \quad (6)$$

where the “ideal gas” contribution:

$$F_{\text{id}}(\{m_i\}) = k_B T \sum_i \left( \frac{1+m_i}{2} \ln \frac{1+m_i}{2} + \frac{1-m_i}{2} \ln \frac{1-m_i}{2} \right), \quad (7)$$

is the free energy of  $N$  non-interacting, *free* spins and is simply the sum over the entropies of individual, standalone spins, times  $(-T)$ . This expression can be easily derived by noting that the energy of a free spin is zero while the entropy of a spin with average magnetisation

$$\langle \sigma_i \rangle = m_i \quad (8)$$

is equal to the log-number of distinct configurations of a macroscopic number  $N$  of spins, of which  $N(1+m_i)/2$  point up and  $N(1-m_i)/2$  point down (divided by  $N$  and multiplied

by  $k_B$ ). Thus the entropy of a free spin with average magnetisation  $m_i$  is simply the Gibbs mixing entropy of two ideal gases with mole fractions  $(1 + m_i)/2$  and  $(1 - m_i)/2$ , per particle. Now, the excess term includes all other contributions to the free energy and is difficult to write down except in a few cases [26, 77]. We will content ourselves with a mean-field approximation, which becomes exact when each spin interacts infinitely weakly with an infinite number of other spins. For the Ising magnet from Eq. (5), this would imply  $J_{ij} = J/N$ , so that the energy scales linearly with  $N$ , see Problem 2-2 of Goldenfeld [26]. Because each spin is in “contact” with  $(N - 1)$  spins, this situation formally corresponds to an infinite dimensional space, the exact dimensionality depending on the type of lattice. For a cubic lattice, the dimensionality would be  $(N - 1)/2$ . In the mean-field limit, the correlations between spin flips can be ignored, since  $\langle \sigma_i \sigma_j \rangle \approx \langle \sigma_i \rangle \langle \sigma_j \rangle + O(1/N) \xrightarrow{N \rightarrow \infty} m_i m_j$ . The entropy of such a collection of uncorrelated spins is equal to that of  $N$  free spins, and so  $F_{\text{ex}}$  is simply the average energy, since  $F = E - TS$ . Averaging energy (5) in the mean-field limit  $\langle \sigma_i \sigma_j \rangle = m_i m_j$  readily yields:

$$F_{\text{ex}}(\{m_i\}) = - \sum_{i < j} J_{ij} m_i m_j \quad (\text{mean-field limit}). \quad (9)$$

Note that given the knowledge of the free energy as a function of  $m_i$ 's, the couplings  $J_{ij}$  can be determined by varying the free energy with respect to the magnetisation on sites  $i$  and  $j$ :

$$J_{ij} = - \frac{\partial^2 F_{\text{ex}}}{\partial m_i \partial m_j}. \quad (10)$$

( $\partial^2 F_{\text{id}} / \partial m_i \partial m_j$ ) = 0, of course.

From now on, assume for concreteness that all of the couplings are positive:  $J_{ij} > 0$ . In a translationally invariant system,  $J_{ij} = J(\mathbf{r}_i - \mathbf{r}_j)$ , the local magnetisation that minimises the functional is spatially uniform:  $m_i = m$ , and is an appropriate order parameter. In this strictest, spatially-uniform limit of the mean-field approximation, the Helmholtz free energy of the magnet reads, per spin:

$$F(m)/N = k_B T \left( \frac{1+m}{2} \ln \frac{1+m}{2} + \frac{1-m}{2} \ln \frac{1-m}{2} \right) - \frac{1}{2} (\sum_j J_{ij}) m^2. \quad (11)$$

The bulk free energy (11) is the analog of the bulk free energy  $V(\phi)$  from Eq. (4).

The free energy cost of *deviations* from the strictly uniform configuration in Eq. (11) can be estimated by still using a mean-field approximation. The thermally-averaged interaction energy from Eq. (9) can be re-written as  $-(1/2) \sum_i m_i \sum_j J_{ij} m_j \simeq -(1/2) \sum_i m_i \sum_j J_{ij} \{1 + (\mathbf{r}_j - \mathbf{r}_i) \cdot \nabla + (1/2) [(\mathbf{r}_j - \mathbf{r}_i) \cdot \nabla]^2\} m(\mathbf{r})|_{\mathbf{r}=\mathbf{r}_i}$ , where we have truncated the Taylor expansion of  $m_j \equiv m(\mathbf{r}_j)$  around point  $\mathbf{r}_i$  at the 2nd order; this suffices to account for the longest wavelength fluctuations relative to the average magnetisation. If, on the other hand, we have an anti-ferromagnet, then an expansion around a finite wave-vector  $\mathbf{q} = \mathbf{q}_0$  should be performed, not  $\mathbf{q} = 0$ . Now, after summation in  $j$ , the 0th order term in the expansion gives the 2nd term on the r.h.s. of Eq. (11), while the 1st order term drops out by symmetry  $(\mathbf{r}_i - \mathbf{r}_{i+j}) = -(\mathbf{r}_i - \mathbf{r}_{i-j})$  and the 2nd order term simplifies to  $-(1/2) [\sum_j J_{ij} (\mathbf{r}_j - \mathbf{r}_i)^2 / (2 \cdot 3)] \sum_i m_i \nabla^2 m(\mathbf{r}_i)$ . In this expression, we switch from discrete summation to volume integration and integrate by parts to obtain, per spin:

$$\frac{1}{2} \left[ \frac{1}{6} (\sum_j r_{ij}^2 J_{ij}) \right] (\nabla m)^2. \quad (12)$$

This term represents the square-gradient term  $\kappa(\nabla\phi)^2/2$  in the Landau-Ginzburg expansion (3) for our ferromagnet. (The one-particle, entropic term from Eq. (6) does not contribute to

the square-gradient term.) The coefficient  $(\sum_j r_{ij}^2 J_{ij})$ , which corresponds with the coefficient  $\kappa$  in Eq. (3), follows a general pattern: Insofar as the interaction  $J_{ij}$  possesses a finite range  $l$ , the coefficient scales with  $l^2$  times an energy scale that characterises the interaction.

Now, returning to the bulk energy (11), the interaction term is second order in the order parameter  $m$  and is proportional to the coupling constant  $J$ , in reflection of its two-body origin. The entropic contribution *also* has a quadratic contribution, but of positive sign; it stabilises the symmetric phase,  $m = 0$ , at high temperatures. The total coefficient at the second order term reads as:  $A = -(\sum_j J_{ij}) + k_B T$  and vanishes at the critical (Curie) temperature  $T_c = (\sum_j J_{ij})/k_B$  leading to a ferromagnetic ordering below the Curie point, whereby macroscopic regions acquire non-zero magnetisation,  $m = \pm(-A/C)^{1/2} \neq 0$ . (The Curie point is lowered when non-meanfield effects are included in the treatment [26].) Note that the entropic part of the free energy limits the possible value of magnetisation:  $|m| < 1$ —and thus renders the functional stable. In the low order expansion (4), such stability is guaranteed by the quartic term, whereby  $C > 0$ , however there is no hard constraint on the magnitude of  $m$ . (This is reasonable so long as  $|m|$  is not too close to its maximum value of 1.) The spontaneous magnetisation  $m = \pm(-A/C)^{1/2}$  below the critical point corresponds to a non-zero (local) field which, in effect, breaks the time-reversal symmetry of the full Hamiltonians  $E(\{\sigma_i\}) = E(\{-\sigma_i\})$ . Incidentally, because of the time-reversal symmetry, the coefficient  $B$  at the cubic term in the functional is identically zero for the Ising model, which is an exception rather than the rule, as we shall see shortly.

To build a free energy functional of the form (4) that is appropriate for *particles*—we first specify that the order parameter reflect fluctuations of the density around its equilibrium value  $\rho_{\text{eq}}(\mathbf{r})$ , which we regard for now as coordinate-dependent, for the sake of generality:

$$\delta\rho(\mathbf{r}) \equiv \rho(\mathbf{r}) - \rho_{\text{eq}}(\mathbf{r}). \quad (13)$$

Analogously to Eq. (6), we present the total Helmholtz free energy of the liquid (whether uniform or not) as the sum of the “ideal gas” and interacting, or “excess” free energy contributions [78, 79]:

$$F[\rho(\mathbf{r})] = F_{\text{id}}[\rho(\mathbf{r})] + F_{\text{ex}}[\rho(\mathbf{r})], \quad (14)$$

The “ideal gas” part is given by the expression

$$F_{\text{id}}[\rho(\mathbf{r})] = k_B T \int d^3\mathbf{r} \rho(\mathbf{r}) [\ln(\rho(\mathbf{r})\Lambda^3) - 1]. \quad (15)$$

This equation is the Helmholtz free energy of an ideal gas whose concentration is not necessarily spatially-uniform. We split space into elemental volumes  $V_i$ , each containing  $N_i$  gas particles:  $F_{\text{id}} = \sum_i F_{\text{id}}^{(i)} = -k_B T \ln Z_{\text{id}}^{(i)} = k_B T V_i (N_i/V_i) [\ln(N_i/V_i) - 1]$ , each of the partial free energies  $F_{\text{id}}^{(i)}$  corresponds to Eq. (1) with  $V_f = V_i$ . Switching to continuum integration  $V_i \rightarrow d^3\mathbf{r}$  and replacing  $N_i/V_i$  with its value  $\rho(\mathbf{r})$  yields Eq. (15). The ideal-gas free energy (15) is the liquid analog of the entropic free energy Eq. (7). The only (and non-essential) difference that it also has an energetic contribution due to the kinetic energy of individual particles; this contribution obligingly renders the argument of the logarithm in Eq. (15) dimensionless.

Note Eq. (14) is formally exact; it embodies the main idea of the classical density functional theory (DFT). The DFT builds on the Hohenberg-Kohn-Mermin theorem [80, 81], which states that there is a unique free energy functional  $F[\rho(\mathbf{r})]$  that is minimised by the equilibrium density profile  $\rho_{\text{eq}}(\mathbf{r})$ . As in the ferromagnet case, the interacting part  $F_{\text{ex}}$  can be computed in 3D only approximately. Appropriate approximations will be discussed in due time. For now, let us formally expand the free energy (14) as a power series in terms

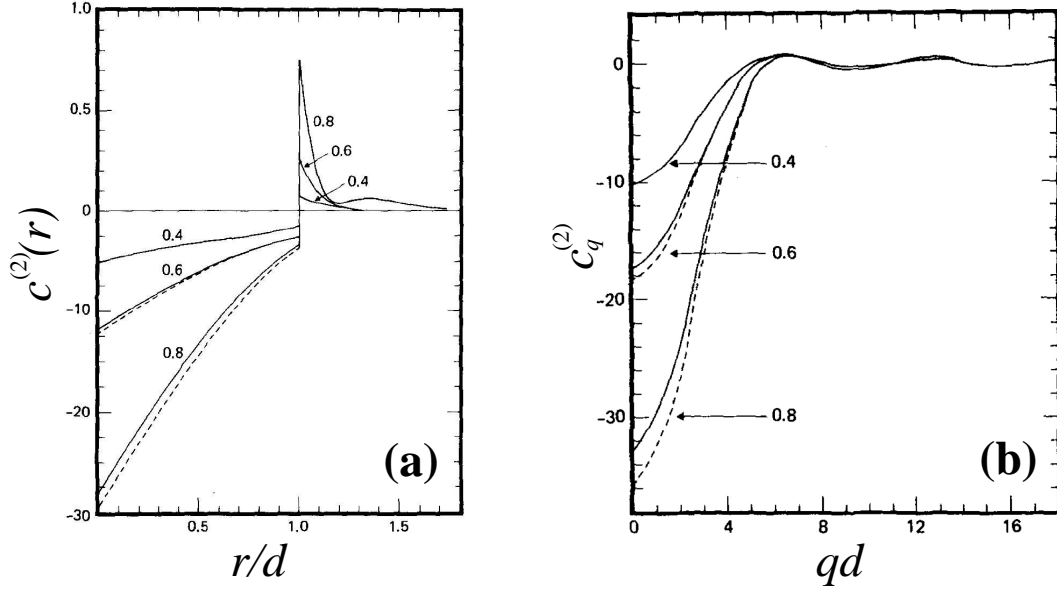


FIG. 5. We display two specific examples of the direct correlation function, corresponding to the Percus-Yevick (dashed line) and Henderson-Grundke [83] (solid line) approximations for the hard sphere liquid. Panels (a) and (b) show the function and its Fourier image respectively. Note the significantly finer scale on the positive portion of the vertical axis in panel (a).

of  $\delta\rho(\mathbf{r})$ , up to the second order:

$$F[\rho(\mathbf{r})] = F[\rho_{\text{eq}}(\mathbf{r})] + k_B T \int d^3\mathbf{r} \left[ \ln(\rho_{\text{eq}}(\mathbf{r})\Lambda^3) - c^{(1)}(\mathbf{r}) \right] \delta\rho(\mathbf{r}) \quad (16)$$

$$+ \frac{k_B T}{2} \int d^3\mathbf{r}_1 d^3\mathbf{r}_2 \delta\rho(\mathbf{r}_1) \left[ \frac{1}{\rho_{\text{eq}}(\mathbf{r}_1)} \delta(\mathbf{r}_1 - \mathbf{r}_2) - c^{(2)}(\mathbf{r}_1, \mathbf{r}_2) \right] \delta\rho(\mathbf{r}_2)$$

where, by definition,

$$c^{(1)}(\mathbf{r}) \equiv -\beta \frac{\delta F_{\text{ex}}}{\delta\rho(\mathbf{r})}. \quad (17)$$

and  $c^{(2)}(\mathbf{r}_1, \mathbf{r}_2)$  is the standard direct correlation function:

$$c^{(2)}(\mathbf{r}_1, \mathbf{r}_2) \equiv -\beta \frac{\delta^2 F_{\text{ex}}[\rho(\mathbf{r})]}{\delta\rho(\mathbf{r}_1) \delta\rho(\mathbf{r}_2)} \Big|_{\rho(\mathbf{r})=\rho_{\text{eq}}(\mathbf{r})}, \quad (18)$$

c.f. Eq. (10). Note that the direct correlation function is translationally invariant and isotropic for a bulk uniform liquid

$$\begin{aligned} \rho_{\text{eq}}(\mathbf{r}) &= \rho_{\text{liq}} \\ c^{(1)}(\mathbf{r}) &= c_{\text{liq}}^{(1)} \\ c^{(2)}(\mathbf{r}_1, \mathbf{r}_2) &= c^{(2)}(|\mathbf{r}_1 - \mathbf{r}_2|), \end{aligned} \quad (19)$$

but this assumption is not strictly correct in liquids that are not uniform—as would be the case in an otherwise homogeneous fluid near a wall or liquid-vapour interface [79] and, of course, in crystals [82].

As in the ferromagnet case, the second order term in Eq. (16) accounts for the two-body contributions to the free energy. Appropriately, it can be seen from Eq. (16) that in the



weak-interaction limit [78]:

$$c^{(2)}(\mathbf{r}_1, \mathbf{r}_2) \rightarrow -\beta v(\mathbf{r}_1, \mathbf{r}_2), \quad \text{as } \rho \rightarrow 0, \quad (20)$$

and so in this limit, the direct correlation function has the same range as the pairwise interaction  $v(\mathbf{r}_1, \mathbf{r}_2)$ . Even near critical points, where the full density-density correlation function becomes so long-ranged that the compressibility diverges, the direct correlation function remains integrable (see Eq. (69) and (70) below). The direct correlation function  $c^{(2)}(\mathbf{r}_1, \mathbf{r}_2)$  includes all interactions between these two particles, including those induced by the rest of the particles. For instance,  $c^{(2)}(r)$  for the hard sphere liquid has a positive—i.e., “attractive” by Eq. (20)—tail around  $r = d$ , see Fig. 5(a). Two neighbouring particles are effectively pushed together by being repelled from the surrounding particles. (This is analogous to the so called “depletion interaction” that can be induced between molecules by adding polymer to the solution [84].) At short separations,  $r < d$ , the direct correlation function has a rather different meaning. Namely, it scales (with the negative sign) with the bulk modulus of the liquid. This notion will be made precise in a short while. For now, it is instructive to compare the free energy cost of quadratic fluctuations in Eq. (16) to the free energy cost of a weak deformation of an elastic continuum [85]:

$$F = \iint d^3\mathbf{r}_1 d^3\mathbf{r}_2 D(\mathbf{r}_1 - \mathbf{r}_2) \left[ \left( \frac{K}{2} - \frac{\mu}{3} \right) u_{jj}(\mathbf{r}_1) u_{ll}(\mathbf{r}_2) + \mu u'_{ij}(\mathbf{r}_1) u'_{ij}(\mathbf{r}_2) \right] \quad (21)$$

where the deformation tensor  $u_{ij}$  is defined in the standard fashion:

$$u_{ij} = (1/2) (\partial u_i / \partial x_j + \partial u_j / \partial x_i) \quad (22)$$

and  $u'_{ij}$  stands for its traceless portion  $u'_{ij} \equiv u_{ij} - \frac{1}{3} \delta_{ij} u_{ll}$  that corresponds to pure shear. The vector  $\mathbf{u}$  gives a particle’s displacement relative to its equilibrium position, while its divergence  $u_{ii}$  yields the relative volume change of a compact region encompassing a specific group of atoms, due to uniform contraction or dilation. Eq. (21) corresponds to a non-local form of the elasticity theory [86–88], which is reduced to the classic, ultra-local approximation [85] by taking the limit  $D(\mathbf{r}) \rightarrow \delta(\mathbf{r})$ . In this continuum limit, the coefficient  $K$  corresponds with the macroscopic bulk modulus:

$$K \equiv -V \left( \frac{\partial p}{\partial V} \right)_T, \quad (23)$$

while  $\mu$  becomes the standard shear modulus. This is where we can make connection with the functional in Eq. (16), since the  $\delta\rho$ ’s in that equation *also* scale with local volume changes. For a region containing an appreciable number of particles,  $\delta\rho/\rho = -u_{ii}$ . Despite this relation, we note that there is generally no one-to-one correspondence between the deformation tensor  $u_{ij}$  and the local density variation  $\delta\rho$  because the former is a quantity coarse-grained over a mesoscopic region, while the latter is defined on an arbitrarily small length scale and can change arbitrarily rapidly in space. For instance, for a stationary particle at the origin,  $\rho(\mathbf{r}) = \delta(\mathbf{r})$ . Now, to connect the functionals (16) and (21), we first set  $\mu = 0$  as is appropriate for uniform liquids. Because only long-wavelength density variations can be compared between the two functionals, we can adopt the continuum limit of the elasticity:  $F = (1/2) \int d^3\mathbf{r} K u_{jj}^2(\mathbf{r})$ , yielding  $K u_{jj}^2(\mathbf{r})/2$  for the free energy density at location  $\mathbf{r}$ . By Eq. (16), the same quantity is given by  $(k_B T/2) \delta\rho^2(\mathbf{r}) \int d^3\mathbf{r} [1/\rho_{\text{eq}} - c^{(2)}(r)]$ , where we used that the direct correlation function decays much faster than the lengthscale for density variations. For such slow variations,  $\delta\rho/\rho = -u_{ii}$ , and we obtain:

$$-\rho_{\text{liq}} \int d^3\mathbf{r} c^{(2)}(r) = \frac{K}{k_B T \rho_{\text{liq}}} - 1, \quad (24)$$

c.f. the systematically derived Eq. (71).

Now, as a rule of thumb, the bulk modulus is about  $(10^1 - 10^2)k_B T / \rho_{\text{liq}}$  for liquids and  $10^2 k_B T / \bar{\rho}$  for solids (consistent with the Lindemann criterion of melting) [67]. The above argument explains why the direct correlation function should be mostly large and negative at the high densities in question, see Fig. 5(a). We observe that the direct correlation function is thus a rather complicated, rich object; it will be central to our further developments.

The free energy expansion (16), when applied to a *uniform* liquid, Eq. (19), looks particularly revealing in the Fourier space as it is simply a sum over independent harmonic oscillators represented here by the distinct Fourier modes:

$$F - F(\rho_{\text{liq}}) = \frac{k_B T}{2} \int \frac{d^3 \mathbf{q}}{(2\pi)^3} \left( \frac{1}{\rho_{\text{liq}}} - \tilde{c}_q^{(2)} \right) |\delta \tilde{\rho}_q|^2. \quad (25)$$

We have omitted the term linear in  $\delta \rho(\mathbf{r})$ , which is equal to  $(\partial F / \partial N)_{V,T} (N - \langle N \rangle) = \mu (N - \langle N \rangle)$ , where  $\mu \equiv (\partial F / \partial N)_{V,T}$  is the bulk chemical potential. This linear term can be set to zero by fixing the total particle number  $N$  at its expectation value  $\langle N \rangle$  and is not relevant to *local* density fluctuations. An example of the Fourier transform of the direct correlation function is provided in Fig. 5(b).

Consistent with the pattern in Eq. (12), the square gradient term in the Landau-Ginzburg functional corresponding to the liquid free energy (14) is given by [89]:

$$\frac{1}{2} \left[ \frac{k_B T}{6} \int d^3 \mathbf{r} r^2 c^{(2)}(r) \right] (\nabla \rho)^2, \quad (26)$$

which can be seen by expanding  $c_q^{(2)}$  up to second order in  $q$ :  $c_q^{(2)} = \int d^3 \mathbf{r} e^{-i\mathbf{q}\mathbf{r}} c^{(2)}(r) \approx \int d^3 \mathbf{r} [1 - i(\mathbf{q}\mathbf{r}) - (\mathbf{q}\mathbf{r})^2/2] c^{(2)}(r) = \int 4\pi r^2 dr [1 - q^2 r^2/6] c^{(2)}(r)$ .

Now returning to the issue of the liquid-to-crystal transition, the emergence of a solid will be signalled by the appearance of a finite, non-uniform component in the density profile, see Fig. 6(a). Because the density variations of interest for an ordinary liquid-to-crystal transition are periodic, for that situation it is convenient to present the variations as a Fourier series in terms of the vectors  $\mathbf{q}$  of the reciprocal lattice:

$$\delta \rho(\mathbf{r}) = \sum_{\mathbf{q}} \delta \tilde{\rho}_{\mathbf{q}} e^{i\mathbf{q}\mathbf{r}}. \quad (27)$$

According to Eq. (25), the second order term in the Landau expansion can be presented in the form  $\sum_{\mathbf{q}} \tilde{A}_{\mathbf{q}} |\delta \tilde{\rho}_{\mathbf{q}}|^2 / 2$ . To avoid confusion, we note that for a general form of  $\tilde{A}_{\mathbf{q}}$ , the bulk free energy  $V(\phi)$  from the Landau-Ginzburg functional (3) no longer has the ultralocal form from Eq. (4). Instead, non-local interactions are now explicitly included, as in Eqs. (16) and (21):  $\int d^3 \mathbf{r} A \phi^2 / 2 \rightarrow \int d^3 \mathbf{r}_1 d^3 \mathbf{r}_2 A(\mathbf{r}_1, \mathbf{r}_2) \phi(\mathbf{r}_1) \phi(\mathbf{r}_2) / 2$ , and likewise for higher-order interactions  $\int d^3 \mathbf{r} B \phi^3 / 3 \rightarrow \int d^3 \mathbf{r}_1 d^3 \mathbf{r}_2 d^3 \mathbf{r}_3 B(\mathbf{r}_1, \mathbf{r}_2, \mathbf{r}_3) \phi(\mathbf{r}_1) \phi(\mathbf{r}_2) \phi(\mathbf{r}_3) / 3$ , etc. Still, we shall see that when only the dominant Fourier modes are included, the stability analysis of the functional will simplify to that of the original form (4).

In the symmetric, uniform phase the coefficients  $\tilde{A}_{\mathbf{q}}$  are all positive. A (mean-field) instability toward a density wave at a particular value of  $\mathbf{q}$  such that  $|\mathbf{q}| = q_0$  will reveal itself through vanishing of the corresponding coefficient  $\tilde{A}_{q_0}$ , see Fig. 6(b). Landau states that simultaneous vanishing of  $\tilde{A}_{\mathbf{q}}$  at more than one value of  $q$  is “unlikely,” which is consistent with the  $\tilde{c}_q^{(2)}$  from Fig. 5(b). We will go along with this mean-field view for now and write the second order term as  $\tilde{A}_{q_0} |\delta \tilde{\rho}_{q_0}|^2 / 2$  but should recognise that  $A_{\mathbf{q}}$  is a smooth function of  $q$  and thus should be rather small in a *finite* range of  $q$  around the vicinity of  $q_0$ . The latter quantity, of course, reflects the spacing  $a$  between the particles.

We can now focus on this most unstable set of modes  $|\mathbf{q}| = q_0$ . In the Fourier sum corresponding to the third-order term in the free energy,  $\sum_{\mathbf{q}_1} \sum_{\mathbf{q}_2} \sum_{\mathbf{q}_3} \tilde{B}_{\mathbf{q}_1, \mathbf{q}_2, \mathbf{q}_3} \delta \tilde{\rho}_{\mathbf{q}_1} \delta \tilde{\rho}_{\mathbf{q}_2} \delta \tilde{\rho}_{\mathbf{q}_3} / 3$

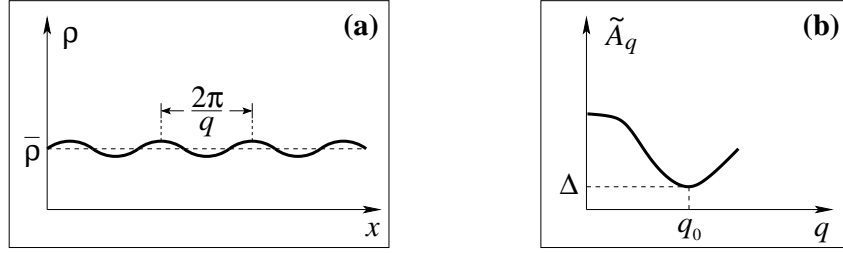


FIG. 6. **(a)** The emergence of a solid is signalled by the a deviation of the equilibrium density profile  $\rho(\mathbf{r})$  from uniformity  $\rho(\mathbf{r}) \neq \text{const}$ . When the solid is periodic, the density profile is, too. **(b)** The wavevector dependence of the coefficient  $\tilde{A}_q$  at the Fourier component of the second order term in the Landau-Ginzburg functional (3), see Eq. (28), as originally envisioned by Landau [75, 76]. Consistent with Eq. (25) and Fig. 5(b), the second order term in Landau-Ginzburg expansion will vanish at a select, finite value of the wave-vector  $q = q_0$ , as  $\Delta \rightarrow 0$ . The resultant excitation spectrum is determined by the absolute value of  $\mathbf{q}$ , but not its direction, and is thus quasi-one-dimensional.

only the term such that  $\mathbf{q}_1 + \mathbf{q}_2 + \mathbf{q}_3 = 0$  survives, if the coupling  $B(\mathbf{r}_1, \mathbf{r}_2, \mathbf{r}_3)$  between density fluctuations is translationally invariant:  $B(\mathbf{r}_1, \mathbf{r}_2, \mathbf{r}_3) = B(\mathbf{r}_1 + \mathbf{R}, \mathbf{r}_2 + \mathbf{R}, \mathbf{r}_3 + \mathbf{R})$  for any vector  $\mathbf{R}$ . Given that we are limited to  $|\mathbf{q}_i| = q_0$ , the constraint  $\mathbf{q}_1 + \mathbf{q}_2 + \mathbf{q}_3 = 0$  implies the three wavevectors form an equilateral triangle with side  $q_0$ . As pointed out by Alexander and McTague [90], the crystal types whose reciprocal lattices contain equilateral triangles are easy to enumerate: In 2D, these are the triangular and hexagonal lattice. (That the triangular lattice is essentially a sum of three properly phased plane waves propagating at 60, 180, and 300 degrees is particularly obvious [91].) Note the triangular lattice maximises the packing density of monodisperse circles in 2D, both locally and globally [92]. In 3D, only the body-centred cubic (bcc) fits the bill but that alone enables us to make the crucial conclusion that the coefficient  $B$  at the 3rd order term is generally non-zero for liquids, in contrast with the Ising magnet for example. This result (of a somewhat tortuous argument) is consistent with the simple intuition that a three-body term—hence, a three-body contact—is necessary to build a mechanically stable structure in spatial dimensions 2 and 3. Of course, three-body interactions are present in actual liquids, as chemical bonds are generally directional. Finally note that the regular icosahedron also consists of the equilateral-triangle motifs but does not tile the (reciprocal) space owing to its fivefold symmetry. Likewise its reciprocal (dual) polyhedron, i.e., the regular dodecahedron, does not tile the direct space. Still note that the regular dodecahedron is the Voronoi cell for the *locally* densest packing of monodisperse spheres. That such cells do not tile (flat) 3D space, makes the problem of the densest packing 3D difficult. Indeed, the Kepler conjecture about the volume fraction of the closest-packed arrays of monodisperse spheres has been proven only recently [92]. To summarise, the third-order term accounts for the instability of liquids toward *density*-driven solidification, however given the constraint of periodicity, this term favours the BCC lattice.

For the functional (4) to be stable, the coefficient  $C$  at the quartic term must be positive; let us fix it at a certain value for now and focus solely on the coefficients  $A$  and  $B$  at the quadratic and cubic term respectively. The coefficients  $A$  and  $B$  are generally linearly independent functions of pressure and temperature:  $A = A(p, T)$ ,  $B = B(p, T)$ . As a result, we may consider the phase diagram of the system in the  $(A, B)$  plane, shown in Fig. 7, with the understanding that the  $(p, T)$  phase diagram can be obtained from that in Fig. 7 by a simple coordinate transformation  $p = p(A, B)$ ,  $T = T(A, B)$ .

It is easy to see that there are three distinct phases, as we discuss in the following and graphically summarise in Fig. 7: The symmetric phase  $\langle \phi \rangle = 0$  is separated from two distinct

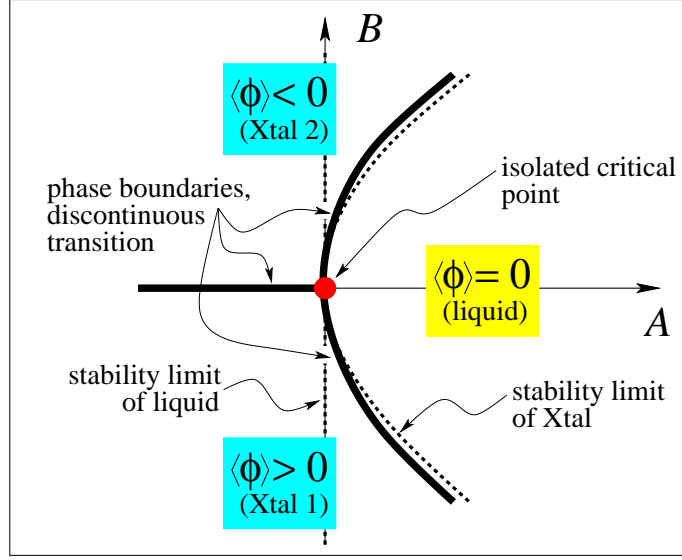


FIG. 7. The mean-field phase diagram of the Landau-Ginzburg functional (3) in the  $(A, B)$  plane,  $C = \text{const} > 0$ . The thick solid lines correspond to phase boundaries between the symmetric ( $\langle \phi \rangle = 0$ ) and two symmetry broken phases,  $\langle \phi \rangle < 0$  and  $\langle \phi \rangle > 0$  respectively. The symmetric phase corresponds to the uniform liquid, while the symmetry broken phases to crystalline solids with complementary density profiles. At each point along the boundaries, the transition is discontinuous, except at the isolated critical point  $A = B = 0$ . In finite dimensions, the critical point is avoided thus allowing one to argue that the liquid-to-crystal transition is always discontinuous in equilibrium, see text for detailed discussion.

ordered phases of lower symmetry,  $\langle \phi \rangle \neq 0$ , by a discontinuous transition at  $A = 2B^2/9C$ , except in one isolated point,  $A = B = 0$ , where the transition is continuous. The higher and lower symmetry phases correspond to the uniform liquid and crystal states respectively. The two ordered phases themselves are separated by a discontinuous transition, corresponding to the phase boundary at  $B = 0$ ,  $A < 0$ . These two ordered phases are intimately related: Because the  $B$  term switches sign across their mutual boundary, the density patterns of the two ordered phases are complementary to each other; to a particle in one structure, there corresponds a void in the other structure and vice versa. Finally note that there are two families of curves corresponding to the mechanical stability limit of the phases involved: To left of the  $A = 0$  line, the free energy minimum corresponding to the symmetric phase vanishes, while in the region  $A > B^2/4C$  the symmetric phase is the sole possible phase.

According to the phase diagram in Fig. 7, there cannot be a line of continuous phase transitions separating liquid from crystal. At most, there is a unique, isolated point at which the transition could be continuous. It should be understood that in the direct vicinity of this point, the transitions across the  $A = 2B^2/9C$  boundary will be only weakly first order, i.e., they are accompanied by a small change in the order parameter and a low latent heat, among other things. Landau notes that whether or not the critical point of the type in Fig. 7 can be observed in nature is unclear. Alexander and McTague go further to argue that, in fact, it *cannot*, owing to the “Brazovskiy” [93, 94] effect: Because the free energy contribution of modes  $\delta\tilde{\rho}_{\mathbf{q}}$  depends only on the length of the vectors  $\mathbf{q}$ , while  $\tilde{A}_{\mathbf{q}}$  vanishes at a finite value  $q = q_0$ , see Fig. 6(b), the dispersion relation for these modes is effectively one-dimensional. Indeed, just above the critical temperature  $T_c$ , the free energy cost for spatial

density variations reads (in the quadratic approximation and in  $D$  spatial dimensions):

$$F - F_{\text{uni}} = \frac{1}{2} \int \frac{d^D \mathbf{q}}{(2\pi)^D} \tilde{A}_q |\delta \tilde{\rho}_q|^2 \propto \int q^{D-1} dq [\Delta + (q - q_0)^2] |\delta \tilde{\rho}_q|^2, \quad (28)$$

c.f. Eqs.(25) and Fig. (5)(b). Clearly, the r.h.s. integral above is one-dimensional. On the other hand, the Landau-Ginzburg bulk energy describes the breaking of a discrete symmetry,  $\phi \leftrightarrow -\phi$ , as  $B \rightarrow 0$ . The Curie point of an Ising ferromagnet is a good example of such a discrete symmetry breaking. Critical points of this type are generally suppressed by fluctuations in one-dimensional systems at *finite* temperatures [55]. (This is true unless the interactions are very long range,  $1/r^2$  or slower [95, 96]; note excitations in elastic 3D solids interact at best according to  $1/r^3$  [85], see also below.) In the present context, these criticality-destroying fluctuations are motions of domain walls separating the two symmetry broken phases corresponding to  $B > 0$  and  $B < 0$  and are indeed quasi-one dimensional for interfaces with sufficiently low curvature. The Brazovsky effect implies that not only is the phase boundary between the symmetric and broken-symmetry phases moved down toward lower values of  $A$  owing to fluctuations—as it generally would—it also dictates that the continuous transition at  $B = 0$  will be pushed all the way down to  $T = 0$ . Thus, the liquid-to-crystal transition is always first order in equilibrium. (Conversely, one may be able to sample some of this criticality by using rapid quenches, to be discussed in due time.) We also note that to understand what actually happens at  $B = 0$ ,  $A < 0$ , i.e., which polymorph will be ultimately chosen by the system, generally requires knowledge of higher order terms in the functional (4).

The erasure of the critical point is not the only non-meanfield effect we should be mindful of. Recall that the coefficient  $\tilde{A}_q$  is small in a *finite* vicinity of the vector  $\mathbf{q}$ . This means that lattice types other than BCC, such as FCC, can become stable [97]. It is these structures in which the system could settle when the critical point at  $A = B = 0$  is avoided. Indeed, elemental solids display a variety of structures, with bcc being far from prevalent. Still, Alexander and McTague have argued that even if the BCC structure is not the most stable, it is likely most kinetically-accessible, especially near weakly discontinuous liquid-to-solid transitions, consistent with experiment [90].

The simplest possible approximation (4), in which one truncates the Landau-Ginzburg expansion at the fourth-order term, apparently covers the worst-case scenario in the sense that the presence of negative terms of order higher than three will only act to further suppress a *continuous* liquid-to-crystal transition. Indeed, suppose the coefficient  $C$  at the fourth-order term in Eq. (4) is negative, which dictates that we now expand the free energy up to the *sixth* order or higher. A negative fourth-order term stabilises a broken-symmetry phase,  $\phi \neq 0$ , even if the third-order term is strictly zero. Important examples of crystal-lattice types for which the fourth or higher order terms must be non-zero include the graphite, diamond, and simple-cubic lattices. For instance, to stabilise the graphite lattice, not only should the bond-angle be fixed at sixty degrees, for which a third-order term alone would suffice. In addition, the three bonds emanating from an individual particle must be stabilised in the planar arrangement. In the case of the diamond lattice, it is likely that the fifth-order term is non-zero, too: While a fourth-order term alone could stabilise local pyramidal configuration in which the bond-angles are at the requisite value of  $109.4^\circ$ , the resulting energy function could also favour stacked double-layers giving rise to a rhombohedral lattice, in addition to the diamond structure. (The latter stacked structure is exemplified by arsenic, however the angle is intermediate between  $109.4^\circ$  and  $90^\circ$ .) Likewise, a structure with enforced  $90^\circ$  bond-angles could, in principle, be simple-cubic but such a structure is often unstable toward tetragonal distortion. Interestingly, the only elemental solid that has the simple-cubic lattice structure at normal pressure is polonium. (Arsenic, phosphorus, and, of all things, calcium can be made simple-cubic by applying pressure [98, 99].) Consistent with

these notions, we know for a fact that interactions in actual crystals are truly many-body and are even affected by (electronic) relativistic effects [100]. Note the diamond, graphite, and simple-cubic lattices are some of the most open structures encountered in actual crystals. (Low density structure with nanovoids can be readily made [101] but are not uniformly open.)

The following picture emerges from the above discussion: The presence of a significant, fourth (or higher) order stabilising contribution to the free energy of the liquid leads to the formation of open structures with very directional bonding and thus reduces the effects of steric repulsion on the liquid-to-solid transition. At the same time the discontinuity of the liquid-to-crystal transition is relatively large, see discussion at the end of this Section. Liquids that freeze into the diamond lattice and expand alongside illustrate this situation particularly well. Conversely, if such high order terms in the free energy expansion are weak, excluded-volume effects become important that are accounted for by the third-order term. The smaller the third order term, the milder the discontinuity of the liquid-to-solid transition (if the higher-order terms are non-negative!). Still, the third-order terms cannot completely disappear in equilibrium because of the steric effects. On the other hand, quasi-one dimensional fluctuations would destroy the critical point, even if the third-order terms were very small. We thus conclude that those quasi-one dimensional fluctuations are *also* of steric origin. We reiterate that despite their importance, the steric effects are not the only player. It is essential to remember that the liquid is equilibrated at a *finite* temperature and, thus, is not jammed; the particles ultimately are allowed to vibrate and exchange places.

The above argument has a somewhat unsatisfactory feature in that it implies the free energy of a periodic solid can be computed using an expansion from the uniform state, even though the two states are separated by a phase transition. The bulk free energy generally exhibits singularities at phase transitions in finite dimensions and so expressions for low magnitude fluctuations around metastable equilibria cannot be analytically-continued across transitions in a straightforward way, see illustration in Fig. 8(a). Conversely, there are plenty of examples of mean-field free energies that are perfectly analytic near a phase transition, such as the one leading to the familiar van der Waals equation of state  $(V - V_f)[p + c(N/V)^2] = Nk_B T$ . These potential issues with the analytical continuation of the free energy do not invalidate the Landau argument, however. Indeed, if we assumed, for the sake of argument, that the transition did *not* take place, the free energy could extrapolate to a value that could only *exceed*  $F(\delta\rho = 0)$ . Since it does not do so, in fact, we then conclude that our assumption that the transition did not take place was incorrect. Consistent with this notion, a number of workers have, in practice, accomplished the program of building a periodic crystal state starting from the uniform liquid state, starting from the pioneering work of Kirkwood and Monroe [102]. Subsequent, detailed calculations along similar lines [103, 104] explicitly confirmed the discontinuous nature of the transition. At the same time, they showed that physical quantities, such as the liquid and crystal densities at the transition, converge slowly, if at all, with number of the reciprocal vectors in the expansion (27) [104].

These difficulties may stem, at least in part, from the large deviations of the crystalline density profile from a sinusoidal curve. In fact for a perfectly harmonic crystal, the density profile in a harmonic solid is a superposition of Gaussian peaks ([55], Chapter 138):

$$\rho(\mathbf{r}, \alpha) = (\alpha/\pi)^{3/2} \sum_i e^{-\alpha(\mathbf{r} - \mathbf{r}_i)^2}. \quad (29)$$

In contrast with the picture transpiring from Fig. 6(a), the peaks are rather sharp: Empirically [37, 65, 67, 105, 106],  $\alpha \simeq 100/a^2$  nearly universally, see Fig. 9(a). The quantities  $\mathbf{r}_i$  stand for the locations of the vertices of the lattice. The vibrational displacement in crystals goes with temperature roughly as  $T^{1/2}$ , above the Debye temperature, and is numerically close to its value near melting, i.e.,  $1/\sqrt{\alpha}a \simeq 1/10$  of the lattice spacing or so.

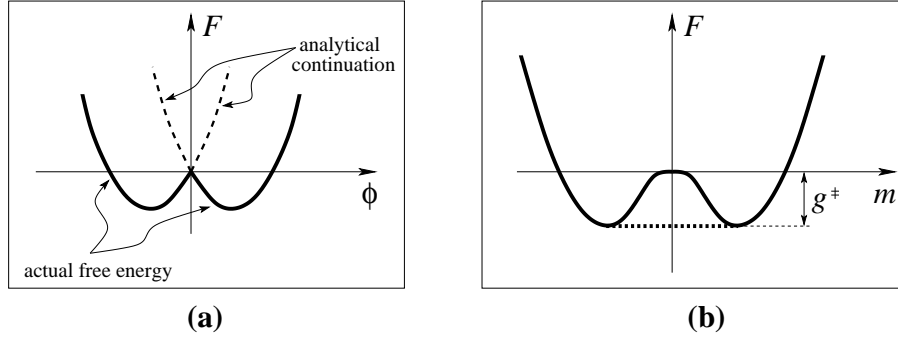


FIG. 8. **(a)** This sketch illustrates that analytical continuation of the free energy between distinct phases is generally ill-defined. **(b)** Thick solid line: The Helmholtz free energy  $F$  of a spatially *uniform* ferromagnet below the Curie point, as a function of the average magnetisation  $m \equiv M/N$  ( $M$  is the total magnetisation). The region separating the two minima is non-concave; one cannot use the Legendre transform to compute the Gibbs free energy  $G$ :  $G = F - Mh$ ,  $h = (\partial F / \partial M)_T$ . In equilibrium, the system phase-separates, and so the actual, equilibrium Helmholtz free energy between the two minima in  $F$  is given by the thick dashed line. The latter line is entirely analogous to the red line in Fig. 1(b).

The latter quotient should be nearly universal, as was argued by Lindemann more than a century ago. It is by no means intuitively obvious that the vibrational displacement near melting, which is often called the Lindemann length, should be as small as one-tenths. Lindemann himself [107] thought that this displacement should be about a half of the particle spacing, which would be more consistent with the mild density variation in Fig. 6(a) than with the sharp peaks in Fig. 9(a). Lindemann’s (correct) logic was that the melting was caused by intense collisions between the atoms. Still, both experiment and theory indicate the dramatic anharmonicities that eventually lead to crystal’s disintegration should become important already at  $\alpha \simeq 100/a^2$ . In Subsection IV A, we shall see that for rigid particles, the quantity  $\alpha a^2$  is essentially given by the number of particles in the first coordination shell (up to a logarithmic correction and a constant factor), which scales as the dimensionality of space squared, see Eq. (83).

It is straightforward to obtain an explicit expression for  $\alpha$ —which is the “spring constant” of an effective Einstein oscillator—given a specific form of the phonon spectrum. For instance, assuming isotropic elasticity with the isothermal bulk modulus  $K$  and shear modulus  $\mu$  and a Debye phonon spectrum with an ultraviolet cutoff at  $|\mathbf{k}| = \pi/a$ , one obtains [42]:

$$\alpha^{-1} \equiv \frac{1}{a} \frac{k_B T}{3\pi\mu} \frac{6K + 11\mu}{3K + 4\mu}. \quad (30)$$

It is particularly straightforward to discuss the driving force for the crystallisation of hard spheres, which do not form actual bonds and for which the enthalpy change during the transition:

$$\Delta H_m = \Delta E_m + p_m \Delta V_m \quad (31)$$

is entirely due to the work needed to compress the liquid:  $\Delta V_m < 0$ , at constant temperature. The stability of the hard sphere crystal, relative to the corresponding liquid (gas), stems from the notion that the densest packing of monodisperse spheres in 3D is a periodic crystal—face-centred cubic (FCC) or hexagonal close-packed HCP—which now appears to be rigorously proven [92]. This notion has resisted systematic effort since time of Kepler and is non-trivial because the most compact Voronoi cell of a particle surrounded by twelve neighbours—the highest number allowed in 3D—is the regular dodecahedron. The latter

has a five-fold symmetry and thus does not tile space. As follows from the proof of the Kepler conjecture, one can say that thermodynamically, the transition is density-driven or, equivalently, *sterically*-driven. Already the original Landau argument from 1937, which neglects fluctuations, suffices to show that the transition in hard spheres is first order: All points on the liquid-crystal phase boundary in the  $(p, T)$  plane are equivalent because the  $p/T$  ratio in hard spheres is determined by the density exclusively. Thus, it is impossible to have an isolated critical point on that phase boundary.

To give a partial summary, the liquid-to-crystal transition is a discontinuous phase transition resulting in a *breaking of translational symmetry*, upon which individual particles occupy specific cells in space as opposed to the whole space. The fusion entropy is essentially the difference between the entropy of translational motion in the uniform liquid and the vibrational entropy in the crystal. Consistent with this, the fusion entropy in open structures often exceeds that for crystallisation of well-packed structures, as we shall see explicitly in Subsection III C. For rigid particles, crystallisation is driven by steric repulsion alone. The liquid-to-crystal transition breaks a *continuous* symmetry. Breaking such a symmetry results in the emergence of Goldstone modes [26] below the transition, which are represented in crystals by the phonons [91]. To put this in perspective, the symmetry of the Hamiltonian to simultaneous flips of all spins  $\{\sigma_i\} \leftrightarrow \{-\sigma_i\}$ , which is broken during ferromagnetic ordering, is a discrete symmetry, see Fig. 8.

## B. Emergence of the Molecular Field

A methodological advantage of studying a monodisperse, hard-sphere liquid is that one can gain qualitative insight into its crystallisation while being able to test the corresponding approximations against simulations. Such tested approximations will come in handy when studying the emergence of rigidity in *aperiodic* systems, since monodisperse hard spheres crystallise too readily thus preventing one from achieving meaningfully deep quenches in a direct simulation.

Most of the quantitative theories of liquid-to-solid transition can be traced back to the very old idea of the “molecular field,” which was originally conceived in the context of the vapour-to-liquid transition by van der Waals [108] and in the context of ferromagnetism by Curie and Weiss [10, 109]. We have already benefited from thinking about the latter system; let us use it again to illustrate the concept of the molecular field. For a collection of Ising spins, Eq. (5), spin  $i$  is subject to an instantaneous field  $\sum_j J_{ij}\sigma_j$ . If we, in the mean-field fashion, ignore correlations in spin flips:  $\langle\sigma_i\sigma_j\rangle \approx \langle\sigma_i\rangle\langle\sigma_j\rangle$ , the (thermally-averaged) value of the molecular field  $h_i^{\text{mol}}$  is simply given by the expression:  $h_i^{\text{mol}} = \sum_j J_{ij}m_j$ . We observe that when a ferromagnet spontaneously polarises, so that  $m_i > 0$  or  $m_i < 0$ , this effective field becomes non-zero thus breaking the time-reversal symmetry  $\{\sigma_i\} \leftrightarrow \{-\sigma_i\}$  of the Hamiltonian  $\mathcal{H} = -\sum_{i<j} J_{ij}\sigma_i\sigma_j$ .

A systematic way to implement the concept of the effective field is to employ an additional ensemble. The Helmholtz free energy in Eq. (6) is the appropriate thermodynamic potential at fixed magnetisation and is analogous to the canonical construction for particulate systems, in which one fixes the volume of the system. Alternatively, one may use the ensemble in which the magnetisation is allowed to fluctuate while the magnetic field is fixed. In gases, this is analogous to allow for volume changes at fixed particle number, while subjecting the gas to external pressure (the isobaric ensemble); the corresponding thermodynamic potential is the Gibbs free energy  $G = F + pV$ . Alternatively, one may allow the particle number to change at fixed  $V$ , while imposing a specific value of the chemical potential (the grand-canonical ensemble); the corresponding free energy is  $\Omega = F - \mu N = -pV$  [55, 110].

To evaluate the Gibbs free energy for the magnet, let us formally write down the partition



function for the energy function from Eq. (5) with an added term  $-\sum_i h_i \sigma_i$ :

$$Z(\{h_i\}) = \sum_{\{\sigma_i = \pm 1\}} \exp[-\beta(\mathcal{H} - \sum_i h_i \sigma_i)]. \quad (32)$$

Clearly, the average magnetisation  $m_i \equiv \langle \sigma_i \rangle$  can be computed according to:

$$m_i = - \left( \frac{\partial G(\{h_i\})}{\partial h_i} \right)_T, \quad (33)$$

where  $G(\{h_i\}) \equiv -k_B T \ln Z(\{h_i\})$  is a function of the fields  $h_i$ . It is easy to convince oneself (without actually computing  $Z$ ) that one can write out this (Gibbs) free energy as  $G = -\sum_i m_i h_i + E - TS$ , where  $E \equiv \langle \mathcal{H} \rangle$  is the energy while the quantity  $S$  is equal to  $-(\partial G / \partial T)_{\{h_i\}}$  and thus must be identified with the entropy. Consequently, the function  $F = G + \sum_i m_i h_i = E - TS$  must be identified with the Helmholtz free energy, which we have seen can be expressed exclusively as a function of local magnetisations  $m_i$ :  $F = F(\{m_i\})$ . On the other hand,  $dF = dG + d(\sum_i m_i h_i) = -SdT + \sum_i h_i dm_i$ , and so one has for spin  $i$ :

$$h_i = \left( \frac{\partial F(\{m_i\})}{\partial m_i} \right)_T. \quad (34)$$

The meaning of Eq. (33) is that one solves for  $h_i$  such that satisfy the equation for a specified set of magnetisations  $m_i$ 's. Likewise, one solves for  $m_i$  such that satisfy Eq. (34) for a chosen set of on-site fields  $h_i$ . It would appear that the two descriptions in Eq. (33) and (34) are equivalent, so that either one can be used. In fact, the Gibbs ensemble is often more computationally convenient and thus is used more frequently. However, the two descriptions, which are related by a Legendre transform:  $F = G + \sum_i m_i h_i$ , are only equivalent if both  $F$  or  $G$  are concave or convex [111], which is certainly not the case for the ferromagnet below its Curie point, see Fig. 8. This figure demonstrates that while to a given value of magnetisation  $m$  there corresponds a unique value of the field  $h = \partial F / \partial m$ , the converse is not generally true: Up to three distinct solutions exist for equation  $h = \partial F / \partial m$  when the  $F(m)$  curve has a convex-up portion. Furthermore, for  $h = 0$ , the two stable solutions for the magnetisation are exactly degenerate in free energy, thus making the choice between distinct solutions of Eqs. (34) particularly ambiguous. Furthermore, if one enforces summation over spin states in the partition function from Eq. (32), at  $h_i = 0$ , one will recover  $m_i = 0$  even below the Curie point, thus missing the transition. This apparent—but incorrectly determined—equilibrium value of  $m_i = 0$  is an unstable solution of the free energy functional! This problematic situation would not arise in the Helmholtz ensemble, which clearly shows the two *polarised* states as minima of the free energy. These notions indicate that the Helmholtz ensemble is more basic than the Gibbs ensemble. In much the same way, the microcanonical ensemble is more basic than the canonical ensemble in the context of Fig. 1(a); the isochoric ensemble is more basic than the isobaric ensemble in Fig. 1(b).

For an individual spin, however, the  $h \leftrightarrow m$  correspondence is one-to-one and we may safely choose to work with either the magnetisation  $m_i$  or the corresponding “molecular field”  $h_i^{\text{mol}}$ :

$$h_i^{\text{mol}} = \frac{\partial F_{\text{id}}}{\partial m_i} \quad \Rightarrow \quad h_i^{\text{mol}} = k_B T \tanh^{-1}(m_i) \quad \Leftrightarrow \quad m_i = \tanh \beta h_i^{\text{mol}} \quad (35)$$

For the field-less energy function in Eq. (5),  $h_i = 0$ , and so the equilibrium configuration of  $m_i$  simply optimises the free energy  $F$ :

$$\frac{\partial F}{\partial m_i} = 0, \quad (36)$$

which, together with Eqs. (6) and (35), yields:

$$\frac{\partial F_{\text{id}}}{\partial m_i} + \frac{\partial F_{\text{ex}}}{\partial m_i} = 0 \quad \Rightarrow \quad h_i^{\text{mol}} = -\frac{\partial F_{\text{ex}}}{\partial m_i}. \quad (37)$$

In the mean-field case (9):

$$h_i^{\text{mol}} = \sum_j J_{ij} m_j, \quad (38)$$

which is expected since at any given time, spin  $i$  is subject to the instantaneous field  $\sum_j J_{ij} \sigma_j$ . In the mean-field approximation, one neglects correlations between spin flips and so, to compute the expectation value of the instantaneous field, one may simply replace  $\sigma_j$ 's by their average values.

Whether or not the *actual* external field  $h_i$  is zero, using Eqs. (34) with an arbitrary value of the parameter  $h_i$  can be quite useful because it allows one to analyse configurations other than the equilibrium ones. Quantifying fluctuations around equilibrium is necessary for determining various susceptibilities or interactions, among other things. For instance, the stiffness of the magnetic response of an isolated spin is  $\partial h_i / \partial m_i = k_B T / (1 - m_i^2)$ ; it is, of course, the reciprocal of the susceptibility. Further,  $\partial h_i / \partial m_j = (\partial^2 F_{\text{ex}} / \partial m_i \partial m_j)$  which is equal to  $-J_{ij}$  in the mean-field limit, c.f. Eq. (10). Likewise, one can use Eq. (33) to compute the spin-spin correlation function

$$\frac{\partial m_i}{\partial(\beta h_j)} = -k_B T \frac{\partial^2 F}{\partial h_j \partial h_i} = \langle \sigma_i \sigma_j \rangle - m_i m_j \equiv \chi(\mathbf{r}_{ij}), \quad (39)$$

which is a key quantity for detecting second order transitions with a diverging correlation length. Note that the two matrices  $\partial m_i / \partial h_j$  and  $\partial h_i / \partial m_j$  are inverse of each other:  $\delta_{ij} = \partial m_i / \partial m_j = \sum_k (\partial m_i / \partial h_k) (\partial h_k / \partial m_j)$ .

Analogously to how one may view the spontaneous magnetisation as the emergence of a non-zero molecular field, we may view each peak in Fig. 9(a) as corresponding to an effective one-particle potential. Suppose the particles' instantaneous locations are  $\mathbf{r}_i$ . In the presence of a one-particle potential  $u(\mathbf{r})$ , we must add the term  $\sum_i u(\mathbf{r}_i) = \int d^3 \mathbf{r} \rho_{\text{inst}}(\mathbf{r}) u(\mathbf{r})$  to the *energy* function of the liquid, where

$$\rho_{\text{inst}}(\mathbf{r}) \equiv \sum_i \delta(\mathbf{r} - \mathbf{r}_i) \quad (40)$$

is the instantaneous, highly inhomogeneous density profile of our liquid, whose thermally *averaged* value (c.f. Eq. (8)):

$$\rho(\mathbf{r}) \equiv \langle \rho_{\text{inst}}(\mathbf{r}) \rangle \quad (41)$$

may or may not be spatially uniform. For instance, in a dilute gas, far from the walls of the container, and in the absence of external field, the density profile  $\rho(\mathbf{r})$  is spatially uniform. In contrast, the density profile consists of relatively sharp, disparate peaks in a mechanically stable solid, as we shall see shortly. Since our free energy is defined as a space integral, which is a summation over fixed (elemental) volumes, this addition to the energy amounts to switching from the canonical to grand-canonical ensemble, in which the chemical potential is spatially-varying and equals  $-u(\mathbf{r})$ . Call the corresponding *free* energy  $\Omega = F + \int d^3 \mathbf{r} \rho(\mathbf{r}) u(\mathbf{r})$ , so that

$$\rho(\mathbf{r}) = \frac{\delta \Omega}{\delta u(\mathbf{r})}, \quad (42)$$

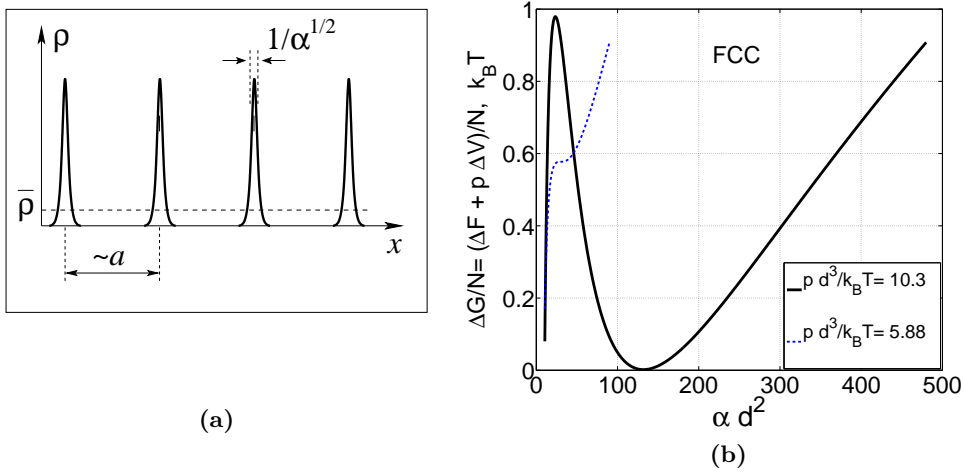


FIG. 9. **(a)** Sketch of the density profile in a periodic crystal. In a purely harmonic solid, the profile is a sum of gaussians,  $(\alpha/\pi)^{3/2} e^{-\alpha(\mathbf{r}-b\mathbf{r}_i)^2}$ , where  $\mathbf{r}_i$  denotes the average position of particle  $i$ , see Eq. (29). In important contrast with the density profile in Fig. 6(a), the density profile is not simply a periodic function of the coordinate, but a superposition of *narrow*, disparate peaks whose width is about one-tenth of the particle spacing:  $1/\alpha^{1/2} \simeq a/10$ . **(b)** The Gibbs free energy of the hard sphere FCC crystal as a function of the force constant  $\alpha$  of the effective Einstein oscillator from Eq. (29). The thick line corresponds to equilibrium between the liquid and crystal. The dashed line corresponds to a liquid that is still well above the fusion transition, but the metastable minimum corresponding to the crystal just begins to appear.

c.f. Eq. (33). Consequently, the appropriate analog of Eq. (34) is

$$u(\mathbf{r}) = -\frac{\delta F}{\delta \rho(\mathbf{r})}. \quad (43)$$

(In the literature, one often uses not the quantity  $u(\mathbf{r})$  but its negative [79], and also additionally multiplied by  $\beta$  [89, 112, 113].) Because here the density is defined over continuum space, not a discrete set over spin sites, we employ functional differentiation in Eqs. (42) and (43). The difference of functional differentiation from regular differentiation is that in the latter, we write an increment of a function  $f$  defined over a discrete set of independent variables  $g_i$  ( $\partial g_i / \partial g_j = \delta_{ij}$ ) as a discrete sum:  $df = \sum_j (\partial f / \partial g_j) dg_j$ . If, on the other hand,  $g$  is defined over a continuum space, we would like to change our definition of the derivative so that one can replace the discrete summation by continuous integration:  $df = \int d^3 \mathbf{r}_j [\delta f / \delta g(\mathbf{r}_j)] dg(\mathbf{r}_j)$ . This convention does work, but only if we define  $\delta f(\mathbf{r}_i) / \delta f(\mathbf{r}_j) \equiv \delta(\mathbf{r}_i - \mathbf{r}_j)$  for any function  $f(\mathbf{r})$ . As a result,  $\frac{\delta}{\delta \rho(\mathbf{r})} \int d^3 \mathbf{r} u(\mathbf{r}) \rho(\mathbf{r}) = u(\mathbf{r})$ , if the function  $u$  does not depend on  $\rho$  or its derivatives; see, for instance, Ref. [26] or [114] for more details. Another useful notion is  $\delta f / \delta h = \int d^3 \mathbf{r}_j [\delta f / \delta g(\mathbf{r}_j)] [\delta g(\mathbf{r}_j) / \delta h]$ . Functional variation of a quantity with respect to the density,  $\delta / \delta \rho(\mathbf{r})$ , is special in that it yields the (differential) response of the quantity to adding a particle to the system in the vicinity of site  $\mathbf{r}$ : On the one hand,  $\int d^3 \mathbf{r} [d\rho(\mathbf{r})] \frac{\delta}{\delta \rho(\mathbf{r})} = \lim_{dV_i \rightarrow 0} \sum_i [d\rho(\mathbf{r}_i)] \frac{\partial}{\partial \rho(\mathbf{r}_i)}$  by construction. On the other hand,  $\int d^3 \mathbf{r} [d\rho(\mathbf{r})] \frac{\delta}{\delta \rho(\mathbf{r})} = \lim_{dV_i \rightarrow 0} \sum_i dV_i [d\rho(\mathbf{r}_i)] \frac{\delta}{\delta \rho(\mathbf{r}_i)}$  by definition of the definite integral. This implies  $\frac{\delta}{\delta [\rho(\mathbf{r}_i)]} \leftrightarrow \frac{\partial}{\partial [dV_i \rho(\mathbf{r}_i)]} = \frac{\partial}{\partial [dN_i]}$ .

As in the ferromagnet case, the variable  $u(\mathbf{r})$  in Eq. (43) can be set to an external potential of relevance, thus resulting in an equation for the density profile. By varying  $u(\mathbf{r})$ , we can explore the density distribution to a desired degree of deviation from equilibrium. As the simplest illustration of Eq. (43), consider an ideal gas in an external potential  $U(\mathbf{r})$ . The Maxwell-Boltzmann distribution dictates that  $\rho(\mathbf{r}) = \Lambda^{-3} e^{-\beta U(\mathbf{r})} \Rightarrow U(\mathbf{r}) =$

$-k_B T \ln[\rho(\mathbf{r})\Lambda^3]$ . Substituting this in  $U(\mathbf{r}) = -\delta F_{\text{id}}/\delta\rho(\mathbf{r})$  and integrating in  $\rho$  readily yields Eq. (15), as expected.

In full correspondence with the ferromagnet case, the descriptions in Eqs. (42) and (43) are generally not equivalent. It is a corollary of the Hohenberg-Kohn-Mermin theorem [80, 81] that to a given density profile, there corresponds a unique external potential, and so the solution of Eq. (42) is unique, while the same is not necessarily true of Eq. (43). This notion will return in full force in the following Subsection, when the degeneracy of the solution is not 2, as was the case for the ferromagnet, but scales *exponentially* with the system size!

The quantity  $\delta F/\delta\rho(\mathbf{r})$  is the free energy cost of adding a particle to the system at location  $\mathbf{r}$ , i.e., the local value of the chemical potential  $\mu$ . In equilibrium and in the absence of external potential, the free energy cost of adding a particle to the system should be uniform in space, lest there be non-zero net particle flux  $\mathbf{j} \propto -\nabla\mu$ . Thus the liquid analog of Eq. (36) is

$$\frac{\delta F}{\delta\rho(\mathbf{r})} = \mu = \text{const.} \quad (44)$$

In correspondence with equations (35) and (37), we can define the molecular field:

$$u^{\text{mol}}(\mathbf{r}) \equiv -\frac{\delta F_{\text{id}}}{\delta\rho(\mathbf{r})} \quad \Rightarrow \quad u^{\text{mol}}(\mathbf{r}) = -k_B T \ln[\rho(\mathbf{r})\Lambda^3] \quad (45)$$

and establish its relation with the interaction part of the free energy:

$$\frac{\delta F_{\text{id}}}{\delta\rho(\mathbf{r})} + \frac{\delta F_{\text{ex}}}{\delta\rho(\mathbf{r})} = \mu \quad \Rightarrow \quad -u^{\text{mol}}(\mathbf{r}) = \mu + \beta^{-1}c^{(1)}(\mathbf{r}). \quad (46)$$

On the one hand, there is one-to-one correspondence between the molecular field and the equilibrium density. On the other hand, the free energy of the liquid is completely determined by the density. Thus calculation of the free energy amounts to finding the molecular field. No approximation is made and no generality is lost hereby.

Eq. (46) is trivially satisfied by the uniform liquid, for which all three terms are spatially-uniform. To see a possibility of non-trivial solutions, we may present the first-order correlation function  $c^{(1)}(\mathbf{r})$  as a power-series expansion in terms of deviations from the (uniform) liquid density  $\rho_l$ :  $\delta\rho(\mathbf{r}) = \rho(\mathbf{r}) - \rho_{\text{liq}}$ , as was done by Ramakrishnan and Yussouff [115]. In the lowest non-trivial order this expansion reads:

$$c^{(1)}(\mathbf{r}_1) - c_{\text{liq}}^{(1)} = \int d^3\mathbf{r}_2 [\delta c^{(1)}(\mathbf{r}_1)/\delta\rho(\mathbf{r}_2)]\delta\rho(\mathbf{r}_2) = \int d^3\mathbf{r}_2 c^{(2)}(\mathbf{r}_1, \mathbf{r}_2)\delta\rho(\mathbf{r}_2), \quad (47)$$

where  $c_{\text{liq}}^{(1)}$  denotes the value of  $c^{(1)}(\mathbf{r})$  in the uniform liquid. The quantity  $c^{(2)}(\mathbf{r}_1, \mathbf{r}_2)$  is the familiar direct correlation function:

$$c^{(2)}(\mathbf{r}_1, \mathbf{r}_2) = \frac{\delta c^{(1)}(\mathbf{r}_1)}{\delta\rho(\mathbf{r}_2)} = -\beta \frac{\delta^2 F_{\text{ex}}[\rho(\mathbf{r})]}{\delta\rho(\mathbf{r}_1)\delta\rho(\mathbf{r}_2)}. \quad (48)$$

In the uniform liquid state,  $c^{(2)}(\mathbf{r}_1, \mathbf{r}_2) = c^{(2)}(\mathbf{r}_1 - \mathbf{r}_2; \rho_{\text{liq}})$ . Eq. (46) thus becomes:

$$\ln[\rho(\mathbf{r}_1)/\rho_{\text{liq}}] = \int d^3\mathbf{r}_2 c^{(2)}(\mathbf{r}_1 - \mathbf{r}_2; \rho_{\text{liq}})\delta\rho(\mathbf{r}_2), \quad (49)$$

where we had to set chemical potential so that  $\beta\mu + c_{\text{liq}}^{(1)} = \ln[\rho_{\text{liq}}\Lambda^3]$ . In view of Eqs. (45) and (49), we observe how a molecular field could self-consistently arise in the presence of a frozen-in density wave  $\delta\rho(\mathbf{r}) \neq 0$ :  $u^{\text{mol}}(\mathbf{r}) = -k_B T \int d^3\mathbf{r}_1 c^{(2)}(\mathbf{r}_1 - \mathbf{r}_2; \rho_{\text{liq}})\delta\rho(\mathbf{r}_2)$ , up to an additive constant. We can attempt to make a connection with the ferromagnet case by considering the weak interaction limit, in which  $c^{(2)}(\mathbf{r}) \rightarrow -\beta v(\mathbf{r})$ , as in Eq. (20). The

resulting expression,  $u^{\text{mol}}(\mathbf{r}) = \int d^3\mathbf{r}_1 v(\mathbf{r}_1 - \mathbf{r}_2) \delta\rho(\mathbf{r}_2)$ , is quite similar to the expression  $h_i^{\text{mol}} = \sum_j J_{ij} m_j$  we obtained in the mean-field limit for the ferromagnet. We will see in a bit that the two expressions are in fact identical in structure.

Before that, let us write down an *exact* expression that connects the molecular field with the full density of the solid, which will turn out to be instructive in other contexts as well. In the presence of external potential  $U(\mathbf{r})$  and in equilibrium, we must set  $u(\mathbf{r}) = U(\mathbf{r})$  in Eq. (43). As a result, Eqs. (14), (15), (43), and (17) yield  $\beta U(\mathbf{r}) = -\ln[\rho(\mathbf{r})\Lambda^3] + c^{(1)}(\mathbf{r})$ . Taking the gradient of this equation results in  $\nabla[\beta U(\mathbf{r}) + \ln \rho(\mathbf{r})] = \nabla c^{(1)}(\mathbf{r})$ . To evaluate  $\nabla c^{(1)}(\mathbf{r})$ , we note that the dependence of  $c^{(1)}(\mathbf{r})$  on the coordinate arises exclusively through the density profile  $\rho(\mathbf{r})$ , by Eqs. (14) and (17). Consequently, a change in the direct correlation function upon a small shift  $d\mathbf{r}$  in the coordinate  $c^{(1)}(\mathbf{r}_1 + d\mathbf{r}) - c^{(1)}(\mathbf{r}_1) = \int d^3\mathbf{r}_2 [\delta c^{(1)}(\mathbf{r}_1)/\delta\rho(\mathbf{r}_2)] \delta\rho(\mathbf{r}_2)$ , where  $\delta\rho(\mathbf{r}_2)$  is the (small) change in the density profile resulting from the increment  $d\mathbf{r}$  in the coordinate. This change is equal to  $\delta\rho(\mathbf{r}_2) = \rho(\mathbf{r}_2 + d\mathbf{r}) - \rho(\mathbf{r}_2)$ . (Note the change is in the *argument* of the density, be this argument a dummy variable or not.) Using this notion and the definition of the direct correlation function Eq. (48), we thus obtain [112, 116]:

$$\nabla_1[\ln \rho(\mathbf{r}_1) + \beta U(\mathbf{r}_1)] = \int d^3\mathbf{r}_2 c^{(2)}(\mathbf{r}_1, \mathbf{r}_2) \nabla_2 \rho(\mathbf{r}_2). \quad (50)$$

The equation demonstrates that, on the one hand, the liquid density obeys the Boltzmann law in the absence of correlations between particles:  $(\rho \rightarrow 0) \Rightarrow (\rho \propto e^{-\beta U(\mathbf{r})})$ . Conversely, it directly shows how the particles produce an effective force onto each other, via the correlations, since the r.h.s. enters in the equation additively with external force  $-\nabla U(\mathbf{r})$ . Note that even given a high quality functional form for the density profile, such as in Eq. (29), the equation above cannot be used to determine the parameters of the profile self-consistently because it requires the knowledge of the direct correlation function in the solid. Such knowledge is currently lacking (see however the insightful analysis by McCarley and Ashcroft [82]).

For a homogeneous liquid,  $c^{(2)}(\mathbf{r}_1, \mathbf{r}_2) = c^{(2)}(\mathbf{r}_1 - \mathbf{r}_2)$ , the equation above is easily integrated to yield, in the absence of external potential [117]:

$$\ln \rho(\mathbf{r}_1) = \int d^3\mathbf{r}_2 c^{(2)}(\mathbf{r}_1 - \mathbf{r}_2) \rho(\mathbf{r}_2) + \text{const.} \quad (51)$$

In the weak-interaction limit, Eq. (20), we obtain an equation that has an identical structure to the simplest type of molecular field theory:  $\ln \rho(\mathbf{r}_1) = -\beta \int d^3\mathbf{r}_2 v(\mathbf{r}_1 - \mathbf{r}_2) \rho(\mathbf{r}_2) + \text{const.}$  Despite its clear structure, the latter equation is explicitly missing three-body interactions, which are essential for building a solid, as remarked earlier. In addition, it is obviously useless for hard spheres, for which  $v(\mathbf{r})$  is either zero or infinity. Now, the additive constant in Eq. (51) can be fixed by noticing that for the uniform liquid,  $\ln \rho_{\text{liq}} = \int d^3\mathbf{r}_2 c^{(2)}(\mathbf{r}_1 - \mathbf{r}_2) \rho_{\text{liq}} + \text{const.}$  Subtracting this from Eq. (51) yields Eq. (49). We remind that Eq. (51) was derived in the assumption of the liquid's uniformity and so it could be valid only up to terms of order  $(\delta\rho)^2$ .

Continuing this line of thought, we realise that Eq. (49) can be obtained by varying (w.r.t. to the density) the free energy from Eq. (14), in which the *excess* part of the free energy  $F_{\text{ex}}$  is expanded as power series in terms of the deviation of the local density from its value in the uniform liquid, where the expansion is truncated at the second order. But this expansion is exactly the expression (16) combined with the conditions (19) to account for the liquid's uniformity. We spell it out explicitly here for future use:

$$\begin{aligned} F[\{\rho(\mathbf{r})\}] &= k_B T \int d^3\mathbf{r} \rho(\mathbf{r}) \{ \ln[\rho(\mathbf{r})\Lambda^3] - 1 \} \\ &\quad - \frac{k_B T}{2} \int d^3\mathbf{r}_1 d^3\mathbf{r}_2 \delta\rho(\mathbf{r}_1) c^{(2)}(\mathbf{r}_2 - \mathbf{r}_1; \rho_{\text{liq}}) \delta\rho(\mathbf{r}_2) + F_{\text{ex}}(\rho_{\text{liq}}), \end{aligned} \quad (52)$$

where  $F_{\text{ex}}(\rho_{\text{liq}})$  is the excess free energy of the uniform liquid at  $\rho = \rho_{\text{liq}}$ . We have again dropped the term linear in  $\delta\rho(\mathbf{r})$ , as in Eq. (25). Functional (52) is commonly called the Ramakrishnan-Yussouff [115] (RY) functional, even though it was first written down in this simple form by Haymet and Oxtoby [113], see also Ref. [89].

Eqs. (49) and (52) can be used to search for crystalline free energy minima in cases when the direct correlation function is available, either from a calculation or experiment. Good approximations for  $c^{(2)}(\mathbf{r}; \rho_{\text{liq}})$  are available for hard spheres at densities comparable to or below the density at the melting point. One such approximation is that by Percus and Yevick [118], for which the explicit expression is available [119, 120]. Following exactly this route, Ramakrishnan and Yussouff have recovered a periodic solution of the liquid free energy in equilibrium with the liquid. In this method, one expands the candidate crystal density field in a Fourier series in terms of the reciprocal lattice vectors  $\mathbf{q}$ , see Eq. (27). Note the  $\mathbf{q} = 0$  component corresponds to the bulk density, which is generally different between the liquid and solid. In practice, one assumes a specific lattice type and spacing and uses a modest number of Fourier components in the expansion. The expansion coefficients are then determined by solving the (non-linear) Eq. (49). One can further compute the free energy of both the uniform liquid and the crystal as functions of the density and thus compute the pressure  $p$  and Gibbs free energy  $F + pV$  of both states. The equality of the pressure and chemical potential of the liquid and the crystal signals the two phases are in equilibrium. Thus, although the procedure does not predict the lattice type, it does yield the relative stability of distinct lattice types, which simplifies the search for the true equilibrium configuration. Likewise, the procedure predicts the densities of the phases at ambient conditions and thus enables one to evaluate the density and entropy jumps during the transition.

On a historical note, the first successful attempt to quantify the liquid-to-solid transition along the lines of the molecular field theory is due to Kirkwood and Monroe [102], who sought solid density profiles in the form of periodic waves. These workers approximated the crystal field by a sum of effective pairwise potentials and derived a self-consistent equation for the crystal density distribution similar in structure to Eq. (49). The treatment by Kirkwood and Monroe superseded earlier treatments by Bragg and Williams [121], Hershfeld, Stevenson, and Eyring [71], Born [63], and Mott and Gurney [64], to name a few. These treatments viewed the crystal-to-liquid transition as an order-disorder transition and were similar in spirit to treatments of the critical point by Lennard-Jones and Devonshire [70]. Hereby one regards liquefaction as substitutional disorder in alloys [121], or a proliferation of local molecular rotations [71], dislocations [63], or domain walls between relatively ordered crystallites [64]. While achievable near a critical point—where density fluctuations are relatively facile—creation of such defects is too costly near the melting point. As mentioned in the Introduction, such defect-based treatments correspond to the *mechanical* melting, which takes place in the bulk, not at the surface; they predict melting points that are too high. We shall see in the following that the view of supercooled liquids or glasses as a collection of such ultra-local defects is similarly flawed.

A more modern approach to building a solid starting from the liquid state is to note that Eq. (44) is an optimisation problem with respect to *any* parameter on which the density depends; the optimal values of such parameters are then found by minimisation of the functional (52). The superposition  $\rho(\mathbf{r}, \alpha)$  of gaussians in Eq. (29) is an excellent ansatz for the crystal density profile. Exact for a harmonic lattice, it has the flexibility to effectively include anharmonic effects in a variational fashion [122]. Once the lattice type is chosen, the free energy of the solid can be computed for any values of the density and the effective spring constant  $\alpha$ :

$$F(\alpha) \equiv F[\{\rho(\mathbf{r}, \alpha)\}], \quad (53)$$

where  $F[\{\rho(\mathbf{r})\}]$  is the functional from Eq. (52). The  $\alpha$ -dependence of the free energy,  $F(\alpha)$ , at fixed density, is of the type shown in Fig. 9(b). This dependence is particular noteworthy since it allows one to directly see that the vibrational amplitude in the crystal is determined by a competition between two factors. On the one hand, the entropic cost of localisation—as reflected by the ideal free energy of the crystal  $F_{\text{id}}$ —grows approximately logarithmically with increasing  $\alpha$ :

$$F_{\text{id}} \approx k_B T N \left\{ \ln \left[ \Lambda^3 \left( \frac{\alpha}{\pi} \right)^{\frac{3}{2}} \right] - \frac{5}{2} \right\}. \quad (54)$$

The approximation is quantitatively adequate for not too small  $\alpha$ , namely,  $\alpha$  exceeding 20 or so. On the other hand, the increasing localisation mitigates the mutual collision rate and, hence, the pressure that the particles exert on each other, thus providing progressive stabilisation in a certain range of  $\alpha$ 's. Formally this stabilisation comes about because the direct correlation function is large and negative at small separations owing to the repulsion. As the peaks in Fig. 9(a) and Eq. (29) become progressively narrower, at a given density, the excess free energy decreases. The resulting interplay of the localisation entropy and stabilisation due to reduced collisions results in a minimum in the  $F(\alpha)$  curve at a finite value of  $\alpha$ . The equilibrium solid corresponds to the bottom of the minimum, of course. We note that an analogous sterically-driven symmetry breaking takes place during nematic ordering in liquid crystals, as elucidated by Onsager a long time ago [123]. In the liquid crystal case, it is the rotational symmetry that gets broken when the molecules spontaneously align, locally. (The translational symmetry remains preserved in liquid crystals, as particles can still exchange places readily.)

When the direct correlation function is not available, we can take advantage of the intrinsic relation between  $c^{(2)}(\mathbf{r})$  of a uniform liquid and the liquid structure factor, which is experimentally measurable. Indeed, let us rewrite  $\delta u(\mathbf{r}_1)/\delta u(\mathbf{r}_2) = \delta(\mathbf{r}_1 - \mathbf{r}_2)$  as

$$\int d^3 \mathbf{r}_3 \frac{\delta u(\mathbf{r}_1)}{\delta \rho(\mathbf{r}_3)} \frac{\delta \rho(\mathbf{r}_3)}{\delta u(\mathbf{r}_2)} = \delta(\mathbf{r}_1 - \mathbf{r}_2). \quad (55)$$

Eqs. (14), (15), (43), and (17) yield

$$\beta u(\mathbf{r}) = -\ln[\rho(\mathbf{r})\Lambda^3] + c^{(1)}(\mathbf{r}) \quad (56)$$

and, with the help of Eq. (48),

$$\beta \frac{\delta u(\mathbf{r}_1)}{\delta \rho(\mathbf{r}_2)} = -\frac{1}{\rho(\mathbf{r}_1)} \delta(\mathbf{r}_1 - \mathbf{r}_2) + c^{(2)}(\mathbf{r}_1, \mathbf{r}_2). \quad (57)$$

On the other hand,

$$\beta^{-1} \frac{\delta \rho(\mathbf{r}_1)}{\delta u(\mathbf{r}_2)} = \langle \rho_{\text{inst}}(\mathbf{r}_1) \rho_{\text{inst}}(\mathbf{r}_2) \rangle - \rho(\mathbf{r}_1) \rho(\mathbf{r}_2), \quad (58)$$

yields the density-density correlation function, c.f. Eq. (39). The thermally averaged quantity on the r.h.s. is closely related to the pairwise correlation function

$$\rho^{(2)}(\mathbf{r}_1, \mathbf{r}_2) \equiv \left\langle \sum_{i \neq j} \delta(\mathbf{r}_1 - \mathbf{r}_i) \delta(\mathbf{r}_2 - \mathbf{r}_j) \right\rangle \quad (59)$$

that reflects the probability of finding a particle at location  $\mathbf{r}_2$ , if there already is a particle at location  $\mathbf{r}_1$ . With the help of Eq. (40), one obtains

$$\langle \rho_{\text{inst}}(\mathbf{r}_1) \rho_{\text{inst}}(\mathbf{r}_2) \rangle = \rho^{(2)}(\mathbf{r}_1, \mathbf{r}_2) + \rho(\mathbf{r}_1) \delta(\mathbf{r}_1 - \mathbf{r}_2). \quad (60)$$

We have used the equality  $\langle \sum_i \delta(\mathbf{r}_1 - \mathbf{r}_i) \delta(\mathbf{r}_2 - \mathbf{r}_i) \rangle = \rho(\mathbf{r}_1) \delta(\mathbf{r}_1 - \mathbf{r}_2)$ , which can be established by checking that this latter sum is non-zero only for  $\mathbf{r}_1 = \mathbf{r}_2$ , while the multiplicative factor  $\rho(\mathbf{r}_1)$  is verified by integrating the equality in  $\mathbf{r}_1$  or  $\mathbf{r}_2$ .

The connection with experiment is made by realising that (the coherent part of) the intensity of light scattered off a sample at wave-vector  $\mathbf{q}$  is proportional to  $\langle |\sum_i e^{-i\mathbf{q}\mathbf{r}_i}|^2 \rangle$ , as light scattering is much faster than the thermal motions [78]. This quantity, up to a multiplicative factor, is commonly known as the structure factor  $S_{\mathbf{q}}$ :

$$\begin{aligned} S_{\mathbf{q}} &\equiv \frac{1}{N} \left\langle \sum_{ij} e^{-i\mathbf{q}(\mathbf{r}_i - \mathbf{r}_j)} \right\rangle = \frac{1}{N} \int d^3\mathbf{r}_1 d^3\mathbf{r}_2 e^{-i\mathbf{q}(\mathbf{r}_1 - \mathbf{r}_2)} \langle \rho_{\text{inst}}(\mathbf{r}_1) \rho_{\text{inst}}(\mathbf{r}_2) \rangle \\ &= 1 + \frac{1}{N} \int d^3\mathbf{r}_1 d^3\mathbf{r}_2 e^{-i\mathbf{q}(\mathbf{r}_1 - \mathbf{r}_2)} \rho^{(2)}(\mathbf{r}_1, \mathbf{r}_2). \end{aligned} \quad (61)$$

Combining Eqs. (55), (57), (58), and (60) yields [79, 124]:

$$\begin{aligned} \rho^{(2)}(\mathbf{r}_1, \mathbf{r}_2) - \rho(\mathbf{r}_1)\rho(\mathbf{r}_2) &= \rho(\mathbf{r}_1)\rho(\mathbf{r}_2)c^{(2)}(\mathbf{r}_1, \mathbf{r}_2) \\ &+ \rho(\mathbf{r}_2) \int d\mathbf{r}_3 [\rho^{(2)}(\mathbf{r}_1, \mathbf{r}_3) - \rho(\mathbf{r}_1)\rho(\mathbf{r}_3)] c^{(2)}(\mathbf{r}_3, \mathbf{r}_2). \end{aligned} \quad (62)$$

The quantity on the l.h.s. and inside the brackets in the integrand is important. By Eqs. (60) and (40), its integral is equal to

$$\int d^3\mathbf{r}_1 d^3\mathbf{r}_2 [\rho^{(2)}(\mathbf{r}_1, \mathbf{r}_2) - \rho(\mathbf{r}_1)\rho(\mathbf{r}_2)] = \langle N^2 \rangle - \langle N \rangle^2 - \langle N \rangle. \quad (63)$$

At the same time, the mean square deviation of the particle number from its average value for *uniform* liquids is directly related to the isothermal compressibility:

$$\chi_T \equiv -\frac{1}{V} \left( \frac{\partial V}{\partial p} \right)_T \equiv K^{-1}. \quad (64)$$

via  $\chi_T = \frac{\langle (\delta N)^2 \rangle}{N} \frac{V}{T}$  [55]. The quantity  $K$  is the isothermal bulk modulus. In addition, the l.h.s. of Eq. (63) can be also readily evaluated for a harmonic solid with isotropic elasticity to yield [32, 125]:  $[k_B T \bar{\rho} (K + 4\mu/3)^{-1} - 1] \bar{\rho} V$ , where  $\mu$  is the shear modulus and  $\bar{\rho}$  is the density. We thus obtain an important sum rule that, among other things, discriminates between uniform liquids and solids:

$$\frac{1}{\bar{\rho} V} \int d^3\mathbf{r}_1 d^3\mathbf{r}_2 [\rho^{(2)}(\mathbf{r}_1, \mathbf{r}_2) - \rho(\mathbf{r}_1)\rho(\mathbf{r}_2)] + 1 = \begin{cases} \frac{k_B T \bar{\rho}}{K}, & \text{liquid} \\ \frac{k_B T \bar{\rho}}{K + 4\mu/3}, & \text{solid} \end{cases} \quad (65)$$

Interestingly, if we had the *adiabatic* values for the elastic coefficients on the r.h.s. of Eq. (65), the r.h.s. would yield the same expression in terms of the speed  $c_l$  of longitudinal sound, since for liquids,  $K_S = \rho_m c_l^2$ , while for solids,  $(K_S + 4\mu_S/3) = \rho_m c_l^2$ , where  $\rho_m$  is the mass density. (The adiabatic and isothermal shear moduli are strictly equal [85], while the bulk moduli are usually close numerically.) The distinction of the sum rule between the liquid in solid is not widely known but is not too surprising, if one thinks of the density fluctuations not in terms of particle number fluctuations at constant volume, as in Eq. (63), but in terms of volume fluctuations at fixed particle number. Because of a finite shear modulus, the fluctuations of two subvolumes of a solid are coupled, however large the subvolumes are. The only way to decouple such fluctuations is to clamp the sides of the subvolumes. The restoring force for deformation of an elastic body with clamped sides is greater than that for a free solid and this force corresponds precisely to a modulus  $(K + 4\mu/3)$ , see Chapter 5 of Ref. [85].



For an equilibrium uniform liquid, both the density-density and the direct correlation functions are translationally invariant and isotropic:  $\rho^{(2)}(\mathbf{r}_1, \mathbf{r}_2) = \rho^{(2)}(|\mathbf{r}_1 - \mathbf{r}_2|)$ ,  $c^{(2)}(\mathbf{r}_1, \mathbf{r}_2) = c^{(2)}(|\mathbf{r}_1 - \mathbf{r}_2|)$ . After introducing the standard, dimensionless pair-correlation function  $g(r)$ :

$$g(r) \equiv \frac{1}{\rho_{\text{liq}}^2} \rho^{(2)}(r), \quad (66)$$

Eq. (62) reduces to the familiar Ornstein-Zernike equation [79, 110, 126]:

$$g(r) - 1 = c^{(2)}(r) + \rho_{\text{liq}} \int d^3 \mathbf{r}' [g(r') - 1] c^{(2)}(|\mathbf{r} - \mathbf{r}'|). \quad (67)$$

Upon defining a new function

$$h(r) \equiv g(r) - 1, \quad (68)$$

Eq. (67) looks particularly simple in the Fourier space:

$$\tilde{h}_q = \tilde{c}_q^{(2)} + \rho_{\text{liq}} \tilde{h}_q \tilde{c}_q^{(2)}, \quad (69)$$

while the structure factor becomes (for a uniform liquid!):

$$S_q = 1 + \rho_{\text{liq}} \tilde{g}_q. \quad (70)$$

Eqs. (68)-(70) form the sought connection between the experimentally determined structure factor and the direct correlation function. The functions  $g(r)$  and  $c^{(2)}(r)$  are exemplified in Fig. 10. The pair-correlation  $g(r)$  looks intuitive: It reflects the steric repulsion between the particles at short distances, while its oscillating nature at larger separations accounts for the short-range order in the liquid. The interpretation of the direct correlation function is more complicated. The (very weak) “attractive” tail at large distances is consistent with Eq. (20). What is the meaning of the much larger, and negative, portion at small  $r$ ? By Eqs. (65), (66), and (67), we obtain:

$$-\rho_{\text{liq}} \int d^3 \mathbf{r} c^{(2)}(r) = \frac{K}{k_B T \rho_{\text{liq}}} - 1. \quad (71)$$

Note also that, by Eqs. (65) and (68-70),

$$\lim_{q \rightarrow 0} S_q = k_B T \rho_{\text{liq}} \chi_T, \quad (72)$$

where  $\chi_T = K^{-1}$  is the usual compressibility, Eq. (64). This equation helps one mitigate the (usually significant) uncertainty in the measured structure factor at small wavevectors. Note  $q$  should remain strictly positive in the limit above, which is usually the case in experiment anyway because the  $q = 0$  component includes the incident light.

Given the shape of the direct correlation function in Fig. 10, the aforementioned rule of thumb  $K \simeq (10^1 - 10^2) k_B T \rho_{\text{liq}}$  along with Eq. (71) explains the large and negative value of the direct correlation function at the origin. Furthermore this notion implies that upon compression, the direct correlation function becomes increasingly negative at the origin since both the pressure and its derivative  $\partial p / \partial V$  will increase in magnitude with density.

Like the Landau expansion that we used to demonstrate the discontinuous nature of the liquid-to-crystal transition, the approximation in Eq. (49) amounts to analytically continuing the free energy from the liquid state to the solid state. Although Eq. (49) is derived by a systematic expansion—which can be, in principle carried out to higher orders—one is left wondering whether the direct correlation function at the density  $\rho_{\text{liq}}$  can adequately describe correlations in the solid. Despite the somewhat decreased entropy, the crystal becomes more

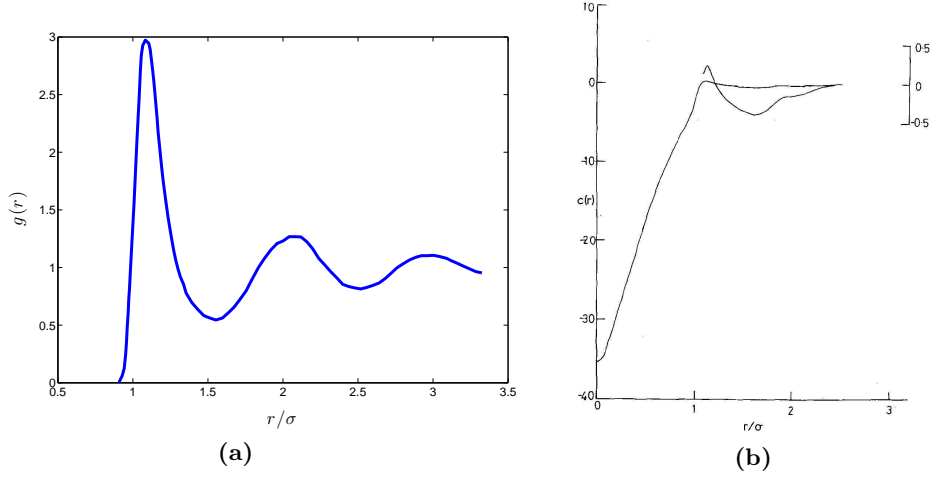


FIG. 10. **(a)** Pair-distribution function  $g(r)$  for the Lennard-Jones liquid near its triple point, data from Allen and Tildesley [127]. **(b)** Direct correlation function  $c^{(2)}(r)$  for the Lennard-Jones liquid. Magnified version of the attractive tail at large separation is shown as the dashed line. From Dixon and Hutchinson [128].

stable than the liquid above certain liquid densities because the particles in the crystal do not collide with each other as much, which is another way to say that crystallisation of hard spheres is sterically-driven. At a first glance, this decrease in the collision rate may sound counter-intuitive given that the close-packed crystal is, of course, denser than the liquid. On the other hand, the coordination in the crystal exceeds that in the liquid, suggesting the particles do not have to spend as much time near each other. It turns out that appropriate quantitative tools to address this, somewhat subtle aspect of crystallisation are *also* supplied by the classical density functional theory.

The excess free energy of a hard sphere liquid has the form  $k_B T f_{\text{liq}}(\rho_{\text{liq}})$  because there is no finite energy scale in the problem other than the temperature. As mentioned, good approximations for this free energy, such as Percus-Yevick, are available. Because the particles in the crystal occupy disparate, well defined cells in space, an individual particle is subject to collisions with many fewer molecules than in the uniform liquid. We thus anticipate that correlation functions in the crystal, for short particle-particle separations, should be similar to those in a *uniform* liquid at an effective density which is *lower* than the actual density of the liquid in equilibrium with the solid. Specifically, in the modified-weighted density approximation (MWDA) due to Denton and Ashcroft [129]:

$$F_{\text{ex}}[\rho] = k_B T N f_{\text{liq}}(\hat{\rho}), \quad (73)$$

where the effective—or “weighted”—density  $\hat{\rho}$  is defined by the equation:

$$\hat{\rho}[\rho(\mathbf{r})] \equiv N^{-1} \int \int \tilde{w}(\mathbf{r}' - \mathbf{r}; \hat{\rho}) \rho(\mathbf{r}) \rho(\mathbf{r}') d^3 \mathbf{r} d^3 \mathbf{r}'. \quad (74)$$

This quantity scales linearly with the actual, non-uniform density but with a weight. The weight function  $\tilde{w}$  is chosen so that in the uniform limit, the exact density is recovered:

$$\int \tilde{w}(\mathbf{r}' - \mathbf{r}; \hat{\rho}) d^3 \mathbf{r}' = 1 \quad (75)$$

and, likewise, so that the direct correlation function is reproduced:

$$c^{(2)}(\mathbf{r} - \mathbf{r}'; \rho) = -\beta \lim_{\rho(\mathbf{r}) \rightarrow \rho} \frac{\delta^2 F_{\text{ex}}[\rho(\mathbf{r})]}{\delta \rho(\mathbf{r}) \delta \rho(\mathbf{r}')} \quad (76)$$

Multiplying the equation above by  $\rho(\mathbf{r})\rho(\mathbf{r}')$ , integrating over  $\mathbf{r}$  and  $\mathbf{r}'$ , and using Eqs. (74)-(75) and the density ansatz (29) yield an expression that can be used to determine the weighted density  $\hat{\rho}$  self-consistently [130]:

$$2\hat{\rho} \left. \frac{f_{\text{liq}}}{\partial \rho} \right|_{\rho=\hat{\rho}} + \rho \hat{\rho} \left. \frac{\partial^2 f_{\text{liq}}}{\partial \rho^2} \right|_{\rho=\hat{\rho}} = - \left( \frac{\alpha}{\pi} \right)^3 \int d^3 \mathbf{r} \int d^3 \mathbf{r}' \int d^3 \mathbf{R} c_{\text{HS}}^{(2)}(|\mathbf{r} - \mathbf{r}'|; \hat{\rho}) \times \exp \left\{ -\alpha \left[ (\mathbf{r} - \mathbf{R})^2 + \mathbf{r}'^2 \right] \right\} [\delta(\mathbf{R}) + \rho g(\mathbf{R})]. \quad (77)$$

We remind that the function  $f_{\text{liq}}(\rho)$  must be specified for this equation to be useful. Good approximations, such as Percus-Yevick, are available for this function at not too high densities. Note that to evaluate the effective density  $\hat{\rho}$ , determining an explicit form for  $\tilde{w}$  is not required. (The weighting function can be readily computed and is related to the direct correlation function [129].) The quantity  $g(\mathbf{R})$  is the site-site correlation function of the lattice:  $g(\mathbf{R}) \equiv (1/N) \sum_{i \neq j} \delta[\mathbf{R} - (\mathbf{R}_i - \mathbf{R}_j)]$ . A density ansatz other than the superposition of Gaussians from Eq. (29) could be used if desired but would lead to a different equation for  $\hat{\rho}$ . The above expression can be formally applied to any lattice. If the latter is periodic, the double integral can be conveniently recast as a Fourier sum [129].

One can now use Eqs. (73), (77), and (54) to determine the Helmholtz free energy  $F$  of the solid as a function of the density—which is specified automatically given a lattice—and the effective spring constant  $\alpha$ . This free energy is further optimised with respect to  $\alpha$  thus giving an approximation for the free energy of the solid as a function of the density, thus allowing one to compute the pressure. A solid at a density such that its pressure and chemical potential are equal to their counterparts in the uniform liquid, is in equilibrium with the liquid (at the same temperature of course). To illustrate this, we show in Fig. 9(b) the Gibbs free energy difference between crystal and liquid,  $\Delta F(\alpha) + p\Delta V$ , as a function of the order parameter  $\alpha$ . The solid line corresponds to  $F(\alpha)$  at the density and pressure such that the solid and liquid would be in equilibrium for the optimal value of  $\alpha$ . The dashed line in Fig. 9(b) shows the *spinodal* of the solid with respect to the liquid. It corresponds to the density at which a metastable minimum in  $F(\alpha)$  just begins to appear. The respective pressure is, of course, considerably lower than the pressure at which the two phase would coexist. Note that Fig. 9(b) is a *prima facie* evidence of the discontinuous nature of the liquid-to-crystal transition since the uniform liquid is *also* described by the density ansatz (29) if one sets  $\alpha = 0$ . The transition thus corresponds to a discontinuous jump from  $\alpha = 0$  to  $\alpha \simeq 10^2/a^2$ . Note the latter value is in agreement with the phenomenological criterion of melting due to Lindemann [67, 105, 107], which has been rationalised relatively recently based on the surface character of crystal melting [65].

It turns out that whenever there exists a crystal solution to the free energy functional, the weighted density  $\hat{\rho}$  is always lower than the actual density. This is consistent with our earlier expectation that the effective local density, which determines the collision rate, is lowered in the solid compared with the uniform liquid, even though the actual density has increased. Because of the relative smallness of the effective density, it is adequate to use the Percus-Yevick (PY) expressions [78, 110] for the free energy  $f_{\text{liq}}$  and the translationally-invariant portion of the direct correlation function  $c^{(2)}$  in Eq. (77) in the solid. Importantly, the weighted-density approximation alleviates our earlier concerns about using the direct correlation function at the liquid density  $\rho_{\text{liq}}$  in a (solid) phase separated from the uniform liquid by a free energy barrier. Here we explicitly obtain that the correlations do experience a discrete jump during the transition.

Because of the self-consistency requirement on the weighted density, the MWDA is a non-perturbative approximation; the corresponding free energy contains an infinite subset of exact high order terms in the corresponding perturbative expansion [129]. This is in addition to the PY approximation itself being non-perturbative in the first place. The PY

|                               | $\rho_s \sigma^3$ | $\rho_l \sigma^3$ | $\Delta \rho \sigma^3$ | $\Delta s / k_B$ | $L$          |
|-------------------------------|-------------------|-------------------|------------------------|------------------|--------------|
| <b>Simulation<sup>a</sup></b> | <b>1.04</b>       | <b>0.94</b>       | <b>0.10</b>            | <b>1.16</b>      | <b>0.126</b> |
| <b>MWDA</b>                   | <b>1.036</b>      | <b>0.910</b>      | <b>0.13</b>            | <b>1.35</b>      | <b>0.097</b> |
| <b>WDA<sup>b</sup></b>        | <b>1.045</b>      | <b>0.916</b>      | <b>0.13</b>            | <b>1.41</b>      | <b>0.093</b> |
| <b>RY<sup>c</sup></b>         | <b>1.147</b>      | <b>0.967</b>      | <b>0.18</b>            | <b>2.24</b>      | <b>0.055</b> |

TABLE I. Densities of hard sphere solid ( $\rho_s$ ) and liquid ( $\rho_l$ ) at liquid-crystal equilibrium.  $\Delta \rho \equiv \rho_s - \rho_l$ . The quantity  $\Delta s$  is the fusion entropy per particle and  $L$  is the Lindemann ratio from Eq. (80). Letter references: (a): Ref. [72]; (b): see Ref. [129]; (c): Ref. [131] and also see Ref. [129].

approximation is of excellent quality at liquid densities in question, judging by comparison with simulations [110]. Perhaps for these reasons, the MWDA yields predictions for the transition entropy and densities during the transition, and the vibrational particle displacement in the crystal that are in good agreement with simulations, see Table I. Furthermore, the MWDA can be extended to non-rigid and weakly interacting systems, such as Lennard-Jones particles [132]. Here the long range interaction can be included as a perturbation, while the now soft repulsion at small separations can be handled by using an effective hard-core repulsion. Hereby the effective hard-sphere diameter can be determined using, for instance, the Barker-Henderson prescription [78]:

$$d(T) = \int_0^\sigma dr [1 - e^{-V_{LJ}(r)/k_B T}], \quad (78)$$

and

$$V_{LJ}(r) \equiv 4\epsilon[(\sigma/r)^{12} - (\sigma/r)^6] \quad (79)$$

is the Lennard-Jones interaction potential. The resulting prediction for the phase diagram is in remarkable agreement with simulations, with respect to the equilibrium between all three phases of the system [132], see Fig. 11. This approximation yields the following estimates for several key characteristic of the transition close to the triple point (result of simulation [78] in brackets):  $\rho_{liq} d^3 = 0.855(0.875)$ ,  $\rho_{xtal} d^3 = 0.970(0.973)$ ,  $\rho d^3 / \epsilon = 0.970(0.973)$ ,  $T \Delta S / \epsilon = 1.1(1.31)$ , and for the Lindemann displacement [132]:

$$L \equiv \langle (\delta r)^2 \rangle^{1/2} / r_{nn}, \quad (80)$$

$L = 0.127(0.145)$ . Here,  $r_{nn}$  is the nearest-neighbour spacing.

A rather different—and early—line of attack on the problem of crystallisation of hard spheres, which will be also relevant later, is due to Fixman [73]. He has expanded the singular interaction potential between the rigid particles in terms of Hermite polynomials. In the lowest order, his method amounts to variationally finding the best value of the effective spring constant  $\alpha$  from Eq. (29) that approximates the effect of the hard repulsion between particles when combined with their thermal motion. This method, which can be systematically improved, produced excellent estimates for the pressure and free energy. It is often referred to as the “self-consistent phonon theory.”

### C. Transferability of DFT results from model liquids to actual compounds

We finish this Section by remarking on whether the results for hard spheres and Lennard-Jones systems are transferable to actual, non-model liquids. Except for argon, which is a Lennard-Jones liquid to a good accuracy, most substances exhibit much more complicated

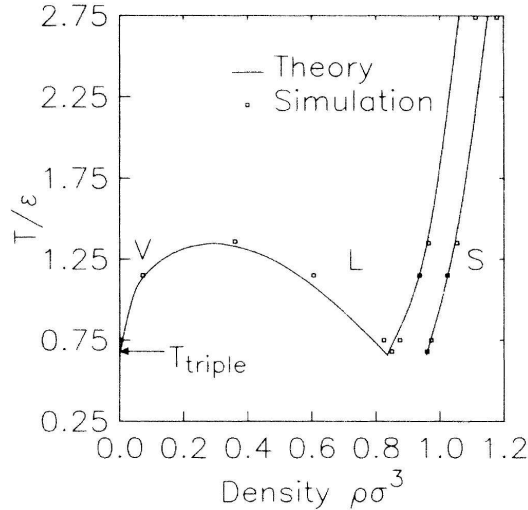


FIG. 11. The phase diagram of the Lennard-Jones system in the density-temperature plane. The continuous lines are obtained using the classical DFT in the modified weighted density approximation [132]. The symbols correspond to simulation studies [133].

interactions. Already in molecular liquids, such as organic compounds, molecules have complicated shapes. Covalently bonded substances are exemplified by various chalcogenides, such as  $\text{As}_2\text{Se}_3$  and elemental compounds such as Ge and Si, while  $\text{ZnCl}_2$  is a good example of an ionic compound. Hydrogen bonding is also very common, as in water and various alcohols. In contrast, the model systems we have considered so far exhibit only isotropic steric repulsion and a weak (isotropic) attraction, which can be treated perturbatively. Clearly, the cohesive forces in germanium cannot be treated as a perturbation to the steric repulsion since germanium *expands* upon freezing. The significance of bonding during the latter process is also witnessed by germanium's fusion entropy, which is  $\sim 3.5k_B$  per atom and thus significantly exceeds the fusion entropy of Ar, which is  $\sim 1.68k_B$ . Generally, the work contribution  $p\Delta V$  in the fusion enthalpy (31) is very small— $10^{-4}$  or so—compared to the energy contribution at ordinary pressures.

One reason it is difficult to apply the DFT to actual substances is our lack of knowledge of the functional form of the interactions. However, even if available, such functional forms would probably be too complicated to allow for a tractable analytical approach. Incidentally, while Quantum Chemistry, combined with various evolutionary algorithms, has made impressive progress in predicting structures of solids and assessing relative stability of distinct polymorphs, adequate sampling of the *liquid* state for actual substances near melting temperature and below is still out of reach for direct molecular modelling. In developing a computationally-tractable description of the glass transition, our best bet may be to find a minimal simplified model for the actual interactions that can reproduce only select, but key features of their crystallisation or glass transition. An example of such a simplified interaction is the pairwise potential for  $\text{SiO}_2$  due to Beest, Kramer, and Santen [134].

A distinct—and equally phenomenological—approach is to ask whether we can make a correspondence between the actual substances and *isotropically* interacting particles that exhibit repulsion at short distances and modest attraction at long distances, such as argon. Such a description is motivated by our good knowledge of the thermodynamics and packing properties of isotropically interacting objects, and their being amenable to semi-analytical treatments such as the classical density functional theory. The key dimensionless number characterising crystallisation of such particles is the fusion entropy per particle.

| substance                       | $s_m/k_B$ , per atom | $s_m/k_B$ , per group       |
|---------------------------------|----------------------|-----------------------------|
| HS                              | 1.19                 |                             |
| LJ                              | 1.75                 |                             |
| Ar                              | 1.68                 |                             |
| Pb                              | 0.96                 |                             |
| SiO <sub>2</sub>                |                      | 0.58 (SiO <sub>4/2</sub> )  |
| ZnCl <sub>2</sub>               | 0.69                 | 2.07 (ZnCl <sub>4/2</sub> ) |
| NaCl                            | 1.58                 |                             |
| CsCl                            | 1.34                 |                             |
| As                              | 2.70                 |                             |
| Se                              | 1.62                 |                             |
| As <sub>2</sub> Se <sub>3</sub> | 1.51                 | 3.78 (AsSe <sub>3/2</sub> ) |
| TNB                             |                      | 1.54 (ring)                 |
| OTP                             |                      | 2.1 (ring)                  |
| C                               | 2.97                 |                             |
| Ge                              | 3.67                 |                             |
| H <sub>2</sub> O                |                      | 2.65 (OH <sub>2</sub> )     |

TABLE II. Fusion entropy,  $s_m = h_m/T_m$ , for a variety of substances, elemental, compound, and model such as the monodisperse hard sphere (HS) and Lennard-Jones (LJ) system, the latter near the triple point [78]. Enthalpy of fusion  $h_m$  and melting temperature  $T_m$  for actual substances are from CRC Tables [57], except TNB [135] and Ar [56]. The polymorphs are as follows: SiO<sub>2</sub> (cristobalite), Se (grey), rhombohedral As (grey). OTP (ortho-terphenyl) consists of three aromatic rings, TNB (tris-naphthyl benzene) of seven rings.

In assessing the possibility of such an effective description, we list the fusion entropies for a small set of model liquids and actual substances that cover a broad range of bonding patterns in Table II. We observe that the fusion entropy per particle or rigid molecular unit is quite consistent between these distinct systems; it is numerically close to its value in model systems, represented here by hard spheres and Lennard-Jones particles, and some actual systems, such as argon and lead, both of which crystallise into close-packed structures.

Among the materials listed in Table II, stand out the very open structures represented by the three substances at the bottom and arsenic. All four lose significantly more translational entropy per particle, upon freezing, than the rest of the substances. Of these four, solid carbon (graphite) consists of weakly bonded, flat graphene sheets; germanium crystallises into the diamond lattice, in which each atom is bonded equally strongly to four atoms located at the corners of a regular tetrahedron; the normal, hexagonal ice is, in a sense, an intermediate case between the graphite and diamond lattice: First of all, we need to focus on the oxygens since the protons are mobile and probably contribute comparably to the entropies of the liquid and solid state. Each oxygen atom is bonded to three oxygens (within a sheet) while being bonded to one atom from the adjacent sheet, which is shifted accordingly sideways. Each sheet is in reality a puckered, double layer consisting of hexamers in the chair conformation; if flattened out, each double layer would be just like a graphene sheet [136]. The structure of rhombohedral (grey) arsenic is also a stack of sheets. Each arsenic atom is strongly bonded to three atoms within its sheet and only weakly bonded to three atoms across the inter-sheet gap. Note all four substances are poor glassformers and all, except for As, *expand* upon freezing. (Note that antimony and bismuth, which are in the same group as arsenic, *do* expand upon freezing. These two elements are even

worse glassformers and better electric conductors than As.) To avoid confusion we note that having relatively little entropy per atom does not guarantee being a good glass-former, as can be seen by comparing NaCl and CsCl (poor glass-formers forming a simple-cubic-like and BCC-like structures respectively) and ZnCl<sub>2</sub> and As<sub>2</sub>Se<sub>3</sub>, the latter two being good glass-formers. Zinc chloride consists of relatively rigid, corner-sharing ZnCl<sub>4/2</sub> tetrahedra (but apparently not as rigid as in SiO<sub>4/2</sub>) while As<sub>2</sub>Se<sub>3</sub> consists of relatively rigid AsSe<sub>3/2</sub> pyramids co-joined through the Se corners and forming puckered sheets like those of black phosphorus but with vacancies [29].

To appreciate just how open the diamond structure is, and to rationalise its high fusion entropy, we first consider the FCC lattice, which is a close-packed structure. The FCC structure has two types of cavities: two octahedral (cornered by the six face-centred vertices) per three tetrahedral. The diamond lattice can be produced from the FCC lattice by placing a particle in every other tetrahedral cavity in a (3D) checker pattern. Alternatively, to generate the diamond lattice, one can superimpose two identical FCC lattices, with lattice constant 1, which are shifted by  $\sqrt{3}/4$  along the main diagonal. On the other hand, the simple-cubic lattice can be obtained by superimposing two identical FCC lattices, with lattice constant 1, but which are shifted by  $\sqrt{3}/2$  along the main diagonal. Consequently, two diamond lattices complement each other to form a BCC lattice. Thus roughly, the entropy of freezing of the diamond lattice is the total entropy due to the ordering of an equal measure of particles and vacancies into a BCC lattice. Per *particle*, we get about twice as much fusion entropy as for a BCC lattice made of two distinct particles. (We should be mindful of the mixing entropy, too.) Indeed, the fusion entropy of CsCl per atom is at least twice less than that of germanium or water. The high fusion entropy of open structures is in full harmony with our earlier analysis of the discontinuous nature of the liquid-to-crystal transition. Per that discussion, materials with open structures freeze well before the steric effects—which are signalled by relatively low values of the fusion entropy—become important. It is instructive to note that the filling fraction in the diamond lattice made of touching, identical spheres is only  $\pi\sqrt{3}/16 \approx 0.34$ , to be compared with the filling fraction of the FCC lattice,  $\pi/3\sqrt{2} \approx 0.74$ , or the random close-packed structure, viz.,  $\approx 0.64$  [137]. Conversely, many example of pressure-induced amorphisation of relatively open structures are known [138–141].

We thus tentatively conclude that with the exception of these very open structures, steric interactions contribute significantly to the thermodynamics of freezing. The degree of “openness” is positively correlated—but not without exception—with the sign of the volume change during freezing and the value of the fusion entropy; it is *negatively* correlated with the glass-forming ability. We will be able to rationalise this negative correlation in the following Section, where we show that *equilibrium* aperiodic structures are stabilised by steric effects. Now, the glass forming ability is also decreased when a relatively well-packed structure is agreeable with the stoichiometry, even if the fusion entropy is not too high. (The rock salt structure is, in fact, rather well-packed for NaCl, because of the disparity in the ion sizes and despite the relatively low coordination number of six.) Thus it appears that at least for structures that are not too open, an effective description in terms isotropically interacting particles is possible. Certain layered compounds, such as As<sub>2</sub>Se<sub>3</sub>, are good glass-formers despite having a relatively large entropy of fusion. We shall see that determining the effective particle size for such compounds is difficult, in contrast with compounds that exhibit less propensity for local ordering.

To avoid confusion, we note that substances with very *isotropic* bonding, such as monodisperse hard-spheres or Lennard-Jones particles, are *also* poor glassformers. These fail to vitrify readily despite the prominence of steric effects because monodisperse spheres easily find close-packed arrangements. We will return to this topic at the end of the article.

#### IV. EMERGENCE OF APERIODIC CRYSTAL AND ACTIVATED TRANSPORT, AS A BREAKING OF TRANSLATIONAL SYMMETRY

The density functional theory (DFT) provides us with reliable tools to determine the free energy of the uniform liquid and, at the same time, the free energy of specific crystalline arrangements. As such, the DFT enables us to assess the stability of distinct crystalline polymorphs relative to each other and to the uniform liquid state in the first place. Likewise, it will enable us to assess the stability of *aperiodic* structures. Until further notice, we will focus on rigid systems exemplified by hard spheres and also with added weak attraction as in Lennard-Jones liquids. These results will be generalised for actual substances in due time.

##### A. The Random First Order Transition (RFOT)

Let us now consider a supercooled liquid just above its glass transition, so that its structure relaxes on a timescale comparable to one hour. The latter time scale is 16 orders of magnitude longer than the vibrational relaxation time, which is numerically a picosecond or so. In other words, the supercooled liquid, despite being able to flow on very long times, is a solid on mesoscopic length scales and below. Frozen glasses, if quenched considerably below the glass transition, not only fail to flow but are often even more rigid than the corresponding crystal. Given their remarkable mechanical stability, it is natural to enquire whether aperiodic structures such as those pertaining to supercooled liquids or glasses are free energy minima.

This question was answered affirmatively by Stoessel and Wolynes in 1984 [142], who used the self-consistent phonon theory and assumed an aperiodic structure characterised by the pair-correlation function  $g(r)$  of a *uniform* liquid. These authors have determined self-consistently the force constant  $\alpha$  from the Gaussian density profile (29), where the lattice is now *aperiodic*. The self-consistent phonon theory also predicts the liquid density above which the aperiodic free energy minima begin to exist.

Soon afterwards, Singh, Stoessel, Wolynes [143] (SSW) reported their stability analysis of aperiodic structures using the Ramakrishnan-Yussouff density functional (52), in which the free energy was determined explicitly as a function of  $\alpha$ , analogously to the periodic-crystal calculation in Fig. 9(b). There are notable differences between how the calculations are set up in the periodic and aperiodic case, in addition to the use of an aperiodic lattice. (SSW employed a lattice generated using the Bennett algorithm [144].) In the regular liquid-to-crystal transition, the two phases occupy distinct parts of the space. The two phases can coexist for an indefinite time, if the temperature, pressure, and chemical potential are uniform throughout the whole system. The appropriate free energy for analysing the relative stability of the two phases is thus the Gibbs free energy. One may still consider a transient coexistence between the two phases when one of them is *metastable*, and so only temperatures and pressures are equal between the two phases, while the metastable free energy is now in excess of the Gibbs free energy. (The metastable phase will eventually convert into the stable phase, subject to pertinent kinetics.) In contrast, there is no phase separation in the aperiodic case. The aperiodic minimum at finite  $\alpha$  is built with the very same particles comprising the liquid and thus *replaces* the uniform liquid, it does not coexist with the uniform liquid; there is no spatial interface involved. Nor is there volume change and so the appropriate free energy is the Helmholtz free energy from Eq. (14).

The result of the SSW calculation of the free energy  $F(\alpha)$  for an aperiodic lattice, relative to the uniform liquid is shown in Fig. 12(a). Here we observe that in complete analogy with the regular liquid-to-crystal transition, a metastable minimum develops at a *finite* value of



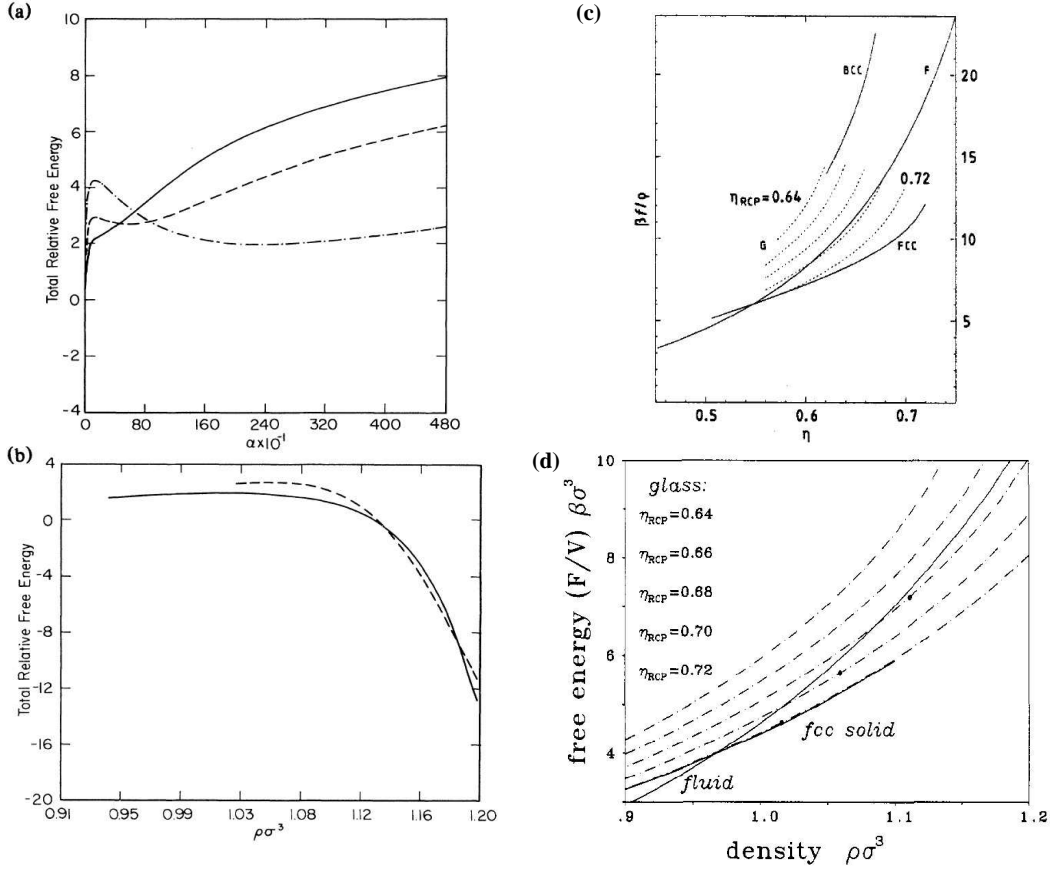


FIG. 12. **(a)** The  $\alpha$  dependence of the relative free energy  $F(\alpha) - F_{\text{uni}}$  from Eq. (52) as computed by Singh, Stoessel, and Wolynes [143] for an *aperiodic*, Bennett [144] lattice, for three values of density:  $\rho\sigma = 1$  (solid line),  $\rho\sigma = 1.05$  (dashed line),  $\rho\sigma = 1.1$  (dash-dotted line). **(b)** Same relative free energy as in panel (a), but as a function of density at constant  $\alpha$ . The solid and dashed curves correspond to two distinct lattices, Bennett and hypothetical-icosahedral, respectively. **(c)** The free energy of an aperiodic (Bennett) structure as a function of filling fraction  $\eta$ , at several values of local coordination, in comparison with the free energy of the FCC and BCC structures, and the uniform liquid. From Ref. [145]. **(d)** The free energy of an aperiodic (Bennett) structure as a function of filling fraction  $\eta$ , at several values of local coordination, in comparison with the free energy of the FCC structure and uniform liquid. From Ref. [130].

$\alpha \simeq 10^1 - 10^2$ . This metastable minimum thus corresponds to an assembly of particles localised to certain locations in space and vibrating about those locations. The locations themselves may still move about—the present article is largely about those movements!—but the movements are much slower than the vibrational oscillations. The metastable minimum in Fig. 12 thus corresponds to a solid in the sense that the vibrationally averaged coordinates of the particles move on significantly longer timescales than the vibrational relaxation time.

The emergence of a minimum at a finite  $\alpha \gg 1/a^2$  implies a discontinuous transition accompanied by a breaking of the translational symmetry, in complete analogy with the emergence of periodic solutions of the free energy considered in the preceding Section. Before we discuss the thermodynamic significance of the metastable minimum, let us review its properties. As in the periodic case, the metastable minimum appears at a certain threshold density. The thus emerged aperiodic-crystal phase is further stabilised with increasing density, see Fig. 12(b). However the latter phase reaches the uniform liquid in stability

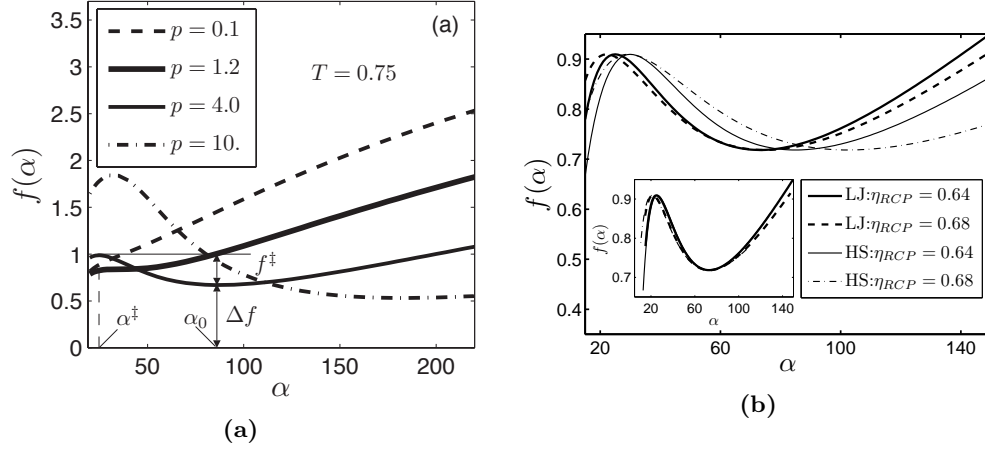


FIG. 13. **(a)** The free energy  $F(\alpha)$  of an aperiodic crystal of Lennard-Jones particles as a function of the force constant  $\alpha$  of the effective Einstein oscillator from Eq. (29). The temperature is fixed near the triple point. Four values of pressure are represented. The liquid is seen to undergo the RFOT at sufficiently high pressure (density). **(b)** The  $F(\alpha)$  plotted for hard spheres and Lennard-Jones particles, each at two distinct values of the parameter  $\eta_{RCP}$  that can be used to effectively vary local coordination. The inset illustrates that given the same barrier height, the shape of the curve is robust with respect to detailed interactions and coordination. Hereby all four curves are rescaled along the horizontal axis and translated vertically, if necessary, so that the locations of the metastable minima coincide. Both graphs are from Ref. [37].

only if the attractive tail is included in the direct correlation function discussed earlier; the specific form tail used by SSW is due to Henderson and Grundke [83], see Fig. 5. Baus and Colot [145] subsequently showed that the stability of the periodic phase is quite robust. These authors have generalised the SSW treatment to account for the circumstance that the lattice not only shrinks uniformly with pressure/density but also that the coordination must *increase* alongside. The specific device they employed to show this is the following ansatz for the site-site correlation function (which corresponds to the pairwise correlation function  $g(r)$  for an equilibrium structure):

$$g(\mathbf{R}) = g_B[(\eta/\eta_{RCP})^{1/3}R], \quad (81)$$

where  $g_B(R)$  is the site-site correlation function for Bennett's lattice of hard spheres with diameter  $d$  [144], and  $\eta$  is the packing fraction. The quantity  $\eta_{RCP}$  is a parameter that enables one to emulate, to a degree, changes in local coordination. For instance, the Bennett function  $g_B(x)$  has a sharp peak at  $x = d$  corresponding to particles in immediate contact, if  $\eta = \eta_{RCP}$ . For such immediate neighbours at distance  $R$ ,  $(\eta/\eta_{RCP})^{1/3}R = d$ , or  $\eta = \eta_{RCP}(d/R)^3$ . Thus raising  $\eta_{RCP}$  at fixed distances between particles and their sizes emulates increasing the volume fraction  $\eta$ —and hence coordination—and vice versa for smaller  $\eta_{RCP}$ . On the other hand, it is straightforward to see that this effective change in volume fraction is local, since modifying  $\eta_{RCP}$  actually does not change the average density, by virtue of the relation  $\rho \int d^3\mathbf{r} g(r) = (N - 1)$ . (To avoid confusion, we note the latter formula is valid in the canonical ensemble, in contrast with Eq. (65), which applies in the grand-canonical ensemble.)

Baus and Colot [145] thus showed that although the aperiodic crystal with the Bennett structure does not ever reach the uniform liquid in stability—if the attractive tail in  $c(r)$  is not included—increasing the local coordination can yield a structure as stable as or more stable than the uniform liquid, see Fig. 12(c). This result was later confirmed by Lowen [130], see Fig. 12(d) who used the more reliable MWDA approximation which is less sensitive to

the large  $r$  form of the direct correlation function. (To avoid confusion, we repeat the “large”  $r$  corresponds to separations just exceeding the particle diameter, see Figs. 5 and 10(b).) As in the periodic crystal case, the effective, weighted density is *lowered* when the liquid transitions to the metastable minimum, implying the collision rate in the aperiodic solid is lowered compared with the uniform liquid. Rabochiy and Lubchenko [37] have extended the results of Lowen to Lennard-Jones systems, see Fig. 13. The graph is instructive in that it confirms that a high-quality free energy function—which successfully reproduces the phase diagram of the LJ system, Fig. 11—robustly yields the RFOT transition. It also explicitly demonstrates that one can vary either density or temperature to cause the crossover, in systems other than fully rigid particles.

Aside from some uncertainty as to the quality of the aperiodic lattice, we observe that an aperiodic arrangement of particles is in fact a minimum of the free energy and, furthermore, could be made more stable than the uniform liquid while remaining less stable than the FCC structure. This observation provides the thermodynamic basis for our understanding of the stability of supercooled liquids and glasses.

Additional support for the density-functional framework comes from the mean-field calculation of Kirkpatrick and Wolynes [146] (KW). We have seen an example of numerically evaluated free energy  $F(\alpha)$ , which can be used to determine the equilibrium value of  $\alpha$  in the aperiodic crystal. One may ask, is there a closed form expression one could use to evaluate the force constant  $\alpha$  self-consistently, similarly to how Eqs. (35) and (38) can be used to determine the spontaneously generated magnetisation below the Curie point? KW start from the Ramakrishnan-Yussouff functional (52) and substitute the gaussian density ansatz (29). Differentiating the resulting expression with respect to  $\alpha$  yields a self-consistent equation for  $\alpha$  (in  $D$  spatial dimensions):

$$\alpha = \frac{1}{6} \int \frac{d^D \mathbf{q}}{(2\pi)^D} q^2 \tilde{c}_q^{(2)} \tilde{S}_0(q) e^{-q^2/2\alpha}, \quad (82)$$

where  $\tilde{S}_0(q)$  is the structure factor of the aperiodic lattice  $\tilde{S}_0(q) = \frac{1}{N} \sum_{ij} e^{-i\mathbf{q}(\mathbf{r}_i - \mathbf{r}_j)}$ , c.f. Eq. (61). In the mean-field,  $D \rightarrow \infty$  limit, only the quadratic term in the free energy expansion survives and so both the Ramakrishnan-Yussouff and the Eq. (82) become exact. Also in this limit, the functional form of the direct correlation function simplifies. Thus Eq. (82) yields [146]:

$$\alpha \sigma^2 = \frac{n^*}{8\pi} e^{-D^2/2\alpha\sigma^2}, \quad (83)$$

where  $\sigma$  is the diameter of the hard (hyper)sphere in  $D$  dimensions and the quantity  $n^* \equiv \bar{\rho} \sigma^D \pi^{D/2} / \Gamma(1 + D/2)$  is closely related to the packing fraction since the volume of a  $D$ -dimensional hypersphere is equal to  $\sigma^D \pi^{D/2} / 2^D \Gamma(1 + D/2)$ . For large  $D$ ,  $n^* \sim O(D)$ . Eq. (83) is the liquid analog of the Weiss equation for the spontaneous magnetisation of a uniform ferromagnet:  $m = \tanh[\beta(\sum_j J_{ij})m]$ . Like the latter equation, Eq. (83) always has the  $\alpha = 0$  solution corresponding to the uniform phase. At sufficiently high densities, two new solutions at *finite* values of  $\alpha$  emerge that correspond to the metastable minimum and the saddle point on the  $F(\alpha)$  curve in Figs. 12(a) and 13. (Exactly at the spinodal, there is only one finite- $\alpha$  solution.) Thus in contrast with the Ising magnet, the liquid-to-solid transition is discontinuous, be the solid periodic or otherwise. By Eq. (83),  $\alpha \simeq D^2/\sigma^2$  and thus simply reflects the number of particles in the first coordination shell. The  $\alpha \simeq D^2/\sigma^2$  scaling implies the transition is the more discontinuous the closer the system is to the strict mean-field limit.

Yet to fully appreciate the thermodynamic significance of the aperiodic minimum in  $F(\alpha)$ , we must ask ourselves how many distinct amorphous structures could represent such a minimum. It appears à priori likely that when generating a sufficiently large sample, the

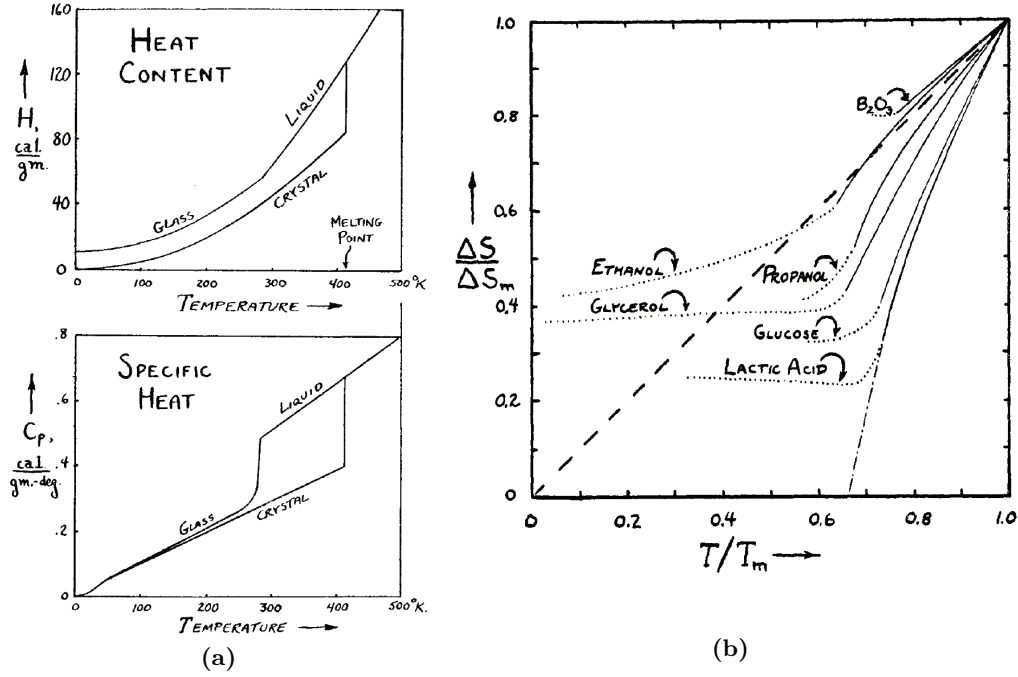


FIG. 14. (a) Top: The enthalpies of the liquid and the corresponding crystal, as inferred by integrating the heat capacity data (bottom) [147]. (b) Excess liquid entropy  $\Delta S$ , relative to the corresponding crystal (thin solid line) as a function of temperature, for a number of specific substances. Extrapolation of this excess entropy below the glass transition temperature, due to Kauzmann [147].  $\Delta S_m$  and  $T_m$  stand for the fusion entropy and the melting temperature respectively.

variety of such structures scales exponentially with the sample size. One way to appreciate this is to recall our earlier discussion of the 3rd order term in the Landau expansion (4) for the liquid. There we noted that the regular icosahedron is one of the polyhedra that contains equilateral triangles made of reciprocal lattice vectors. Alexander and McTague [90] estimate the coefficient at the 3rd order term due to icosahedra is about 0.63 of that for the bcc lattice. They however note that because icosahedra do not tile space, we can dismiss their contribution to the 3rd order term. Yet we should recognise that on the one hand, the tiling does not have to be perfect, since the second order term is still quite small even for  $q$ 's that are not strictly equal to  $q_0$ , see Fig. 6(b). On the other hand, the number of ways to put together such an imperfect lattice using nearly-equilateral triangle motifs scales exponentially with the lattice size: An individual “tile” does not fit in perfectly; there are more than one way to insert it in the matrix with a comparable degree of mismatch. The full multiplicity is the configuration multiplicity for an individual tile, taken to power  $N$ . This multiplicity of alternative tilings will make a bulk contribution to the stability of the 3rd order term.

Returning to the direct space, we quickly recognise that the multiplicity of alternative structures in equilibrated liquids *is* in fact exponential in the system size: Assuming the vibrational entropy of the periodic and aperiodic crystals are similar, the multiplicity of the dissimilar aperiodic structures is reflected in the excess entropy of a supercooled liquid relative to the corresponding *periodic* crystal [74]. At melting, the excess entropy is the same as the fusion entropy; representative values for the latter are listed in Table II. To summarise, the metastable minimum on the  $F(\alpha)$  curve corresponds to an exponentially large number of actual free energy minima. The  $F(\alpha)$  curve is thus a one-dimensional projection of the full free energy surface where the order parameter is the localisation parameter  $\alpha$ .

Since the vibrational entropy of an individual minimum is numerically close to that of the crystal, the exponentially large multiplicity of the free energy minima results in an excess contribution to the entropy of the liquid, relative to the crystal. This contribution is directly seen by calorimetry, Fig. 14, in the form of an excess heat capacity. The latter can be integrated in temperature to infer both the excess liquid enthalpy and entropy, by virtue of  $C_p = (\partial H/\partial T)_p = T(\partial S/\partial T)_p$ . Furthermore, since molecular translations freeze out below the glass transition—apart from some ageing—the excess entropy is approximately temperature-independent below  $T_g$ . This leads to an observable jump in the heat capacity at the glass transition:

$$\Delta c_p(T_g) = T \left( \frac{\partial s_c}{\partial T} \right)_{p, T=T_g^+} - T \left( \frac{\partial s_c}{\partial T} \right)_{p, T=T_g^-} \approx T_g \left( \frac{\partial s_c}{\partial T} \right)_{p, T=T_g^+}, \quad (84)$$

see Fig. 14 and the inset of Fig. 2.

To determine the microscopic consequences of this multiplicity of minima it is instructive to assume first that fluctuations around the free energy minima are such that the system is allowed to transition between minima only as a whole, but not locally. This mean-field constraint—which will be lifted shortly—concerns the mutual transitions between the individual distinct aperiodic free energy minima but also the transitions between the uniform liquid state and individual aperiodic minima. Let us denote the free energy of an individual minimum as  $F_i$ . This quantity contains the energy proper  $E_i$  of the configuration plus the vibrational free energy:

$$F_i = E_i - TS_{\text{vibr},i}. \quad (85)$$

Suppose the multiplicity of the minima, or “configurations”, at a given value of  $F_i$  is  $\Omega(F_i)$ . We define the *configurational entropy* as the logarithm of this multiplicity times  $k_B$ . Per particle,

$$S_c = k_B \ln \Omega(F_i). \quad (86)$$

Apart from the the contribution of the periodic crystal to the thermodynamic ensemble, the partition function can be written as

$$Z = e^{-\beta F_{\text{liq}}} + \Omega(F_i) e^{-\beta F_i} = e^{-\beta F_{\text{liq}}} + e^{-\beta [F_i - TS_c(F_i)]}, \quad (87)$$

where  $F_{\text{liq}}$  is the free energy of the uniform-liquid state. Clearly, when

$$F_i < F_{\text{liq}} + TS_c, \quad (88)$$

the aperiodic crystal state will be more stable than the uniform liquid. More precisely, in the assumption of spatial homogeneity of transitions between the distinct aperiodic states, exactly one will be realised at a time. Owing to the vast superiority of the second term on the r.h.s. of Eq. (87)—the exponents all scale linearly with the particle number—the system will spend a vanishing fraction of time in the uniform liquid state if the condition (88) is satisfied.

Is this condition satisfied in actual liquids? According to Fig. 12, the altitude of the aperiodic minimum, relative to the uniform liquid, is about  $1-1.5k_B T$  at liquid densities near melting, see Table I for numerical values of those densities. If one accounts for the increase in coordination with density, the excess free energy of an individual aperiodic minimum relative to the uniform liquid could be significantly lower. According to Table II, the excess liquid entropy per rigid molecular unit does, in fact, have similar values near melting. Of particular value in the present context are results of Mézard and Parisi [148, 149], who used a replica methodology to estimate the exact type of the mean-field configurational entropy

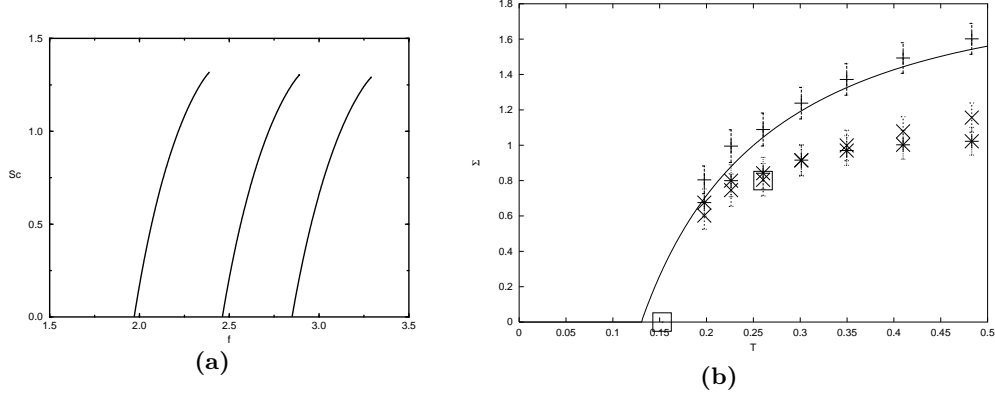


FIG. 15. **(a)** The configurational entropy of hard spheres computed as a function of the free energy, per particle and  $k_B T$ , at three distinct values of temperature [148]. **(b)** The configurational entropy for a binary mixture of soft spheres as a function of temperature according to a replica calculation (—), alongside with results of alternative numerical procedures including direct Monte-Carlo (\*). From Ref. [149].

that enters in Eq. (88). Their results are shown in Fig. 15 and indicate that indeed the configurational entropy is sufficiently large to stabilise the aperiodic phase at sufficiently high density. In the strict mean-field limit, the transition from the uniform liquid to the aperiodic solid occurs at a sharply defined temperature, which we will denote with  $T_A$ . The transition itself is called the Random First Order transition (RFOT), to reflect that the liquid freezes into a random lattice, while the freezing itself is a discontinuous transition. It would not be obvious from the preceding discussion whether the RFOT would take place at the same temperature at which the metastable minimum in the  $F(\alpha)$  curve just begins to develop or below that temperature. We shall see shortly, in Subsection IV C, that the mean-field spinodal does in fact take place exactly at the temperature  $T_A$  at which the (degenerate) aperiodic crystal becomes thermodynamically stable. We shall also observe in Subsection IV D that this is a rather general pattern that also covers spin systems.

The formation of long-lived aperiodic structures predicted by the RFOT theory is consistent with neutron scattering data [150], see Fig. 16, which clearly shows that below a certain temperature, each particle becomes trapped in a cage made of the surrounding molecules. The time needed for relaxation of these long-lived structures is considerable already above the glass transition and becomes even longer below the transition, see Fig. 16. We postpone the calculation of the structural relaxation rate until Subsection V A, where we go beyond the mean-field limit.

The presence of the random first order transition imply that the fluid is no longer represented by a unique free energy minimum; the exponentially many free energy minima all correspond to non-uniform density profiles. Conversely, one may ask what happens to the free energy minimum corresponding to the uniform liquid. This minimum becomes *metastable* below the RFOT. One may further ask under which conditions the uniform minimum disappears, which would correspond to the mechanical stability limit of the uniform liquid. The appearance of a marginally stable mode can be detected by standard stability analysis [117]. First note that a density response to a weak, coordinate-dependent external field  $U(\mathbf{r})$  can be written generally as:

$$\delta\rho(\mathbf{r}_1) = \int d^3\mathbf{r}_2 \chi(\mathbf{r}_1, \mathbf{r}_2) U(\mathbf{r}_2). \quad (89)$$

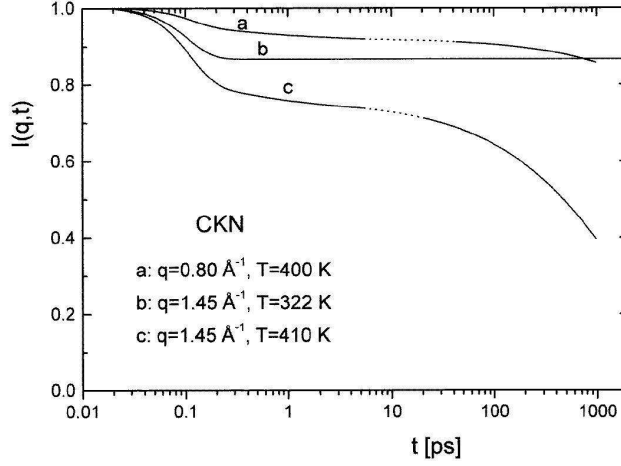


FIG. 16. Intermediate structure factor as determined by neutron scattering [150]. Note curve (b) was measured below the glass transition.

Where the susceptibility:

$$\chi(\mathbf{r}_1, \mathbf{r}_2) \equiv \left. \frac{\delta \rho(\mathbf{r}_1)}{\delta U(\mathbf{r}_2)} \right|_{U=0}, \quad (90)$$

can be expressed through the density-density correlation function  $\rho^{(2)}(\mathbf{r}_1, \mathbf{r}_2)$  and the density, according to Eqs. (58) and (60). For the uniform liquid, which is translationally invariant, Eq. (89) can be rewritten as simple equations for individual Fourier components of the functions in question:

$$\delta \tilde{\rho}_{\mathbf{q}} = \tilde{\chi}_{\mathbf{q}} \tilde{U}_{\mathbf{q}}, \quad (91)$$

while each Fourier component of the response function is straightforwardly related to the that of the direct correlation function, by Eqs. (66)-(69):

$$\chi_{\mathbf{q}} = \frac{\rho_{\text{liq}} k_B T}{1 - \rho_{\text{liq}} \tilde{c}_{\mathbf{q}}^{(2)}}. \quad (92)$$

This expression is consistent with Eq. (25), since the latter implies  $(k_B T/2)V(\rho_{\text{liq}}^{-1} - \tilde{c}_{\mathbf{q}}^{(2)}) \langle |\delta \tilde{\rho}_{\mathbf{q}}|^2 \rangle = k_B T/2$  by virtue of the equipartition theorem. On the other hand,  $\chi_{\mathbf{q}} = \langle |\delta \tilde{\rho}_{\mathbf{q}}|^2 \rangle / V$  by Eq. (58). Note also that the  $q \rightarrow 0$  limit of Eq. (92) could have been inferred from Eqs. (65), (66) and (71).

According to Eq. (92)—and in full correspondence with our earlier analysis of the possibility of a continuous liquid-to-crystal transition, Eq. (25)—the first liquid modes to reach the spinodal are spatially-varying patterns with  $|\mathbf{q}| = q_0$  such that

$$1 - \rho_{\text{liq}} \tilde{c}_{q_0}^{(2)} = 0. \quad (93)$$

Lovett [117] points out that at least within the Percus-Yevick approximation, the uniform liquid state remains (meta)stable at densities such that the pressure is finite. Whether these conclusions applies to actual liquids remains an open question.

We conclude by reiterating the central features of the random first order transition in liquids, see Fig. 17: It is a transition from a truly uniform liquid characterised by a single free energy minimum, Fig. 17(a) and (b), into a symmetry-broken state characterised by an exponentially large number of free energy minima, Fig. 17(c). It is the translational

### Liquid Kinetic Regimes:

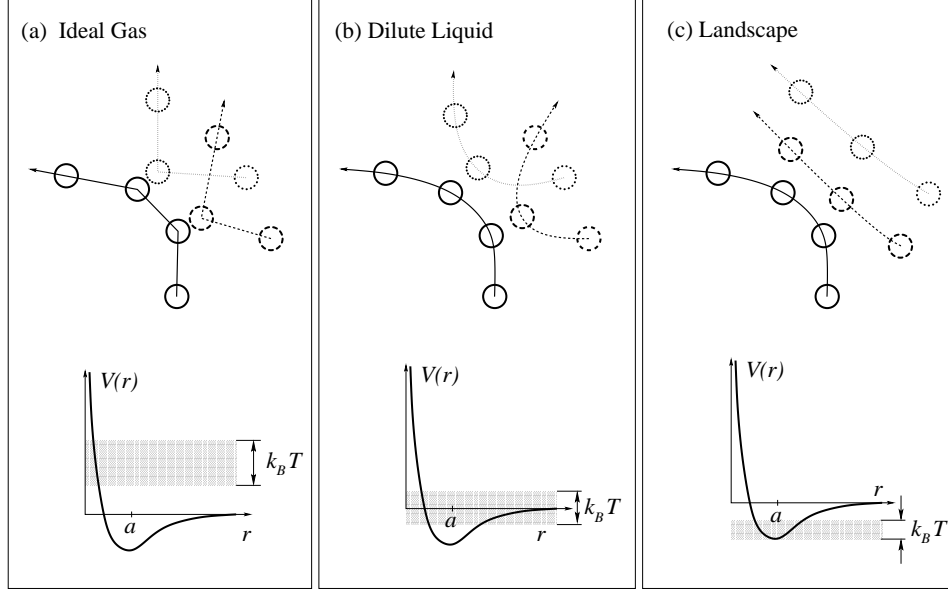


FIG. 17. The three relatively distinct kinetic regimes of an equilibrium liquid, or a conditionally equilibrium liquid, as the case would be below the melting temperature  $T_m$ . See text for explanation. The bottom portions illustrate the region of the two-particle potentials explored in the corresponding regimes. (a) Nearly ideal gas, (b) dilute liquid, and (c) landscape.

symmetry that becomes broken, whereby the uniform density profile for individual particles no longer minimises the free energy. Instead, the optimum density profile consists of a collection of disparate narrow peaks. The translational symmetry is eventually restored by activated transitions between distinct metastable configurations. The transition is sharp in the mean-field limit but becomes a soft crossover in finite dimensions because distinct metastable configurations have a finite lifetime. As a result, the translational degrees of freedom freeze out gradually, starting from the highest frequency motions. Despite the gradual character of the crossover, one may define a temperature,  $T_{cr}$ , that corresponds to the mid-point of the crossover [35]. In the mean-field limit, the crossover would be a sharp (first-order) transition at a well-defined temperature  $T_A$ . Although it is customary to assign a *temperature* to the RFOT crossover, we must bear in mind that crossover is better thought of as *density*-driven, as is clear from the argument. In actual substances characterised by finite interactions, compactification is realised most readily by cooling, hence our use of a temperature  $T_{cr}$ . The notion of the steric origin of the RFOT transition is consistent with the fact that substances that are characterised by open structures and very directional bonding crystallise *before* the steric effects become significant—in ways other than dictating the nearest-neighbour distance—and thus are poor glassformers, as discussed in Subsection III C. Conversely, pressurising such open structures leads to their vitrification [138–141].

Finally we make an important remark, terminology-wise, that the crossover from the collisional to activated transport could occur either above or below the melting temperature, the former and latter situations corresponding to strong and fragile substances respectively, see Section VII. As a result, a strong liquid can be in the activated transport regime while not being technically supercooled. At the same time, a very fragile substance can be supercooled even though its molecules still move in a largely collisional manner. To avoid ambiguity in this regard, we will term liquids below the crossover *glassy* or will say the liquid is in the



*landscape* regime.

## B. Configurational Entropy

We just saw that the magnitude of the configurational entropy is key to whether the emerging aperiodic structures can compete, free-energy wise, with the uniform liquid state. We shall also see shortly that knowing the configurational entropy is central to computing the activation barrier for liquid relaxations below the crossover. The configurational entropy has been evaluated from first principles only for the simplest systems, even if approximately, see Fig. 15. Such calculations for actual substances are very difficult, especially given that the explicit form of the actual quantum-chemical interactions is complicated and not known in closed form. On the other hand, the classical DFT calculations for aperiodic lattices, from Subsection IV A, strictly apply only to isotropically interacting particles that repel at short distances and attract modestly at large distances. It is thus imperative to be able to take advantage of the *measured* excess liquid entropy of actual liquids, which, however, must be calibrated in terms the entropy content of such a model liquid that is amenable to the DFT analysis.

Before we discuss the calibration, we provide in Fig. 14(b) a graph of the excess liquid entropy, as a function of temperature, from the seminal paper of Kauzmann [147]. Kauzmann emphasised, following Simon [151], that the excess entropy would vanish at a *finite* temperature,  $T_K > 0$ , if extrapolated beyond the glass transition. Approximately, one may write:

$$s_c \approx \Delta c_p(T_K)(T - T_K)/T_K. \quad (94)$$

In practice, one often uses the following functional form for the temperature dependence of the configurational entropy [152, 153]:

$$s_c \simeq \Delta c_p(T_g)T_g(1/T_K - 1/T), \quad (95)$$

c.f. Eq. (84), which works very well for many substances.

To calibrate the excess liquid entropy of an actual substance we first consider a useful, extreme limit of the hard sphere: The entropy of monodisperse spheres depends only on the density. Likewise, the fusion entropy is also temperature independent and is about  $1.19k_B$  per particle (Table I). Furthermore, we also understand fairly well how hard spheres pack: For instance, the highest filling fraction for monodisperse spheres is  $\pi/3\sqrt{2} \approx 0.74$ . We know accurately the density of the liquid and crystal in equilibrium (Table I), and have a good idea as to the filling fraction of the random close-packed structure, 0.64 or so. A somewhat better reference system can be obtained by starting with hard spheres and then including a weakly attractive tail to the particle-particle interaction. The next step is to find a naturally occurring system that shows strong—but not infinitely strong—repulsion at short distances and weak attraction otherwise. The finiteness of the energy scale associated with both the repulsive and attractive portion of the interaction affords one more flexibility in calibrating actual interactions. (We have already seen an example of this in Section III, see Fig. 11.) Argon is a good choice: On the one hand, Ar is a closed-shell atom and so two argon atoms repel at short distances owing to the Pauli exclusion principle while being attracted through weak, dispersive forces at larger separations. On the other hand, Ar is not too light so quantum effects are not large, and it is not too heavy, so that polarizability is not too high.

In all known glassformers—in contrast with argon—the interactions are *directional*, to a lesser or greater degree. For instance, suppose the magnitude of the fusion entropy per atom in an actual glass-former is smaller than in argon, see Table II. This means that fewer

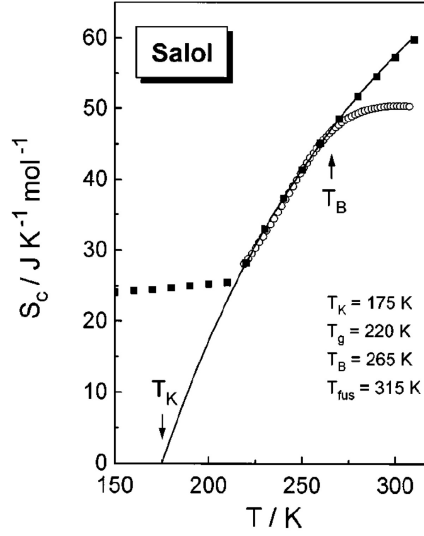


FIG. 18. Extrapolation of the configurational entropy for a number of specific substances below the glass transition temperature for salol (symbols) superimposed on inverse log-relaxation time data (solid line), showing a clear correlation between the decrease in configurational entropy and the increase in the relaxation time [153].

degrees of freedom freeze out at the liquid-to-crystal transition, *per atom*, than for isotropically interacting particles: Some of the degrees that would be available to isotropically interacting particles are, in fact, constrained by the directionality. One may thus think of the solidification of a substance with directional bonding as the freezing of weakly attractive, isotropically-interacting particles, but with an effective size *exceeding* the average atomic size. These qualitative conclusions apply equally to solidification into a periodic or aperiodic crystal.

Thus, we will usually calibrate the configurational entropy content of actual substances in the following way. We divide the substance's fusion entropy per molecule by the fusion entropy of argon per atom. This gives us the number  $N_b$  of rigid molecular units, or “beads,” per molecule [35, 36]:

$$N_b = \frac{\Delta H_m}{s_{\text{bead}} k_B T_m}, \quad (96)$$

where  $\Delta H_m$  and  $T_m$  are the fusion enthalpy and temperature respectively. The quantity  $s_{\text{bead}}$  is the entropy content per bead in units  $k_B$  in a reference liquid. If the latter is Ar (which is usually the case),  $s_{\text{bead}} = 1.68$ . As a result, the volumetric bead size is given by

$$a^3 = v_m^3 / N_b, \quad (97)$$

where  $v_m$  is the specific volume of the substance. Clearly, the calorimetric way to determine the bead size is phenomenological. Yet it turns out to produce bead counts that are chemically sensible [35]. In those cases where the bead size does affect the final answer, one should be mindful of potential ambiguities, as will be discussed in due time. In any event, many of the RFOT-based quantitative predictions are universal in that they are independent of the bead size.

In view of the potential numerical uncertainty in the bead size, it is reassuring that there is another sense in which this size can be defined, viz., the ultraviolet cut-off of the theory [154, 155]. In this elasticity theory-based view, all vibrational motions whose wave

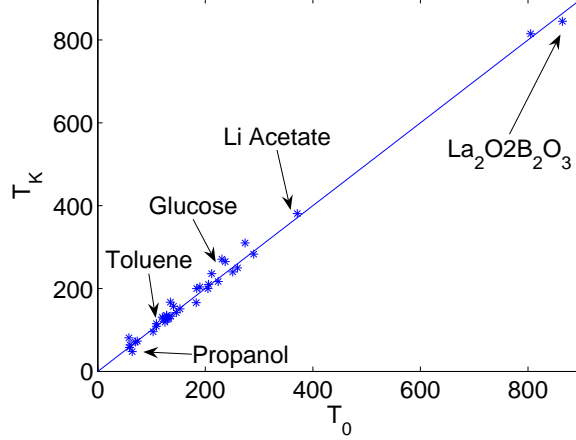


FIG. 19. The Kauzmann temperature  $T_K$  plotted versus the temperature  $T_0$ . At  $T_K$ , the configurational entropy extrapolated below the glass transition vanishes. At  $T_0$  the viscosity extrapolated below the glass transition diverges.

vector exceeds  $\pi/a$  do not affect the structural reconfigurations and are not included in the phonon sums, see Section VII.

To finish the discussion of calibration of the excess liquid entropy we note that the experimental values of this entropy, when calibrated according to the bead-counting procedure above, are in fact consistent with the magnitude of the configurational entropy requisite for the thermodynamical stability of the (degenerate) aperiodic-crystal state, relative to the uniform liquid state. These calculations are described in Section VII.

Now, the vanishing of the (extrapolated) configurational entropy is in apparent contradiction with the Nernst law and suggests that there is something special about the translational degrees of freedom in liquids. It may appear that the question of whether the entropy crisis would actually take place is somewhat of an academic nature: All known liquids become too slow to equilibrate on the laboratory scale well before the configurational entropy vanishes: Empirically, the liquid relaxation time diverges *exponentially* according to an empirical relation

$$\tau = \tau_0 e^{DT_0/(T-T_0)}, \quad (98)$$

known as the Vogel-Fulcher-Tammann (VFT) law. The coefficient  $D$  is called the fragility. Despite being somewhat academic, the question of the vanishing of the configurational entropy is fundamentally interesting and, ultimately, must be confronted if one were to reliably estimate the configurational entropy for actual substances from first principles.

Early on, Adam and Gibbs [156] argued that liquid transport above the glass transition is activated with a barrier scaling inversely proportionally to the configurational entropy. Motivated by these ideas, one may ask whether, in fact, the putative vanishing of the configurational entropy and divergence of the viscosity would take place at the same temperature. Richert and Angell [153] have carefully analysed uncertainties in the extrapolation beyond the glass transition temperature. This analysis demonstrates that the temperature dependences of the configurational entropy and relaxation data clearly correlate, see Fig. 18. Consistent with this detailed analysis, extrapolation of fitted kinetic and thermodynamic data for many more substances indicate a very tight correlation, if not downright coincidence of the temperatures  $T_0$  and  $T_K$ , see Fig. 19.

The putative Kauzmann entropy crisis adds another layer of complexity to the already intriguing behaviour of glassy liquids. In addition to freezing into one of the exponentially

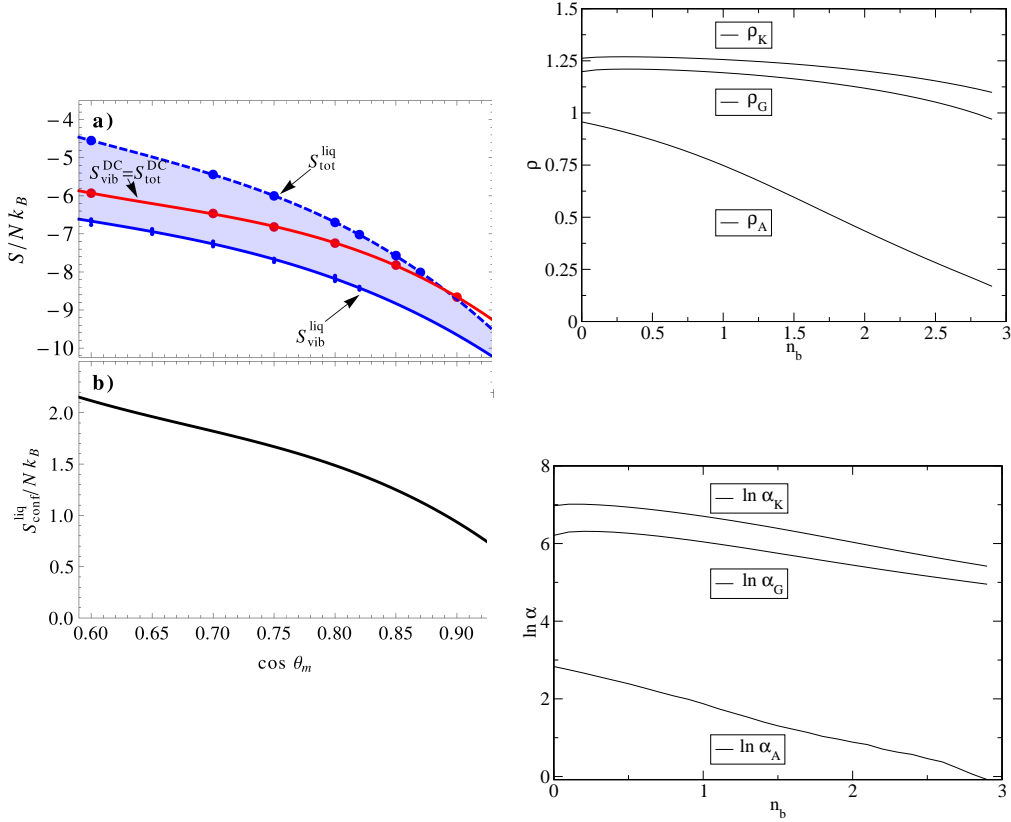


FIG. 20. **(a)** The (extrapolated)  $T = 0$  entropy of the liquid and diamond crystal (DC) made of patchy colloidal particles as a function of the angular width  $\theta_m$  of the patch. To large values of  $\cos \theta_m$ , there correspond smaller patches. Both the vibrational and full entropy of the liquid are shown. The density is fixed at  $\rho\sigma = 0.57$ , which corresponds to the filling fraction  $\approx 0.30$ . Note this value is below the filling fraction of the diamond lattice, viz.,  $\approx 0.34$ . **(b)** The configurational entropy of the patchy colloid, computed by subtracting the vibrational entropy of the liquid from the full liquid entropy, extrapolated to zero temperature. Due to Smallerburg and Sciortino [157]. **(c)** Dependence of the densities at the Kauzmann ( $\rho_K$ ), glass transition ( $\rho_g$ ), and mean-field RFOT ( $\rho_A$ ) transitions on the network connectivity in the Hall-Wolynes model [158]. **(d)** Dependence of the force constant of the effective Einstein oscillator  $\alpha$  from Eq. (29), according to Ref. [158].

many aperiodic minima—in the mean-field limit—an equilibrium liquid appears to be able to reach, as least in principle, a state in which the log-number of those minima scales *sublinearly* with the system size. In other words, there is essentially a unique aperiodic configuration that a liquid could presumably reach if sufficiently pressurised or cooled in a quasi-equilibrium fashion. Because this state is unique, it is also mechanically stable, as is a periodic crystal! To avoid confusion, we emphasise that this mechanical stability would be achieved even in *finite* dimensions. (In contrast, the mean-field system would become stable already below the temperature  $T_A$ .) Kauzmann himself suggested that the entropy crisis would be avoided if the liquid reached its mechanical stability limit and crystallised before  $T_K$  is reached. Stevenson and Wolynes [50] suggest that the actual story about the ultimate fate of molecular liquids is more complicated, to be discussed in due time.

In this regard, it is interesting to mention a relatively recent simulation study by Smallerburg and Sciortino [157] on patchy colloids with highly anisotropic interactions, see Fig. 20(a) and (b). The model particles are rigid spheres with four added attractive patches in a tetra-

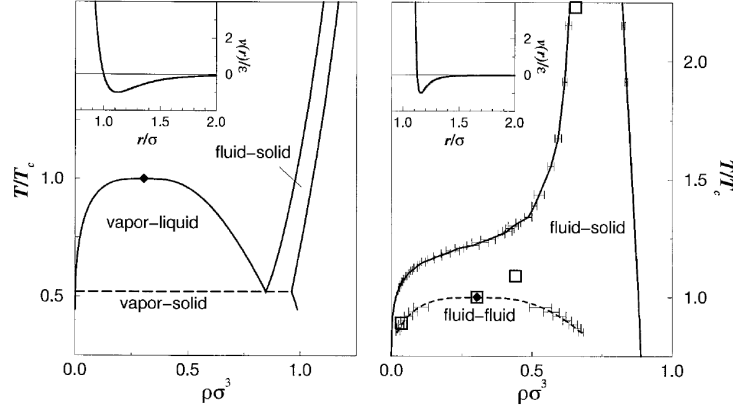


FIG. 21. Concentration-temperature phase diagrams for isotropically interacting particles. The l.h.s. and r.h.s panels show two distinct situations in which the width of the attractive well in the interaction potential is comparable to or significantly less than the particle size, see insets [159]. The former situation is typical in ordinary liquids while the latter is characteristic of protein or colloidal solutions, as in Ref. [157]. Given a sufficiently narrow attractive well, the vapour-liquid coexistence line is moved under the liquidus. As a result the liquid can exist only as a metastable phase, while in equilibrium, the vapour transitions directly to the crystal phase. Since colloids are suspended in a solution, the vapour-liquid coexistence is observed as a coexistence between a relatively dilute and concentrated solution, and is often called “liquid-liquid” coexistence.

hedral arrangement, each patch of angular width  $\theta$ . The patches are attractive, but only in a rather narrow distance range  $\delta = 0.12\sigma$ ; one contact per patch is enforced. The (extrapolated) configurational entropy of this patchy colloid, *at constant volume*, remains positive down to absolute temperature, implying a negative Kauzmann temperature! This entropy is so large, in fact, that the liquid remains more stable than the diamond lattice that the particles can form at the density in question. The large configurational entropy should not be too surprising in light of our discussion in Subsection III C; fixing the density at a value below that of the very open, diamond structure minimises the steric effects that lead to the crossover and, eventually, to the (putative) Kauzmann crisis. Indeed, according to Fig. 1 of Ref. [157], the ground state of the colloid at constant pressure is close-packed. The short-range character of the attraction in the model is also important. Because of the narrow width of the attractive minimum, relative to the particle size, the gas-liquid coexistence region of the system is “hidden” under the liquidus, see Fig. 21. This phenomenon is well known—and often irksome—to X-ray crystallographers, and has been elucidated by Wolde and Frenkel some time ago [159]. In equilibrium, such a gas condenses into the crystal while bypassing the liquid state. (Since protein solutions are often very hard to equilibrate, structural biologists often observe a liquid-liquid separation that may lead to gelation and other types of aggregation and preventing the protein crystal from forming.) This type of gas-crystal coexistence can indeed be seen in Fig. 1(a) of Ref. [157]. The notion that we are dealing with a gas here buttresses our earlier statements that steric repulsion is key to understanding the temperature dependence of the configurational entropy and the glass-forming ability of actual substances.

It would be fair to say that at present, we do not have a reliable way to evaluate the configurational entropy of actual glass-formers from first principles. Aside from approximations and the model nature of the liquid, the Mézard-Parisi calculation [148] is still subject to the assumption that the entropy of the *uniform* liquid can be extrapolated to  $T_K$ . This may introduce some numerical uncertainty, if the Kauzmann state is *below* the mechanical stability limit of the uniform liquid. Regardless of various technical difficulties, one can es-

establish useful connections between the bonding patterns in the liquid and its configurational entropy using a microscopically-motivated model. Hall and Wolynes [158] (HW) used the self-consistent phonon theory to analyse a hard sphere liquid with randomly added bonds between particles, so that a particle is bonded on average to  $n_b$  neighbours. Adding bonds stabilises contacts energetically but destabilises them entropically. As expected, increasing the number of bonds dramatically decreases the density  $\rho_A$  at which metastable structure begin to form while affecting the density  $\rho_K$  of the Kauzmann state only modestly, Fig. 20(c). The rapid decrease of  $\rho_A$  with the number of rigid bonds is consistent with the results from Fig. 20(a) and (b) in that increasing directionality makes local bonding patterns more open. Beyond a certain critical value of bonds a rigid percolation takes place in the network, as signalled by  $\alpha^{-1/2}$  approaching the particle size  $a$ , see Fig. 20(d). The rigidity percolation at  $n_b \simeq 2.8$  is not inconsistent with independent estimates by Thorpe and coworkers [160, 161], who obtain  $n_b \simeq 2.4$ . Similarly to the behaviour of the density, adding bonds also affects the temperature  $T_A$  much more than  $T_K$  (both increase), so that the  $T_K/T_A$  ratio *decreases*. We shall see in Section VII that the laboratory glass transition occurs at a nearly universal value of the configurational entropy. This notion, in combination with Eq. (95), implies that a smaller value of the  $T_K/T_A$  corresponds with the smaller value of the heat capacity jump at the glass transition  $\Delta c_p(T_g)$ . This is qualitatively consistent with observation [61], see also the inset in Fig. 2.

One should be cautious in interpreting the results in Figs. 20(c) and (d) at values of  $\alpha$  significantly below  $10^2/a^2$ . While these graphs give correct qualitative trends for large to medium values of  $\alpha$ , they could not correspond to an equilibrated liquid for the smallest values of  $\alpha$ , certainly not as small as  $1/a^2$ . Indeed, we know that the vibrational displacement near the mechanical stability limit in directionally bonded materials, such as silicon, is quite similar in magnitude to that in well-packed materials, see Ref. [105]. In other words, the model liquid in Figs. 20(c) and (d), if equilibrated, should melt well before the percolation transition at  $\alpha \sim 1/a^2$  can be reached. Consequently, the liquid is not in the landscape regime on the low end of the investigated range of  $\alpha$ . Conversely, given the apparent metastability of the network-like states with  $\alpha \sim 1/a^2$ , one may infer from the Hall and Wolynes model that such small values of  $\alpha$  could be still be reached, but only *off-equilibrium*, i.e., by preparing the glass through rapid quenching or vapour deposition. This notion will be of use toward the end of the article.

Finally, given the complexity of the interactions in actual materials, it is reasonable to ask whether one could evaluate the configurational entropy semi-phenomenologically. This way, those interactions enter in the form of the measured values of materials constants such as elastic moduli and thermal expansion coefficient, etc. Bevzenko and Lubchenko [154, 155] have, in part, accomplished this program, to be discussed in Subsection IV D.

We reiterate that it is imperative to recognise that whether or not the configurational entropy strictly vanishes at some low temperature is not directly relevant to the translational symmetry breaking that results from the random first order transition. In fact, it is a common misconception that the existence of the entropy crisis at  $T_K$  is the essential feature of the the RFOT. It is not. The only prerequisite for the translational symmetry breaking at  $T_A$  is that condition (88) be satisfied. We note also that there is a rigorous sense, in which the Kauzmann crisis can be defined for a liquid that would not ordinarily have one in a *macroscopic* sample. This crisis can be achieved when a *finite* sample runs out of configurations, to be discussed in Section V C.

**C. Qualitative discussion of the transition at  $T_A$  as a kinetic arrest, by way of mode-mode coupling. Connection between kinetic and thermodynamic views on the transition at  $T_A$ . Short discussion on colloids, binary and metallic mixtures, and ionic liquids.**

Studying the thermodynamic stability of aperiodic solids is certainly not the only way to approach the problem of the glass transition. Much effort toward understanding the dramatic slowing-down in supercooled liquids, Fig. 2, was undertaken in the early 1980s starting from a purely kinetic prospective. This work culminated in the creation of the mode coupling theory [11, 12, 162] (MCT), which predicts that under certain conditions, the traditional view of the dynamics of a liquid as being that of a dense gas fails. This theory builds on early theories of collisional transport [163] and arrives at the conclusion that already in a uniform liquid, the view of particle transport as a memory-less, Langevin process eventually becomes internally-inconsistent as the density increases. Given the difficulty of summing high-order terms in the mode-mode coupling expansion [164], one has to resort to a mean-field approximation. In this mean-field limit, one discovers that at a high enough density, a particle’s memory extends indefinitely implying that it no longer moves about but, instead, forever vibrates around a certain location in space. This behaviour is often called “caging.” As the cages form, the viscosity diverges, leading to a kinetic catastrophe. These “cages” turn out to correspond to the metastable structures that emerge during the RFOT. Indeed, Kirkpatrick and Wolynes [146] have shown that in the mean-field limit, the kinetic catastrophe of the MCT theory and the RFOT theory are equivalent. In this approach, the response of the liquid becomes elastic while the equation that self-consistently specifies the force constant  $\alpha$  of the effective Einstein oscillator from Eq. (29) has the same structure as the DFT-based Eq. (83) for determining  $\alpha$  self-consistently:

$$\alpha = \frac{\rho}{6} \int \frac{d^D \mathbf{q}}{(2\pi)^D} q^2 \tilde{c}^{(2)} \tilde{h}(\mathbf{q}) e^{-q^2/2\alpha}, \quad (99)$$

where the function  $h$  is defined in Eq. (68). It turns out that this equation identically coincides with Eq. (82) in the mean-field limit  $D \rightarrow \infty$ . Indeed,  $\tilde{S}_q \rightarrow \bar{\rho} \tilde{g}_q$  in this limit (since the  $i = j$  contribution in Eq. (61) becomes vanishingly small), and so  $\bar{\rho} \tilde{h}_q \rightarrow \tilde{S}_q$  (at  $q > 0$ ), by Eq. (68). On the other hand, it can be shown [146] that  $\alpha \propto D^2$  as  $D \rightarrow \infty$ , c.f. Eq. (83); thus  $\tilde{S}_0(q) \rightarrow \tilde{S}(q)$ . As a result, the kinetic arrest of the MCT exactly coincides with the inception of the spinodal in  $F(\alpha)$ , in the mean-field limit. Furthermore, since the system is equilibrated and must obey detailed balance, it must be true that the set of states corresponding to the finite value of  $\alpha$  at the spinodal are thermodynamically stable. Otherwise, the system would not have been arrested in a state characterised by a finite  $\alpha$  but, instead, would remain in the uniform state  $\alpha = 0$ . In other words, the temperature  $T_A$  of the RFOT transition strictly coincides with the mean-field spinodal. The above argument is somewhat subtle because in the strictest mean-field limit, the system could, in principle, get arrested even in a *metastable* free energy minimum because the barrier for escape would be infinite. To make the argument work, we must assume a finite  $D$  at the onset, to make the escape barrier finite and take advantage of detailed balance. At finite  $D$ , the temperature of the spinodal may or may not strictly coincide with the temperature  $T_A$  at which the aperiodic-crystal state becomes thermodynamically stable. In the  $D \rightarrow \infty$  limit, however, the two temperatures become equal. We shall observe a similar pattern for mean-field spin models in the next Subsection.

In finite dimensions, the cages do not live forever and eventually disintegrate via activated processes, as will be discussed in detail in Section V. Reproducing the activated processes formally within the the MCT framework appears to be difficult and has not been accomplished to date, to the author’s knowledge and judgement [165]. Adding activated

processes on top of the MCT effects can be done phenomenologically and results in good fits of temperature dependences of relaxation times [166, 167]. At any rate, the correspondence between the thermodynamics-based RFOT treatment and the MCT survives in finite dimensions in the sense that the sharp RFOT transition becomes a soft crossover, while the kinetic catastrophe becomes a gradual rise in viscosity.

Even in its simplest version, the MCT is rather formal in that it discusses correlations in liquid in terms of coupling between hydrodynamic modes, not molecular motions themselves; discussing the technical details of the MCT would be beyond the scope of the article. Extensive reviews of the MCT can be found elsewhere [168, 169]. Here, instead, we discuss the kinetic perspective on the RFOT transition in a qualitative, phenomenological fashion, yet with relatively explicit reference to molecular motions.

Suppose first that particle motions have no memory whatsoever. Under these circumstances, we can connect the (thus frequency-independent) self-diffusivity  $D$  with the viscosity  $\eta$  via the Stokes-Einstein relation:  $D = k_B T / (6\pi(a/2)\eta)$ , where we set the hydrodynamic radius of the particle at one-half of its volumetric size. By Einstein's formula, the typical travelled distance squared goes with time  $t$  as  $\langle r^2 \rangle = 6Dt$ . Thus the time it takes for a particle to diffuse its own size is given by:

$$\tau_{\text{ex}} = \frac{\pi\eta a^3}{2k_B T}. \quad (100)$$

Note that this size represents a secure upper bound on the time it takes for two particles to exchange identities and thus locally establish configurational equilibrium.

Now suppose that transient structures could, in principle, form in the same system, whether as a result of a phase transition or not. According to the phenomenological Maxwell relation (which can be derived constructively, see Section IX), the lifetime of the metastable structures in such a liquid is intrinsically related to its viscosity and elastic constants:

$$\tau \simeq \frac{\eta}{K} \quad (101)$$

The liquid may be regarded as uniform only insofar as we cannot distinguish the particles by their location. Consequently, when the viscosity is so high that the time a particle “sticks around” becomes comparable to the lifetime of a transient structure from Eq. (101), we must conclude that the assumption of the liquid's uniformity is internally-inconsistent and that transient structures do, in fact, form. This is the essence of the symmetry breaking that takes place during the crossover from collisional to activated transport, if expressed in kinetic terms. Equating the times in Eqs. (100) and (101) yields  $\eta = \infty$ . (There is no  $\eta = 0$  solution because the viscosity of hard spheres is finite and concentration-independent in the infinite dilution limit.) The  $\eta = \infty$  solution is internally consistent and corresponds with the kinetic catastrophe of the MCT, by which the liquid would be completely arrested, in the mean-field limit.

If one attempts to equate the timescales from Eqs. (100) and (101), with the aim to estimate the viscosity at which the crossover would actually occur, one quickly discovers a potential issue. These two equations, in combination with the Lindemann criterion,  $Ka^3 \simeq \alpha a^2 k_B T \simeq 10^2 k_B T$ , would seem to indicate that the exchange time is *always* longer than the structural relaxation time  $\tau$ , whenever the transient structures could exist. (Some of this excess is intrinsic and some is due to a likely overestimate in Eq. (100).) Yet there is not necessarily a contradiction here. The condition that  $\tau_{\text{ex}} > \tau$  simply implies that the emergence of the solid is driven *thermodynamically*, not kinetically. The finite difference between  $\tau_{\text{ex}}$  and  $\tau$  is inevitable because the kinetic arrest is due to a solidification transition and is thus a *discontinuous* transition, as we saw in Section III for the regular liquid-to-crystal transition and in Subsection IV A for the random-first order transition; this implies that the viscosities in “pure” uniform liquid and aperiodic crystal should differ by a



finite amount. The viscosity of actual substances interpolates between the values given in Eqs. (100) and (101) and thus changes continuously through the crossover. It seems worthwhile to recall that the finite (and large) value of the inverse Lindemann length squared  $\alpha$ , at a liquid-to-solid transition, is crucial in avoiding the critical point in Fig. 7. Likewise, the present, crude argument suggests that a *continuous* kinetic arrest would also be avoided, in equilibrium, owing to the finite value of  $\alpha$  in a solid, be it periodic or aperiodic.

Still, is there a simple way to estimate the viscosity at which the crossover takes place based on the simplistic reasoning above? To do so, we must use a measure of liquid's memory that would be more appropriate at the crossover than that afforded by Eq. (100). The latter equation clearly does not apply when nearby particles' movements are tightly correlated, as in Fig. 17(b). In this regime, the configurational and velocity equilibration processes are *coupled* and so one expects the corresponding equilibration times to be mutually tied. Indeed, the hopping time of vibrational packets is tied to the particle hopping time in that the latter is an upper bound for the former. On the other hand, the vibrational hopping time is directly connected with the velocity equilibration. To put this in perspective, the configurational equilibration is much faster in dilute gases, Fig. 17(a), and vice versa in very dense liquids or solids, in which collisions are very frequent, Fig. 17(c). In both of these cases configurational and velocity equilibration processes are decoupled. Velocities equilibrate on the times comparable to auto-correlation time  $\tau_{\text{auto}}$ :

$$\tau_{\text{auto}} = \frac{m}{\zeta} \simeq \frac{a^2 \rho}{3\pi\eta}, \quad (102)$$

where  $m = \rho a^3$  is the particle mass. Thus, *near the crossover*, we may associate the duration of a particle's memory with the time  $\tau_{\text{auto}}$  multiplied by a dimensionless number  $C$  that signifies how many collisions the particle must undergo before the memory of its location is completely erased:  $\tau_{\text{memory}} \sim C\tau_{\text{auto}}$ . Substitution of typical values of the density, particle size and viscosity in Eq. (102) shows that  $\tau_{\text{auto}}$  is very short, shorter than molecular vibrations. (This is expected as each molecule directly interacts with molecules from several coordination shells.) The velocity equilibration time should be about two orders of magnitude greater than  $\tau_{\text{auto}}$ , while the configurational equilibration is even slower. Consequently, the numerical factor  $C$  is, very roughly,  $10^3$  or greater. We reiterate that  $\tau_{\text{auto}}$  reflects the configurational equilibration only in a *narrow* density range; note the inverse scaling of  $\tau_{\text{auto}}$  with the viscosity, which is the opposite of what is expected for the configurational equilibration timescale. Equating  $\tau_{\text{memory}}$  with  $\tau$  from Eq. (101) yields the following estimate for the viscosity at the crossover:

$$\eta \sim K(a/c_s) C^{1/2}, \quad (103)$$

where  $c_s$  is the speed of sound and so  $a/c_s$  scales with but exceeds a typical vibrational period of a molecule. Quantitative criteria for crossover will be presented in Section VII, where we shall see that at  $T_{\text{cr}}$ ,  $\eta \simeq K\tau_{\text{vibr}} \times 10^3$ , where  $\tau_{\text{vibr}}$  stands for the vibrational relaxation time.

Although lacking the sophistication of the mode-coupling theory, the qualitative discussion above on the kinetic aspects of the emergence of the landscape makes one realise that in liquids made of indistinguishable particles, particle collisions and configurational equilibration are intrinsically connected: Each particle collides exclusively with particles it must exchange places with for the liquid to equilibrate. Conversely, the viscous drag on a given particle is solely due to particles that are identical to that given particle. Colloidal suspensions, among other systems, present a radically different situation. The viscous drag on a colloidal particle is now largely due to the solvent. Thus by varying the solvent or the particle size, one can vary the timescale for configurational equilibration at a fixed filling

fraction. Alternatively said, the bulk viscosity and structural relaxation are largely *decoupled* in colloidal suspensions. Owing to this decoupling, one can make colloidal particles arbitrarily sluggish—by increasing their size—without them ever entering the landscape regime. To quantify these notions, we note the dynamic range accessible to an ordinary, molecular liquid between the melting point ( $\tau \simeq 10^{-12}$ ) and the crossover to the landscape regime ( $\tau \simeq 10^{-9} \dots 10^{-8}$ ) is about 3-4 order of magnitude. By Eq. (100), the exchange time  $\tau_{\text{ex}}$  for micron-sized colloidal particles exceeds that for ordinary liquid easily by ten orders of magnitude, at the same value of the bulk viscosity. This implies that on ordinary laboratory timescales, such mesoscopic colloids only *begin* to sample the landscape regime when their arrest becomes macroscopically apparent.

Likewise, one expects some decoupling between collisions and structural relaxations in viscous metallic mixtures and heterodisperse mixtures of model particles employed in simulational studies of slow liquids. In such mixtures, the mole fractions of the ingredients are comparable and so the degree of decoupling is not nearly as large as in colloids. An alternative, thermodynamic way to see this is as follows: One often employs eutectic mixtures of elements to destabilise the crystal state, relative to the liquid, at the same value of viscosity. By the same token, employing carefully chosen size ratios or molar fractions in mixtures, one may lower the temperature  $T_A$ , while not affecting the liquid’s viscosity. Again, this will lead to an increased dynamic range of the pre-landscape regime. We shall see additional indications in Subsection XII A that metallic glasses freeze just below the crossover.

Room temperature ionic liquids represent an intermediate case between colloidal suspensions and metallic mixtures. Like the metals, such liquids are mixtures of molecules that do not have obvious crystalline ground states. On the other hand, the decoupling between collisional processes and structural relaxation is significantly greater than in those mixtures. Because of the very long range of the Coulomb interaction, each molecule directly collides with a very large number of molecules, not just its nearest neighbours. Indeed, although the intensity of an individual collision decays as  $1/r$  with distance, the number of molecules grows as  $r^2$  with distance. (The author does not have a simple argument to determine the collisional range.) We thus conclude ionic liquids are at least as slow and are likely slower than metallic mixtures and thus are further away from the landscape regime, at a given value of viscosity. To avoid confusion we note that the above logic does not apply to traditional ionic liquids such as  $\text{ZnCl}_2$ , since these exhibit a great deal of covalent bonding. Such liquids are more appropriately thought of as dipolar.

#### D. Connection with spin models

The formal status of the RFOT theory as of the late 80s–mid 90s was somewhat uncertain for a number of reasons. Given the inherent approximations of the density-functional theory, the mean-field character of the DFT-MCT connection, and the technical complexity of the MCT theory [168], many regarded the picture advanced by the RFOT theory of the structural glass transition as lacking in formal foundation or were unaware of the theory in the first place. The replica-based calculation of the configurational entropy by Mézard and Parisi [148] was not available until 1999. Although constructive, that replica calculation, again, is approximate and relies on the assumption that the mechanical stability limit of the uniform liquid is not reached above the (putative) temperature  $T_K$ . On the other hand, calorimetry data for *actual* supercooled liquids yield the magnitude of the configurational entropy requisite for the stability of the aperiodic crystal. Perhaps the most forceful proof of the activated nature of the liquid transport near the glass transition is that the rate of the transport is Arrhenius-like below the glass transition, as emphasised in Ref. [170]. Thus, although the premise of the RFOT theory is clearly consistent with observation—and so are

its many predictions!—some of the aspects of the theory itself could be perceived as having been established only phenomenologically. To fill this perceived formal gap, much technical effort has been directed at finding solvable models that exhibit features reflecting those of the structural glass transition.

By the late 1980s, a very interesting disordered model having a glass-like transition had already been worked out, viz., the mean-field Sherrington-Kirkpatrick (SK) model [171, 172]. This model exhibits a proliferation of metastable minima below a certain temperature, similar to what happens during the RFOT. The model is an Ising magnet from Eq. (5), but with randomly distributed couplings  $J_{ij}$ . The distribution's mean is zero. In the mean-field limit, the couplings should scale not as  $1/N$ , but  $1/\sqrt{N}$ , in contrast with the Ising ferromagnet. Most commonly, the distribution is assumed to be Gaussian:

$$p(J_{ij}) = \frac{1}{\sqrt{2\pi J^2/N}} e^{-\frac{J_{ij}^2}{2J^2/N}} \quad (104)$$

In an interesting contrast with the regular Ising magnet, we must retain the second order term in the expression for the molecular field even in the strict mean-field limit:

$$h_i^{\text{mol}} = \sum_j J_{ij} m_j - m_i \sum_j \beta J_{ij}^2 (1 - m_j^2), \quad (105)$$

c.f. Eq. (38). The reader will recognise  $\beta(1 - m_j^2)$  at the susceptibility of a spin with magnetisation  $m_j$  discussed following Eq. (38). Thus the second order term on the r.h.s. gives the effective field spin  $i$  exerts on itself through interactions with the rest of the spins, consistent with this term being proportional to  $m_i$  itself. This term corresponds to the Onsager cavity field in electrodynamics [173] and turns out to make a finite contribution to the molecular field in disordered magnets even in the mean-field limit; this contribution is in fact numerically equal to the first term at the glass transition and thus must be retained in the free energy expansion [172, 174].

Combined with Eq. (35), which connects the molecular field with local magnetisation, Eq. (105), forms a closed system of equations, often called the Thouless-Anderson-Palmer [175] (TAP) equations that can be used, in principle, to determine the equilibrium magnetisation in the SK magnet. The corresponding free energy reads:

$$\begin{aligned} F(\{m_i\}) = k_B T \sum_i & \left( \frac{1 + m_i}{2} \ln \frac{1 + m_i}{2} + \frac{1 - m_i}{2} \ln \frac{1 - m_i}{2} \right) \\ & - \sum_{i < j} J_{ij} m_i m_j - \frac{1}{2} \sum_{ij} \beta J_{ij}^2 (1 - m_i^2)(1 - m_j^2), \end{aligned} \quad (106)$$

c.f. Eqs. (6), (7), and (9).

The mean-field system freezes into a “spin-glass” state below a certain, sharply defined temperature, whereby the number of possible states to freeze into scales with the system size, in contrast, for instance, with the ordinary Ising magnet, in which the number of such distinct states is just two. All free energy minima are automatically aperiodic—owing to the disorder in the couplings—similarly to the liquid below the RFOT. Yet the ergodicity-breaking transition in the SK model is *continuous*, in contrast with the liquid. The continuity of the transition is consistent with the discrete symmetry of the time-inversion symmetry of the SK hamiltonian,  $\{\sigma_i\} \leftrightarrow \{-\sigma_i\}$ , by which the cubic term and the rest of the odd terms in the Landau-Ginzburg expansion are expressly forbidden by symmetry.

An equally important piece of distinction between the SK model and the liquid case is that in the former, the disorder is built-in, or *quenched*. The multiplicity of the solution is due to the vast number of configurations available to a magnet with the disordered couplings from Eq. (104) and a lack of a unique stable state. This type of frustration can be seen already

with an Ising *antiferromagnet* on the 2D triangular lattice:  $E = -J(\sigma_1\sigma_2 + \sigma_1\sigma_3 + \sigma_2\sigma_3)$  with  $J < 0$ . The ground state of this system is six-fold degenerate ( $E = J$ ) and the excited state is two-fold degenerate ( $E = -3J$ ). In contrast with the SK model, there is no built-in disorder in liquids. Instead, the interactions between molecules are perfectly translationally invariant. The disorder in structural glass is thus entirely *self-generated*. Although the latter fact is often cited as a most enigmatic feature of the structural glass transition, it is not hard to see how frustration could, in principle, arise in 3D liquids. For instance, the Voronoi cell corresponding to the locally-densest packing in 3D is the regular dodecahedron, which has a 5-fold symmetry axis and thus does not tile space.

It turns out that the solutions of the free energy (106) have an incredibly rich structure. The free energy minima are organised into a multi-tiered hierarchy, by which distinct solutions can be classified according to the degree of mutual similarity. It is convenient to think of these solutions as distinct replicas in the Gibbs ensemble that happened to freeze into distinct free energy minima, below the glass transition, the same way extensive portions of an Ising ferromagnet could polarise up or down below the Curie point. For the mean-field SK model, the similarity of distinct solutions—or replica overlap—is continuously distributed. This multi-tiered ergodicity breaking was elucidated by Parisi [172], among others, in the early 1980s and is often called *full* replica symmetry breaking (RSB).

Already in their 1985 paper, Singh, Stoessel, and Wolynes [143] point out that the free energy landscape of an aperiodic crystal can bear similarities to the Parisi solution of the SK model, as the distinct replicas are also aperiodic upon ergodicity breaking. Still, a meaningful connection between the two systems, if any, was difficult to establish given their distinct symmetries, even setting aside the lack of quenched disorder in liquids.

Spin models that afford such a connection must not have the time-inversion symmetry of the Ising model. One such model is the so called  $p$ -spin model with an odd  $p$ :

$$E = - \sum_{i_1 < i_2 < \dots < i_p} J_{i_1 i_2 \dots i_p} \sigma_{i_1} \sigma_{i_2} \dots \sigma_{i_p}, \quad (107)$$

where the couplings are distributed according to

$$p(J_{i_1 i_2 \dots i_p}) = \frac{1}{\sqrt{p! \pi J^2 / N}} e^{-\frac{J_{i_1 i_2 \dots i_p}^2}{p! J^2 / N}}. \quad (108)$$

This model exhibits a one-stage replica symmetry breaking (RSB), for  $p > 2$  [176]. (In the limit  $p \rightarrow \infty$ , the  $p$ -spin model reduces to the so called random energy model (REM) [177, 178] while the calculations simplify significantly.) That all the replica overlaps are the same implies that all free energy minima are equivalent.

In contrast with the SK model (which corresponds to  $p = 2$ ), the ergodicity breaking in the  $p$ -spin model is *discontinuous* for  $p > 2$  [177]. Motivated by this notion and the mean-field equivalence between the kinetic catastrophe of the MCT and the RFOT [146] discussed in Subsection IV C, Kirkpatrick and Thirumalai [179, 180] have analysed, upon Wolynes's suggestion, a dynamic version of the  $p$ -spin model. One way to impart the model with dynamics is to treat the length of an individual spin as a particle with a finite mass, whose motion is subject to a soft, bistable potential. Aside from some potential uncertainty stemming from approximations, these workers discovered that the dynamic  $p$ -spin model undergoes, in mean-field, a kinetic catastrophe at a temperature  $T_g$  *above* the temperature  $T'_g$  at which the replica symmetry is broken.

In 1987, Kirkpatrick and Wolynes [181] (KW) definitively rationalised those intriguing but enigmatic findings by obtaining a complete solution of the mean-field version of the so called Potts glass model, using a state-counting strategy employed by Thouless, Anderson, and Palmer [175]. A formally exact calculation of the free energy of the mean-field Potts glass had been furnished two years prior, by Gross, Kanter, and Sompolinsky [182]. The

Potts model is similar to the SK model, but generally does not exhibit the time-inversion symmetry and may exhibit a discontinuous ergodicity-breaking transition under certain circumstances, similarly to the  $p$ -spin model. In its most basic form [183], the Potts model is a generalisation of the Ising model to an energy function of the form  $E = -\sum_{i<j} J_{ij} \sigma(s_i, s_j)$ , where the (generally vectorial) spin variables  $s_i$  are allowed to have a chosen, discrete set of values. The test-function  $\sigma(s_i, s_j) = \delta_{s_i, s_j}$  singles out only the configurations in which the spin variables on sites  $i$  and  $j$  have the same value. More generally, one may use a test function that assigns a non-zero weight to  $s_i \neq s_j$  configurations also; this weight, however, must be different from that of the identical configuration, by definition. A common test function of this kind is simply the scalar product of the vectors, as would be natural in a Heisenberg model:  $\sigma(s_i, s_j) = s_i s_j$ , however in contrast with Heisenberg-like models, the spins are not continuous but are allowed to point only in specified directions. Specifically one often dictates that the spins point toward the vertices of a  $p$ -cornered hypertetrahedron in a flat  $(p-1)$ -dimensional space [184]. Here we set the length of each vector at  $\sqrt{p-1}$ , by definition. For  $p=2$ , we recover the usual Ising spins; the corresponding test function  $s_i s_j$  is equal to either 1 ( $s_i = s_j$ ) or  $-1$  ( $s_i \neq s_j$ ). When  $p=3$ , the spins point toward the corners of an equilateral triangle with the side  $\sqrt{6}$ . The test function can have the value 2 ( $s_i = s_j$ ) or  $-1$  ( $s_i \neq s_j$ ). For  $p=4$ , the spins could point toward the corners of the regular 3D tetrahedron, which implies four distinct orientations, and so on. KW considered exactly this version of the Potts model (for an arbitrary value of  $p$ ):

$$E = -\sum_{i<j} J_{ij} s_i s_j, \quad (109)$$

where the couplings  $J_{ij}$  are random and obey the distribution (104).

For  $p > 4$ , the mean-field Potts glass exhibits a discontinuous transition at a temperature  $T_A$ , in which an *exponential* number of solutions emerge, each solution corresponding to a free energy minimum. The transition exhibits itself as a spinodal at a finite value of the replica-overlap order parameter, call it  $q$ . The free energy just below the spinodal, as a function of  $q$ , looks like the  $F(\alpha)$  curve in Fig. 12(a) corresponding to  $\rho\sigma = 1.05$ . It turns out that each individual solution is higher in free energy than the symmetric phase exactly by  $TS_c$ , where  $S_c$  is the log-number of those solutions times  $k_B$ . Despite the spectacular symmetry breaking at  $T_A$ , the *full* free energy or entropy of the mean-field Potts glass does not experience a singularity of any sort. In further contrast with the SK model, the replica-symmetry breaking at  $T_A$  is *one-stage*, not infinite-stage.

Furthermore, the configurational entropy  $S_c$  is found to vanish at a finite temperature  $T_K < T_A$ . Note that in the mean-field model from Eq. (109), the barriers separating the distinct minima emerging below  $T_A$  are strictly infinite. This means that the system is already completely arrested at a temperature  $T_A > T_K$  even as its entropy is finite! KW [181] pointed out that in finite dimensions, however, the barriers separating the distinct free energy would be, in fact, finite and so activated transitions between the minima would be allowed. Accounting for spatial fluctuations already in the long-wavelength approximation, dictates that there be correlation lengths diverging both at  $T_A$ , owing to critical-like fluctuations at the spinodal, and diverging at  $T_K$ , to be discussed in detail in Section V. The infinite-range correlations at  $T_A$  would be destroyed by the aforementioned activated transitions. Complemented by these notions, the exact solution of the mean-field Potts glass model was important in that it showed that the RFOT-advanced picture of the glass transition as a kinetic arrest into a *degenerate* aperiodic crystal is not unique from a purely formal standpoint. As an added bonus, the Potts glass also exhibits a Kauzmann state.

Because of these apparent similarities between the thermodynamics and kinetics of glassy liquids and the disordered Potts model, it is still very common to see statements in the literature that the RFOT picture of the structural glass transition is simply an analogy

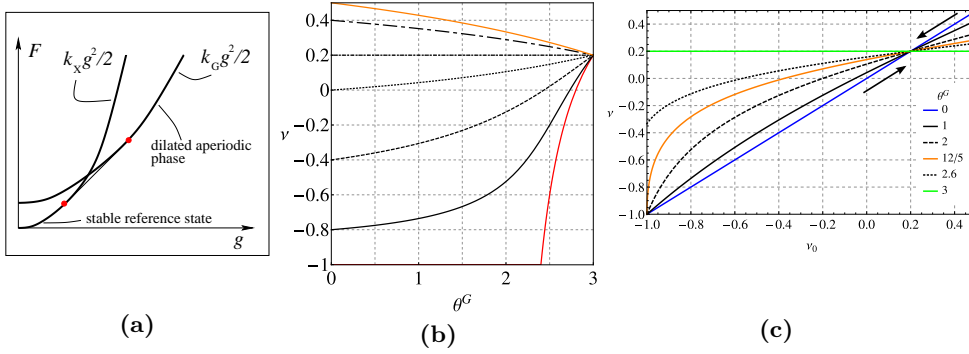


FIG. 22. **(a)** The two parabolas correspond to the free energy of a reference, mechanically stable state (“X”) and a metastable, aperiodic state (“G”). The tangent construction demonstrates the excess free energy at the contact between the two states, after Ref. [154]. **(b)** The renormalisation of the Poisson ratio  $\nu$  in an equilibrium, aperiodic solid, as a function of the built-in stress  $\theta^G$  [155]. **(c)** Renormalised value of the Poisson ratio  $\nu$  plotted versus its bare value  $\nu_0$ , for several values of the built-in stress  $\theta^G$  (expressed in terms of temperature). Note the attractive fixed point at  $\nu = 1/5$ . The discontinuities at  $\nu = 1/2$  ( $\mu = 0$ ) and  $\nu = -1$  ( $K = 0$ ) correspond to the discontinuous transitions (uniform-liquid  $\leftrightarrow$  aperiodic-solid) and (stable-solid  $\leftrightarrow$  aperiodic-solid) respectively [155].

with the (mean-field) Potts glass. It is not. As we have already remarked, the emergence of the aperiodic solid in the form of the RFOT has been shown independently and, in fact, prior to the solution of the mean-field Potts glass model.

More recently, the applicability of mean-field Potts models to liquids has been questioned [185]. Additionally, some renormalisation-group analysis of  $p$ -spin-like models that exhibit both the kinetic and thermodynamic catastrophes suggests, with the aid of a perturbative argument, that the Kauzmann crisis disappears in finite dimensions and so do the corresponding long-range correlations [186–188]. On the other hand, two recent works have shown that finite-dimensional Potts-like models could in fact exhibit the RFOT, given sufficient frustration [189, 190]. These notions are, perhaps, not surprising in light of an earlier discussion by Eastwood and Wolynes [191] who argued that spin systems are “softer” than liquids, in the following sense: The surface tension between distinct free energy minima is significantly lower in the former than in the latter. This softness is expected to result in a significant rounding of the RFOT in finite-dimensional (!) spin systems.

We next mention a separate set of works that directly map the dynamics of glassy liquids onto those of spin or spine-like systems. The earliest such work, to the author’s knowledge, is due to Stevenson et al. [192], who have used a combination of the replica methodology [193] and classical density-functional theory to map liquid dynamics onto an Ising model with randomly distributed couplings *and* on-site fields. Such random on-site fields will turn out to be of special significance in the next Section.

Bevzenko and Lubchenko [154, 155] (BL) have arrived at a spin-like description of glassy liquids from a very different, purely elastic perspective. In this view, a glassy liquid—which is an equilibrated, degenerate aperiodic crystal—is obtained by expanding a crystal, then letting the atoms settle into one of the many aperiodic arrangements, and then letting the volume relax. According to a heuristic construction in Fig. 22(a), the free energies of the periodic crystal and the degenerate aperiodic crystal correspond to two distinct terms, as functions of deformation. The two terms must cross since the glass term starts at a higher value of the free energy, but has a lower curvature because the bonding in the aperiodic sample is softer. This construction explicitly demonstrates there is a mismatch penalty between the crystal and glass, which corresponds to the excess free energy above the common

tangent [194, 195]. To make the glassy state metastable, the aperiodic crystal must be sufficiently stabilised entropically by the multiplicity of distinct aperiodic arrangements and by steric repulsion between ill-fitting molecular fragments. The built-in stress pattern resulting from this repulsion is of shorter wavelength than the regular elastic waves. Thus in the full free energy of an aperiodic crystal,  $\int dV u_{ij} \Lambda_{ijkl} u_{kl}/2$ , the full displacement  $u_{ij}$  can be profitably presented as a sum of a short-wavelength contribution  $u_{ij}^>$  and long-wavelength contribution  $u_{ij}^<$ . The former and latter take care of the built-in and regular elastic stress, respectively. The the elastic-moduli tensor  $\Lambda_{ijkl}$  looks particularly simple for isotropic elasticity [85]:  $\Lambda_{ijkl} = (K - 2\mu/3)\delta_{ij}\delta_{kl} + 2\mu(\delta_{ik}\delta_{jl} + \delta_{il}\delta_{jk})$ , c. f. Eq. (21). The model is made non-linear by fixing the magnitude of the local built-in stress; three specific ways to do so are described in Ref. [155].

The component of the deformation corresponding to the built-in stress violates the so-called Saint-Venant compatibility condition, whereby a certain combination of the derivatives of the strain (or stress) tensor, called the “incompatibility”, is non-zero:

$$\text{inc}(u^>)_{ij} \equiv -\epsilon_{ikl}\epsilon_{jmn}\partial u_{ln}^>/\partial x_k\partial x_m \neq 0. \quad (110)$$

Setting the incompatibility to zero in the ordinary elasticity theory allows one to obtain the displacement field  $\mathbf{u}$  from the tensor of the derivatives  $u_{ij}$  from Eq. (22) unambiguously; this way the result is independent of the integration contour [196, 197]. In physical terms the Saint-Venant compatibility condition guarantees, among other possibilities, that no bonds are broken. To illustrate this point with a more familiar analogy, one imposes the rotor-free constraint on the electric field in electrodynamics:  $\nabla \times \mathbf{E} = 0$  so that the electric field can be expressed as the gradient of a single-valued, scalar field, viz., the electrostatic potential. In turn, this implies the energy of an electric charge subject to electric field is a well defined, single-valued function of the coordinate. Note that the existence of a unique reference state in continuum mechanics is analogous to stipulating that vacuum be unique in electrodynamics; it allows one to unambiguously match the particles in the ground and any excited vibrational state. In contrast, a glassy liquid is a spatial superposition of many distinct vacua, which thus invalidates the premise of the ordinary elasticity theory. BL [155] have shown that as long as the degenerate solid is equilibrated, finite-frequency elastic moduli can still be defined and, in fact, are renormalised versions of the elastic constants in the individual vibrational “vacua,” as is briefly described below.

Integrating out the regular vibrations,  $u^<$  in the partition function  $\text{Tr} \exp(-\beta \int dV u_{ij} \Lambda_{ijkl} u_{kl}/2)$ , leads to a Hamiltonian of the type  $E = -\sum_{i<j} s_i J_{ij} s_j$ , c. f. Eq. (109), where the variables  $s_i$  are now *six*-component vectors that are allowed to point in any direction and  $J_{ij}$  is a six-by-six matrix. The number six stems from the number of independent entries in the elastic strain (stress) tensor. (The variables  $u_{ij}^>$  and  $s$  are linearly related.) The coupling  $J_{ij}$  is rather complicated and spatially anisotropic, see the explicit expression in Ref. [155], but scales with the distance and elastic constants as  $1/\mu(1-\nu)r^3$  ( $\nu$  is the Poisson ratio). In the BL approach, there is no built-in disorder. The frustration comes about exclusively because of the anisotropy of the interaction between local structural excitations. This anisotropy is similar to, but more complicated than that in the electric dipole-dipole interaction.

In the strict mean-field limit [154], the BL model yields a second order transition between two regimes corresponding to two types of frozen-in stress, namely, mostly shear and uniform dilation/contraction respectively. The transition takes place at a specific value of the Poisson ratio  $\nu = 1/5$ . BL argued the two regimes typically correspond to strong and fragile liquids respectively. At the next level of approximation [155], the Onsager cavity term was included, as in the last term in Eqs. (105) and (106). This results in much richer thermodynamics compared with the strictest mean-field limit. In addition, the effective (finite-frequency) elastic constants of the degenerate aperiodic solid can be determined self-consistently, similarly to how Onsager determined the dielectric constant of a polar liquid

based on the molecular dipole moment. The role of the dipole moment is played here by the magnitude of the built-in stress, which determines the length of the 6-spin. The transition at  $\nu = 1/5$  now becomes an *attractive* fixed point, see Fig. 22(b) and (c). In addition, one recovers two more fixed points: one at the uniform liquid ( $\mu/K = 0$ ) and the other at the infinitely compressible liquid ( $K = 0$ ). The former transition is self-consistently determined to be first order, consistent with the RFOT theory. The transition at  $K = 0$ —which corresponds to an infinite compressibility—was speculated to correspond to a mechanical instability that occurs during pressure-induced amorphisation.

Recently, Yan, Düring, and Wyart [198] have put forth an elasticity-based model for glassy-liquid dynamics in which local groups of particles are postulated to possess multiple alternative states; the associated particle motions are coupled via elastic force fields.

## V. QUANTITATIVE THEORY OF ACTIVATED TRANSPORT IN GLASSY LIQUIDS

We begin by remarking that the mean-field limit—which is often a good starting point for analysing phase transitions—could be somewhat confusing in the case of the random first order transition. On the one hand, the aperiodic crystal state becomes thermodynamically stable partially owing to its degeneracy, which in itself is somewhat counter-intuitive since ordinarily, transitions driven by lowering temperature are accompanied by a *decrease* in the (total) entropy. (No discontinuity in the total entropy occurs at the RFOT transition.) In any event, because the multiplicity of the aperiodic states is a key part of the stabilisation, it is essential that the system be able to sample all of those aperiodic structures without exception. Yet, there are no transitions between the alternative aperiodic minima in the mean-field limit. This seeming paradox is resolved by noting that the transitions between the distinct aperiodic are *not* subject to infinite barriers in finite dimensions. As already mentioned, Kirkpatrick and Wolynes[181] discussed a mechanism by which individual aperiodic minima would locally interconvert by means of activated transitions already in 1987. The driving force for the transitions to occur is *precisely* the multiplicity of the distinct aperiodic minima. According to this early argument, the barriers for the activated transport would scale inversely with the square of the configurational entropy. While the experimental viscosity curves could be fitted with such a dependence, the inverse *linear* scaling matches the empirical Vogel-Fulcher-Tammann law (98) better. In the following, we discuss  $\alpha$ -relaxation in great detail.

Throughout this Section, we will assume the liquid is already in the landscape regime, i.e., below the temperature  $T_{\text{cr}}$  of the crossover between mainly collisional and activated transport, so that the locally-stable aperiodic structures live significantly longer than the vibrational relaxation time. In this limit, counting the metastable free energy minima, each of which corresponds to individual mechanically-metastable structures, becomes unambiguous. Consequently, the configurational entropy, too, is well defined, while the structural relaxation can be quantitatively described as rare, activated processes, with the help of the transition state theory [199, 200].

### A. Glassy liquid as a mosaic of entropic droplets

We are used to systems whose free energy surface is essentially independent of the system size: For instance, the free energy surface of a macroscopic Ising ferromagnet below its Curie point has two distinct free energy minima that can be distinguished by their average magnetisation, which can be taken to be up or down respectively. If the system is made thrice bigger, the free energy is simply multiplied by a factor of three; that is, while the number



of states within each minimum increases exponentially, the number of minima themselves remains the same, i.e., two. In contrast, the number of free energy minima in a glassy liquid scales exponentially with the system size  $N$ :  $e^{s_e N}$ , as already mentioned. Under these circumstances, the system will break up into separate, contiguous regions that are relatively stabilised; the contiguous regions are separated by relatively strained interfaces characterised by a higher free energy density. To see this, suppose the opposite were true and the free energy density were uniform throughout. Owing to the multiplicity of distinct free energy minima, the nucleation rate for another relatively stabilised configuration is finite, as we will see shortly. As a result, the original configuration will be *locally* replaced by another configuration while the boundary of the replaced region will be relatively strained because of a mismatch between the new structure and its environment. Thus in equilibrium, there is a steady-state concentration of the strained regions; local reconfigurations take place at a steady rate between distinct aperiodic structures. The concentration of the strained regions and the escape rate from the current liquid configuration can be determined self-consistently, as discussed by Kirkpatrick, Thirumalai, and Wolynes [30], Xia and Wolynes [31], and Lubchenko and Wolynes [40].

First we provide a somewhat more explicit, “microcanonical” version of that argument, as detailed recently in Ref. [34]. In a standard fashion, thermodynamic quantities are Gaussianly distributed in a sufficiently large system. Thus the partition function of a thermodynamic system in contact with a thermal bath at temperature  $T \equiv 1/k_B\beta$  and pressure  $p$  can be expressed as a Gaussian integral over the fluctuating value of the Gibbs free energy  $G$ :

$$Z = \int \frac{dG}{\sqrt{2\pi\delta G^2}} e^{-\beta\overline{G}} e^{-(G-\overline{G})^2/2\delta G^2}. \quad (111)$$

Here  $\overline{G}$  is the most probable value of the Gibbs free energy and  $\delta G = \langle (G - \overline{G})^2 \rangle^{1/2}$  is the corresponding standard deviation. It is easy to show [34] that for a region containing  $N$  particles,

$$\delta G = N^{1/2} \left[ \frac{k_B T K}{\bar{\rho}} + (K\alpha_t - \tilde{s})^2 \frac{k_B T^2}{\bar{\rho}\tilde{c}_v} \right]^{1/2}, \quad (112)$$

where  $K \equiv -V(\partial p/\partial V)_T$  is the bulk modulus, and  $\alpha_t \equiv (1/V)(\partial V/\partial T)_p$  the thermal expansion coefficient. The quantities  $\tilde{c}_v$  and  $\tilde{s}$  are, respectively, the heat capacity at constant volume and entropy, both per unit volume. The average particle density  $\bar{\rho}$  can be rewritten in terms of the volumetric particle size  $a$ :

$$\bar{\rho} \equiv 1/a^3. \quad (113)$$

There is some freedom in choosing the identity and/or size of the effective particle of the theory. Often one chooses actual atoms as effective particles so that the particle-particle interaction can be directly estimated using quantum-chemistry calculations. It is also common to use a coarse-grained description, in which the particle contains several atoms or even a non-integer number of atoms. For instance, when treating a molecular substance, it is often most convenient to use computed from scratch or suitably parametrised potentials, the most common example of such a parametrised interaction is the Lennard-Jones potential. (Incidentally, evaluating such intermolecular interactions *ab initio* is not necessarily an easy task even for small molecules.) Here we assign the effective particle of the theory as the bead defined in Eq. (96). This way, we shall be able to take advantage of several quantitative predictions of the DFT theory, as discussed in Subsection IV B.

Let us now consider a liquid below the crossover to activated transport but above the glass transition; the liquid is thus equilibrated. Below the crossover, the reconfigurations are rare

events compared with vibrational motions, which amounts to a well-developed time scale separation between net translations and local vibrations. This time-scale separation takes place in ordinary liquids at viscosities of order 10 Ps. [35, 170] Because of it, the entropy of the liquid can be written as a sum of distinct contributions:

$$\overline{G} = \overline{H}_i - T\overline{S}_{\text{vibr},i} - TS_c \quad (114)$$

$$\equiv \overline{G}_i - TS_c(\overline{G}_i), \quad (115)$$

where  $H_i$  is the enthalpy of an individual aperiodic state, while the total entropy is presented here as the sum of the vibrational and configurational contributions, the configurational contribution taking care of particle translations. The subscript “ $i$ ” refers to “individual” metastable aperiodic states. The quantity  $\overline{G}_i \equiv \overline{H}_i - T\overline{S}_{\text{vibr},i}$  would be the Gibbs free energy of the sample if the particles were not allowed to reconfigure but were allowed to vibrate only. Despite an entropic contribution due to the vibrations the quantity  $G_i$  is an enthalpy-like quantity as far as the configurational equilibration is concerned. Although superficially similar in structure to the standard canonical free energy, the “microstates” characterised by the “enthalpy”  $G_i$  are much different from the microstates from the canonical ensemble in that the configurational entropy numbers *long-lived* states. In contrast, the conversion between microstates in the conventional canonical ensemble is assumed to be faster than any meaningful observation time.

It is interesting that the free energy of liquid was written in the form similar to Eq. (115) already in 1937 by Bernal, [74] who apparently assumed that molecular vibrations and translations were distinct motions at *any* temperature, even though this notion is well-justified only below the crossover. Bernal used his formulation of the liquid entropy to argue that liquid-to-crystal transitions are always discontinuous, owing to the non-zero configurational component of the liquid entropy, which, then, effects a non-zero latent heat.

Of direct interest is the distribution not of the full free energy  $G$  but that of the free energies  $G_i$  of individual metastable states:

$$Z = \int \frac{dG_i}{\sqrt{2\pi\delta G_i^2}} e^{S_c(\overline{G}_i)/k_B - \beta\overline{G}_i} e^{-(G_i - \overline{G}_i)^2/2\delta G_i^2}. \quad (116)$$

The corresponding width of the distribution,  $\delta G_i \equiv \langle (G_i - \overline{G}_i)^2 \rangle^{1/2}$ , can be evaluated similarly to  $\delta G$  from Eq. (112) [34]:

$$\delta G_i = N^{1/2} \left\{ \left[ K - T \left( \frac{\partial S_c}{\partial V} \right)_T \right]^2 \frac{k_B T}{K\tilde{\rho}} + [K\alpha_t + (\Delta\tilde{c}_v - \tilde{s}_{\text{vibr}})]^2 \frac{k_B T^2}{\tilde{\rho}\tilde{c}_v} \right\}^{1/2}, \quad (117)$$

where  $\Delta\tilde{c}_v \equiv T(\partial\tilde{s}_c/\partial T)_V$  is the configurational heat capacity at constant volume and  $\tilde{s}_{\text{vibr}}$  the vibrational entropy, both per unit volume.

It is convenient, for the present purposes, to shift the energy reference so that  $\overline{G}_i = 0$ :

$$Z = \int \frac{dG_i}{\sqrt{2\pi\delta G_i^2}} e^{S_c/k_B} e^{-G_i^2/2\delta G_i^2}. \quad (118)$$

This way, the partition function gives exactly the number  $e^{S_c/k_B}$  of the (thermally available) states that is not weighted by the Boltzmann factor  $e^{-\beta\overline{G}_i}$ .

Consider now a local region that is currently *not* undergoing a structural reconfiguration. Because the region is certainly known not to be reconfiguring, its free energy—up to finite-size corrections—is equal to  $G_i$ , which is typically higher than the equilibrium free energy  $\overline{G}$  from Eq. (115). The free energy difference  $\overline{G} - \overline{G}_i = -TS_c < 0$  is the driving force for the eventual escape from the current structure, and, hence, relaxation toward equilibrium. Next

we estimate the actual rate of escape and the typical region size that will have reconfigured as a result of the escape event.

We specifically consider escape events that are local. Therefore, the environment of a chosen compact region is static, up to vibrations. Consider the partition function for a compact region of size  $N$  surrounded by such a static, aperiodic lattice. The vast majority of the configurations do not fit the region's boundary as well as the original configuration, and so there is a free energy penalty  $\Gamma_i > 0$  due to the mismatch between the static boundary and any configuration of the region other than the original configuration. We anticipate that since local replacement of a structure amounts to a legitimate fluctuation,  $\Gamma$  and  $\delta G_i$  should be intrinsically related, which will indeed turn out to be the case.

In the presence of the mismatch penalty, the density of states can be obtained by replacing  $\overline{G}_i \rightarrow \overline{G}_i + \Gamma$  under the integral in Eq. (116), where  $\Gamma \equiv \overline{\Gamma}_i$  is the typical value of the mismatch. The latter generally scales with the region size:

$$\Gamma = \gamma N^x, \quad (119)$$

but in a sub-thermodynamic fashion:  $x < 1$ , where the coefficient  $\gamma(N \rightarrow \infty) = \text{const.}$  Thus we obtain for the total number of thermally available states for a region embedded in a static lattice:

$$Z = \int \frac{dG_i}{\sqrt{2\pi\delta G_i^2}} e^{S_c/k_B - \beta\Gamma} e^{-(G_i - \Gamma)^2/2\delta G_i^2}, \quad (120)$$

where we set the expectation value of the free energy in the *absence* of the penalty at zero, as before. (The expectation value of  $G_i$  corresponding to Eq. (120) is *not* zero at  $N > 0$ .) Note the argument of the first exponential on the r.h.s. is independent of  $G_i$  but does depend on the region size  $N$ , and so does the total number of thermally available states  $Z$ :

$$Z(N) = e^{s_c N/k_B - \beta\gamma N^x}, \quad (121)$$

where  $s_c \equiv S_c/N$  is the configurational entropy per particle.

Because of the sub-linear  $N$ -dependence of the mismatch penalty, the number of thermally available states  $Z(N)$  depends non-monotonically on the region size. For small values of  $N$ , this number *decreases* with the region size, which is expected since the region is stable with respect to weak deformation such as movement of a few particles. At the value  $N^\ddagger$  such that  $(\partial Z/\partial N)_{N^\ddagger} = 0$ , the number of available states reaches its smallest value and increases with  $N$  for all  $N > N^\ddagger$ . This critical size  $N^\ddagger$ :

$$N^\ddagger = \left( \frac{x\gamma}{Ts_c} \right)^{1/(1-x)}, \quad (122)$$

corresponds to the least likely size of a rearranging region, and thus corresponds to a bottleneck configuration for the escape event: Indeed, any state at  $N < N^\ddagger$  is less likely than the initial state and so cannot be a final state upon a reconfiguration; such final state must thus be at  $N > N^\ddagger$ . On the other hand, to move any number of particles  $N$  in excess of  $N^\ddagger$ , one must have moved  $N^\ddagger$  particles as an intermediate step.

The size  $N^* > N^\ddagger$  such that

$$Z(N^*) = 1 \quad (123)$$

is special in that the region of this size is guaranteed to have a thermally available configuration, distinct from the original one, even though the boundary is fixed. By construction, this configuration is mechanically (meta)stable. This implies that a region of size  $N^*$ :

$$N^* = \left( \frac{\gamma}{Ts_c} \right)^{1/(1-x)}, \quad (124)$$

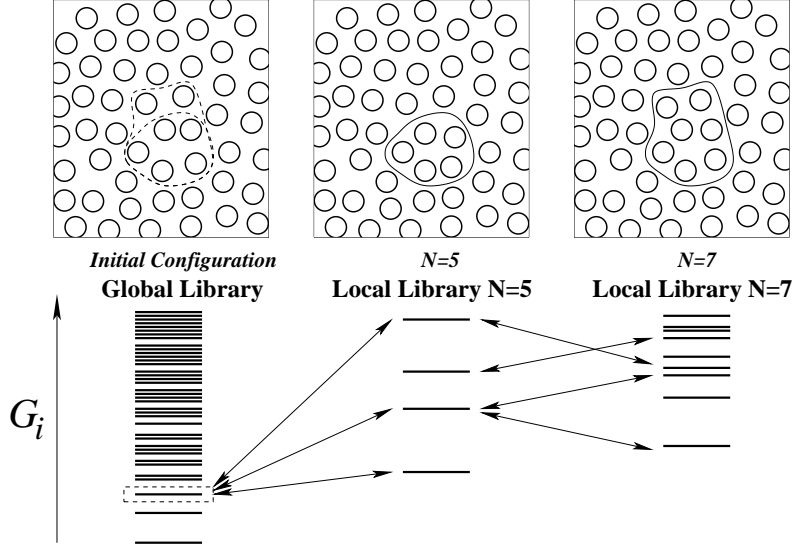


FIG. 23. Illustration of the library construction of aperiodic states [40]. On the left, we start out with some metastable structure. The density of the horizontal bars reflects the increase of the density of states (DoS)  $e^{S_c(G_i)/k_B}$  with  $G_i$ . This DoS is distinct from the probability distribution in Eq. (120), which also includes the Boltzmann factor  $e^{-\beta G_i}$ . In the centre and right panels, 5 and 7 particles have been moved. The density of states pertaining to the corresponding local regions are much lower than the global density of states. In addition, the majority of the thus obtained configurations are higher in free energy than the original configuration, owing to the mismatch with the environment. As the region size grows, the distribution of free energies  $G_i$  of individual structures is determined by a competition between a depletion due to the mismatch and an entropically-driven increase in the DoS. For a large enough  $N = N^*$ , there will be a configuration whose free energy  $G_i$  is comparable to that of the original structure.

can always reconfigure. What happens physically is that the centre of the free energy distribution from Eq. (120) moves to the right with  $N$  according to  $\gamma N^x$  because the mismatch typically increases with the interface area. This alone would lead to a depletion of states that are degenerate with the original state, which is typically at  $G_i = 0$ . Yet as  $N$  increases, the free energy distribution also *grows* in terms of the overall area, height, and, importantly, width, as more states become available. For a sufficiently large size  $N^*$ , the distribution is so broad that the region is guaranteed to sample a state at  $G_i = 0$  even though the distribution centre is shifted to the right by  $\Gamma$ . One may say that in such a state, a negative fluctuation in the free energy exactly compensates the mismatch penalty. For this to be typically true, we must have

$$\Gamma(N) = \delta G_i(N) \quad \text{at} \quad N = N^*, \quad (125)$$

where we have emphasised that both  $\Gamma$  and  $\delta G$  depend on  $N$ .

Finally note that the physical extent  $\xi$  of the reconfiguring region:

$$\left(\frac{\xi}{a}\right)^3 \equiv \frac{4\pi}{3} \left(\frac{R^*}{a}\right)^3 \equiv N^* \quad (126)$$

yields the volumetric cooperativity length for the reconfigurations.

The above notions can be discussed explicitly in terms of particle movements, within the library construction of aperiodic states [40], graphically summarised in Fig. 23. We start out with the original state, which is some state from the full set of states available to the

system. We then draw a surface encompassing a compact region containing  $N$  particles and consider all possible configurations of the particles inside while the environment is static up to local elastic deformations, i.e., vibration. Most of the resulting configurations are, of course, very high in energy because of steric repulsion between the particles comprising the region itself and between the particles on the opposite sides of the the boundary. Only few configurations will contribute appreciably to the actual ensemble of states, and even those are offset upwards, free energy-wise, by the mismatch penalty. As the chosen region is made progressively bigger, three things happen at the same time: (a) the mismatch penalty typically increases as  $\gamma N^x$ ; (b) the log-number of available states first decreases but then begins to increase, asymptotically as  $\propto N$ ; and (c) the spectrum of states becomes broader, the width going as  $\propto \sqrt{N}$ . Think of (a) as a density of states  $e^{S(G_i)/k_B}$  that moves up according to  $\gamma N^x$  with the region size (see Fig. 23), thus leading to a “depletion” of the density of states at low  $G_i$ . Items (b) and (c), on the other hand, mean the density of states increases in magnitude roughly as  $e^{s_c N - \Gamma - (G_i - \Gamma)^2 / 2\delta G^2}$ , at fixed  $G_i$  ( $\delta G \propto \sqrt{N}$  and  $\Gamma \propto N^x$ ). For a large enough  $N$ , this growth of the density of states, at fixed  $G_i$ , dominates the depletion due to the mismatch penalty and so the free energy of the substituted configuration eventually stops growing and begins to decrease with the region size  $N$ , after the latter reaches a certain critical value  $N^\ddagger$ . Eventually, at size  $N^*$ , one will typically find an available state that is mechanically stable.

The discussion of the statistical notions embodied in Eqs. (119)-(124) in terms of particle motions helps one to recognise that the full set of configurations in some range  $[0, N_{\max}]$  can be sorted out into (overlapping) subsets according to the following protocol: (a) within each subset, every region size is represented at least once and (b) two configurations characterised by sizes  $N$  and  $(N + 1)$  differ by the motion of exactly one particle. The subsets thus correspond to dynamically-connected paths, along each of which particles join the reconfiguring region *one at a time*. Along each of the dynamically connected paths, one could thus think of the reconfiguration as a *droplet* growth. A certain path will dominate the ensemble of the paths given a particular final configuration. This dominating path is the one that maximises the number of states  $Z(N)$  from Eq. (121) (including all intermediate values of  $N$ , of course). This is entirely analogous to the Second Law, whereby the equilibrium configurations are those that maximise the density of states (subject to appropriate constraints).

One may take the notion of the dynamic connectivity even further by noting that consecutive movements must be directly adjacent in space because the nucleus grows as a sequence of individual bead movements. Such movements—whether belonging to the same or distinct reconfigurations—interact, the interaction scaling with distance  $r$  as  $1/r^3$ , similarly to the electric dipole-dipole interaction [154]. The nucleus growth in Eq. (128) differs, for instance, from nucleation of liquid inside vapour in that in the latter, gas particles can join the nucleus from any side, while in the former, consecutive bead movements are relatively likely to be neighbours in physical space, in which case the movements form a contiguous chain. Now, how extensive are these individual bead displacements? At the crossover, the individual free energy minima are marginally stable with respect to transitions between each other and with respect to the decay into the uniform liquid state  $\alpha = 0$ . Xia and Wolynes [31] thus concluded that the vibrational displacements within individual free energy minima should be numerically close to the value prescribed by the Lindemann criterion of melting, i.e., one-tenth of the volumetric particle size or so:

$$d_L \simeq a/10. \quad (127)$$

Conversely, displacements just beyond this length will result in a transition between distinct free energy minima. An important corollary of the result in Eq. (127) is that individual bead motions are nearly harmonic, that is, *no bonds are broken*. The total combination of the individual moves is, of course, an anharmonic process since both the initial and final state are

metastable and are thus separated by a barrier. A well-known example of such anharmonic processes consisting of individual harmonic motions are rotations of rigid  $\text{SiO}_{4/2}$  tetrahedra in silica [201]. Another explicit example will be considered in Subsection XII B, in which a covalent bond does not break but, instead, becomes a weaker, secondary bond. The energy cost of an individual bead movement is modest.

One may question whether the most likely bottle-neck configuration in the set of all dynamically connected paths leading to the final state at  $N^*$  is, in fact, as likely as what is prescribed by  $Z(N^\ddagger)$  with  $Z(N)$  from Eq. (121). The answer is yes because sampling of all possible shapes and locations for a region of size  $N$  is implied in the summation in Eq. (120). By backtracking individual dynamically-connected trajectories from  $N = N^*$  to  $N = 0$ , we can determine the precise reconfigured region that produces the most likely bottle-neck configuration with probability  $Z(N^\ddagger)$ .

Now, for region sizes in excess of  $N^*$ , the number  $Z(N)$  of available states exceeds one, implying that, for instance, *two* distinct metastable configurations are available to a region of size  $N$  such that  $Z(N) = 2$ . According to the above discussion, the trajectories leading to these two states are generally distinct, though the probabilities of the respective bottle-neck configurations and the corresponding critical sizes  $N^\ddagger$  should be comparable.

Structural reconfiguration can be equally well discussed not in a microcanonical-like fashion, through the number of states  $Z(N)$ , but, instead, in terms of the corresponding free energy  $F(N) = -k_B T \ln Z(N)$ , as was originally done by Kirkpatrick, Thirumalai, and Wolynes [30]. This yields the following activation profile for the reconfiguration:

$$F(N) = \Gamma - Ts_c N \equiv \gamma N^x - Ts_c N, \quad (128)$$

Since we are considering all possible configurations for escape, subject to the appropriate Boltzmann weight, this amounts to locally replacing the original configuration encompassing  $N$  particles by the *equilibrated* liquid while the particles in the surrounding are denied any motion other than vibration. Upon the replacement, the local *bulk* free energy is typically lowered by  $\overline{G} - \overline{G}_i = -Ts_c N$ , hence the driving term  $-Ts_c N$  in Eq. (128).

The equilibrated liquid is a Boltzmann-weighted average of alternative, metastable aperiodic structures that are mutually distinct and are also generally distinct from the initial configuration. Another way of saying two structures are distinct is that the particles belonging to the structures inside and outside do not fit as snugly—at the interface between the structures—as they do within the respective basis structures. This is quite analogous to the mismatch between two distinct crystalline polymorphs in contact, such as must occur during a first order transition between the polymorphs. In contrast with a polymorphic transition, the scaling of the mismatch penalty with the area of the interface will turn out to be somewhat complicated, viz, the exponent  $x$  need not be  $(D - 1)/D$ .

Combining the free energy view with the notion of dynamically connected trajectories, due to the library construction, we conclude that the activation profile in Eq. (128) is also a *nucleation* profile. Naturally, the bottle-neck configuration corresponding to  $N = N^\ddagger$  from Eq. (122) thus corresponds to the critical nucleus size. The corresponding barrier is equal to

$$F^\ddagger \equiv F(N^\ddagger) = \gamma \left( \frac{x\gamma}{Ts_c} \right)^{x/(1-x)} (1 - x) = \gamma(1 - x) (N^\ddagger)^x. \quad (129)$$

This directly shows that the escape rate from a specific aperiodic state is indeed finite. Note also that the cooperativity size is always equal to the critical size  $N^\ddagger$  times an  $x$ -dependent numerical coefficient:

$$N^* = N^\ddagger x^{-1/(1-x)} > N^\ddagger. \quad (130)$$

Yet there is more to the activation profile in Eq. (128). In ordinary theories of nucleation, the nucleus continues to grow indefinitely once it exceeds the critical size, unless it collides with other growing nuclei, as happens during crystallisation, or, for instance, when the supply of the contents for the minority phase runs out, as happens when a fog forms. This essentially unrestricted growth takes place because this way, the system can minimise its free energy by fully converting to the minority phase. Such a view is adequate when there are only two free energy minima to speak of and the system converts between those two minima.

However in the presence of an exponentially large number of free energy minima, we must think about the meaning of the  $F(N)$  curve more carefully. We must recognise that both the initial and *final* state for the escape event are individual aperiodic states that are, on average, equally likely. In fact, because we have chosen  $G_i = 0$  as our free energy reference,  $F(N)$  gives exactly the log-number (times  $-k_B T$ ) of thermally available states to the selected region. As a result, that the free energy  $F(N)$  reaches its initial value of zero indicates that a mechanically metastable state has become available to escape to. One is accustomed to situations in which the initial and final state for a barrier-crossing event are *minima* of the free energy, which does not seem to be the case in the above argument. There is no paradox here, however. The quantity  $F(N)$  is not the actual free energy of the system. Instead, by construction, it is the free energy under the constraint that the outside of the selected compact region is not able to relax in the usual manner, but, instead, is forced to be in a specific, metastable aperiodic minimum. The monotonic decrease of  $F(N)$  at  $N = N^*$  is trivial in that it simply says the surrounding of the droplet will eventually proceed to reconfigure again and again, as it should in equilibrium. As we have already emphasised, the state to which the initial configuration has escaped is perfectly *metastable*.

We now shift our attention to the *energy*. Suppose the liquid is composed of particles that are not completely rigid, and so the mismatch penalty has an energetic component. Furthermore, it is instructive to suppose that the penalty is *mostly* energetic, which is probably the case for covalently bonded substances such as silica or the chalcogenides. [29] At a first glance, the energy of the system appears to grow with each nucleation event, since the driving force in Eq. (128) is exclusively entropic, at equilibrium. Such unfettered energy growth is, of course, impossible in equilibrium. On the contrary, the configurations before and after a reconfiguration are typical and the energy must be conserved, on average. The energy change following a transition must be within the typical fluctuation range, which reflects the heat capacity  $C_V$  at constant volume and the bulk modulus  $K$ : [55]

$$\delta E = \{k_B C_V T^2 - V[T(\partial p / \partial T)_V - p]^2 T / K\}^{1/2}. \quad (131)$$

Note both  $C_V$  and  $V$  pertain to a single cooperative region. The conservation of energy, on average, means that since one new interface appears following an escape event, an equivalent of one interface must have been *subsumed* during an event, as emphasised in Ref. [54].

We thus conclude that the equilibrium concentration of the interface configurations is given by  $1/\xi^3$  with  $\xi$  from Eq. (126), and so a glassy liquid is a *mosaic* of aperiodic structures, [31] each of which is characterised by a relatively low free energy density, while the interfaces separating the mosaic cells are relatively stressed regions characterised by excess free energy density due to the mismatch between stabilised regions. This stress pattern is not static, but relaxes at a steady pace so that a region of size  $\xi$  reconfigures once per time  $\tau$ , on average:

$$\tau = \tau_0 e^{F^\ddagger / k_B T}, \quad (132)$$

where the pre-exponent  $\tau_0$  corresponds to the vibrational relaxation time. It is the same vibrational-hopping time we encountered in Subsection IV C. Since the nucleation is driven

by the multiplicity of distinct aperiodic configurations, i.e., by the configurational entropy, a glassy liquid may be said to be a *mosaic* of entropic droplets [31].

Note that the total free energy stored in the strained regions corresponding to the domain walls is equal to  $\Gamma(N/N^*) = T s_c N$ , i.e. the enthalpy difference between the liquid and the corresponding crystal at the temperature in question, up to possible differences in the vibrational entropy between the crystal and an individual aperiodic structure.

Note that every metastable configuration—which contains both the relatively relaxed and strained regions—is a true free energy minimum of the liquid. This is in contrast with the mean-field view we usually take of *macroscopic* phase coexistence, by which extensive portions of the sample are occupied by structures corresponding to true minima of the bulk free energy density, such as the two minima in Fig. 8. Appropriately, the physical boundary between those macroscopic regions then corresponds to the saddle-point in the bulk free energy in Fig. 8 *and* to a saddle point solution of the free energy of a nucleating droplet. Thus only in the mean-field limit do the relatively stabilised regions in glassy liquids correspond with true free energy minima. (Their multiplicity is still given by the configurational entropy!) In finite dimensions, there is a steady-state, uniform density of both relatively stabilised and relatively strained regions, whose spatial density can be determined self-consistently, as explained above.

We finish this Subsection by describing a somewhat distinct way to think about the mosaic, due to Bouchaud and Biroli [202]. In this view, the ensemble of all states of a compact region of size  $\xi$  consists of a contribution from the current state and contributions of the full, exponentially large set of alternative structures. As in the library construction, the surrounding of the chosen region is constrained to be static up to vibrational displacement. What sets apart the current state from all the alternative states is that it fits the environment better. The partition function for the region thus goes roughly as:

$$Z_{\text{BB}} \simeq e^{-\beta(-\gamma N^x)} + e^{N s_c / k_B}. \quad (133)$$

The mismatch free energy  $\gamma N^x$  scales with the region size  $N$  sublinearly,  $x < 1$ , while the log-number of alternative states scales linearly. Thus the stability of sufficiently *small* regions—smaller than  $\xi$ —can be understood thermodynamically in a straightforward manner: The energetic advantage of being in the current state, due to the matching boundary, outweighs the multiplicity of poorer matching, higher energy states. This is not unlike the stability of a crystal relative to the liquid below freezing. Indeed, at liquid-crystal equilibrium, the partition function of the system can be written as  $Z = e^{-\beta(-\Delta H)} + e^{\Delta S / k_B}$ , where  $\Delta H > 0$  and  $\Delta S > 0$  are the fusion enthalpy and entropy respectively.

The just listed aspects of the Bouchaud-Biroli picture are essentially equivalent to the library construction, and, in particular, with regard to the entropic nature of the driving force for the activated transport. In contrast with the KTW [30] and library construction [40], however, the BB scenario is agnostic as to the concrete mechanism of mutual reconfiguration between alternative aperiodic states, other than the reconfigurations must be rare, activated events. In the absence of such a concrete mechanism, BB posited a generic scaling relation between the cooperativity size and the relaxation barrier that is similar to that transpiring from Eqs. (129) and (130). In this view, a region *larger* than the size  $N^*$  can still reconfigure via a *single* activated event but would do so typically *more slowly* than the region of size  $N^*$ . Combining this notion with the lower bound on the cooperativity size obtained above one concludes that the cooperativity size is in fact  $N^*$  and one does not face the subtlety stemming from the downhill decrease of the free energy profile  $F(N)$  from Eq. (128). The present picture contrasts with the Bouchaud-Biroli approach in that it specifically prescribes that the activated reconfigurations take place through a process akin to *nucleation*.

Now, according to Eqs. (122)-(126), we need to evaluate the exponent  $x$  and the coefficient  $\gamma$  for the mismatch penalty, to estimate the escape rate and the cooperativity size for the



activated reconfigurations, to which we proceed next.

### B. Mismatch Penalty between Dissimilar Aperiodic Structures: Renormalisation of the surface tension coefficient

The mismatch penalty between two ill-fitting structures can be evaluated with the help of the free energy functional. This evaluation is particularly straightforward in the long wavelength approximation represented by the Landau-Ginzburg functional from Eq. (3), which is often called the Cahn-Hilliard [203] functional in the context of nucleation. Further simplification is achieved when the nucleus is very large [194, 195], provided that the interface remains of finite width. Hereby the interface can be effectively regarded as flat while the total mismatch penalty scales asymptotically linearly with the interface *area*. Under these circumstances, the characteristics of the interface are determined by two parameters. One parameter is the coefficient  $\kappa$  at the square gradient term in Eq. (3), the other is the barrier height  $g^\ddagger$  in the bulk free energy density  $V(\phi)$ , see Fig. 8. The expressions for the width  $l$  and the surface tension coefficient  $\sigma$  read

$$l \sim \sqrt{\kappa/g^\ddagger}, \quad (134)$$

and

$$\sigma \sim \sqrt{\kappa g^\ddagger} \sim g^\ddagger l, \quad (135)$$

respectively; both equalities are within factors of order one, which depend on the specific form of the free energy functional. The total mismatch penalty goes as  $4\pi r^2 g^\ddagger l$ , consistent with simple dimensional analysis. Roughly speaking, the excess free energy  $g^\ddagger l$  per unit area reflects the free energy penalty due to unsatisfied bonds at the interface, see also Eq. (12). In the case of rigid particles, bonds are not defined, but analogous expressions involving the direct correlation function instead of the pair-interaction potential can be written, as in Eq. (26). One recognises that the interface width  $l$  reflects the interaction (or direct correlation) range—according to Eqs. (12) and (26)—and thus is not directly tied to the molecular size, even though the two are often numerically similar.

Because the states on both sides of our interface are aperiodic, the degree of mismatch is distributed [204, 205]. Thus in some places the two structures may fit quite well and so the scaling of the surface energy term  $\Gamma$  from Eq. (128) with the droplet size  $N$  may be weaker than the  $N^{(D-1)/D}$  scaling expected for interfaces separating periodic or spatially uniform phases. The mechanism of this partial lowering of the mismatch penalty is as follows: The number of distinct aperiodic structures available to a sufficiently large region, we remind, scales exponentially with the region size. The free energies  $G_i$  of individual structures from Eq. (115) are *distributed*; they are equal on average but differ by a finite amount for any specific pair of aperiodic states. Fluctuations of extensive quantities scale with  $\sqrt{N}$  as functions of size  $N$ . [55] (The size  $N$  at which the  $\sqrt{N}$  scaling sets in can be rather small in the absence of long-range correlations, such as those typical of a critical point.) Thus the free energy difference between the configurations outside and inside scales as  $\sqrt{N}$ , for two regions of the same size  $N$ , and could be of either sign. Suppose now, for concreteness, that the configuration on the outer side of the domain wall happens to be lower in free energy than the adjacent region on the inside. Imagine distorting the domain wall so as to replace a small portion of the inside configuration by that from the outside. It turns out the free energy stabilisation due to the replacement outweighs the destabilisation due to the now increased area of the interface, as we shall see shortly.

Before we proceed with this analysis, it is instructive to discuss why such surface renormalisation and the consequent stabilisation would *not* take place during regular discontinuous

transitions when one phase characterised by a *single* free energy minimum nucleates within another phase also characterised by a *single* free energy minimum. After all, both phases represent superpositions of microstates whose energies are *also* distributed. Furthermore, there seems to be a direct correspondence between, say, the regular canonical ensemble and the situation described in Eq. (115). Hereby, the free energies  $G_i$  in Eq. (115) seem to correspond to the energies of the microstates, while the configurational entropy  $S_c$  seems to correspond to the full entropy in the canonical ensemble. One difference between the situation in Eq. (115) and the canonical ensemble is that in the latter, transitions between the microstates within individual phases occur on times much shorter than the observation time or mutual nucleation and nucleus growth of the two phases. As a result, the energies of the phases on the opposite sides of the interface are always equal to their *average* values. In contrast, the distinct aperiodic states from Eq. (115) are long-lived. In fact, the fastest way to inter-convert between those states is via creation of the very interface we are discussing! In the canonical ensemble analogy, this would correspond to having *individual* microstates on the opposite sides of the interface as opposed to ensembles resulting from averaging over all microstates (with corresponding Boltzmann weights). Conversely, the situation in Eq. (115) would be analogous to the canonical ensemble only at sufficiently long times that much exceed the nucleation time from Eq. (132). Note that at such long times, we have identical, equilibrated liquid on both sides and so there is no surface tension in the first place.

Now, the situation where the system can reside in long-lived states whose free energies are distributed in a Gaussian fashion can be equivalently thought of as a perfectly ergodic, equilibrated system in the presence of a *static*, externally-imposed random field whose fluctuations scale in the Gaussian fashion. In the absence of this additional random field, the mismatch penalty between such two regular phases would be perfectly uniform along an interface with spatially uniform curvature. The simplest system one can think of, in which this situation is realised, is the random field Ising model:

$$\mathcal{H} = -J \sum_{i < j} \sigma_i \sigma_j - \sum_i h_i \sigma_i, \quad \sigma_i = \pm 1, \quad (136)$$

where  $J > 0$  while the Zeeman splittings  $h_i$ 's are random, Gaussianly distributed variables. In the Hamiltonian above, if one were to impose a smooth interface between two macroscopic domains with spins up and down, the domain wall would distort some to optimise the Zeeman energy. However, the amount of distortion is also subject to the tension of the interface between the spin-up and spin-down domains. The overall lowering of the free energy, due to the interface distortion, corresponds to the optimal compromise between these two competing factors. Likewise, a smooth interface between two distinct aperiodic states will distort to optimise with respect to local bulk free energy, which is distributed. The energy compensation will scale, again, as the square root of the variation of the volume swept by the interface during the distortion. The final shape of the interface will be determined by the competition between this stabilisation and the cost of increasing the area of the interface.

The mapping between the random field Ising model (RFIM) and large scale fluctuations of the interface between aperiodic liquid structures was exploited by Kirkpatrick, Thirumalai, and Wolynes (KTW) [30], who used Villain's argument [206] for the renormalisation of the surface in RFIM to deduce how the droplet interface tension scales asymptotically with the droplet size. The mapping relies crucially on the condition that the undistorted interface must not be too thick, as it would be near a critical point. This assumption turns out to be correct since the width of the undistorted interface is on the order of the molecular length  $a$  [32].

Let us now review a variation on the KTW-Villain argument concerning the surface tension renormalisation. This argument produces the scaling relation we seek for the mismatch

penalty but some of its steps are only accurate up to factors of order one, and so the latter will be dropped in the calculation. All lengthscales will be expressed in terms of the molecular length  $a$ , which simply sets the units of length. Now, consider two dissimilar aperiodic states in contact, and assume we have already coarse-grained over all length-scales less than  $r$ , while explicitly forbidding interface fluctuations on greater lengthscales. The interface is thus *taut*. Further, consider spatial variations in the shape of the interface on lengthscales limited to a narrow interval  $[r, r(1 + \Delta)]$ . The dimensionless increment

$$\Delta = d \ln r \quad (137)$$

is the increment of the running argument for our real-space coarse-graining transformation  $r \rightarrow r(1 + \Delta)$ . (Ultimately,  $r$  will be set at the droplet radius). We may assume, without loss of generality, that the mismatch penalty may be written in the following form, in  $D$  spatial dimensions:

$$\Gamma = \sigma(r)r^{D-1}, \quad (138)$$

The quantity  $\sigma(r)$  may be thought of as a renormalised surface tension coefficient, where the amount of renormalisation generally depends on the wavelength, which is distributed in the (narrow) range between  $r$  and  $r(1 + \Delta)$ . Our task is to determine under which condition such renormalisation takes place, if any.

To do this, let us deform the interface so as to create a bump of (small) height  $\zeta$  and lateral extent  $r$ , see sketch in Fig. 24. Because the interface is taut, the area will increase quadratically with  $\zeta$ . The resulting increase in the interface area will incur a free energy cost

$$\delta F_s \sim \sigma(r)r^{D-1}(\zeta/r)^2 \Delta, \quad (139)$$

when  $\zeta \ll r$ . It will turn out to be instructive to use a more general form

$$\delta F_s \sim \sigma(r)r^{D-1}(\zeta/r)^z \Delta. \quad (140)$$

This generalised form is convenient because (a) rough interfaces may exhibit a  $z$  other than 2, (b) the scaling of the interface tension with  $r$  will turn out to be independent of  $z$  at the end of the calculation. Thus the obtained  $\sigma$  vs.  $r$  scaling can be argued to still apply even to situations when  $\zeta/r$  is not necessarily small. (Which it will not be!) Now, as already mentioned, one can always flip a region (of size  $N$ ) at the interface so as to lower its bulk free energy by  $\sim h\sqrt{N}$ . The resulting bulk free energy gain is thus:

$$\delta F_b \sim -h\sqrt{N}\Delta \sim -h(r^{D-1}\zeta)^{1/2}\Delta, \quad (141)$$

where the constant  $h$  is straightforward to estimate in light of our earlier discussion that the bulk stabilisation above is the result of fluctuations of the Gibbs free energy. Thus,

$$h \sim \delta G_i / \sqrt{N}, \quad (142)$$

with  $\delta G_i$  from Eq. (117). Properly, we should have written  $h^2 = 2(\delta G_i)^2/N$  in Eq. (142) because the bulk free energy stabilisation is a *difference* between two random Gaussian variables, whose distribution widths are  $\delta G_i$  each, but we have agreed to drop factors of order one in the derivation, see also below.

Next we find the value of  $\zeta$  that optimises the total free energy stabilisation:  $\partial(\delta F_s + \delta F_b)/\partial\zeta = 0$ , which yields:

$$\zeta \sim (h/\sigma)^{2/(2z-1)} r^{(2z-D+1)/(2z-1)}. \quad (143)$$

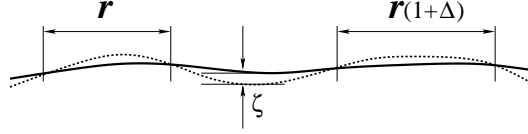


FIG. 24. Illustration of a step in the coarse-graining procedure of an interface distorted because of frozen-in free energy fluctuations, à la Villain [206]. The interface has already been coarse-grained over lengthscales less than  $r$ . At each spectral interval  $[r, r(1 + \Delta)]$ , the optimal value of the distortion  $\zeta$  and the resulting free energy stabilization are determined using Eq. (144).

The resulting energy gain per unit area,

$$\begin{aligned} \min_{\zeta} \{ \delta F_s + \delta F_b \} / r^{D-1} &\sim \\ &\sim - (h^z / \sigma^{1/2})^{1/(z-1/2)} r^{-z(D-2)/(2z-1)} \Delta, \end{aligned} \quad (144)$$

thus represents the renormalisation  $\delta\sigma(r)$  of the  $r$ -dependent “surface tension coefficient” that resulted from integrating out degrees of freedom in the  $k$ -vector range between  $1/r$  and  $1/(1 + \Delta)r$ .

The energy gain per unit area from Eq. (144), due to the real-space renormalisation in the wavelength range  $[r, r(1 + \Delta)]$ , can be viewed as an iterative relation, by Eq. (137):

$$d\sigma \sim - (h^z / \sigma^{1/2})^{1/(z-1/2)} r^{-z(D-2)/(2z-1)} d \ln r. \quad (145)$$

A quick inspection of this differential equation shows that the surface tension coefficient *decreases* with  $r$ . To determine the actual  $r$ -dependence of  $\sigma$ , we must decide on the boundary condition  $\sigma(r = \infty) \equiv \sigma_\infty$ . Suppose for a moment that  $\sigma_\infty > 0$ , which implies that at sufficiently large distances, the interface width tends to some *finite* value  $l_\infty$ , however large, given by Eq. (134). At the same time, the free energy excess per unit volume  $g^\ddagger$  tends to a finite value  $g_\infty^\ddagger$ . This is because in the  $r \rightarrow \infty$  limit, a steady value of  $\sigma$  implies the interface becomes truly flat and none of its parameters could depend on  $r$ . Since the free energy excess per unit volume  $g^\ddagger$  tends to a finite value  $g_\infty^\ddagger > 0$  for a flat interface, so should  $l_\infty$ , if  $\sigma_\infty$  is finite, by Eq. (135). The surface tension coefficient is thus given by the expression

$$\sigma^{2z/(z-1)}(r) = h^{2z/(2z-1)} r^{-z(D-2)/(2z-1)} + \sigma_\infty^{2z/(z-1)}.$$

Inserting the above formula in expression (143) yields:

$$\zeta \sim \frac{r^{(2z-D+1)/(2z-1)}}{[r^{-z(D-2)/(2z-1)} + (\sigma_\infty/h)^{2z/(2z-1)}]^{1/z}}. \quad (146)$$

The above formula indicates that although incremental changes in the interface curvature following the renormalisation are small, the compound increase in the interface thickness—due to the curvature changes in the broad wavelength range spanned by the coarse-graining procedure—is not necessarily so.

Eq. (146) indicates that there are two internally-consistent options regarding the value of the surface tension coefficient  $\sigma_\infty$ . In the conventional case of zero random field,  $h = 0$ ,  $\sigma_\infty$  is finite while  $\zeta = 0$ , and so no renormalisation takes place while the interface width tends to a steady value  $l_\infty$  at diverging droplet radii. If, on the other hand, the random field is present, the only remaining option is  $\sigma_\infty = 0$ . Indeed, by Eq. (146), the interface width  $\zeta$  diverges as  $r \rightarrow \infty$ , when  $h > 0$ , implying the supposition of a finite  $\sigma_\infty$  and, hence, finite  $l_\infty$  was internally inconsistent. For this argument to be valid, the renormalised interface width  $\zeta$  should exceed the width  $l$  of the original, flat interface. Condition  $\zeta > l$  and Eq. (146), combined with  $\sigma_\infty = 0$ , yield

$$r > l, \quad (147)$$

which happens to coincide with the criterion of validity of the thin interface approximation. Note that in their analysis of barrier softening effects near the crossover, Lubchenko and Wolynes [35] self-consistently arrived at a similar criterion, viz.,  $r > a$ , for when interface tension renormalisation would take place.

It follows that an arbitrarily weak, but finite random field  $h$  makes an interface with a sufficiently low curvature unstable with respect to distortion and lowering of the effective surface tension:

$$\sigma(r) \sim \frac{h}{a^{D-1}}(r/a)^{-(D-2)/2}, \quad (148)$$

independent of  $z$ , apart from a proportionality constant of order one, giving us confidence in the result even when the undulation size  $\zeta$  is not very small. Notice we have restored the units of length for clarity.

Eq. (148) yields that the renormalised mismatch energy  $\Gamma$  from Eq. (138) scales with the droplet size  $N$  in a way that is independent of the space dimensionality, namely  $\sqrt{N}$ :

$$\Gamma \sim \sigma(r)r^{D-1} \sim h(r/a)^{D/2} \sim h\sqrt{N}, \quad (149)$$

which is ultimately the consequence of the Gaussian distribution of the free energy. Because of the lack of a fixed length scale in the problem—other than the trivial molecular size  $a$ , which sets the units—it should not be surprising that the interface width  $\zeta$  scales with the radius  $r$  itself:

$$\zeta \sim r, \quad (150)$$

again independent of  $z$ . The numerical constant in the above equation is of order one, as is easily checked, and so  $\zeta/r$  is not small generally.

The large effective interface width can be thought of as a result of the distortion of the original thin interface where the extent of the distortion is not determined by a fixed length, but the curvature of the interface itself. In other words, this interface is a *fractal* object. Because of this fractality, the structure at the interface is not possible to characterise as either of the aperiodic structures on the opposite sides of the original flat interface before the renormalisation. We could thus informally think of this fractal interface as the original thin interface *wetted* [31] by other structures that interpolate, in an optimal way, between the two original aperiodic structures. While we are not aware of direct molecular studies with regard to the fractality of cooperative regions in non-polymeric liquids, such studies of polymer melts do suggest the mobile regions have a fractal character [207].

According to Eq. (149), the scaling exponent  $x$  is equal to  $1/2$ . Thus the matching condition in Eq. (125) is valid at all values of  $N$  and so we arrive at a central result [30, 31, 34]:

$$\Gamma = \gamma\sqrt{N}. \quad (151)$$

where

$$\gamma = \delta G_i / \sqrt{N} = \text{const.} \quad (152)$$

The resulting free energy nucleation profile:

$$F(N) = \gamma\sqrt{N} - Ts_c N, \quad (153)$$

is shown in Fig. 25(a).

In retrospect, the square-root scaling in Eq. (151) is natural: In view of Eq. (119), the  $(G_i - \Gamma)^2 / 2\delta G_i^2$  term under the second exponential in Eq. (120) scales asymptotically with  $N$  according to  $N^{2x-1}$ , see also Ref. [208]. For any  $x$  other than  $1/2$ , this would result in an

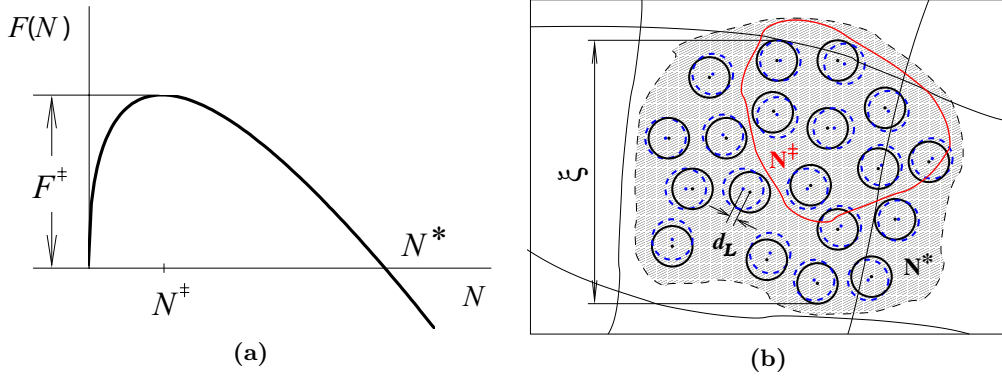


FIG. 25. **(a)** The free energy nucleation profile for structural reconfiguration in a glassy liquid from Eq. (153). Indicated are the critical size  $N^\ddagger$ , cooperativity size  $N^*$ , and the barrier  $F^\ddagger$ . **(b)** Cartoon illustrating a cooperative reconfiguration. The latter becomes downhill typically past the critical size  $N^\ddagger$  and is completed when  $N^* \equiv (\xi/a)^3$  particles moved. Individual particle displacements are typically  $d_L \simeq a/10$ , but decrease toward the edge of the reconfiguring region [23, 51].

anomalous scaling [26] of the density of states with the system size that would be hard to rationalise given the apparent lack of criticality in actual liquids between the glass transition and fusion temperatures.

We thus obtain for the nucleation barrier from Eq. (129):

$$F^\ddagger = \frac{\gamma^2}{4Ts_c}, \quad (154)$$

see Fig. 25(a). In view of Eq. (94), the scaling of the expression is consistent with the VFT law, Eq. (98), provided the coefficient  $\gamma$  does not exhibit a singularity at the temperature at which the configurational entropy is extrapolated to vanish.

### C. Quantitative estimates of the surface tension, the activation barrier for liquid transport, and the cooperativity size

Lubchenko and Rabochiy [34] (LR) have argued for a direct identification between the mismatch penalty at the cooperativity size  $N^*$  and the typical value of the free energy fluctuation at that size, Eq. (125), as was explained in Subsection V A. Except for this identification, the arguments in Subsections V A and V B represent an expanded version of the original argument of Kirkpatrick, Thirumalai, and Wolynes [30] (KTW), with additional clarification due to the library construction [40]. Already the original KTW argument yields that  $\Gamma = \delta G(N)$  up to a factor of order one. LR [34] have, in a sense, completed the KTW programme and directly estimated the surface tension coefficient  $\gamma$  based on the notion that the renormalisation of the surface tension is driven by local fluctuations of the free energy. According to Eqs. (117) and (152), we obtain:

$$\gamma = \left\{ \left[ K - T \left( \frac{\partial S_c}{\partial V} \right)_T \right]^2 \frac{k_B T}{K \bar{\rho}} + [K \alpha_t + (\Delta \tilde{c}_v - \tilde{s}_{\text{vibr}})]^2 \frac{k_B T^2}{\bar{\rho} \tilde{c}_v} \right\}^{1/2}. \quad (155)$$

Next we estimate the  $\gamma$  from Eq. (155). As a rule of thumb, the bulk modulus is about  $(10^1 - 10^2)k_B T / \bar{\rho}$  for liquids and  $10^2 k_B T / \bar{\rho}$  for solids near the melting temperature  $T_m$  [67] (consistent with the Lindemann criterion of melting [65, 107]). The rate of change of the configurational entropy with volume is not known but can be crudely estimated based on the

observation that upon freezing, the hard sphere liquid loses  $\approx 1.2k_B$  worth of entropy per particle while its volume reduces by about 10%. [72, 78] Assuming our liquid will run out of configurational entropy at about the same rate—though gradually—we obtain  $(\partial S/\partial V)_T \sim 10^1 k_B/a^3$ . This is consistent with the theoretical prediction for this quantity in Lennard-Jones systems by Rabochiy and Lubchenko, see Fig. 10 of Ref. [37]. Further,  $\tilde{s}$  is about  $10^0 k_B/a^3$ . The dimensionless expansivity  $\alpha_t T$  is generically  $10^{-1}$ , although could be much smaller for strong substances, see Fig. 12 of Ref. [37].  $\Delta\tilde{c}_v$  and  $\tilde{s}_c$  are both  $\sim 10^0 k_B/a^3$ , while  $\tilde{c}_v \sim 10^1 k_B/a^3$ . As a result, we conclude that the volume contribution to the free energy fluctuation in Eq. (117) generically exceeds the temperature contribution by one-two orders of magnitude, thus yielding:

$$\gamma^2 \approx \left[ K - T \left( \frac{\partial S_c}{\partial V} \right)_T \right]^2 \frac{k_B T}{K \bar{\rho}}, \quad (156)$$

since  $\bar{\rho} \equiv a^{-3}$ . Consequently,

$$F^\ddagger \approx \left[ K - T \left( \frac{\partial S_c}{\partial V} \right)_T \right]^2 \frac{k_B}{4K \tilde{s}_c}, \quad (157)$$

where  $\tilde{s}_c$  is the configurational entropy per unit volume.

According to the above estimate of the  $(\partial S_c/\partial V)_T$  term, it is likely that at least for rigid, weakly attractive systems, the second term in the square brackets is an order of magnitude smaller than the first term. We thus expect the following, simple expression for the surface tension coefficient  $\gamma$  to be of comparable accuracy to Eq. (156):

$$\gamma \approx \left( \frac{K k_B T}{\bar{\rho}} \right)^{1/2} \equiv \sqrt{K a^3 k_B T}. \quad (158)$$

It is interesting that the coefficient  $\gamma$  above, which reflects coupling of structural fluctuations to its environment, has exactly the same form as the coupling between the structural reconfigurations corresponding to the two-level systems (TLS) in cryogenic glasses and the phonons [23, 51] to be discussed in Subsection XII A.

The simplified form in Eq. (158) implies for the nucleation barrier:

$$F^\ddagger \simeq \frac{K}{4(\tilde{s}_c/k_B)}. \quad (159)$$

Given that the temperature dependence of the bulk modulus is usually rather weak, Eq. (159) yields to a good approximation the venerable Adam-Gibbs functional relation [156]. The relation in Eq. (159) is a central result of the theory. Note that it allows one to compute the reconfiguration barrier, an expressly kinetic quantity, using thermodynamic quantities. All these quantities can be experimentally determined. We will compare the predictions due to Eq. (159) with observation shortly, after we discuss alternative approximations for the mismatch penalty.

A welcome feature of the expression (155) for the coefficient  $\gamma$  is that it yields, when combined with Eq. (154), an expression for the barrier that is expressly independent of the bead size. This notion, of course, also applies to the simplified expressions in Eqs. (157) and (159). Thus, in the end, these results do not rely on the phenomenological assumption of an effective particle of the theory.

The expression for the cooperativity size  $\xi \equiv a(N^*)^{1/3} = (\gamma/Ts_c)^{2/3}$  corresponding to the approximation in Eq. (159) reads:

$$\xi \simeq \left[ \frac{K}{k_B T (\tilde{s}_c/k_B)^2} \right]^{1/3} \quad (160)$$

This formula can be rewritten in a convenient form for the cooperativity volume:

$$\xi^3 \equiv N^* a^3 = [4 \ln(\tau/\tau_0)]^2 \frac{k_B T}{K}. \quad (161)$$

Given the rule of thumb that  $K a^3/k_B T \simeq 10^2$ , we obtain that at the glass transition, where  $\ln(\tau/\tau_0) \approx 35$ , the cooperativity size is about  $10^2$  beads.

Note that neither of the expressions (157), (159) and (160) depends explicitly on the molecular length scale  $a \equiv \bar{\rho}^{-1/3}$ . In this sense, these expressions are truly *scale-free*, consistent with the scale-free character of the ordinary, gaussian fluctuations of thermodynamic quantities. In contrast, the presence of anomalous scaling generally requires that a molecular length scale be present explicitly [26], see also our earlier comment on the square-root scaling of the mismatch penalty following Eq. (152). The simple result in Eq. (159) has another notable feature with regard to scaling [34]. It is the only expression of units energy one could write down using the bulk modulus and the configurational entropy per unit volume that does not involve temperature. The proportionality of the barrier to the bulk modulus is a direct indication of the activated nature of the reconfigurations and implies that the latter must involve bond stretching.

On the other hand, the configurational entropy in the denominator of Eq. (159) reflects the progressively smaller number of degrees of freedom available to the liquid at lower temperatures (or higher pressures), which thus leads to fewer possibilities to find an alternative metastable state and a downhill trajectory to reach that state. This is also reflected in the entropy dependence of the cooperativity length (160): Given the decreasing log-number of states per unit volume, at lower temperatures, searching through larger regions is required to find an alternative structural state.

We have already remarked that the square-root scaling of the mismatch penalty is natural in the absence of criticality because otherwise the free energy would exhibit anomalous scaling. The square root scaling is due to the Gaussian nature of the fluctuations that lead to reconfigurations. But why would generic Gaussian fluctuations lead to non-generic consequences in glassy liquids? The answer lies in the exponential multiplicity of distinct free energy minima, which introduces new physics in the problem. Following Bouchaud and Biroli [202], one may think of the long-lived structures as residing in traps that are enthalpically stabilised relatively to a state in which such traps are only marginally stable and in which the liquid rearrangements are thus nearly barrierless. This is similar to the way a crystal in equilibrium with the corresponding liquid can be thought of as a trap which is lower in enthalpy than the liquid whereby the enthalpic stabilisation due to the trapping exactly matches the excess liquid entropy times temperature. A similar situation takes place when a folded protein molecule is in equilibrium with the unfolded chain. Now, in the presence of a thermodynamically large number of free energy minima, fluctuations become possible that enthalpically stabilise local regions. The extent of such a special fluctuation is not arbitrary; its value can be determined self-consistently, in equilibrium, by matching the (enthalpic) stabilisation due to the fluctuation with the log-multiplicity of the minima:  $\delta G_i = T s_c$ . (To avoid confusion we repeat that the quantity  $G_i$  is enthalpy-like with respect to the configurational degrees of freedom even though it includes entropic contributions due to vibrations.) Combined with Eq. (152), this yields  $\gamma \sqrt{N^*} = T s_c N^*$  at the cooperativity size. No such local trapping is possible when the multiplicity of the minima is sub-thermodynamic, i.e., when the system is not in the landscape regime. Indeed, this equation has no solutions, if the log-number of the minima per particle,  $s_c/k_B$ , is identically set to zero.

This simple result above would be modified in the presence of long-range correlations such as those near critical points. Yet we have seen that a liquid-to-solid is an *avoided* critical point, the degree of separation from criticality reflected in the substantial value of the force constant of the effective Einstein oscillator  $\alpha \sim K a/k_B T \sim 10^2/a^2$ , see Eq. (30).



Consistent with this notion, the energetics of structural fluctuations are dominated by the elastic modulus  $K$ , see Eqs. (152) and (158), which greatly exceeds the thermal energy scale  $k_B T/a^3$ . On the other hand, the appearance of the bulk modulus in Eqs. (158) and (159) is consistent with our earlier notion that no bonds are broken during the structural reconfigurations.

It is quite possible that in addition to the trivial, Gaussian fluctuations, smaller-scale fluctuations of distinct nature are also present. For instance, in their recent replica-based work, Biroli and Cammarota [209] argue there is a “wandering” length scale associated with fluctuations of the domain wall shape. This length diverges with lowering the temperature as  $1/s_c^{1/2}$ , as opposed to the stronger divergence  $\xi \propto 1/s_c^{2/3}$  from Eq. (160). Such wandering could be important at higher temperatures, see Section VII.

The preceding discussion pertains exclusively to glassy liquids. It seems instructive to consider now an apparent counterexample in the form of an amorphous silicon film. When quenched sufficiently below the glass transition, a glassy liquid forms an amorphous solid. Just below the glass transition, the glass can still undergo activated reconfigurations of the type discussed above, but somewhat modified for the initial state being off-equilibrium; this will be explained in detail in Subsection VIII A. In contrast, silicon is a very poor glass-former and so its amorphous form must be prepared by means other than quenching, for instance, by sputtering on a cold substrate. The poor glass-forming ability of silicon is consistent with our earlier notion that this substance would not crossover into the landscape regime; instead it crystallises at relatively low densities such that the steric effects are still relatively unimportant. Still, according to the present discussion it would seem that amorphous silicon could undergo structural reconfigurations similar of glassy liquids. After all, silicon films are aperiodic and low-density thus resulting in vast structural degeneracy. Indeed, the density of such films is at least 10% less than that of the crystal (p. 1004 of Ref. [210]) let alone the liquid. The liquid excess entropy of *equilibrated* silicon at this density much exceeds the configurational entropy below the crossover. To be fair, the landscape of amorphous silicon is largely energetic, not free-energetic; it is well above the equilibrium energy at the ambient conditions. But this would not seem to make a huge difference as far as the barriers between the (metastable) energy minima are concerned. Are these barriers given by an expression of the type in Eq. (159)? First note that in contrast with glassy liquids, we may no longer use the expression (155) for the mismatch penalty, since it was derived assuming equilibrium. Furthermore, since the enthalpy of the film is dominated by the (highly anisotropic) bonding, it is likely that silicon will rearrange by *breaking bonds*; the mismatch penalty will thus reflect the corresponding, higher energy scale. Additional complications arise from the fact that the films do not correspond to a structure that was equilibrated at any temperature, see Subsection VIII A. Another indicator that reconfigurations in amorphous silicon films must involve bond breaking is that such films host bulk quantities of dangling bonds [210], something of relevance in the context of photovoltaic applications of the material. In addition to being efficient scatterers of charge carriers, the dangling bonds are directly witnessed by a substantial ESR signal; in contrast, a proper bond is formed by a filled molecular orbital. Reconfigurations, if any, clearly fail to “heal” such dangling bonds in silicon films. Conversely, glasses made by quenching equilibrated liquids do not exhibit significant numbers of dangling bonds. Thus based on the high energy cost of rearrangements and the relationship between the barrier and the cooperativity size from Eq. (129), we tentatively conclude that the cooperativity size in amorphous silicon likely exceeds that in glasses made by quenching. We will continue this discussion later on.

Now, the linear scaling of the activation barrier in Eq. (159) with the elastic modulus hearkens back to earlier, enthalpy based approaches to activated dynamics by Hall and Wolynes [211] and the so called “shoving model” [212]. Some of the particular realisations of the shoving model [213, 214] posit that the dominant contribution to the temperature

dependence of the barrier is due to the temperature dependence of the elastic moduli. More specifically, the shoving model postulates that the barrier goes as  $KV_c$ , where  $V_c$  stands for the volume of a rearranging region which is prescribed by system specific interactions and is temperature independent. In contrast, the RFOT theory demonstrates that the configurational entropy is the leading contributor to the  $T$ -dependence of the barrier, and increasingly so at lower temperatures [33], see also below. Appropriately, the cooperativity volume must increase with decreasing entropy, see Eq. (160).

In view of the intrinsic relation between the elastic constants and the localisation parameter  $\alpha$  [42], Eq. (30), the above argument connects the mismatch penalty  $\gamma$  with the “localisation” of the particles upon the crossover at  $T_{cr}$ . Yet this connection is only indirect. The original calculation of  $\gamma$ , due to Xia and Wolynes [31], *explicitly* connects the mismatch penalty to the formation of the metastable structures in which the particles vibrate around steady-state average locations. It is this original calculation, dating from 2000, that enabled the majority of quantitative predictions by the RFOT theory. This calculation will be reviewed next.

The activation profile from Eq. (153) can be rewritten in terms of the droplet radius (assuming a spherical geometry) as:

$$F(r) = 4\pi r^2 \sigma_0 (a/r)^{1/2} - (4\pi/3)(r/a)^3 T s_c, \quad (162)$$

using the following connection between the particle number contained within the droplet and the droplet radius:

$$N \equiv \frac{4\pi}{3} (r/a)^3. \quad (163)$$

This yields for the reconfiguration barrier:

$$\frac{F^\ddagger}{k_B T} = \frac{3\pi(\sigma_0 a^2 / k_B T)^2}{s_c / k_B}. \quad (164)$$

and the cooperativity length:

$$\xi/a = (4\pi/3)^{1/3} \left( \frac{3\sigma_0 a^2}{T s_c} \right)^{2/3}. \quad (165)$$

To estimate the surface tension coefficient  $\sigma_0$ , which corresponds to the mismatch penalty at the molecular scale:  $\sigma = \sigma(r = a)$ , we begin with the density profile from Eq. (29) in which the lattice sites  $\mathbf{r}_i$  are arranged in an aperiodic fashion, as in Subsection IV A. This profile is an excellent approximation to the actual density distribution, even though it ignores the possibility that the force constant  $\alpha$  of the effective Einstein oscillator may be somewhat spatially distributed. The aperiodic crystal forms despite the *one-particle* entropic cost  $\Delta f_{loc} > 0$  of the localisation of a particle around a certain location in space. The reason is that this localisation also offers a free energy gain, due to multi-particle effects, as the collisions are now less frequent, as we have already discussed following Eq. (54). In the presence of chemical interactions, there is also an enthalpy gain due to bond formation. Both gains contribute to the free energy in formally equivalent ways (through the direct correlation function) and thus can be formally termed “bonding;” denote the corresponding free energy difference  $\Delta f_{bond} < 0$ . Additional stabilisation comes from the multiplicity of aperiodic states:  $-T s_c < 0$ .

The mismatch between two degenerate states can be thought of as partial lack of “bonds”—a half or so—for a particle at the interface, leading to about  $(-\Delta f_{bond})/2$  per particle in missing free energy. Estimating the bonding free energy appears generally difficult, however obtaining a formal lower bound on  $-\Delta f_{bond}$  is not: Below the

crossover, the aperiodic crystal is stable, implying  $\Delta f_{\text{loc}} + \Delta f_{\text{bond}} - Ts_c \leq 0$  and, hence,  $-\Delta f_{\text{bond}} \geq \Delta f_{\text{loc}} - Ts_c$ , the equality achieved strictly at the crossover. The one-particle localisation penalty is computed in the standard fashion:

$$\Delta f_{\text{loc}}/k_B T = N^{-1} \int \rho(\mathbf{r}) [\ln \rho(\mathbf{r}) - 1] d^3 \mathbf{r} - (\ln \bar{\rho} - 1) \simeq (3/2) \ln(\alpha a^2/\pi e), \quad (166)$$

where  $\bar{\rho} \equiv 1/a^3$  is the number density of beads, Eq. (113). The density profile  $\rho(\mathbf{r})$  is from Eq.(29). We thus arrive at

$$\sigma_0 \geq [(3/2) \ln(\alpha a^2/\pi e) - s_c/k_B] k_B T/2a^2. \quad (167)$$

To simplify the expression in the square brackets we compare the  $T$ -dependences and magnitudes of the first and second terms: First off,  $\alpha$  increases, while  $s_c$  decreases upon lowering the temperature. At the crossover, Rabochiy and Lubchenko's (RL) estimates [37] yield  $\alpha$  ranging from 71 to 104, hence  $(3/2) \ln(\alpha a^2/\pi e) \simeq 3.2 \dots 3.7$ . For  $s_c$  at the crossover, Stevenson et al. [41] predict  $\approx 1.2k_B$ , while RL have argued it could be as high as  $1.75k_B$ . On the other hand, at  $T_g$ ,  $s_c \simeq 0.8 \dots 0.9k_B$ . [31, 35] Judging from its high-density trend (Fig. 3 of Ref. [37]),  $\alpha(T_g)$  is probably 200 or so, yielding  $(3/2) \ln(\alpha a^2/\pi e) \simeq 4.7$ . Xia and Wolynes argued a good estimate for  $\sigma_0$  would be obtained by taking the smallest value of  $\alpha$ , i.e. that achieved at the crossover, and disregarding  $s_c$ ; the latter we have seen becomes progressively smaller than the localisation term as the temperature is lowered. Note the  $T$ -dependence of  $s_c$  may well be immaterial to the  $T$ -dependence of  $\sigma_0$ , since Eq. (167) is stated as an inequality. Note also that at temperatures at which  $s_c$  is not small, it is the barrier softening effects that determine  $\sigma_0$ , in the first place [35], see Section VII. These effects can be thought of as resulting from fluctuations of the parameter  $\alpha$  near the crossover, which leads to "short-circuiting" of the activated transitions by partial melting of the lattice. (This is another way of saying that near the crossover, the usual collisional transport becomes important [170].) Finally we note that the linear temperature dependence of  $\sigma_0$  is obvious for rigid systems but makes just as much sense for strongly interacting systems: The free energy cost of localisation is determined by the *kinetic* pressure, which is determined by the ambient temperature (and is usually much greater than the ambient pressure). We thus obtain

$$\sigma_0 = \frac{3}{4} (k_B T/a^2) \ln(\alpha a^2/\pi e) \approx 1.85 k_B T/a^2, \quad (168)$$

if one adopts the generic value for the vibrational displacement,  $a^2 \alpha = 100$ , c.f. Figs. 9 and 12. In terms of  $\gamma$ :

$$\gamma = \frac{3}{2} \sqrt{3\pi} k_B T \ln(\alpha_L a^2/\pi e) \approx 11.3 k_B T. \quad (169)$$

Eqs. (168) and (164) yield an extremely simple expression for the activation barrier [31]:

$$\frac{F^\ddagger}{k_B T} \simeq \frac{32}{s_c}. \quad (170)$$

Note that the configurational entropy is per *bead*, not per unit volume, in contrast with Eq. (159). In the XW [31] approximation for the mismatch penalty, it is the Arrhenius exponent that does not explicitly depend on the temperature, not the barrier itself. Similarly simple to Eq. (170) is the formula for the cooperativity size that can be easily obtained using Eq. (129):

$$N^* \equiv (\xi/a)^3 \simeq [\ln(\tau/\tau_0)/2.83]^2 = [(F^\ddagger/k_B T)/2.83]^2 \approx 130/s_c^2. \quad (171)$$

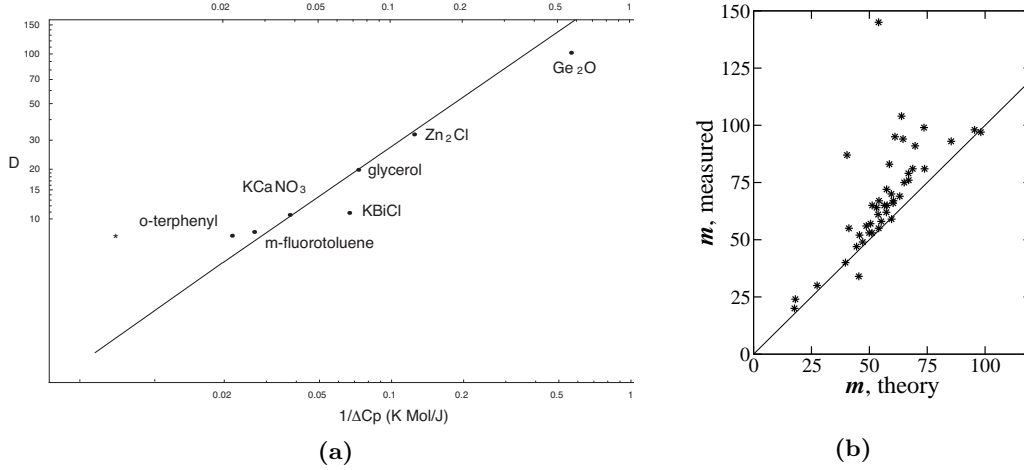


FIG. 26. Tests of the Xia-Wolynes relation between the barrier for activated transport and the configurational entropy per bead (170), from Ref. [31]. **(a)** The relation (172) between the fragility from (98) and heat capacity jump per bead, is shown with the solid line. The experimental points are indicated with symbols. The bead count is determined based on chemical considerations. **(b)** The straight line corresponds to the Lubchenko-Wolynes [35] relation (174). The experimental points, shown with the symbols, were compiled by Stevenson and Wolynes [36]. The bead count is from Eq. (96). No adjustable constants used in either estimate.

Notwithstanding its approximate nature, the argument leading to Eq. (170) makes explicit use of the physical picture emerging from the RFOT theory in that it directly traces the origin of the mismatch penalty to the confinement of the particle following the breaking of the translational symmetry and the general inability of arbitrary aperiodic arrays of such localised particles to mutually fit. The approximations boil down to a few simple notions: On the one hand, we have neglected the configurational entropy, which would be strictly valid only at  $T_K$ . On the other hand, we have replaced the inequality in Eq. (167) by the equality, which would be strictly valid at the crossover temperature  $T_{cr}$ . In addition, there is an uncertainty in the value of  $\alpha$ , which, however, is only logarithmic. As a result, the energy scale in Eq. (168) could, in principle, vary between  $k_B T_{cr}$  and  $k_B T_K$ , but not much beyond that. In any event, the temperature dependence of the numerator in Eq. (170) is much weaker than that of the configurational entropy. According to this equation, the barrier should, in fact, diverge if the configurational entropy vanishes. This prediction is, arguably, the most important result of the RFOT theory. It shows that the kinetic catastrophe and the thermodynamic singularity, which are the landmarks of the glass transition, are intrinsically related. The kinetic catastrophe manifests itself through the rapid growth of the viscosity above the glass transition that implies the viscosity would diverge at some putative temperature  $T_0$ , Fig. 2, if one had the ability to equilibrate the liquid on the correspondingly increasing time scales. The thermodynamic singularity is the vanishing of the configurational entropy at the (putative) Kauzmann temperature  $T_K$ , as in Fig. 18. According to Eq. (170), the temperatures  $T_0$  and  $T_K$  must coincide, which is consistent with available extrapolations of kinetic and calorimetric data, see Fig. 19.

In addition to prescribing that  $T_0 = T_K$ , Eq. (170) predicts that the *rate* of change of the barrier with temperature is determined by the rate of change of the configurational entropy. Both of these rates have a clear physical meaning and value in themselves: The slope of the  $T$ -dependence of the log-viscosity actually reflects the width of the temperature window in which the supercooled liquid will be in a certain viscosity interval of convenience for processing. The broader the window, the less need for maintaining a constant temperature during the processing. The corresponding materials are called “long” glasses. Conversely

substances with a narrow processing window are called “short” glasses. In a more modern parlance, due to Angell [61], the former and latter are often called “strong” and “fragile,” see Fig. 2. Accordingly, the coefficient  $D$  from the VFT law in Eq. (98) is called the fragility. On the other hand, the rate of change of the configurational entropy with temperature is directly related to the excess heat capacity associated with the translational degrees of freedom, see Eq. (84). Using Eqs. (98), (170), and (94), Xia and Wolynes (XW) obtain [31]:

$$D \simeq \frac{32.}{\Delta c_p}, \quad (172)$$

where  $\Delta c_p$  is the heat capacity jump at the glass transition, *per bead*. XW tested their formula using the chemically-reasonable bead size, whereby the bead was identified with a chemically rigid unit, such as  $\text{CH}_3$ . The results are certainly very encouraging, see Fig. 26(a), especially considering that no adjustable constants are involved. In other words, the straight line in Fig. 26(a) is not a fit but a prediction.

To determine the fragility  $D$ , one must extrapolate kinetic data below the glass transition temperature. One may reasonably object to such extrapolation into regions that are inaccessible in experiment, both on formal grounds and because such extrapolations are likely to result in some numerical uncertainty. In view of these potential ambiguities, an alternative way to test the connection between the kinetics of the activated transport and the driving force behind the transport, as predicted by relation (170) is to compare the *slope* of the temperature dependence of the relaxation time (or its logarithm) with the rate of change of the configurational entropy at some standard temperature. The most obvious choice for such standard temperature is the glass transition temperature  $T_g$  itself since the time scale for the latter usually does not vary much between different labs or substances. It is convenient, for the sake of comparing different substances, to work with a dimensionless slope, called the *fragility coefficient*:

$$m = \left. \frac{\partial \log_{10} \tau}{\partial (T_g/T)} \right|_{T=T_g}. \quad (173)$$

Low values of the fragility coefficient correspond to strong substances, while high values correspond to fragile substances, see Fig. 2.

With the help of the calorimetric bead count, Eq. (96), Lubchenko and Wolynes [35] (LW) have written down the following simple relation

$$m = \frac{T_g \Delta c_p(T_g)}{\Delta H_m} \left\{ s_{\text{bead}} (\log_{10} e) \frac{32.}{s_c^2(T_g)} \frac{T_m}{T_g} \right\}. \quad (174)$$

Generically, the ratio of the melting and glass transition temperatures  $T_m/T_g$  is about 3/2 (the actual figure seems to vary between 1.2 and 1.6 or so). Also, by virtue of Eq. (170), the value of the configurational entropy per bead, at the glass transition on timescale of  $10^5$  sec, is  $s_c(T_g) = 32./\ln(10^5/1e^{-12}) \simeq 0.82$ . Using these generic figures and  $s_{\text{bead}} = 1.68$  (see discussion of Eq. (96)), LW obtain  $m = 52T_g \Delta C_p / \Delta H_m$ , which is rather close numerically to the empirical relation  $m = 56T_g \Delta C_p / \Delta H_m$  first noticed by Wang and Angell [215]. Stevenson and Wolynes went further and used the actual measured values of  $T_m$  and  $T_g$  to compare the value of the fragility coefficient determined in kinetic measurements with the one determined using the thermodynamic quantities according to Eq. (174). The results of this comparison are shown in Fig. 26(b); again, no adjustable parameters are involved. We observe a clear correlation between the kinetics and thermodynamics on approach to the glass transition, although the precise form of the correlation seems to deviate somewhat from the simple expression (174) for the more fragile substances. One possible source of the deviation are the barrier-softening effects [35], to be discussed in Section VII.

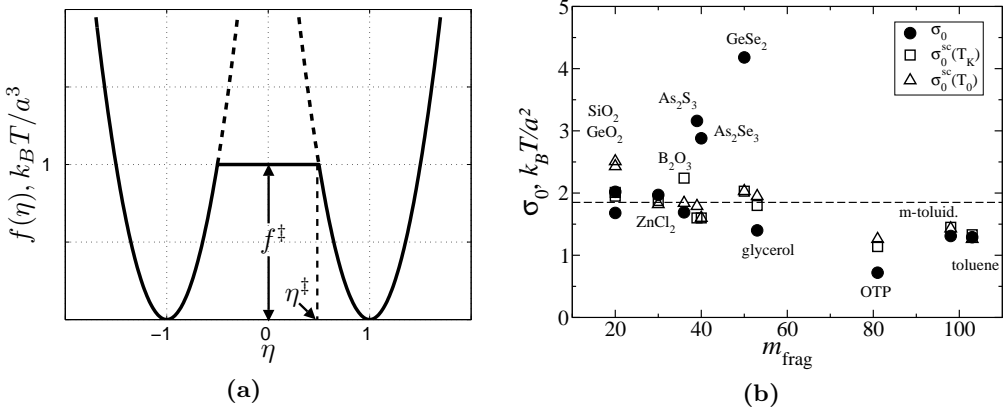


FIG. 27. **(a)** The bulk free energy density  $f(\eta)$  from the Landau-Ginzburg-Cahn-Hilliard density functional (175) [32]. **(b)** The resulting predictions for the mismatch penalty  $\sigma_0$  at the molecular scale [32]. There are three distinct values for each substance that correspond to three distinct ways to determine the bead size, see text. The substances can be distinguished by the value of the fragility coefficient  $m$ , except  $\text{SiO}_2$  and  $\text{GeO}_2$ , whose  $m$ -values are numerically equal. See Ref. [32] for the tabulated values of  $\sigma_0$ .

Although it directly reflects microscopic aspects of the RFOT, the XW argument leading to Eq. (170) is an estimate, not a fully microscopically-based calculation of the penalty for bringing two dissimilar aperiodic states in contact. Rabochiy and Lubchenko [32] attempted to perform such a calculation using standard methods of the classical density-functional theory. They employed the Landau-Ginzburg-Cahn-Hilliard [194, 203] functional, c.f. Eq. (3):

$$F[\eta(\mathbf{r})] = \int \left[ \frac{\kappa(\eta)}{2} (\nabla\eta)^2 + f(\eta) \right] d^3\mathbf{r}, \quad (175)$$

where the order parameter  $\eta$  ( $-1 < \eta < 1$ ) allows one to consider arbitrary spatial superpositions of two distinct structures with density profiles  $\rho_1(\mathbf{r})$  and  $\rho_2(\mathbf{r})$  respectively:

$$\rho(\mathbf{r}) = \rho_1(\mathbf{r}) \frac{1-\eta}{2} + \rho_2(\mathbf{r}) \frac{1+\eta}{2}. \quad (176)$$

A reasonable approximation for the bulk free energy density  $f(\eta)$ , see Fig. 27(a), can be obtained by first noticing that the two aperiodic packings are mechanically stable. Thus for small deviations of the order parameter from its values  $\eta = \pm 1$ , the free energy is quadratic, denote the corresponding curvature by  $m$ :

$$f(\eta) \approx \frac{m_i(\eta - \eta_i)}{2}, \quad (177)$$

where  $\eta_i = \pm 1$ . Already using the quadratic approximation in the full range of the order parameter—a parabola per each minima—could suffice so long as the two parabolas cross at a value below  $k_B T/a^3$ . Otherwise, the potential  $f(\eta)$  must be corrected to account for the fact the one-particle barrier for a transition between the crystal and liquid in mutual equilibrium equals  $k_B T$  [65], which sets the upper bound for the barrier height in  $f(\eta)$ . Under these circumstances, it is sufficient to “cut off” the portion of the potential in excess of  $k_B T/a^3$ , see Fig. 27(a). Interestingly, computations of the coefficients  $m$  for actual substances show that the two parabolas cross at an altitude  $f^\ddagger$  that always turns out to be numerically close to  $k_B T/a^3$ , at least near  $T_g$ .

Straightforward calculation shows that [32]:

$$m_i = -\frac{k_B T}{4V} \iint d^3\mathbf{r}_1 d^3\mathbf{r}_2 c_i^{(2)}(\mathbf{r}_1, \mathbf{r}_2) \left[ \tilde{\Delta}\rho_1(\mathbf{r}_1) \tilde{\Delta}\rho_1(\mathbf{r}_2) + \tilde{\Delta}\rho_2(\mathbf{r}_1) \tilde{\Delta}\rho_2(\mathbf{r}_2) \right] \quad (178)$$

and

$$\kappa_i = \frac{k_B T}{8V} \iint d^3 \mathbf{r}_1 d^3 \mathbf{r}_2 z_{12}^2 c_i^{(2)}(\mathbf{r}_1, \mathbf{r}_2) \left[ \tilde{\Delta} \rho_1(\mathbf{r}_1) \tilde{\Delta} \rho_1(\mathbf{r}_2) + \tilde{\Delta} \rho_2(\mathbf{r}_1) \tilde{\Delta} \rho_2(\mathbf{r}_2) \right], \quad (179)$$

where  $\Delta \rho(\mathbf{r}) \equiv \rho_1(\mathbf{r}) - \rho_2(\mathbf{r})$ , c.f. Eq. (26). As expected, the coefficients at the quadratic terms in the density functional couple density fluctuations that correspond to two-body interactions; only fluctuations within individual states are coupled. The inter-state fluctuations drop out because the structures are uncorrelated by construction. Since both states 1 and 2 are typical, we have  $m_1 = m_2 = m$  and  $\kappa_1 = \kappa_2 = \kappa$ .

Next, one may repeat the analysis analogously to that following Eq. (21), but also including the shear component of the elastic free energy, in computing the pairwise correlation function  $\rho^{(2)}(\mathbf{r}_1, \mathbf{r}_2)$ . Note that individual aperiodic structures are mechanically (meta)stable and so  $\mu > 0$ . This analysis results in the sum rule for the solid listed in Eq. (65). Combined with the long-wavelength, Debye approximation for the vibrational spectrum of our aperiodic solid and the generalised Ornstein-Zernike relation (62), this allows one to write down the following expression for the Fourier image of the direct correlation function from Eq. (18):

$$\hat{c}^{(2)}(\mathbf{k}_1, \mathbf{k}_2) \simeq -(2\pi)^3 \delta(\mathbf{k}_1 + \mathbf{k}_2) \theta(\pi/a - k) \frac{M c_l^2}{k_B T \bar{\rho} N_b}, \quad (180)$$

Note in this long-wavelength approximation, the direct correlation function turns out to be translationally-invariant:  $c^{(2)}(\mathbf{r}_1, \mathbf{r}_2) = c^{(2)}(\mathbf{r}_1 - \mathbf{r}_2)$ , which is generally not the case for solids [82]. Note that in writing down the equation above, we have ignored the difference between the isothermal and adiabatic speeds of longitudinal sound; this difference is not substantial in solids, see our earlier comments following Eq. (65).

The density-density correlations within each phase are straightforwardly related to the structure factor, by Eq. (61). Combining this with Eqs. (113), (180), (178), and (179) yields the following simple expressions for the coefficients  $\kappa$  and  $m$  [32]:

$$\kappa = \frac{M c_l^2 a^{-2} S'(\pi/a)}{24 N_b}, \quad (181)$$

and

$$m = \frac{M c_l^2}{4\pi^2 N_b} \int_0^{\pi/a} S(k) k^2 dk. \quad (182)$$

where  $S'(k) = dS/dk$ .

Finally, we note that the surface tension coefficient  $\sigma_0$  corresponds to the mismatch penalty at the molecular lengthscale, implying no surface tension renormalisation takes place, as if the interface were entirely flat. Combining the standard formula for the surface tension coefficient for a flat interface [195],  $\sigma = \int_{-1}^1 d\eta [2\kappa f(\eta)]^{1/2}$ , and the two equations above one can write down an explicit expression for the surface coefficient  $\sigma_0$  in terms of measured quantities:

$$\sigma_0 = \frac{k_B T}{a^2} \left[ \frac{M c_l^2 a^{-1} S'(\pi/a)}{12 N_b k_B T} \right]^{1/2} \left\{ 2 - \left[ \frac{M c_l^2}{8\pi^2 k_B T N_b} \int_0^{\pi/a} S(k) k^2 dk \right]^{-1/2} \right\}, \text{ if } m \geq 2f^\ddagger \quad (183)$$

$$\sigma_0 = \frac{M c_l^2 a^{-1}}{4\sqrt{6} N_b} \left[ S'(\pi/a) \int_0^{\pi/a} S(k) k^2 dk \right]^{1/2}, \text{ if } m < 2f^\ddagger \quad (184)$$

Note that the value of the factor in the curly brackets varies between 1 and 2.

Despite its relatively computational complexity and requiring the knowledge of many experimental inputs, the RL formalism leading to Eqs. (181) and (182) has a side dividend of allowing one to compute the correlation length in the landscape regime. By Eqs. (175) and (177), the correlation length is simply  $\sqrt{\kappa/m}$ . According to RL’s estimates for actual glass-formers, this length is of molecular dimensions, consistent with our earlier conclusions that glassy liquids are far away from any sort of criticality.

The values of  $\sigma_0$  predicted by Eqs. (183) and (184) computed using experimentally determined values of the input parameters are plotted in Fig. 27(b), where they are compared with the XW-predicted value  $1.85k_BT/a^2$  from Eq. (168). The filled circles correspond to the calculation that employs the calorimetric bead count from Eq. (96). As noted in Ref. [32], in instances where the  $\sigma_0$  value differed particularly significantly from the XW prediction, the value of the configurational entropy at  $T_g$  also turned out to differ quite a bit from the XW prediction that  $s_c(T_g) \approx 32/\ln(\tau(T_g)/\tau_0)$ , see Eq. (170). (Such differences seem to come up often for substances with a significant degree of local ordering, such as the chalcogenide alloys [54].) This suggests that the bead count may be off for these specific substances. To test for the significance of the precise bead count, Rabochiy and Lubchenko also determined the bead count self-consistently by requiring that the barrier from Eq. (164) yield exactly  $k_BT \ln(3600/10^{-12})$ , which corresponds to the glass transition on 1 hr scale. The resulting bead count depends on whether the temperature  $T_0$  or  $T_K$  is used for the location of the putative Kauzmann state. The values of  $\sigma_0$  corresponding to both ways to determine the bead count self-consistently are shown in Fig. 27(b) with squares ( $T_K$ ) and triangles ( $T_0$ ). The self-consistently determined bead count turned out to be chemically reasonable in all cases, except for OTP.

The general agreement between the  $\sigma_0$  values for different substances and the XW-estimate, even for the calorimetrically determined bead size, is notable. On the one hand, there would appear to be little *à priori* reason for a complicated combination of several material constants to be so consistent among chemically-distinct substances. On the other hand, one expects that the several approximations involved and some uncertainty in the experimental input parameters, especially the structure factor, would introduce a potential source of error in the final result, see detailed discussion in Ref. [32]. In any event, it is an important corollary of the XW calculation that despite apparent differences in detailed interactions among distinct substances, the value of  $\sigma_0$  is expected to be relatively universal in that it can be expressed approximately through very few materials constants.

Elastic constants enter the expressions (183) and (184), similarly to Eq. (155) but in a more complicated way. Still, in Eq.(183), which applies when  $m \geq 2f^\ddagger$ , i.e., when the “ledge” in the  $f(\eta)$  is present (Fig. 27(a)), the resulting barrier clearly has a contribution that is linear in the bulk modulus.

We have thus discussed three distinct approximations for the mismatch penalty in this Subsection. The Xia-Wolynes [31] (XW) approximation (168) and Rabochiy-Lubchenko [32] (RL) approximation (183)-(184) for  $\sigma_0$  can be combined with Eq. (164) to compute the free energy barrier for activated transport in glassy liquids in an extended temperature range. This was accomplished recently by Rabochiy, Wolynes, and Lubchenko [33] (RWL) for eight specific substances. Likewise, the barrier can be computed, in principle, using the Lubchenko-Rabochiy [34] (LR) approximation for the coefficient  $\gamma$ , Eq. (155), combined with Eq. (154). The simplified form (159) only requires the knowledge of two experimental quantities, which has enabled LR to estimate the barrier for seven actual substances. In Fig. 28(a) we display the values for the barrier, as a function of temperature, as predicted by all three approximations for a specific substance (m-toluidine). We plot the barriers within the dynamical range representative of actual liquids, viz.  $\ln(\tau/\tau_0) \leq 35.7$ , which corresponds to a glass transition on 1 hr time scale and  $\tau_0 = 1$  ps. This way, the error of the approximation exhibits itself through an error in the temperature corresponding to a particular value



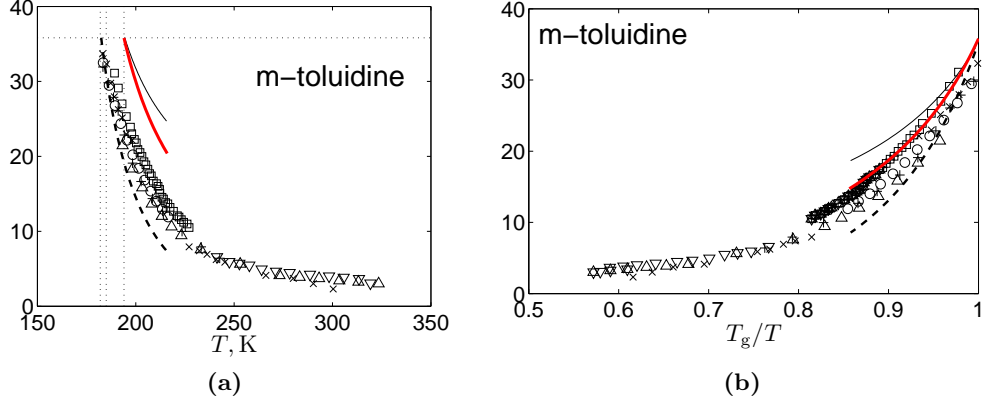


FIG. 28. **(a)**  $\alpha$ -relaxation barrier (divided by  $k_B T$ ) as a function of temperature, computed using three distinct approximations for the mismatch penalty, due to Xia and Wolynes [31] (XW), Rabochiy and Lubchenko [32] (RL), and Lubchenko and Rabochiy [34] (LR). **(b)** Same as (a), but as a function of the inverse temperature scaled by  $T_g$  and adjusted so that the barrier at  $T_g$  corresponds to 1 hr relaxation time (Eq. (132) with  $\tau = 3600$  sec and  $\tau_0 = 1$  psec). Both figures are from Ref. [33].

of the relaxation time. As already mentioned, the RL and XW approximations require the knowledge of the bead size. In addition, the RL approximation requires the knowledge of the structure factor in an extended temperature range. For the lack of this knowledge, the  $S(k)$  at a fixed temperature (usually around  $T_g$ ) were used by RWL, which introduces another source of uncertainty. Given the aforementioned potential sources of uncertainty, it is interesting to rescale the computed barriers by a constant so that the barrier at  $T_g$  matches its known value. This way, one may better judge the error of the approximation as regards the *slope* of the temperature dependence of the barrier. We show the so rescaled barriers in Fig. 28(b). The LR approximation does not rely on the bead size, and so any discrepancy with experiment is due to the error of the approximation itself and the uncertainty in the experimental values of the elastic constants and the configurational entropy. The rescaled LR-based barrier is *also* shown in Fig. 28(b). The results in Fig. 28(b) are representative of the results for the rest of the substances analysed in Refs. [33] and [34] in that the XW approximation tends to underestimate the fragility coefficient in the *extended* temperature range, while the RL-based estimate tends overestimate the fragility coefficient. (Note the fragility  $D$  and fragility coefficient  $m$  anti-correlate!) None of the three approximations account for the barrier softening effects (Section VII), although the RL and LR approximation may partially include those effects through the temperature dependence of the bulk modulus. The LR-based values appear to fare better than the other two approximations as far as the slope is concerned, but not the absolute value of the barrier. Overall, the predictions due to all three approximations, Fig. 28(a), leave room for improvement but agree with experiment reasonably well given that no adjustable parameters are used.

It is encouraging that the results of three, rather distinct-looking approximations for the mismatch penalty yield results that are numerically similar. These results also imply that there is an intrinsic connection between the material constants and structure factor entering in Eqs. (156), (168-169), and (183-184). Such a connection should have been expected in view of Eqs. (82), (83), and (99).

The results displayed in Fig. 28(a) are of very special significance for testing the theory because they do not use any adjustable parameters. Because no adjustable parameters are involved, these calculations allow one to *predict* the glass transition temperature, a kinetic quantity, based on measured quantities that are entirely static. We compile the predictions

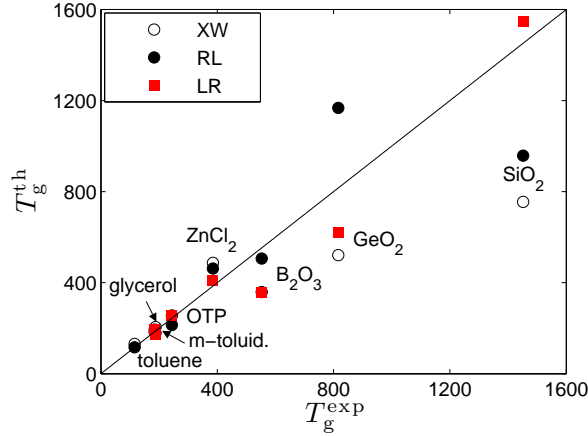


FIG. 29. The glass transition temperature computed using the three distinct approximations for the mismatch penalty, due to Xia and Wolynes [31] (XW), Rabochiy and Lubchenko [32] (RL), and Lubchenko and Rabochiy [34] (LR). These theoretically predicted glass transition temperatures are plotted against their experimental values.

for the glass transition temperatures due to the XW and RL approximations, for eight substances, and due to the LR approximation, for seven substances, all in Fig. 29. We note the larger degree of deviation from experiment for the stronger substances. This may well be related to the greater uncertainty in determining the putative Kauzmann temperature  $T_K$  for strong substances, for which  $T_K$  differ from  $T_g$  easily by a factor of two. Note that in addition to the uncertainties inherent in the approximations and in the experimental input parameters used to compute the barrier, there is also some uncertainty in the experimentally determined glass transition itself, as the latter depends on the cooling protocol and sample purity.

Also of particular significance is the ability of these RFOT-based methodologies to predict the cooperativity length  $\xi$ . In Fig. 30(a), we show the temperature dependence of  $\xi$  for m-toluidine, as computed according to Eq. (165) with the help of the XW and RL approximations for  $\sigma_0$  (thin and thick solid lines respectively). The dashed line shows the dynamical correlation length  $\xi$  computed according to the procedure of Berthier et al.[216, 217]:

$$\xi_B/a = \left\{ \frac{1}{\pi} \left[ \frac{\beta}{e} \frac{\partial \ln \tau}{\partial \ln T} \right]^2 \frac{k_B}{\Delta c_p} \right\}^{1/3}, \quad (185)$$

where  $\beta$  is the stretching exponent in the stretched exponential relaxation profile:  $e^{-(t/\tau)^\beta}$ . (The quantity  $\beta$ , not to be confused with the inverse temperature  $\beta \equiv 1/k_B T$ , will be discussed in Section VI). The dynamical correlation length from Eq. (185) is an experimentally-inferred lower bound on the cooperativity length. As before,  $\Delta c_p$  is the (temperature dependent) excess liquid heat capacity.

First we note that the cooperativity length is on the order of a nanometre, consistent with experimental determinations using non-linear spectroscopy [218–220], and also *direct* observation of cooperative reconfigurations on the surface of metallic glasses [221]. Furthermore, the temperature dependence of  $\xi$  is also clearly consistent with that determined according to the Berthier et al. procedure [216]. The dimensionless measure of the spatial extent of cooperativity  $\xi/a$  is shown in the inset of Fig. 30(a). According to Eq. (171), the cooperativity size at the glass transition depends only the quench speed and only logarithmically at that. Thus it is expected to be quite consistent between different substances. For the glass

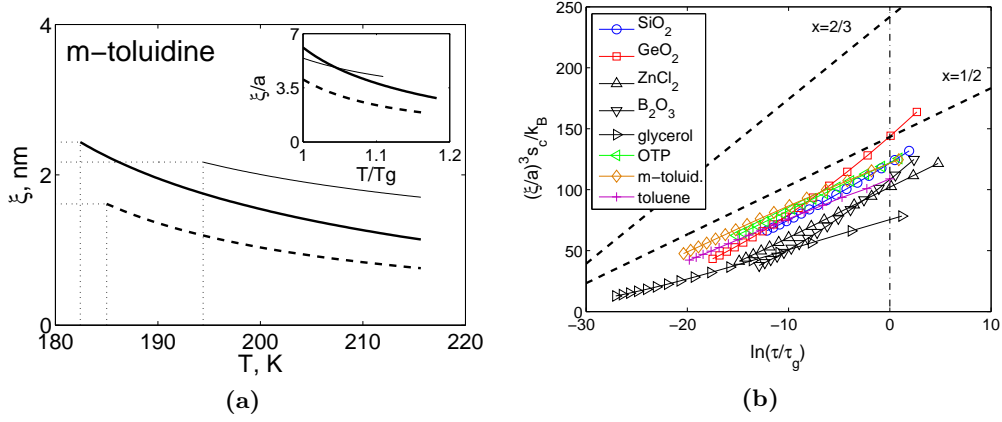


FIG. 30. **(a)** The cooperativity length  $\xi$  as a function of temperature computed using Eq. (165) with the value of the surface tension coefficient  $\sigma_0$  estimated using the XW (thin solid line) and RL (thick solid line) approximation. The dashed line corresponds to the cooperativity length  $\xi$  estimated as in Ref.[217], according to the procedure by Berthier et al. [216]. **(b)** The complexity of a rearranging region  $s_c(\xi/a)^3$  is plotted as a function of  $\ln(\tau/\tau_g)$ , where  $\tau_g$  is the relaxation time  $\tau$  at  $T_g$ . The cooperativity length  $\xi$  in this graph is estimated as in Ref.[217], except here we use the Xia-Wolynes-Lubchenko expression (193) for the temperature dependence of the stretching exponent  $\beta$  normalised so that it matches its experimental value at  $T_g$ .

transition on 1 hr timescale, the cooperativity size  $N^*$  is about  $[\ln(3600/10^{-12})/2.83]^2 \simeq 160$  beads. For the glass transition on the timescale of  $10^5$  sec, this size is 190 or so.

Finally we calculate the so called *complexity* of a rearranging region, which is defined as the amount of configurational entropy contained within the region, i.e,  $N^*s_c$ . This quantity is of interest partially because it is independent of the bead count. Indeed, dividing Eq. (164) by (165), one obtains that the complexity of a rearranging region is simply the barrier, in units of  $k_B T$ , times a factor of four:

$$N^*s_c/k_B \equiv (\xi/a)^3 s_c/k_B = 4(F^\ddagger/k_B T) = 4 \ln(\tau/\tau_0) \quad (186)$$

It turns out that similarly universal relationship between the complexity and the reconfiguration barrier exists for all values of the exponent  $x$  that gives the scaling of the mismatch penalty with the region size, Eq. (119). Indeed, Eqs. (124) and (129) yield:

$$N^*s_c/k_B = (F^\ddagger/k_B T) \left[ x^{x/(1-x)} (1-x) \right]^{-1}. \quad (187)$$

The relationships in Eqs. (186) and (187) can be interpreted as saying that rearrangement involves searching through all the states of a fixed fraction of the rearranging region [222]. Note the numerical coefficient in Eq. (187) does *not* depend on the magnitude of surface tension coefficient  $\sigma_0$ , but is quite sensitive to the precise scaling of the mismatch penalty with the droplet size.

The relationship in Eq. (186) was tested by Capaccioli, Ruocco, and Zamponi [217] for a large number of actual substances using the cooperativity length from Eq. (185). Here we show the complexities for the eight substances from Fig. 29 as functions of  $\ln(\tau/\tau_g)$ , where  $\tau_g \equiv \tau(T_g)$ , see Fig. 30(b). In contrast with Ref. [217], here we employ a temperature dependent stretching exponent  $\beta$ , Eq. (193). The dashed line in Fig. 30(b) corresponds to the universal prediction by the RFOT theory, Eq. (186). This result does not depend on substance.

The data in Fig. 30(b) demonstrate that the RFOT-based estimates of the complexity are consistent with experiment; we remind the reader that the length  $\xi_B$  is a lower bound. The

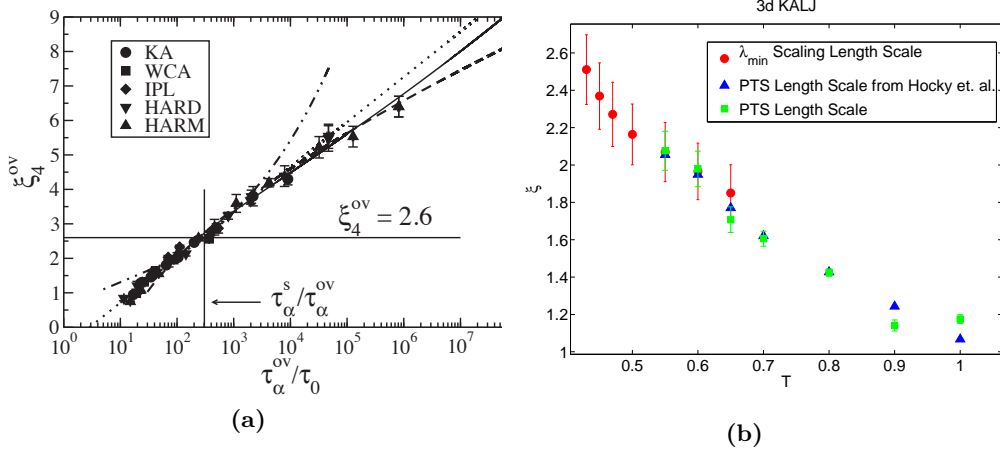


FIG. 31. **(a)** The dependence of the four-point correlation length on the relaxation time, according to computational studies by Flenner, Staley, and Szamel [223]. The fitted solid line has slope 1, the dashed line slope 2/3. **(b)** Comparison between the point-to-set length and the extent  $\lambda_{min}$  of marginally stable harmonic modes in the inherent structures derived from samples equilibrated at temperature  $T$ , from Biroli, Karmakar, and Procaccia [224]. The blue triangles give data due to Hocky, Markland, and Reichman [225].

complexity graph also allows one to test the RFOT-predicted value of the scaling exponent  $x$  for the mismatch penalty from Eq. (119). Indeed, if the exponent were equal to its conventional value 2/3, the numerical coefficient  $[x^{x/(1-x)}(1-x)]^{-1}$  in Eq. (187) would be equal to 6.75, which significantly exceeds its value of 4 for  $x = 1/2$ , see Fig. 30(b). The exponent 1/2 is clearly much more consistent with observation.

The complexity trends exhibited by actual liquids directly contradict the basic premise of the Adam-Gibbs (AG) argument [156] on the connection between the configurational entropy and relaxation rates in liquids. In short, Adam and Gibbs posited that the reconfiguration barrier is determined by the enthalpic cost of deforming a region of a specific size. AG argued the size should be such that the liquid has exactly two structural states available to the region:  $N^*s_c = \ln 2$ . Such a view would be probably adequate at high temperatures, however clearly fails for actual substances: First, given that  $s_c$  is of order  $k_B$  per particle, the AG argument predicts the dynamical size that is too small. Second, the total entropy content of a reconfiguring region,  $N^*s_c$ , clearly depends on the temperature, in contrast with the premise of Adam and Gibbs. Aside from these shortcomings, the AG ideas must be credited for bringing attention to the possibility of an intrinsic connection between the thermodynamics and kinetics in glassy liquids and for spurring much experimental work that has studied this connection empirically. In any event, it should be clear to the reader that the RFOT theory is not a variation on the phenomenological Adam-Gibbs scenario, as is often mistakenly stated in the literature, but is a constructive argument.

On a somewhat related note, the data in Fig. 30 can be used to refute the premise of the so called “shoving model,” which postulates that the reconfiguration barrier is determined by the product of an elastic modulus and the volume of the rearranging region, which is assumed to be fixed [212–214], in direct contradiction with Eq. (171), which predicts the region’s volume changes by at least factor of a few hundred, within the dynamical range of a typical experiment. (The quantity  $\ln(\tau/\tau_0)$  changes between 0 and 35 or so, in Eq. (171). Alternatively, the configurational entropy per bead changes between 1.5 and 0.8 or so.)

Despite system-specific deviations of the predicted values for the barrier and the cooperativity size from experiment, it is clear that the predictions of the RFOT theory are consis-

tent with observation both with regard to the absolute value of the parameters and the key scaling relationships. Given this consistency with measurement on actual substances, the reader may reasonably wonder if similar trends have been observed in computer simulations of glassy liquids. It appears that at present, simulations are largely in the mode-coupling regime and are only beginning to reach into the activated regime. Recent simulations on a variety of model binary mixtures by Flenner et al. [223], indicate that the dependence of the dynamic correlation length  $\xi_4$  on  $\log \tau$  can be well fit by a power law with the exponent 1 over the full temperature range. Still, the low-temperature flank of the data are more consistent with the exponent  $2/3$ , see Fig. 31. This is exactly what the RFOT theory predicts for the scaling of the cooperativity length  $\xi$  in the activated transport regime, see Eq. (171). Note that for the conventional scaling of the mismatch with the region size  $x = 2/3$ , the exponent on the Flenner et al. plot would be equal  $1/2$ , by Eqs. (129) and (126). The four-point correlation length  $\xi_4$  from Fig. 31 is readily evaluated in simulations and, at the same time, is naturally computed in field-theoretical approaches such as the mode-coupling theory. The latter, however, has not been extended to the landscape regime characterised by an exponential multiplicity of free energy minima. In meanfield, the correlation length  $\xi_4$  of the MCT diverges at the temperature  $T_A$  thus signalling the emergence of macroscopic rigidity. As already mentioned and will be discussed in more detail in Section VII, the establishment of such macroscopic rigidity is avoided, owing to the activated reconfigurations, because the metastable structures do not extend beyond the reconfiguration size  $\xi$ . Consequently, while the length  $\xi$  represents a trivial lower bound on  $\xi_4$  above the crossover, it is a non-trivial *upper* bound on  $\xi_4$  sufficiently *below* the crossover. A semi-phenomenological way to estimate  $\xi_4$  within the RFOT theory, through spatial correlations in the mobility field, has been discussed by Wisitsorasak and Wolynes [226] (see their Eqs. (14)-(16)); it appears from the latter work that the lengths  $\xi_4$  and  $\xi$  are asymptotically equal as  $T$  tends to  $T_K$ . The mobility field that will be discussed in the context of glass rejuvenation, see Section VIII B.

One way to quantify the spatial extent of the cooperativity—in a simulation—that is the closest in spirit to the present formalism comes about in the library [40] or the Bouchaud-Biroli construction [202], but goes back to the concept of the entropic droplet developed by Wolynes and coworkers in the 1980s [30, 181]. Take a typical configuration and fix particles outside a compact region, up to vibration. Now perform this procedure for regions of various size. The size at which exactly two states are available corresponds with the cooperativity length of the library construction and is often called the point-to-set length  $\xi_{PS}$ . Alternatively, one may fix particles outside of a compact region not at positions corresponding to an equilibrated liquid but, instead, at some generic positions. This length can be shown to be equivalent to  $\xi_{PS}$  for a large enough region [227]. Equilibration of the thus confined liquid is computationally difficult, and so only rather small system sizes have been investigated. At any rate, the cooperativity length does increase with lowering temperature, see Fig. 31(b). This confirms the basic notion that the lower the temperature, the fewer states are available to a liquid region and the larger region must rearrange to find an alternative structural state. Incidentally, the relative difficulty of equilibrating a region in a confined geometry, as compared with periodic boundary conditions, is consistent with the earlier comment that the present day simulations are only beginning to enter the landscape regime. Indeed, subjecting a liquid to a rough wall is equivalent to imposing a quasi-static field similar to that imposed by a long-lived structure.

We thus observe that a finite-size system with pinned surroundings can in fact run out of configurational degrees of freedom—thus effectively undergoing a Kauzmann-like crisis—at a *finite* value of the *bulk* configurational entropy. According to the library (or Bouchaud-Biroli) construction, this finite value of the configurational entropy,  $s_c^*$ , can be evaluated with the help of Eq. (124) by setting  $N^*$  at the system size  $N$ , thus yielding  $s_c^* = \gamma/TN^{1-x}$ .

Whether or not the true Kauzmann crisis, at  $N \rightarrow \infty$ , could truly take place is probably system-specific. We have seen that such crises do take place in mean-field models. It appears likely that chemically homogeneous systems without an obvious periodic ground state, such as atactic polymers, may reach states with very low values of  $s_c$ . Otherwise, some local ordering likely takes place before the thermodynamic temperature  $T_K$  can be reached, in principle.

A cautionary remark concerning common model glass-formers employed in simulational studies is due here. Such model liquids are usually heterodisperse mixtures with a specially chosen size mismatch so as to avoid crystallisation. Such specially chosen mixtures exhibit various, fascinating types of local ordering [228–232]. The slow dynamics in such mixtures can thus be viewed as motions of twin-like objects. Naturally, such motions are subject to high barriers. These notions are consistent with our earlier remarks on destabilisation of the landscape regime, relative to the uniform liquid, that takes place in eutectic-like mixtures while little changes in the viscosity take place, see Subsection IV C. It is an interesting question as to how much local ordering of this type, if any at all, takes place in actual glass-formers. While little crystallites are constantly being formed in liquids below the melting temperature, they should be very short-lived. In addition, in order for a well-ordered local structure to rearrange, bonds may have to deform to a greater degree than is prescribed by Eq. (127). Now, the tendency to form local patterns with very distinct orientational ordering in binary mixtures stems from the discrete nature of particles, of course. The precise relation between this discrete phenomenon, which may or may not occur in actual glass-formers, and the essentially continuum nature of the RFOT theory has not been elucidated to date. In this regard, early work on icosahedral order comes to mind [233].

We finish this Section by summarising the main features of the activated transport in glassy liquids. The transport is realised through local activated events. These events occur in a nucleation-like fashion and are cooperative; they involve between a few tens and hundreds of particles for realistic quenching schedules—bigger cooperativity sizes are expected for slower quenches. Reconfigurations are strongly anharmonic events, according to the free energy profile in Fig. 25(a), yet local deformations are harmonic as individual atoms move relatively little during the reconfiguration, just in excess of the typical vibrational amplitude, see Fig. 25(b). Last but not least, the simple expressions Eqs. (170) and (159), which quantify the escape barrier from the current structure, reveal the essential feature of the free energy landscape of a glassy liquid. The lower the temperature, the fewer “valleys” the landscape exhibits, while their depth becomes greater.

## VI. DYNAMIC HETEROGENEITY

The central feature of the random first order transition is the multiplicity of the distinct aperiodic arrangements available to the liquid below the crossover to the activated transport. This multiplicity constitutes the thermodynamic driving force for the activated transport and directly enters the expression for the activation barrier. The *distribution* of the bulk free energy of distinct stable structures also has observable consequences. One of these is the relatively slow scaling of the mismatch penalty between distinct aperiodic state with the region size. We have seen that the long-lived glassy structures can be thought of as stabilising free energy fluctuations. Such fluctuations naturally produce not one, but a variety of structures. The resulting structural heterogeneity in glassy liquids is subtle in that there seems to be no static length associated with it [234], consistent with the scale-free character of the generic Gaussian fluctuations. The heterogeneity is *dynamic* in that it can be detected by monitoring the activated reconfigurations in real time, which requires either direct observation [221] or non-linear spectroscopy [218–220]. This rather subtle

type of dynamic heterogeneity is distinct from but is often confused with a simpler kind of dynamic heterogeneity, which is *also* intrinsic to glassy liquids and leads to observable consequences in terms of spatially distributed relaxation rates. This we discuss next.

### A. Correlation between non-exponentiality of liquid relaxation and fragility

According to Eqs. (129) and (164), the reconfiguration barrier is determined by the entropy content of the local region. If fewer states are available, the escape time from the current configurations is longer. This is straightforward to rationalise using the landscape picture of the free energy surface of glassy liquids: Because the entropy is a monotonically increasing function of enthalpy, entropy-poor states are also likely to be correspond to deeper “valleys” in the landscape, thus implying a higher barrier must be surmounted in order to escape from the valley. Thus, by Eqs. (129) and (164), the escape barrier—and hence relaxation rate—will fluctuate in reflection of local fluctuations in the configurational entropy. Xia and Wolynes [38] exploited this idea to estimate a lower bound on the barrier fluctuation in glassy liquids. (Local fluctuations in the mismatch penalty, if any, will also contribute to the barrier fluctuation.) By this argument, the relative value of local fluctuation in the escape barrier is given by:

$$\frac{\delta F^\ddagger}{F_{\text{mp}}^\ddagger} = \frac{\delta S_c^*}{S_c^*} = \frac{1}{2\sqrt{D}}, \quad (188)$$

where  $S_c^* \equiv s_c N^*$  is the configurational entropy of a single cooperative region and the index “mp” signifies “most probable.” In the first equality, we assume that  $S_c^*$  is Gaussianly distributed. The second equality gives the relative fluctuation of the configurational entropy for a region of size  $\xi$  and is seen as follows: On the one hand,  $\delta S_c^* = \sqrt{k_B \Delta C_p^*} = \sqrt{k_B \Delta C_p N^*}$ , based on the general expression for entropy fluctuations:  $\delta S = \sqrt{k_B C_p}$  [55] and remembering that  $\Delta C_p$  corresponds to the excess liquid heat capacity relative to the crystal. On the other hand,  $s_c \sqrt{N^*} = (\gamma/T)$  by Eq. (124) with  $x = 1/2$ . Combined with Eqs. (94) and (98), this yields the second equality in Eq. (188). It is interesting that the value  $x = 1/2$  of the scaling exponent for the mismatch penalty is unique in that it is the only value at which the relative value of entropy fluctuations of a cooperative region is independent of its size:  $\delta S_c^*/S_c^* \propto (T - T_K)^{(2x-1)}$ . (For the latter estimate, one has to assume the “generalised” form of the VFT law  $\tau = \tau_0 \exp[D/(T/T_K - 1)^{x/(1-x)}]$ , see Eq. (129)).

Assuming the barrier distribution is Gaussian, it is straightforward to show [38] that the exponential relaxation profile averaged over the barrier distribution yields approximately a stretched-exponential:

$$\langle e^{-t/\tau} \rangle \approx e^{-(t/\tau_{\text{mp}})^\beta}, \quad (189)$$

where the stretching exponent is determined by the width of the barrier distribution and temperature:  $\beta = [1 + (\delta F^\ddagger/k_B T)^2]^{-1/2}$  thus yielding

$$\beta = \left[ 1 + \left( \frac{F_{\text{mp}}^\ddagger/k_B T}{2\sqrt{D}} \right)^2 \right]^{-1/2}. \quad (190)$$

In view of the near universality of the  $F_{\text{mp}}^\ddagger/k_B T$  ratio near the glass transition, the above equation implies the stretching exponent  $\beta$  is a simple function of the fragility  $D$ . The function is particularly simple for fragile substances, for which  $D$  is relatively small:  $\beta \propto \sqrt{D}$ . The predictions due to Eq. (190) for the glass transition on  $10^4$  sec timescale,  $F_{\text{mp}}^\ddagger/k_B T \simeq \ln(10^4/10^{-12}) \approx 37$ , are shown in Fig. 32(a) with the dashed line. The agreement is only

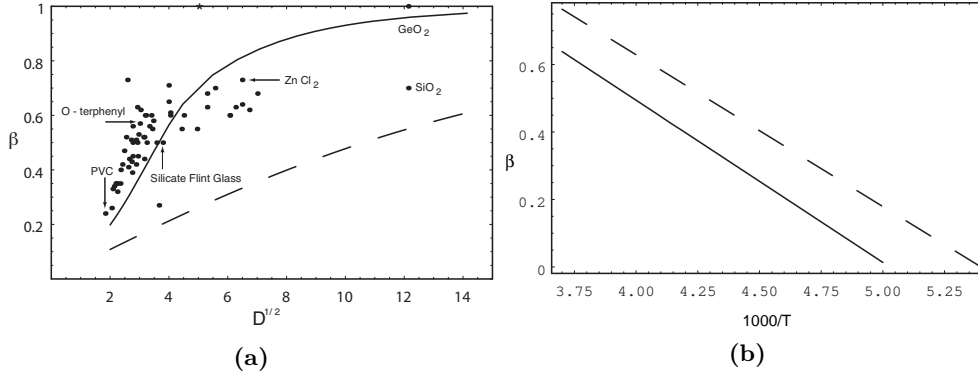


FIG. 32. **(a)** The exponent  $\beta$  from the stretched-exponential relaxation profile  $e^{-(t/\tau)^\beta}$  characteristic of glassy liquids plotted against the square root of fragility  $D$ , as predicted by the RFOT theory [38]. The dashed line corresponds to the simplest assumption of the Gaussianly distributed barrier, while the solid line is obtained using the more complicated form in Eq. (191) that takes into account the “facilitation” effect, by which a very slow region is unlikely to be exclusively surrounded by comparably slow regions and thus will relax not slower than a typical region. **(b)** Solid line: RFOT-predicted temperature dependence of  $\beta$  for a fragile glass-former [38]. Dashed line: experimental measurements of Dixon and Nagel and their extrapolation to lower temperatures for o-terphenyl [235].

qualitative; the lack of quantitative agreement can be explained by the neglect of the following, “facilitation”-like effect. XW argued that a region can be considered unrelaxed insofar as the particles in both the region *and* its immediate environment have not moved; this is non-meanfield effect. A given region may be very slow, but the probability that the immediate surrounding is *also* slow is small. For the same reason in a coin-flipping experiment, the probability of the persistence of a particular pattern, such as many tails in row, is small. XW thus argued that using a Gaussian distribution for the barriers in excess of the most probable value of the distribution is too simplistic. The simplest way to fix this is to replace the r.h.s. of the barrier distribution by a delta function with the area equal to 1/2 and centred at  $F_{\text{mp}}^\ddagger$ :

$$p_1(\tilde{F}) = \frac{e^{-(1/\tilde{F}-1)^2/2\delta\tilde{F}^2}}{\sqrt{2\pi(\delta\tilde{F})^2\tilde{F}^2}} + \frac{1}{2}\delta(\tilde{F}-1), \quad (191)$$

where  $\tilde{F} \equiv F/F_{\text{mp}} < 1^+$ , and we took advantage of the temperature-independence of the relative width in Eq. (188).

The resulting prediction for the  $\beta$  vs.  $D$  relation is shown as the solid line in Fig. 32(a). The agreement is now much improved. Lubchenko [43] has pointed out, in a different context, that an exponential barrier distribution yields a comparable agreement with experiment, while also agreeing with the frequency-dependent dielectric response  $\epsilon''(\omega)$ . The width of this distribution is approximately  $\delta F^\ddagger/4$ , i.e. the average between the l.h.s. of the original Gaussian and the delta function:

$$p(\tilde{F}) = \begin{cases} \frac{c_1}{\tilde{F}^2} e^{-(1/\tilde{F}-1)^2/2\delta\tilde{F}^2}, & \tilde{F} \leq \tilde{F}_e \\ \frac{c_2}{\tilde{F}^2} e^{\tilde{F}/(\delta\tilde{F}/4)}, & \tilde{F}_e < \tilde{F} \leq 1, \end{cases} \quad (192)$$

This leads to a simple formula that works as well as the more complicated XW form con-



sisting of a half-gaussian and a delta function:

$$\beta = \left[ 1 + \left( \frac{F_{\text{mp}}^\dagger / k_B T}{8\sqrt{D}} \right)^2 \right]^{-1/2}. \quad (193)$$

Regardless of the size of the facilitation effects and how they are treated, the RFOT theory unambiguously predicts that given the same value of the relaxation time (or viscosity), the stretching exponent  $\beta$  should be smaller for more fragile substances. At the same time, relaxations in the uniform liquid are exponential. This implies that the temperature dependence of  $\beta$  will be more pronounced the more fragile the substance. We note that the questions of the determination of both the stretching exponent  $\beta$  and its temperature dependence are not without controversy. Xia and Wolynes predictions for the temperature dependence of  $\beta$  for a very fragile substance are shown in Fig. 32(b) alongside experimental data for OTP [235]. These results are also consistent with large-scale simulations of OTP by Eastwood et al. [236]. Now, the temperature dependence of  $\beta$  in many substances seems to deviate significantly [237] from the steady dependence seen in Fig. 32(b). This can be rationalised by the presence of beta-relaxations which overlap frequency-wise with alpha-relaxation, see Fig. 3. Indeed, in the absence of intervening processes, the quantity  $\beta$  can be inferred by either fitting the relaxation profiles in direct time or can be extracted from the slope of the high-frequency wing of the  $\alpha$ -relaxation peak in the Fourier transform of  $\epsilon''(\omega)$ , whereby  $\epsilon''(\omega) \sim \omega^{-\beta}$  [43]. Likewise, there will be one-to-one correspondence between the width of the peak and the value of  $\beta$ . Clearly, the relatively high-frequency  $\beta$ -relaxation, if present, will affect the apparent shape of the  $\alpha$ -peak. (Note the “beta” in beta-relaxation has nothing to do with the stretching exponent  $\beta$  from Eq. (193).) In contrast, the estimates of Xia and Wolynes [38] pertain exclusively to alpha relaxation and do not extend to other processes. Another, early source of confusion on the temperature dependence of  $\beta$  has been discussed by the present author [43]. When measured in even mildly conducting liquids, the  $\alpha$ -relaxation peak in  $\epsilon''(\omega)$  is largely masked by a divergence at zero frequency. At the same time, the *inverse* of the dielectric susceptibility, called the dielectric modulus  $M(\omega)$ , remains perfectly finite. There have been attempts to extract the value of  $\beta$  from the width of the  $\alpha$ -peak in  $M''(\omega)$ . This procedure often yields a temperature dependence of the quantity  $\beta$  opposite from that in Fig. 32(b). This opposite  $T$ -dependence is an artifact of the finite conductivity and does not pertain to the actual  $\alpha$ -relaxation.

## B. Violation of the Stokes-Einstein relation and decoupling of various processes

The diffusivity  $D$  (not to be confused with the fragility  $D$  from Eq. (98)) reflects the efficiency of particle transport, in response to density fluctuations:

$$\mathbf{j} = -D\nabla n, \quad (194)$$

where  $\mathbf{j}$  is the particle flux.

Diffusion of small molecules in a glassy liquid in the activated regime is qualitatively different from largely collisional transport. Indeed, the motion of an individual bead, when in the landscape regime, is completely slaved to the structural reconfigurations. A bead typically moves a distance  $d_L$  during a reconfiguration, Eq. (127), on average once per  $\alpha$ -relaxation time  $\tau_{\text{loc}}$ . Here the index “loc” signifies that the waiting time is distributed and generally differs from location to location, by Eq. (191) or its like. Suppose for a moment the quantity  $\tau_{\text{loc}}$  is not distributed. The relation between the particle displacement  $d_L$  and the waiting time  $\tau_{\text{loc}}$  then implies the particle transport obeys the diffusion equation with

a diffusivity:

$$D_{\text{loc}} = d_L^2 / 6\tau_{\text{loc}}. \quad (195)$$

Now averaging Eq. (194) with respect to the barrier distribution, we obtain the actual diffusivity:

$$D = (d_L^2 / 6) \langle \tau^{-1} \rangle, \quad (196)$$

where we have dropped the label “local.” We observe that the diffusivity—and, thus, any other type of mobility coefficient—is determined by the average of the inverse relaxation time. This is not surprising since mobility has to do with the *rate* of particle transfer. According to Eq. (196), the transport is dominated by faster regions, if the relaxation rates are distributed. Because in this case,  $\langle \tau^{-1} \rangle^{-1} < \langle \tau \rangle$ .

In contrast with the diffusivity, the viscosity  $\eta$  reflects the efficiency of *momentum* transfer, when the velocity profile is spatially non-uniform. In the simplest case of an incompressible liquid and in the limit of low velocity gradients, the non-hydrostatic portion of the stress tensor  $\sigma_{ij}$  can be approximated via a Fick-like law:

$$\sigma_{ij} = \eta(\partial v_i / \partial x_j + \partial v_j / \partial x_i). \quad (197)$$

This quantity reflects the transfer rate of the  $i$ th component of the momentum along the direction  $j$ .

The efficiency of momentum transfer can be related to the transport properties of individual particles via the Stokes formula. For a spherical particle characterised by the hydrodynamic radius  $a/2$  and drag coefficient  $\zeta_{\text{loc}}$ ,  $\eta_{\text{loc}} = \zeta_{\text{loc}} / (6\pi a/2)$ , where we anticipate that the viscosity generally varies from location to location. One may associate, by detailed balance, the above drag coefficient to a diffusion constant. Indeed, in the presence of an external force  $\mathbf{f}$  and in steady state, the diffusive flux  $-D_{\text{loc}} \nabla n$  should be exactly compensated by the force-induced flux  $vn = (f/\zeta_{\text{loc}})n$ . Since  $n \propto e^{\mathbf{f} \cdot \mathbf{r} / k_B T}$ , one obtains (locally) the venerable Einstein relation  $\zeta_{\text{loc}} = k_B T / D_{\text{loc}}$ . The resulting Stokes’ viscosity is thus  $\eta_{\text{loc}} = k_B T / D_{\text{loc}} (6\pi a/2)$ . Substituting Eq. (196) and averaging Eq. (197) with respect to the barrier distribution (and dropping the “local” label) yields for the steady-state viscosity of the actual heterogeneous liquid [43]:

$$\eta = \frac{2k_B T}{\pi a d_L^2} \langle \tau \rangle. \quad (198)$$

That is, the viscosity scales *linearly* with the relaxation time, in contrast with the mobility from Eq. (196), which shows an inverse scaling. The relation in Eq. (198) hearkens back to Maxwell’s phenomenological argument [85] about the intrinsic connection between the elasticity, viscosity, and the relaxation times in very viscous liquids: When  $\tau$  is sufficiently small, the structures do not live long enough to pass on momentum appreciably. In the opposite extreme of very long-lived structures, the response is purely elastic and so momentum is transferred infinitely efficiently, via elastic waves. At high frequencies exceeding the inverse relaxation time, the response is largely elastic so that the stress tensor goes as  $Ku$ , where  $u$  is the magnitude of the deformation. On the other hand, at frequencies below  $\tau^{-1}$ , the response should be purely liquid-like:  $\eta \dot{u}$ . At the crossover between the largely viscous and elastic response,  $\omega\tau \simeq 1$ , and so  $\dot{u} \simeq (d/dt)[u(t=0)e^{-t/\tau}] = u/\tau$ . This yields  $K \simeq \eta\tau^{-1}$ .

It turns out that Eq. (198), which relates microscopic characteristics of the structural reconfigurations, allows one to derive a Maxwell-type expression in a constructive manner. First we recall that the quantity  $(d_L/a)^2$ , which is the typical strain squared, is intrinsically

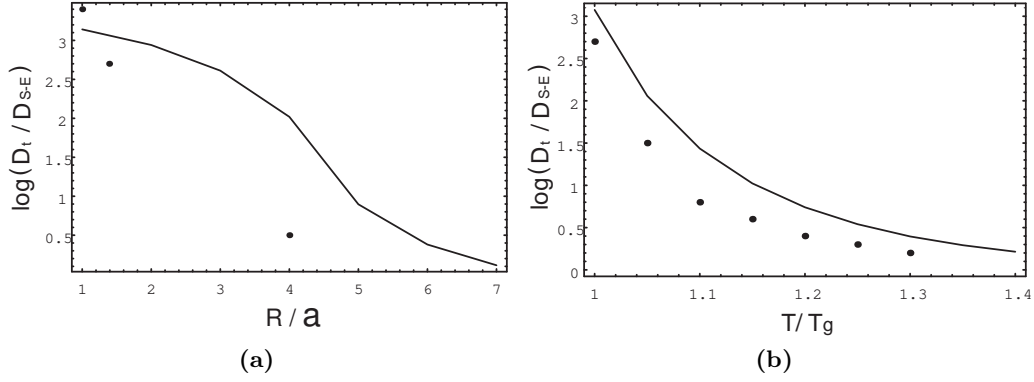


FIG. 33. RFOT-based predictions of the deviation from the Stokes-Einstein relation, due to Xia and Wolynes [39] along with experimental data of Cicerone and Ediger [220] for OTP. **(a)** The ratio of the actual diffusivity to its value predicted by the Stokes-Einstein relation, as a function of the probe radius. **(b)** Same as (a), but a function of temperature [39].

related to the temperature and elastic moduli, via the equipartition theorem:  $Ka^3(d_L/a)^2 = k_B T$ , up to a coefficient of order one. One obtains, as a result:

$$\eta \simeq K \langle \tau \rangle. \quad (199)$$

The above relation works very well in actual liquids. The relaxation times can be measured directly by dielectric response, while the elastic constants can be measured, for instance, by Brillouin scattering. This simple, but nevertheless, fully constructive result thus serves as an important test for the microscopic picture advanced by the RFOT theory. Again, we observe the quantity  $\alpha \sim 1/d_L^2$  enters explicitly in a physical quantity characterising the landscape regime, see Eq. (198).

An important corollary of Eqs. (196) and (198) is that the particle and momentum transport become increasingly *decoupled* from each other for broader barrier distributions because the mobility is dominated by the fastest regions while the viscosity is determined by the typical relaxation time. The simplest quantitative measure of the decoupling is the deviation of the quantity  $\langle \tau^{-1} \rangle \langle \tau \rangle$  from unity. The amount of decoupling increases with the width of the barrier distribution, which, in turn, is greater for more fragile liquids, by Eq. (188). (We remind, a liquid is the more fragile, the larger the fragility coefficient  $m$  from Eq. (173) or the smaller the fragility  $D$  from Eq. (98).) The amount of decoupling will depend on the precise shape of the barrier distribution. Generically, and according to Eq. (188) and Fig. 32,  $\delta F^\ddagger / F_{mp}^\ddagger \simeq 0.25$  while  $F_{mp}^\ddagger / k_B T \simeq 37$  near  $T_g$ . The decoupling, which can be roughly estimated as  $\langle \tau^{-1} \rangle \langle \tau \rangle \sim e^{+\delta F^\ddagger / k_B T}$ , thus could be as large as a few orders of magnitude.

Because  $\langle \tau^{-1} \rangle \langle \tau \rangle > 1$  in the activated regime, the diffusivity predicted from the Stokes-Einstein relation using the measured viscosity is lower than the actual diffusivity. This violation of the Stokes-Einstein reflects the transient breaking of ergodicity that takes place when the landscape sets in. Indeed, the Einstein relation  $D = k_B T / \zeta$  is a consequence of detailed balance, which follows from the ergodic assumption [24, 25]. It is the breaking of the translational symmetry on timescales shorter than the structural relaxation time  $\tau$  that leads to the breaking of ergodicity on the correspondingly short timescales.

Xia and Wolynes [39] have exploited these ideas to quantitatively estimate the amount of decoupling between the diffusion of a spherical probe of an arbitrary radius and momentum transport. They have set up the problem as that of a spatially inhomogeneous viscosity. Consistent with expectation, only probes that are comparable to or smaller than the cooperativity size can “sense” the heterogeneity in the viscous response of the liquid and will

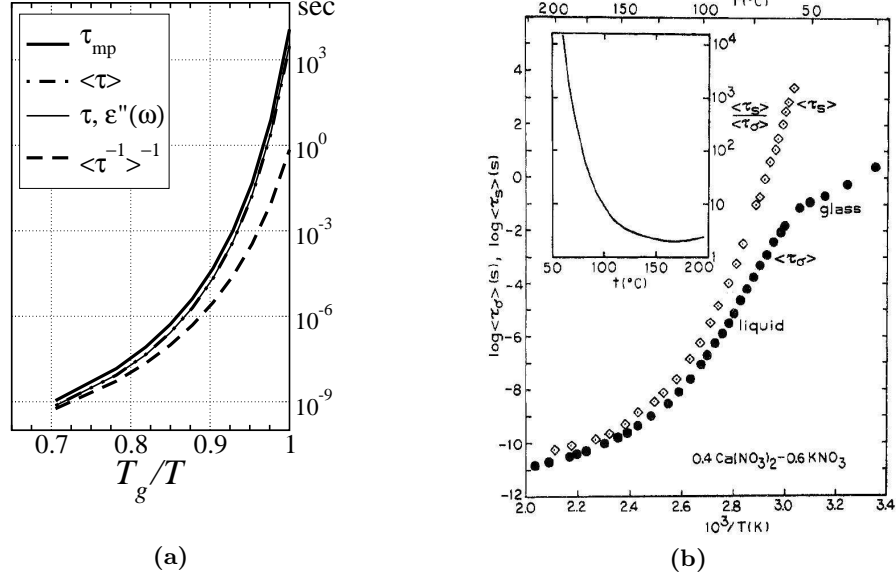


FIG. 34. **(a)** Different relaxation times derived from the barrier distribution in Eq.(192), as functions of temperature.  $\delta\tilde{F} = 0.25$ , corresponding to fragility  $D = 4$  [43]. **(b)** Relaxation time pertaining to the ionic conductivity,  $\tau_\sigma$ , and the structural relaxation time  $\tau_s$ . From Howell et al. [238].

violate the Stokes-Einstein relation. Quantitative predictions of the extent of the violation, due to Xia and Wolynes (XW), are shown in Fig. 33(a), alongside the experimental data of Cicerone and Ediger [220], all near the glass transition. The agreement is good, especially considering that no adjustable parameters were used. As already mentioned, the decoupling goes roughly as  $e^{-\delta F^\ddagger/k_B T}$  and should be greater for lower temperatures since the barrier  $F^\ddagger$ —and hence a measure of the barrier distribution width  $\delta F^\ddagger \propto F^\ddagger$ —increase with lowering temperature. This notion is borne out both in the RFOT-based predictions and in observation, see Fig. 33(b). (To avoid confusion we note that XW used the “slip” boundary conditions in their calculation, which engenders a distinct value of the numerical coefficient in the Stokes formula from the preceding qualitative argument, viz.,  $\eta = \zeta/4\pi R$ .)

Lubchenko [43] has addressed the decoupling between ionic conductivity and momentum transfer in ionic liquids such as CKN (40%  $\text{Ca}(\text{NO}_3)_2$ -60% $\text{KNO}_3$ ). In such liquids, every bead is charged. In the presence of an electric field, there is a non-zero net current density:

$$\mathbf{j} = \langle \mathbf{j}' \rangle = \frac{1}{\xi^3} \left\langle \frac{\boldsymbol{\mu}_T}{\tau} \right\rangle, \quad (200)$$

because the transition barrier, and hence the relaxation time are coupled to the electric field  $\mathbf{E}$ :  $\tau^{-1}(\mathbf{E}) = \tau^{-1}(\mathbf{E} = 0)(1 + \boldsymbol{\mu}_T^\ddagger \mathbf{E}/k_B T)$ , while the the transition dipole moment  $\boldsymbol{\mu}_T^\ddagger$  of a reconfiguring region is correlated with the overall transition dipole moment  $\boldsymbol{\mu}_T$ . A detailed calculation yields for the ionic conductivity tensor:

$$\sigma_{ij} = \delta_{ij} \frac{\Delta \mu_{\text{mol}}^2}{8 a^3 k_B T} \left\langle \frac{1}{\tau} \right\rangle, \quad (201)$$

where  $\Delta \mu_{\text{mol}}$  is the transition dipole moment of a single bead:  $|\Delta \mu_{\text{mol}}| \sim q d_L$ , and  $q$  is the bead charge. Not surprisingly, the above expression for the mobility of charged particles has the same structure as that for the diffusivity in Eq. (196). The resulting temperature dependence of the decoupling for a generic fragile substance is shown in Fig. 34(a), to be compared with the decoupling between ionic transport and viscosity observed in KCN [238]

shown in Fig. 34(b). Fig. 34(a) also demonstrates that the relaxation time, as determined by locating the peak in the imaginary part of the dielectric susceptibility  $\epsilon''(\omega)$  is numerically close to the typical relaxation time, and so is the most probable relaxation time.

Various other types of decoupling have been observed in viscous liquids and, in fact, have been used to *detect* the crossover to the activated transport. We turn to this next.

## VII. AT THE CROSSOVER FROM COLLISIONAL TO ACTIVATED TRANSPORT

Now that we have established a microscopic perspective on both the thermodynamics and kinetics in the activated regime, we are ready to discuss how the landscape regime sets in, in the first place. The crossover spans a dynamical range of a couple of decades in chemically-bonded glassformers, which is much less than the full dynamical range of sixteen decades or so accessible during a quench. Yet the crossover is a very important aspect of any microscopic theory of the structural glass transition. It is the transition that ultimately underlies the formation of the metastable structures and the eventual, complete loss of ergodicity that takes place at the temperature  $T_g < T_{cr}$ . Unfortunately, the crossover is much harder to describe quantitatively than the regime of well-developed activated transport because the activated reconfigurations are no longer decoupled from the vibrations. One may say that the activated reconfigurations are strongly affected by mode-coupling at the crossover. Conversely, one may say the MCT-predicted slowing down becomes short-circuited by the activated transition. Neither approach works quantitatively at the crossover, on its own, nor is it clear at present how to marry the two in a formally satisfactory way. (See however the earlier mentioned work in Refs. [166, 167] for phenomenological, hybrid approaches.) Despite these complications, both quantitative and qualitative characteristics of the crossover can be established by building on the microscopic picture of the activated transport reviewed above.

Already the recognition that particle transport occurs by activation *below* the crossover yields a testable prediction that the temperature dependence of the relaxation time for fragile substances should not obey an Adam-Gibbs (AG) like expression in the full temperature range between the melting temperature  $T_m$  and glass transition temperature  $T_g$ . This is because the crossover temperature for sufficiently fragile liquids is below  $T_m$ . The elegant analysis of Stickel et al. [239] demonstrates that, indeed, temperature dependences of  $\alpha$ -relaxation are well fitted by *two* distinct AG forms, in the low- $T$  and high- $T$  portions of the full temperature interval  $T_g < T < T_m$ .

To actually estimate  $T_{cr}$ , one must first recognise that there will be significant corrections to the RFOT-derived expression for the reconfiguration barrier, Eq. (154), upon approaching the crossover from below. We reiterate that the crossover, which is centred at temperature  $T_{cr}$ , is the finite-dimensional analog of the mean-field transition at temperature  $T_A$ , at which the liquid free energy  $F(\alpha)$  from Eq. (53) develops a metastable minimum. As usual, the transition is lowered in finite dimensions, compared with meanfield:  $T_{cr} < T_A$ . Lubchenko and Wolynes [35] (LW) have elucidated the origin of this lowering. They pointed out that as one approaches from below the temperature  $T_A$ , at which the mean-field free energy  $F(\alpha)$  has a spinodal, fluctuations in the order parameter  $\alpha$  become increasingly strong. The spinodal is illustrated by the thick solid line in Fig. 13(a). Thus the assumption that each metastable minimum is long-living becomes progressively less reliable as the spinodal is approached (from below); consequently, the expression (154) increasingly *overestimates* the barrier.

In assessing the magnitude of the resulting barrier softening effects LW noted that the mismatch penalty between distinct aperiodic minima scales with a positive power of the

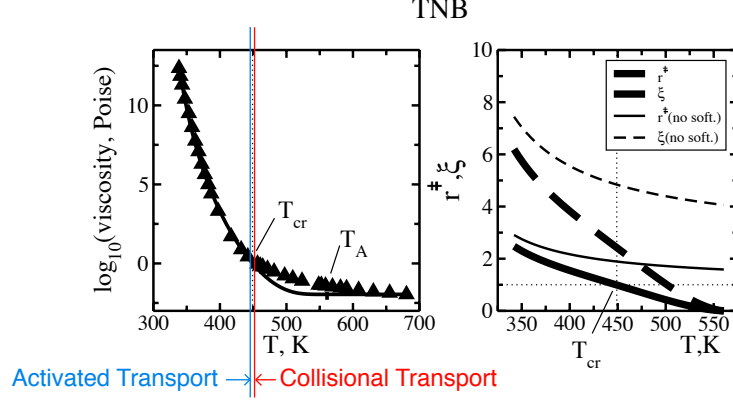


FIG. 35. The left panel shows experimentally-determined viscosity of an organic glass-former TNB (symbols) alongside the theoretical prediction of an RFOT-based treatment that includes the barrier-softening effects [35] (thin line), Eq. (202). The temperature at which the landscape-based prediction of the RFOT theory and the experimental data diverge corresponds to the crossover between activated and collisional transport, above which mode-coupling effects dominate. The right panel compares RFOT-based predictions of the critical radius  $r^\ddagger$  and cooperativity length  $\xi$  with and without the barrier softening effects. Note the crossover happens to coincide with the temperature at which the critical radius for structural reconfigurations is numerically close to the molecular length scale,  $r^\ddagger \approx a$ .

barrier height  $f^\ddagger$  in Fig. 13(a) and thus must vanish at  $T_A$ . (The power is  $1/2$  in the standard thin interface limit.) This is because for a transition between two aperiodic structures to take place, the regions of small  $\alpha$ , such that  $\alpha < \alpha^\ddagger$ , are not visited. We have seen this directly in Subsection V C. The vanishing of the mismatch penalty and, hence, of the activation barrier, at  $T = T_A$ , is in contrast with the simple prediction from Eq. (154), which ignores the effects of fluctuations by assuming that the aperiodic minima are always separated by a finite barrier.

To quantitatively assess the barrier softening effects in actual liquids, LW [35] utilised a simple  $F(\alpha)$  curve that can be parametrised so that  $f^\ddagger(T = T_A) = 0$ , while, at the same time,  $\Delta f(T = T_K) = 0$ , to reflect the vanishing of the configurational entropy at the (putative) Kauzmann temperature  $T_K$ . Note such parametrisation is reasonable, in light of the data in Fig. 13(b): In this Figure, we display results of Rabochiy and Lubchenko's study [37] of the free energy of a Lennard-Jones liquid as a function of temperature, pressure, and coordination. The latter can be controlled, within certain limits, by varying the coefficient  $\eta_{\text{RCP}}$  in the  $g(R)$  ansatz from Eq. (81). One observes that given a fixed value of the barrier  $f^\ddagger$ , the *shape* of the free energy curve  $F(\alpha)$  is nearly universal, not too far from the spinodal. This is an instance of a law of corresponding states.

Alongside the softening of the interface tension, one also expects that there will be a reduction in interface renormalisation, for the following reason: As the reconfiguration barrier becomes vanishingly small, so does the critical nucleus. The latter, however, cannot be smaller than the molecular size  $a$ . Since in the renormalisation scenario, Subsection V B, the width of the interface is tied to the droplet size, by Eq. (150), a renormalisation-like scenario becomes internally inconsistent. LW the proceed to write down a simple expression that interpolates in the simplest way between a fully wetted interface at large  $r$  and non-wetted interface in the  $r \rightarrow 0$  limit, without introducing an extra adjustable parameter:

$$F(r) = \frac{\Sigma_K \Sigma_A}{\Sigma_K + \Sigma_A} - \frac{4\pi}{3} (r/a)^3 T s_c, \quad (202)$$

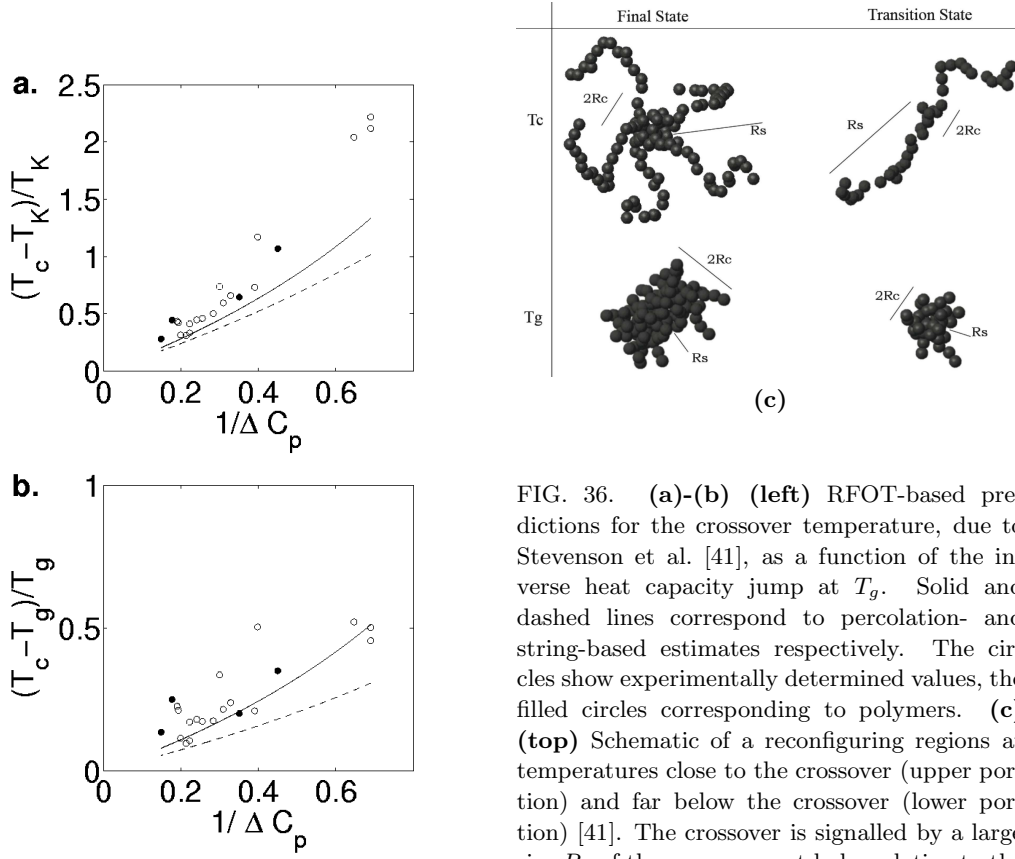


FIG. 36. (a)-(b) (left) RFOT-based predictions for the crossover temperature, due to Stevenson et al. [41], as a function of the inverse heat capacity jump at  $T_g$ . Solid and dashed lines correspond to percolation- and string-based estimates respectively. The circles show experimentally determined values, the filled circles corresponding to polymers. (c) (top) Schematic of a reconfiguring regions at temperatures close to the crossover (upper portion) and far below the crossover (lower portion) [41]. The crossover is signalled by a large size  $R_s$  of the non-compact halo, relative to the size  $R_c$  of the compact core.

where  $\Sigma_K = 4\pi\sigma_0 a^2 (r/a)^{3/2}$  and  $\Sigma_A = 4\pi f^\ddagger a^3 (r/a)^2$  are the wetted and non-wetted mismatch penalties respectively. Experimentally determined  $T$ -dependences of relaxation time data can now be fitted to the barrier predicted by Eq. (202), using only the quantity  $T_A$  and  $\Delta c_p(T_g)$  from Eq. (95) as adjustable parameters. The latter parameter can be used to estimate the bead count which, then, can be independently checked against chemical intuition. ( $T_K$  can be taken from calorimetry while the prefactor  $\tau_0$  can be fixed at a nearly universal value of 1 ps, which may introduce some numerical uncertainty but removes an even greater source of uncertainty due to underconstraint in the fit.) Using only a few low-temperature experimental points produces excellent fits in *extended* temperature ranges, at viscosities above 10 Ps or so, see Fig. 35. Interestingly, at the very same value of the viscosity, the critical radius happens to numerically coincide with the molecular size  $a$ .

The just mentioned value of the viscosity at which the RFOT-predicted relaxation time (now including the softening effects) diverges from experiment signifies the temperature at which collisional effects become important. This temperature thus falls within the temperature range of the crossover. An important message of the work in Ref. [35] is that the fluctuation effects due to the spinodal are most significant in fragile substances, in which the mean-field temperature  $T_A$  and its finite-dimensional analog  $T_{cr}$  and the Kauzmann temperature are numerically close. Thus in fragile substances, the softening corrections likely modify the barrier value predicted by Eq. (154). Conversely, in strong substances, the simple expression for the barrier from Eq. (154) should be adequate in a very broad temperature range.

In a more microscopic vein, Stevenson, Schmalian, and Wolynes [41] have addressed the issue of how one must modify the nucleation scenario from Section V near the crossover

to the mode-coupling-dominated transport. These authors argued that viewing a cooperatively reconfiguring region as a compact object is too simplistic close to  $T_A$ . Indeed, we have already mentioned that the closer to  $T_A$  the smaller the extent of the reconfiguration. In other words, moving *individual* particles becomes less and less costly. Under these circumstances, the penalty for having non-compact shapes is outweighed by the diversity of all possible non-compact shapes even as the compact core of the reconfiguring region may be still of appreciable size, see Fig. 36(c). The multiplicity of all percolated, non-compact shapes is determined by the connectivity of the lattice and does not involve adjustable parameters. One then replaces the mismatch penalty in Eq. (128) with two terms: one is the free energy cost of moving  $N$  particles within a non-compact shape, the other the entropic gain due to the multiplicity of all possible shapes. The cost is computed analogously to how we estimated the molecular surface tension  $\sigma_0$  in Subsection V B, except for a general number of broken contacts. In the XW approximation [31], Eq. (168), this cost is entirely entropic and scales linearly with temperature. In the large  $N$  limit, the free energy cost of moving  $N$  particles within a non-compact shape turns out to scale *linearly* with  $N$ , and so does the overall free energy profile as a result:

$$F(N) = (Ts^{\text{perc}} - Ts_c)N, \quad (203)$$

where the quantity  $s^{\text{perc}} \simeq 1.28k_B$  per particle, gives the full free energy cost of excitations that percolate into a non-compact cluster, divided by temperature. In the absence of structural degeneracy, the cost of moving beads always outweighs the entropic gain due to the multiplicity of the non-compact structures, consistent with individual structures being mechanically (meta)stable.

The linear scaling of the free energy profile in Eq. (203) means the reconfiguration is either exclusively uphill or downhill. If the configurational entropy exceeds a threshold value  $s_c = s^{\text{perc}}$  (which, note, is system-independent) the reconfiguration is exclusively downhill, implying the activation barrier is strictly zero. This, in turn, signals the crossover, thus allowing one to combine system-specific values of  $T_K$  and  $\Delta c_p$  with the universal  $s_c \simeq 1.28k_B$  to estimate the crossover temperature, by Eq. (95); the resulting prediction for  $T_{\text{cr}}$  are shown with the solid line in Fig. 36(a) and (b). (For lower temperatures, non-compactness is still allowed but can be thought of as a perturbation to the relatively simple scenario that led to Eq. (128).)

An instructive variation on the preceding argument is to think of the various non-compact, percolated shapes as a small, compact core dressed by string-like objects. This view is instructive since it emphasises that to create a non-compact shape one must consider contiguous chains (or “strings”) of particle movements that originate at the compact core but end *before* they return to the core. The diversity of all such strings can *also* be estimated without adjustable parameters and gives a similar, system-independent estimate for the threshold value of the configurational entropy:  $s_c \simeq 1.13k_B$ . Thus the “percolation” and “string” views are mutually consistent. The string-based estimates of  $T_{\text{cr}}$  are shown with the dashed line in Fig. 36(a)-(b). One valuable aspect of the string approach is that it allows one to make connections between the RFOT theory and simulations, which show string-like excitations as the viscous slowing-down sets in [240]. The presence of quasi-one dimensional, string-like excitations is also consistent with our early, symmetry-based discussion of the liquid-to-solid transition in Subsection III A. There we observed how quasi-one dimensional modes emerge during incipient solidification driven by steric effects, see Eq. (28).

The above notion of the universality of the magnitude of the configurational entropy at the crossover predicted by Stevenson et al. [41] was soon afterwards utilised by Hall and Wolynes [241], who used the density functional theory to predict the crossover temperature for Lennard-Jones liquids, in addition to the meanfield temperature  $T_A$  and the putative Kauzmann temperature. In particular, these quantities have been computed as functions of



pressure and show good agreement with experiment.

We now return to the law of corresponding states illustrated in Fig. 13(b). Rabochiy and Lubchenko [37] used this notion to argue that the crossover should take place at a universal value of the farrier  $f^\ddagger$ . Indeed, activated reconfigurations become essentially one-particle events at the crossover, as we discussed earlier in this Section, implying fluctuations in the order parameter  $\alpha$  at different spots become mutually uncorrelated. Thus the local value of the bulk density  $f(\alpha)$ —corresponding to the free energy  $F(\alpha)$ —fully characterises the stability of a local region, regardless of its environment. In other words, the sample can be thought of as a collection of uncorrelated, anharmonic degrees of freedom subject to a (free) energy function  $f(\alpha)$ . Each such degree of freedom—and, hence, the aperiodic structures themselves—become marginally stable when at the typical thermal displacement away from the minimum,  $\alpha$  is at its saddle point value  $\alpha^\ddagger$ . In other words,  $\langle(\alpha - \alpha_0)^2\rangle^{1/2} = (\alpha_0 - \alpha^\ddagger)$ , times a factor of order 1. Combined with the near universality of the shape of  $f(\alpha)$ , this implies that the crossover is signalled by a system-independent value of  $f^\ddagger$ . This criterion can be made more practical by noticing [37] that the (computed)  $f^\ddagger = \text{const}$  lines in the  $(p, T)$  plane nearly coincide with the (computed) lines  $L = \text{const}$ , where  $L$  is the Lindemann ratio from Eq. (80), where the lattice is now aperiodic. This is illustrated in Fig. 37(a). We thus arrive, semi-phenomenologically, at a criterion that the crossover corresponds to a universal value of the ratio of the vibrational displacement to particle spacing, irrespective of pressure or temperature. This is in harmony with the systematic version of the Lindemann criterion of melting [65], under which the vibrational displacement at the solid-liquid interface is a universal quotient of the particle spacing, when the solid and liquid are in equilibrium. The crossover *also* corresponds to an equilibrium between liquid and solid, except the latter solid is now aperiodic. RL [37] took this notion further to determine the actual value of  $L$  that signals the crossover. These authors have evaluated the values of the Lindemann ratio  $L$  at the phase boundary for the liquid and the *periodic* crystal as a function of pressure (or  $T$ ), the totality of which form a line in the  $(L, p, T)$  space; this line is shown as the thick solid line in Fig. 37(a). The  $L(p, T)$  plane for the Lindemann ratio in the aperiodic crystal mostly lies above the line  $L(p, T)$  for the periodic crystal, but turns out to intersect it near the triple point. Note the value of  $L$  at the triple point is unique for each substance. On the other hand, the Lindemann ratio at the crossover is nearly unique, as just discussed. Based on these two notions and the fact that the  $(L, p, T)$  plane crosses the  $L(p, T)$  line near the triple point, RL surmised that the Lindemann ratio at the crossover  $L_{\text{cr}}$  should be equal to its value at the triple point. The classical DFT, in the modified weighted density approximation (MWDA), yields the value of 0.12 for  $L_{\text{cr}}$  [37]. The actual value of the Lindemann ratio near the triple point of the Lennard-Jones system is

$$L_{\text{cr}} = 0.145, \quad (204)$$

according to simulations [78]. This number will be of use in short order.

The above findings on the universality of the Lindemann displacement at the crossover can be used to make several testable predictions. Several of these predictions rationalise the pressure dependence of the fragility, depending on the degree of bonding directionality [37]. Here we limit ourselves to covering only two of these predictions.

As pressure is increased, any substance will behave more and more like that made of rigid particles, in the absence of a structural transformation that would increase the coordination in a discontinuous way. Under these circumstances, the external pressure becomes increasingly close to the kinetic pressure, which corresponds to the amount of momentum a particle transfers to its cage per unit time, per unit area:  $p \sim 2(mv_{\text{th}})(v_{\text{th}}/d_0)/a^2 \simeq 2(a/d_0)nk_B T \simeq 2k_B T/d_0 a^2$ , thus implying  $p \simeq 2\frac{k_B T}{a^2} \frac{1}{d_0}$ , where  $v_{\text{th}}$  is the average thermal speed and  $d_0$  is the confinement length of a particle in its cage. Since the confinement length is equal to  $d_L$  and, furthermore, is constant at the crossover, we obtain a simple estimate for pressure

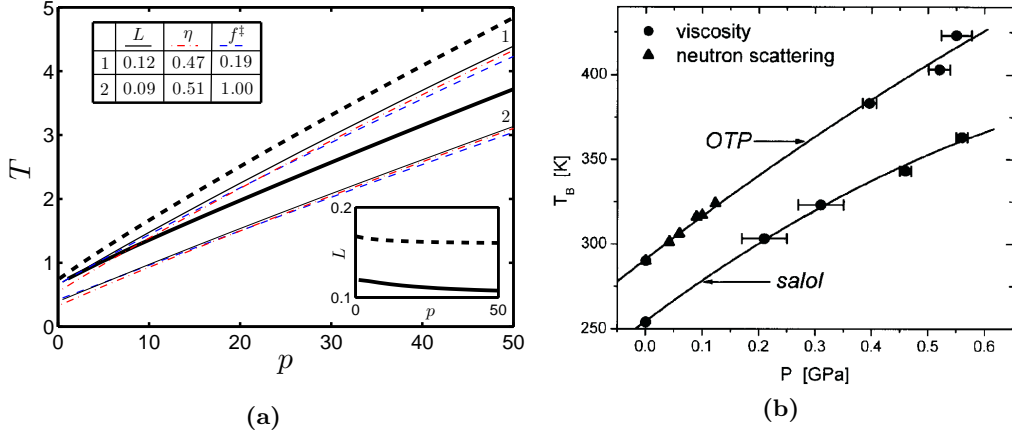


FIG. 37. (a) The pressure and temperature dependence of the barrier height  $f^\ddagger$ , Lindemann ratio  $L$ , and the filling fraction  $\eta$  shown as two sets of isolines of the corresponding surfaces. The thick dashed line shows the pressure dependence of the “spinodal” temperature  $T_A$ ; it is an isoline for  $f^\ddagger$  but not for  $L$  and  $\eta$ . The thick solid line is the liquid-crystal coexistence line; its l.h.s. end is the triple point. The inset shows the pressure dependence of the Lindemann ratio along the “spinodal” and liquid-crystal coexistence lines.  $\eta_{\text{RCP}} = 0.64$ . From Ref. [37]. (b) Pressure dependence of the dynamic crossover temperature, after Casalini and Roland [242], to be compared with the thin solid line 1 in panel (a). Note that the solid lines are a guide to the eye and are not theoretical predictions. In any event, the slope of  $\sim 100\text{K}/1\text{GPa}$  is consistent with the RFOT theory, see text.

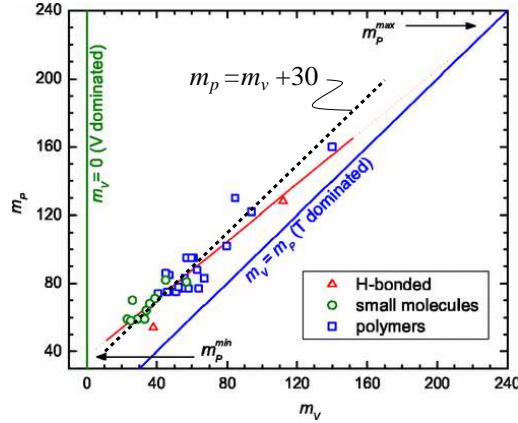


FIG. 38. Experiment (symbols): Fragility indexes at constant pressure and volume for several substances, after Casalini and Roland.[243]. Theory (black dashed line): Prediction from Eq. (207) [37].

dependence of the crossover temperature:

$$k_B T_{\text{cr}} \simeq (d_L/a)(a^3)p, \quad (205)$$

up to an additive correction that reflect the softness of the local molecular field acting on the individual particle [37, 170]. A quick estimate using a typical  $a = 3 \text{ \AA}$  and  $d_L/a = 1/10$  yields that per each extra half-GPa in pressure, the critical temperature will rise by 100 degrees or so. This is clearly consistent with the experimental data in Fig. 37(b).

Consider now a simple identity:  $(\partial s_c / \partial \ln T)_p = (\partial s_c / \partial \ln T)_V + (\partial s_c / \partial \ln V)_T (\partial \ln V / \partial \ln T)_p$ . Combining this with the RFOT-derived Eqs. (170) and (173), we obtain a simple relation between the fragility coefficient at constant pressure ( $m_p$ ) and volume ( $m_v$ ) [37]:

$$m_p \simeq m_v + 18T\alpha_t(\partial s_c / \partial \ln V)_T, \text{ at } T = T_g. \quad (206)$$

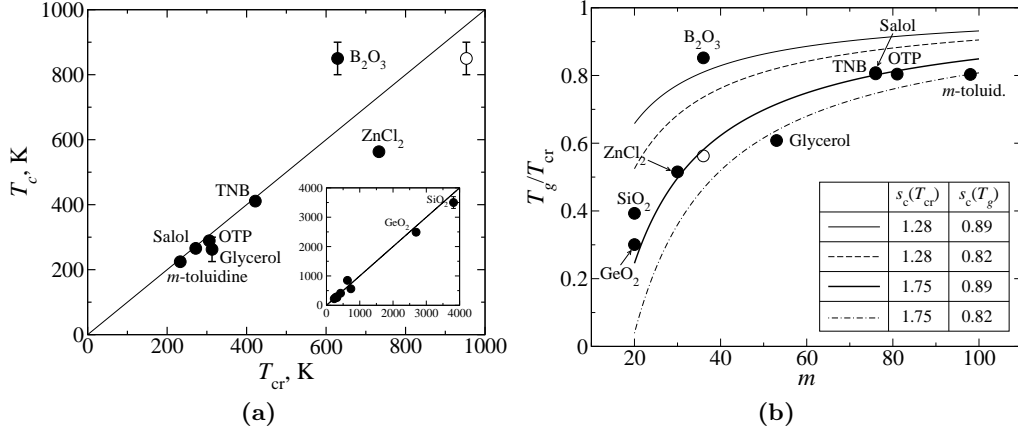


FIG. 39. (a) Predicted values of the crossover temperature  $T_{cr}$  plotted against experimentally determined dynamic crossover temperature  $T_c$ . (b). Same values, in the form of the  $T_g/T_{cr}$  ratio, plotted against the experimentally determined fragility coefficient  $m$ . ( $T_g$  is also experimentally determined.) Both panels are from Ref. [42].

A dimensionless measure of the thermal expansivity  $T\alpha_T \equiv (\partial \ln V / \partial \ln T)$  is an important quantity that determines the pressure dependence of the fragility [37]. It is also an interesting quantity in that it varies remarkably little, 0.16 ... 0.19, between many substances, see Fig. (12) of Ref. [37], which is often called the Boyer-Bondi rule [243, 244]. Note that the thermal expansivity  $\alpha_t$  is entirely determined by the anharmonic response of the lattice.

Using a generic value  $T\alpha_t = 0.17$  and the RL's prediction that for the Lennard-Jones liquid,  $(\partial s_c / \partial \ln V) \approx 10k_B$  (Fig. 10 of Ref. [37]), we obtain a simple relation:

$$m_p \simeq m_V + 30, \quad (207)$$

This prediction matches well the data of Casalini and Roland [243], see Fig. 38.

The above prediction concerning the universality of the Lindemann ratio  $L$  near the crossover has been recently utilised by Rabochiy and Lubchenko [42] to develop a simple way to estimate the crossover temperature based on the elastic properties of the substance. According to their formula in Eq. (30), there is an intrinsic relationship between the elastic constants, temperature, and the typical vibrational displacement in a harmonic solid. Further, the lattice spacing in a random-close packing is approximately given by  $r_{nn} \approx 1.14/\rho^{1/3}$ . Combined with Eqs. (30), (80), and (204), this yields  $\frac{\mu}{\rho k_B T_{cr}} \frac{3K+4\mu}{6K+11\mu} \simeq 5.8$ . After expressing the elastic constants in terms of speeds of longitudinal ( $v_L$ ) and transverse ( $v_T$ ) sounds, one obtains a simple, testable relation:

$$\frac{M}{N_b k_B T_{cr}} \frac{v_T^2 v_L^2}{2v_L^2 + v_T^2} = 5.8 \quad (208)$$

where  $N_b$  is the bead count from Eq. (96). Note the ratio made of the speeds of sound can be written out as  $(2/v_L^2 + 1/v_T^2)$ , which reflects the contributions of the two transverse and one longitudinal phonon branches to the phonon sums. As in Eq. (180), we assume the isothermal and adiabatic sound speeds are numerically close.

Eq. (208) allows one to predict the crossover temperature for actual substances, if data on the temperature dependent speeds of sound are available. RL made such predictions for several specific substances; the results of the calculation are shown in Fig. 39(a) alongside the experimentally determined values of  $T_{cr}$ . As already mentioned, Lubchenko and Wolynes had predicted that the crossover temperature should be relatively close to the glass transition temperature for fragile substances and vice versa for strong substances. Fig. 39(b) directly

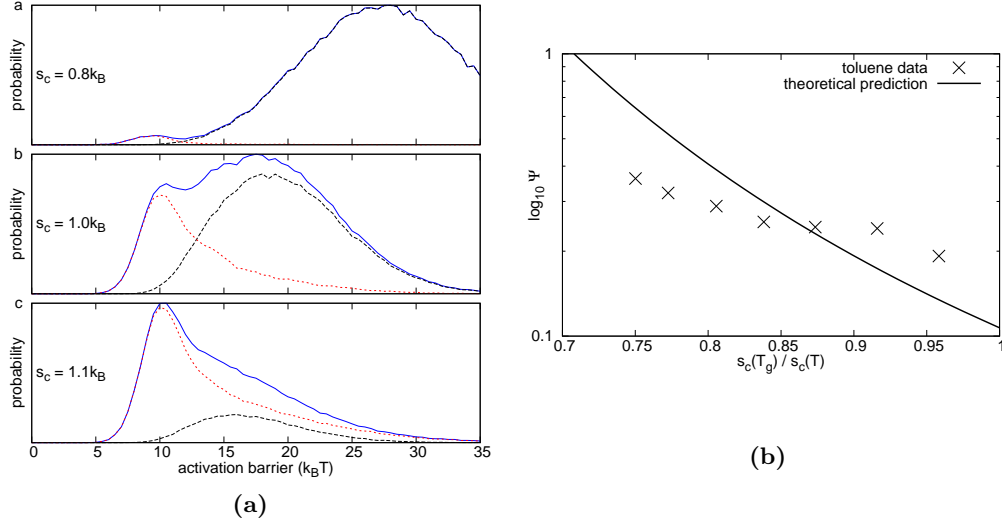


FIG. 40. **(a)** The apparent barrier distribution for the structural relaxations in the landscape regime, where the contribution of the non-compact, string-like excitations on top of the compact nucleation events shows up as a relatively distinct, low-barrier subset of motions. As the temperature is decreased (bottom to top), the stringy subset separates in time from the compact excitations and becomes less important. This is illustrated in panel **(b)**, where the partial contribution of the stringy modes to the overall excitation spectrum is plotted as a function of temperature [44]. The experimental data (symbols) are from Ref. [245].

demonstrates this notion. The ratio  $T_g/T_{cr}$  ( $T_g$  measured,  $T_{cr}$  computed) is shown as a function of experimentally determined fragility coefficient  $m$ . The RFOT theory predicts [41, 42]:

$$\frac{T_g}{T_{cr}} = 1 - \frac{1}{m} \left( \frac{s_c(T_{cr})}{s_c(T_g)} - 1 \right) \frac{32k_B}{\ln(10) s_c(T_g)}. \quad (209)$$

This result is shown by smooth lines in Fig. 39(b). The computed values of  $T_{cr}$  are clearly consistent with observation. Note that predicted values of  $T_{cr}$  are consistently *above*  $T_g$ . This is reassuring as there is little *a priori* reason for a combination of elastic constants and the bead count—neither of which directly have to do with the RFOT or glass transition—to produce a temperature that is consistently above  $T_g$ . This robustness is consistent with the robustness of the Lindemann criterion of melting in crystalline materials [105].

The notion of the crossover as a regime in which the entropic and enthalpic contributions to the free energy balance out, seems to be consistent with findings of Biroli, Karmakar, and Procaccia [224] on the apparent coincidence between the point-to-set length and (a fixed multiple of) the spatial extent of marginally stable vibrational modes, in a finite temperature range, see Fig. 31(b).

We have seen that compact reconfigurations become increasingly “dressed” with string-like excitations [41], upon approaching the crossover from below. This microscopic picture may shed some light on the poorly-understood beta-relaxations, see Fig. 3. Similarly to the way local fluctuations in the configurational-entropy content result in a distribution of the local escape barrier from long-lived configurations, the very same fluctuations will also affect the ease at which the stringy motions can be excited. Indeed, the free energy cost of such motions is directly connected with the local multiplicity of possible particle arrangements. Stevenson and Wolynes [44] (SW) have studied effects of local fluctuations of the landscape degeneracy on the ease of string generation. Clearly, such strings will be more abundant in regions characterised by relatively large values of  $s_c$ , even though the compact core for

the reconfiguration would be smaller than average, by Eq. (154). SW have established that the most facile subset of the string excitations engender the appearance of an additional subset of structural relaxations on the low barrier side of the distribution of the  $\alpha$ -relaxation barriers, see Fig. 40(a). The latter figure demonstrates how the low-cost stringy motions dominate the structural relaxation at high temperatures near the crossover but become increasingly subdominant to the nucleation events proper deeper in the landscape regime. This can also be seen in Fig. 40(b), where the contribution of the low-cost stringy excitations to the overall relaxation is plotted as a function of temperature. The latter predictions are in qualitative agreement with observation. The just described relaxation mechanism overlaps, frequency-wise, with and thus amounts to a universal contribution to the set of excitations discussed under the umbrella of beta-relaxations. It is likely that other, system-specific contributions to the latter relaxations are present.

In concluding this Section, we reiterate the most important qualitative features of the crossover, which is the finite-dimensional realisation of the random first order transition. The crossover can be thought of in two related ways: If approached from above, it is signalled by an increase in collision-driven mode-coupling effects. In the mean-field limit, this increase would lead to a complete kinetic arrest inside a particular free energy minimum, at a temperature  $T_A$ . The latter temperature is above the temperature  $T_K$ , thus implying the liquid is completely frozen even as its configurational entropy is perfectly finite. This seeming paradox is however resolved in finite dimensions, whereby the liquid is allowed to reconfigure by activation. What would be a sharp transition in the mean-field limit, at the temperature  $T_A$ , now becomes a soft crossover centred at a temperature  $T_{cr} < T_A$ . If approached from *below*, the crossover is signalled by a rapid increase in the rate of structural reconfiguration, which is made even more precipitous by the barrier-softening effects stemming from the fluctuations of the order parameter  $\alpha$ . The latter quantity can be thought of as a local “stiffness,” by Eq. (30). As the barrier vanishes, the viscous response of the liquid is now dominated by the collisional effects. Importantly, the vanishing of the curvature of the metastable, aperiodic minimum in  $F(\alpha)$  at  $\alpha_0$ , Fig. 13(a), does not lead to a diverging length scale as it would do during ordinary transitions between phases that are each characterised by a single free energy minimum. The fluctuations in the order parameter  $\alpha$  play a triple role here: First, they lower the transition temperature from its mean-field value  $T_A$  to a lower value  $T_{cr}$ . Second, they also lower the barrier for the activated reconfigurations. The latter then destroy the long-range correlations that seem to be called for, at least superficially, by the vanishing of  $F''(\alpha_0)$  at  $T_A$ . Third, because the activated events are low-barrier and ultra-local near what would be a sharp “spinodal” at  $T_A$  in meanfield, the latter spinodal becomes a gradual crossover in finite dimensions. Alternatively said, high-frequency modes freeze first, followed by the progressively slower modes as temperature is lowered. Consistent with our earlier conclusions that a continuous liquid-to-solid transition would be lowered by quasi-one-dimensional motions, string-like excitations are predicted and appear to be observed in simulation near the crossover.

## VIII. RELAXATIONS FAR FROM EQUILIBRIUM: GLASS AGEING AND RE-JUVENATION

The emergence of the transient structures and, hence, activated transport—as a prelude to the actual glass transition—seems intuitive. Indeed, once exponentially many distinct minima have formed, it is easy to imagine how the minima become progressively deeper with lowering the temperature, since the enthalpy must decrease with cooling. The glass transition then simply signifies a situation in which the minima become so deep that the structure fails to rearrange on the experimental timescale.

Yet, how do we know that transport involves activated events? This is not entirely self-evident in view of the strongly non-Arrhenius behaviour of the relaxation times in glassy liquids. Given these difficulties, can one name a *direct* experimental signature that the transport is an activated process? Such a direct signature is actually provided by the relaxation in glasses themselves *below* the glass transition. This relaxation, called “ageing,” is an attempt for the glass to reach the structure that would be representative of the liquid equilibrated at the ambient temperature. To analyse ageing, the approach we took in Subsection V must be modified to account for the initial structure being different from an equilibrium one.

### A. Ageing

It is most straightforward to describe ageing using the free energy formulation of the activated transport from Eq. (128). Consider an experiment in which an equilibrated liquid is rapidly cooled or heated from temperature  $T_1$  to temperature  $T_2$ , where both  $T_1$  and  $T_2$  are below the crossover temperature  $T_{\text{cr}}$ . Below, we limit ourselves to temperature jumps that are faster than any irreversible structural changes, but slower than the vibrational relaxation. Let's call state 1 the configuration, in which the vibrational degrees of freedom have already equilibrated at temperature  $T_2$ , but where the other, anharmonic structural degrees of freedom have not equilibrated. State 2 is the state *following* a reconfiguration event whereby all degrees of freedom have equilibrated at temperature  $T_2$ . For simplicity, let us pretend for now that structural reconfigurations are not accompanied by any volume change, to be discussed later.

As during relaxation near equilibrium, the reconfiguration is subject to the mismatch penalty, according to Lubchenko and Wolynes [40]:

$$F(N) = \gamma N^{1/2} + \Delta g(T_1, T_2)N, \quad (210)$$

where the driving force  $\Delta g(T_1, T_2) < 0$  for escape from state 1 to state 2,

$$\Delta g(T_1, T_2) \equiv \Delta g(T_1 \rightarrow T_2), \quad (211)$$

is given by the bulk free energy difference between the final and initial state of the region. The reconfiguration barrier is given by

$$F^\ddagger(T_1, T_2) = \frac{\gamma^2}{4[-\Delta g(T_1, T_2)]} \quad (212)$$

State 2 could be *any* structure representative of the liquid at the ambient temperature, i.e.,  $T_2$ . Thus the free energy  $\overline{G}^{(2)}$  of the final state is equal to free energy of the liquid equilibrated at  $T_2$ :

$$\overline{G}^{(2)} = \overline{G}(T_2) = \overline{G}_i(T_2) - T_2 S_c(T_2), \quad (213)$$

c.f. Eq. (115). The (average) free energy of an individual state,

$$\overline{G}_i(T_2) = \overline{H}_i(T_2) - T_2 \overline{S}_{\text{vibr}, i}(T_2), \quad (214)$$

accounts for the vibrational entropy of that state, as before.

If the temperatures  $T_1$  and  $T_2$  were equal, state 1 would correspond to an *individual* free energy minimum at temperature  $T = T_1 = T_2$ . Instead, the structure of state 1 only *approximately* corresponds to an individual minimum that would be representative of a liquid equilibrated at  $T_1$ , since the vibrations have already equilibrated at temperature  $T_2$ .

The vibrations at  $T_1$  and  $T_2$  are of different magnitude, if  $T_1 \neq T_2$ , and so some shift in the average position of the particles is expected upon vibrational relaxation, owing to the anharmonicity of the lattice. Still, the structure in state 1 is completely isomorphic to the structure at  $T_1$ . We will thus assume approximately that the configuration—and hence the enthalpy—of state 1 are the same as in equilibrium at temperature  $T_1$ . On the other hand, the vibrational entropy in state 1 is approximately equal to the equilibrium vibrational entropy at temperature  $T_2$ :

$$\overline{G}^{(1)} \approx \overline{H}_i(T_1) - T_2 \overline{S}_{\text{vibr},i}(T_2). \quad (215)$$

Thus the bulk driving force  $\Delta g$  for reconfiguration, per particle, is given by [40]:

$$\Delta g(T_1, T_2) = \overline{g}^{(2)} - \overline{g}^{(1)} \approx \overline{h}(T_2) - \overline{h}(T_1) - T_2 s_c(T_2). \quad (216)$$

Using Eq. (95), one obtains an explicit expression for the driving force:

$$-\Delta g(T_1, T_2) = \Delta c_p(T_g) T_g \left[ \left( \frac{T_2}{T_K} - 1 \right) - \ln \left( \frac{T_2}{T_1} \right) \right]. \quad (217)$$

We now specifically focus on downward temperature quenches,  $T_2 < T_1$ . Given the postulated quickness of the quench, we must identify  $T_1$  as the glass transition temperature:  $T_1 = T_g$ , while  $T_2$  is the ambient temperature  $T$ . Under these circumstances,  $\overline{h}(T) - \overline{h}(T_g) = \int_{T_g}^T \Delta c_p dT < 0$ . Thus, the driving force for the escape from the structure quenched at  $T_g$ , at the still lower temperature  $T < T_g$ , exceeds the driving force for reconfigurations in a liquid equilibrated at the ambient temperature  $T$ :

$$-\Delta g(T_g, T) > -\Delta g(T, T), \text{ if } T < T_g. \quad (218)$$

It is easy to see that the activation barrier for ageing is only weakly temperature dependent [40]. Indeed, at  $T = T_g$ ,  $\Delta g = -\Delta c_p(T_g)(T_g/T_K - 1)$ . The most stable aperiodic structure corresponds to the putative ideal-glass state that would be equilibrium at the Kauzmann temperature  $T_K$ , where  $s_c = 0$ . Hereby, the driving force is  $\Delta g = \overline{h}(T_K) - \overline{h}(T_g) = -\Delta c_p(T_g) \ln(T_g/T_K)$ . To decide on the temperature dependence of the mismatch penalty, if any, we revisit to Eq. (142), in which the energy prefactor  $h$  now consists of the contribution from the free energy fluctuations on the inside,  $\delta G_i(T_2)$ , and that on the outside  $\delta[H_i(T_1) - T_2 S_{\text{vibr}}(T_2)]$ . According to Eq. (158),  $\gamma \propto [K(T_1 + T_2)/\rho]^{1/2}$ , considering that the bulk modulus and density barely change with temperature in the frozen glass. Thus the reconfiguration barrier goes as  $(2T_g)^2/(T_g/T_K - 1)$  and  $(T_g + T_K)^2/\ln(T_g/T_K)$  at  $T_g$  and  $T_K$  respectively. The two quantities differ by at most 25%, since empirically, the ratio  $T_g/T_K$  is numerically at most 2 (for very strong substances), but is usually considerably less than 2.

Because the activation barrier is only weakly temperature dependent below  $T_g$ , the apparent activation energy (not the free energy!)

$$E_{\text{act}} = \frac{\partial(F^\ddagger/k_B T)}{\partial(1/T)}, \quad (219)$$

which is generally not equal to  $F^\ddagger$ , is predicted to exhibit a discontinuous *jump* following a rapid quench, c.f. Fig. 3. (The activation *free* energy is continuous through the glass transition.) A convenient framework for quantitative discussion of this jump is provided by the Narayanaswamy-Moynihan-Tool formalism [246–248], in which the relaxation rate in quenched glasses is phenomenologically decomposed into a purely activated part and a temperature-independent part reflecting a *fictive* temperature  $T_f$ :

$$k_{\text{n.e.}} = k_0 \exp \left\{ -x_{\text{NMT}} \frac{E_{\text{act, eq}}}{k_B T} - (1 - x_{\text{NMT}}) \frac{E_{\text{act, eq}}}{k_B T_f} \right\}, \quad (220)$$

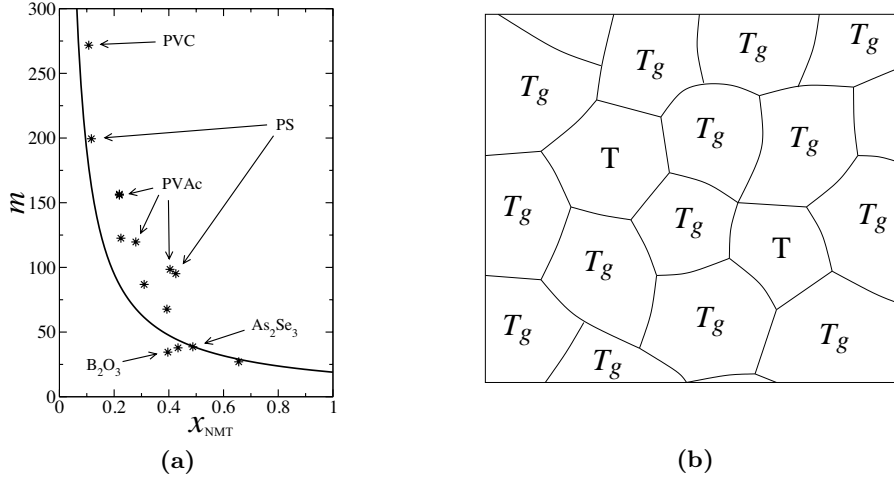


FIG. 41. **(a)** Smooth line: The RFOT-predicted, simple relation between the NMT coefficient  $x$ , which reflects the discontinuity of the apparent activation rate (219) and the fragility. Symbols: Experimental data. Note experimental data show significant scatter even for the same substance. **(b)** After a considerable period of ageing well below  $T_g$  a patchwork of equilibrated and non-equilibrated mosaic cells will be found, leading to a distribution of fictive temperatures and emergence of ultra-slow relaxations. After Ref. [40]

Here  $E_{\text{act, eq}}$  is the apparent activation barrier from Eq. (219) in an equilibrated liquid, i.e., just above the glass transition:  $E_{\text{act, eq}} = E_{\text{act}}(T_g^+)$ . The fictive temperature  $T_f$  is an approximate concept. By construction, it is chosen so that the structure equilibrated at  $T_f$  would be as similar as possible to the *actual* structure. Above  $T_g$ ,  $T_f = T$ , of course. Below  $T_g$ , one often adopts  $T_f = T_g$  since the structure of the frozen glass is quite similar to that of the liquid at the glass transition, apart from some ageing and subtle changes stemming from differences in the vibrational amplitude, which is an anharmonic effect. For the NMT description to be internally-consistent, one must disregard the temperature dependence of the activation barrier below  $T_g$ , which we have seen is a good approximation. This implies  $F^\ddagger|_{T < T_g} \approx F^\ddagger(T_g, T_K)$  leading to  $\partial(F^\ddagger/k_B T)/\partial(1/T)|_{T < T_g} = F^\ddagger(T_g, T_K)$ , where  $F^\ddagger(T_1, T_2)$  is from Eq. (212). Finally, the quantity  $x_{\text{NMT}}$ ,  $0 < x_{\text{NMT}} < 1$ , is a dimensionless measure of the decrease in the apparent activation energy. Thus,  $x_{\text{NMT}} E_{\text{act, eq}} = F^\ddagger(T_g, T_K) \Rightarrow x_{\text{NMT}}^{-1} = E_{\text{act, eq}}/F^\ddagger(T_g, T_K)$ . Further using Eqs. (173), (212), and (217), this straightforwardly leads to the following estimate [40]:

$$x_{\text{NMT}}^{-1} = m \left\{ (\log_{10} e) \frac{F^\ddagger(T_g)}{k_B T_g} \left[ \frac{\gamma(T_K)}{\gamma(T_g)} \right]^2 \frac{(T_g/T_K - 1)}{\ln(T_g/T_K)} \right\}^{-1}, \quad (221)$$

where  $m$  stands for the fragility coefficient  $m$  from Eq. (173). The last ratio on the r.h.s. depends on the  $T_g/T_K$  ratio only weakly, as already remarked. Using a specific, generic value  $T_g/T_K = 1.3$  and ignoring the temperature dependence of the coefficient  $\gamma$ , one obtains a simpler yet relation between the fragility coefficient and the discontinuity of the apparent activation energy at the glass transition [40]:

$$m \simeq \frac{19}{x_{\text{NMT}}}. \quad (222)$$

This simple relation agrees well with experiment, see Fig. 41(a), thus supporting the RFOT-advanced microscopic picture on a very basic level.

We shall now discuss the effects of volume mismatch during ageing. The expression for the driving force in Eq. (216) corresponds to a process at constant pressure and thus is applicable



for relatively shallow quenches. For considerable  $T$ -jumps, however, the situation is more complicated since on the timescale of the nucleation event, the sample is a mechanically stable solid with a non-zero shear modulus. And so, insofar as the equilibrium thermal expansivity  $\alpha_{\text{eq}} \equiv (1/V)(\partial V/\partial T)_p$  exceeds the (largely vibrational) expansivity of a frozen glass  $\alpha_{\text{vibr}}$ , downward  $T$ -jumps will be accompanied by some stretching of the environment: A compact region of the material is essentially replaced by a region with a smaller volume, following an ageing event. The expansivity of an equilibrated liquid usually does significantly exceed that of the corresponding glass, see for instance Ref. [249]. Despite this circumstance, the effects of volume mismatch between the aged and unrelaxed glass do not significantly affect the ageing rate, as we discuss in detail in Appendix A.

After a considerable period of ageing well below  $T_g$ , a patchwork of equilibrated and non-equilibrated mosaic cells will develop [40], see Fig. 41(b). If the equilibrium energy at  $T$  is further than a standard deviation from the typical energy at  $T_g$ , the distribution of energies will be noticeably bimodal and the idea of a single fictive temperature will break down. The typical magnitude of temperature fluctuations is given by  $(k_B T^2/\Delta c_v N^*)^{1/2}$  [55]. Thus, significant deviations from a unimodal distribution of fictive temperatures are not expected if  $\Delta T = T_g - T < (k_B T^2/\Delta c_v N^*)^{1/2} \equiv \delta T^*$ . For  $T_g$  relevant to 1 hr. quenches this gives  $\delta T^*/T_g \simeq 0.07$ . Most of the Alegria et al. [250] data lie in this modest quenching range, while “hyperquenched” samples (with  $\Delta T \gg \delta T^*$ ) will often fall outside the allowed range of using a single fictive temperature. When a sample has a two-peaked distribution of local energies, the RFOT theory predicts an ultra-slow component of relaxation will arise. Notice that an equilibrated region at the temperature  $T = T_g - \delta T^*$  will relax on the tens to hundreds of hours scale, if  $\tau_g$  is taken to be one hour. (The relaxation barrier depends on temperature only weakly.)

## B. Rejuvenation

Let us now switch focus to upward temperature jumps,  $T_2 > T_1$ , which is a different type of ageing experiment. In this type of ageing, the structure locally escapes from being relatively deep in the free energy landscape to the region in the phase space where the free energy minima are relatively shallow, by Eqs. (170) and (159). Consistent with this notion, Eq. (217) prescribes that there is not as much driving force for structural relaxation when  $T_2 > T_1$  than in equilibrium at temperature  $T = T_1 = T_2$ :

$$-\Delta g(T_1, T_2) < -\Delta g(T_2, T_2), \text{ if } T_2 > T_1, \quad (223)$$

c.f. Eq. (218). For this reason, the process of glass *rejuvenation*—i.e., warming up and subsequent equilibration of a vitrified sample at the target temperature—is slower than the relaxation time in equilibrium at that same temperature. On the other hand, the relaxation barrier for a  $T_2 > T_1$  process is lower than the relaxation barrier in equilibrium at  $T_1$ , as follows from Eq. (217) (note  $T_1 > T_K$  of course):

$$-\Delta g(T_1, T_2) > -\Delta g(T_1, T_1), \text{ if } T_2 > T_1. \quad (224)$$

Thus the sample will undergo irreversible relaxation to configurations typical of equilibrium at temperature  $T_2$ , following the temperature jump. Furthermore, due to the relatively high mobility on the edge, to be discussed in Section X, the sample will not melt uniformly but will begin melting preferentially from the edge where it is being heated. Once a region is melted, a *mobility front* will propagate in the sample since the melted regions relax significantly faster than the those regions not reached by the front. It is convenient to

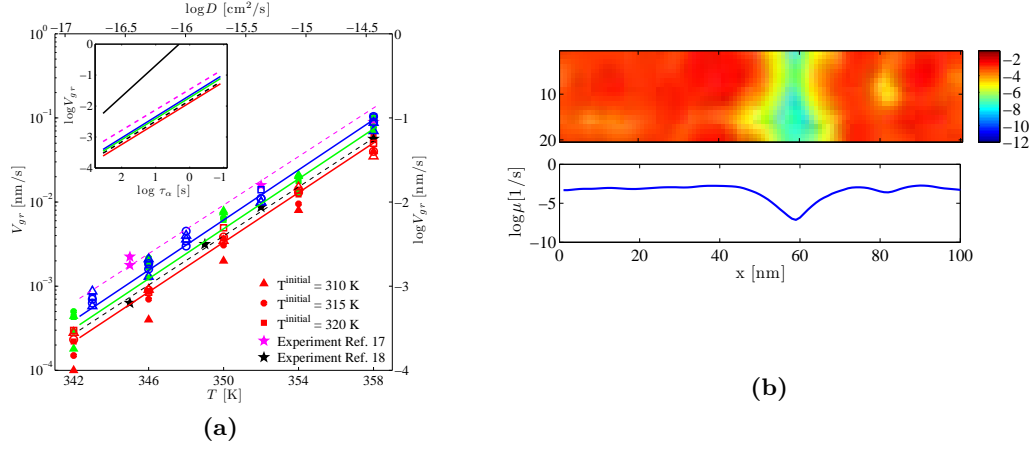


FIG. 42. **(a)** The speed of the mobility front from the dynamics of the 1D deterministic linearised (solid red markers), the 1D deterministic non-linear Eq. (226) (opened red markers), the 1D stochastic linearised (solid green markers), the 1D stochastic non-linear (opened green markers), the 2D stochastic linear (solid blue markers), and the 2D stochastic non-linear (opened blue markers) [49]. Different kinds of symbols indicate different initial fictive temperatures, the triangles are for  $T^{\text{initial}} = 310$  K, circles for  $T^{\text{initial}} = 315$  K, and squares for  $T^{\text{initial}} = 320$  K. The experimental measurements, as reported in Ref. [251], are shown as magenta stars and the black stars represent the more recent results from Ref. [252]. All lines are drawn as guides for the eye. Inset: The front speed versus relaxation time. The continuum approximation for the front speed  $(2/3)^{1/2} \xi \mu^{\text{high}}$  is drawn as the black solid line. **(b)** *Top*: Mobility field snapshot at  $t = 4.6 \times 10^4$  s. The upper plot shows the mobility field from 2D stochastic linearised theory. The colour scheme denotes the mobility on a log-scale with corresponding col-or bars on the right. *Bottom*: Average values of the mobility fields along the y-axis. [49]

define the mobility in direct relation to the fictive temperature  $T_f$ :

$$\bar{\mu}(T_F, T) = \mu_0 \exp \left\{ -\frac{x_{\text{NMT}} E^\ddagger}{k_B T} - \frac{(1 - x_{\text{NMT}}) E^\ddagger}{k_B T_F} \right\}, \quad (225)$$

c.f. Eq. (220). The mobility  $\mu$  (not to be confused with the shear modulus) is a quantity of units inverse time that describes the local relaxation rate for any quantity in question. The mobility can be converted into specific transport coefficients of interest, if desired. For instance, the diffusivity is equal to  $(d_L^2) \mu$ , c.f. Eq. (195). The parameter  $x_{\text{NMT}}$  can be computed using Eq. (221) or (222).

In estimating the speed of the mobility front, one must bear in mind that the earlier derived expressions for the activation barrier only apply to spatially homogeneous samples in the sense that the fictive temperature is spatially uniform. (To avoid confusion we reiterate that even if the fictive temperature is uniform, the dynamics are still heterogeneous in the sense of Section VI.) The actual mobility should smoothly interpolate between slow and fast regions, while the lengthscale of the variation is numerically close to the cooperativity size  $\xi$  from Eq. (126). A simple recipe to determine such a interpolating mobility field is to solve the differential equation  $\xi^2 \nabla^2 \mu = \mu - \bar{\mu}$  with appropriate boundary conditions [46]. Using  $\xi$  in front of the Laplace operator automatically supplies the correct length scale. (Note that since  $\xi$  depends on the mobility only logarithmically, using the typical value of  $\xi$  characteristic of the average mobility  $\bar{\mu}$  suffices.) This phenomenological equation suggests a simple way to go about constructing a hydrodynamic continuum description for the time/space evolution of the mobility field. Indeed, one may generally decompose the rate of change of local mobility into a conserved and non-conserved part:  $\dot{\mu} = -\nabla \cdot \mathbf{j} - \mu(\mu - \bar{\mu})$ . Thus in the absence of spatial heterogeneity,  $\mathbf{j} = 0$ , the mobility relaxes to its expectation

value  $\bar{\mu}$  with the local relaxation rate, which is equal to the mobility itself. Likewise, the flux  $\mathbf{j}$  can be connected to the magnitude of spatial variation in  $\mu$  via a Fick-like law:  $\mathbf{j} = -\xi^2 \mu \nabla \mu$ . Putting these notions together yields the following transport equation [49]:

$$\dot{\mu} = \nabla (\mu \xi^2 \nabla \mu) - \mu (\mu - \bar{\mu}) + \delta g + \nabla \delta \mathbf{j}, \quad (226)$$

where we have also included two terms corresponding to thermal noise,  $\nabla \delta \mathbf{j}$  and  $\delta g$ , for the conserved and non-conserved part of the mobility relaxation rate respectively. The magnitude of these random-noise terms can be fixed using the fluctuation-dissipation theorem [49]. The linearised version of the above equation is easy to write down:  $\dot{\mu} = \nabla (\bar{\mu} \xi^2 \nabla \mu) - \bar{\mu} (\mu - \bar{\mu}) + \delta g + \nabla \delta \mathbf{j}$ . Note either this or the original non-linear equation (226) automatically insure that the mobility varies on the length scale  $\xi$ . The simplest way to quantify the approach of the local fictive temperature to the ambient temperature is through the following, ultralocal relaxation law

$$\dot{T}_F = -\mu (T_F - T) + \delta \eta, \quad (227)$$

where  $\delta \eta$  is the corresponding noise-term. Note the fictive temperature is a structural variable that has no dynamics of its own other than through the mobility transport; thus there is no diffusive term on the r.h.s. of Eq. (227).

Aside from the mobility-dependent “diffusivity,” Eq. (226) is the celebrated Fisher-Kolmogorov-Petrovsky-Piscounov [253, 254] equation that can be used to study migration of organisms, as accompanied by death and procreation, and has also been used to model flame propagation. This equation (in 1D) also governs the generating function for the density distribution in the random directed-polymer problem; curiously, it exhibits a singularity intimately related to the glass transition in the random energy model [255].

In Fig. 42(a), we show the results of the solution of Eq. (226)—together with Eq. (227)—and its linearised version. The solutions in the presence and absence of the noise-terms, called “stochastic” and “deterministic” respectively, are illustrated. One observes good agreement of the predictions with the experimentally observed mobility front propagation. A snapshot of the linearised, stochastic simulation in 2D is provided in Fig. 42(b).

Note that a reasonable approximation for the speed of the mobility front can be obtained without actually solving the differential equations above, by using an analogy with flame fronts [48]. According to this approximation, shown by the black solid line in the inset of Fig. 42(a), the front speed is a fixed fraction of the mobility  $\mu^{\text{high}}$  in the sample equilibrated at the ambient temperature, viz.,  $(2/3)^{1/2} \xi \mu^{\text{high}}$ . While an overestimation, this simple result matches observation qualitatively.

## IX. RHEOLOGICAL AND MECHANICAL ANOMALIES

### A. Shear thinning

We have already seen that the microscopic picture advanced by the RFOT theory can be used to estimate on a microscopic basis the viscosity, which is the key quantity in the science of rheology. Next we shall see how the very same picture allows one to answer an interesting puzzle in the rheology of silicate melts. These melts exhibit pronounced deviations from the Newtonian liquid response, in the form of *shear thinning*, at shear rates that are, universally, about three orders of magnitude *lower* than the inverse relaxation time  $\langle \tau \rangle^{-1}$ . Shear thinning means the viscous response from from Eq. (197) is sublinear in the velocity gradient  $\partial v_i / \partial x_j$ , implying an apparent viscosity that decreases with  $\partial v_i / \partial x_j$ , see Fig. 43(a). Viscosity measurements can be imagined in a simple geometry in which two

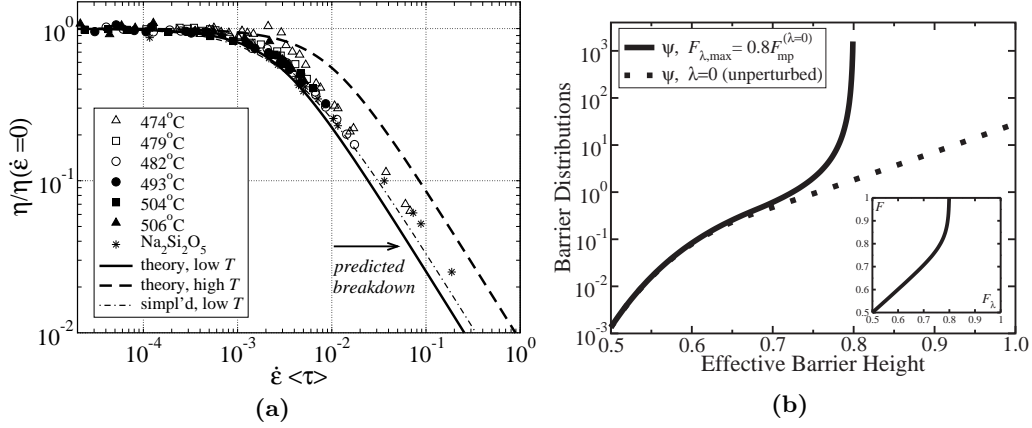


FIG. 43. **(a)** Normalised viscosity,  $\eta/\eta(\dot{\epsilon} = 0)$ , vs. normalised strain rate  $\dot{\epsilon} \langle \tau \rangle$ . *Experiment* [256]: Symbols, other than stars: data for  $\text{Na}_2\text{Si}_4\text{O}_9$  at different temperatures; stars:  $\text{Na}_2\text{Si}_2\text{O}_5$ . Viscosities were determined by fibre elongation. *Theory*: Curves: theoretical predictions from Ref. [45], the thin line corresponding to the approximate formula from Eq. (230). The bottom curve corresponds to the glass transition temperature, the top to the temperature  $T_c$  of the crossover between activated and collisional transport. No adjustable parameters have been used. **(b)** The solid line shows the effective distribution of barriers  $\psi_\lambda$ , in the presence of shear, the unperturbed distribution given by the dotted line. The unperturbed distribution is from Eq.(23) of Ref.[43], with parameters corresponding to a fragile ( $\beta \simeq 0.40$ ) substance near the glass transition on one-hour scale, so that the most probable barrier:  $F_{\text{mp}} = 37k_B T$ . The specific value of  $\lambda$  was chosen to illustrate clearly how the motions at rates that would be slower than  $\lambda$  in unperturbed fluid contribute to the high barrier peak in  $\psi_\lambda$ . These slow motions correspond to  $F > F_{\lambda, \text{max}}$  in the inset. The energy units are chosen so that  $F_{\text{mp}} = 1$ . From Ref. [45]

plates move relative to each other and so only one component of the tensor  $\partial v_i / \partial x_j$  is non-zero, say  $\partial v_y / \partial x$ , which we will denote as  $\dot{\epsilon}$ . The latter quantity is of dimensions inverse time, as is the mobility from Eq. (225), for instance. Thus, one would *a priori* expect that shear thinning, if any at all, would set in at a rate  $\dot{\epsilon}$  comparable to the inverse of the typical relaxation time, or, perhaps, typical relaxation rate. (Because silicates are strong liquids, there is not much difference between the two averages.) In contrast with this expectation, the deviation from the Newtonian response in Fig. 43(a) takes place at shear rates that are much lower, which is in the opposite direction from the decoupling of mobility-like quantities we discussed in Subsection VI B.

Lubchenko [45] has argued that the shear thinning is due to a facilitation-like effect we have encountered earlier when discussing the correlation between the stretching exponent  $\beta$  and the liquid's fragility  $D$ , in Subsection VI A. There, slower than the typical relaxations are facilitated because of nearby regions that happen to be faster than typical. Here, there is additional facilitation performed by the external shear itself. Denote the rate of the additional relaxation of a region's environment with  $\lambda$ . The survival probability for the region's relaxation is now given by  $p_\lambda(t) = \langle e^{-t/\tau} e^{-\lambda t} \rangle_{F, \lambda}$ . The resulting waiting time for the region's relaxation is then

$$\langle \tau_\lambda \rangle_{F, \lambda} = \int_0^\infty dt p_\lambda(t) = \langle \tau / (1 + \lambda \tau) \rangle_{F, \lambda} < \langle \tau \rangle_F, \quad (228)$$

leading to a lowered viscosity:

$$\frac{\eta}{\eta(\dot{\epsilon} = 0)} = \frac{\langle \tau_\lambda \rangle_{F, \lambda}}{\langle \tau \rangle_F} = \left\langle \frac{\tau}{1 + \lambda \tau} \right\rangle_{F, \lambda} \frac{1}{\langle \tau \rangle_F}. \quad (229)$$

The rate  $\lambda$  can be self-consistently determined [45] at a given value of experimentally imposed shear rate, by energy conservation: The energy flow through the domain boundary, due to the external shear, must match the rate of energy dissipation in the sample bulk, due to the shear. It turns out that both at relatively high and low shear rate,  $\lambda$  and  $\dot{\epsilon}$  are proportional to each other while the proportionality constant only differs by a factor of two between the two extremes. Thus a simple approximate expression for the relation between the quantities can be written down, which does not depend on the detailed barrier distribution:

$$\lambda \approx [1.5\sqrt{2}(a/d_L)(\xi/a)^{3/2}] \dot{\epsilon}. \quad (230)$$

This equation indicates that the facilitation rate  $\lambda$ , as sensed by an individual reconfiguring region, is significantly enhanced compared to the experimentally imposed rate  $\dot{\epsilon}$ . The enhancement is, in almost equal measure, is due to the smallness of individual displacements  $d_L$  from Eq. (127) and to the size of the cooperative region, which is about  $(\xi/a)^3 \simeq 10^2$  near  $T_g$ . The numerical factor in the square brackets in Eq. (230) is thus about  $10^3$  near  $T_g$ . Conversely, this enhancement implies that externally imposed shear at rate as low as  $10^{-3}\tau^{-1}$  will significantly increase the effective relaxation rate of a region.

The theoretical prediction for the shear thinning, corresponding to the simple form (230) and to a more accurate relation are shown in Fig. 43(a), alongside with experimental data [256]. The agreement between theory and experiment is very good; note that no adjustable parameters were used. The degree of shear thinning is predicted not to depend sensitively on the width of the barrier distribution.

The argument in Ref. [45] self-consistently predicts the magnitude of the shear rate at which the proposed picture breaks down. In this picture, the external shear does not significantly modify the mechanism of the relaxation itself but, instead, sets a non-zero lower limit on the relaxation rate  $\lambda$ . At the same time, this rate  $\lambda$  may not exceed the intrinsic rate at which the interface of an individual region relaxes, which can be estimated geometrically. One can think of a region roughly as being in the centre of a cube made of  $3 \times 3 \times 3 = 27$  cooperative regions. Thus the boundary of the region will relax, on average, once per time  $(\langle\tau\rangle/27)$  or so. If forced to relax at a higher rate, the boundary must relax via other means, such as bond breaking. This would occur at viscosities indicated by the horizontal arrow in Fig. 43(a). This estimate is quite consistent with the shear rate at which the glassy fibres broke, whose elongation was employed to measure the shear thinning.

Note that the shear-driven decrease in relaxation times, Eq. (228), implies lower effective barriers, by virtue of Eq.(132):

$$F_\lambda \equiv F - k_B T \ln \left[ 1 + e^{(F - F_{\lambda, \max})/k_B T} \right], \quad (231)$$

where  $F_{\lambda, \max}$  is the highest possible effective barrier for a fixed  $\lambda$ :

$$F_{\lambda, \max} \equiv -k_B T \ln(\lambda\tau_0), \quad (232)$$

see the inset of Fig. 43(b). It is straightforward to show that the distribution  $\psi_\lambda$  of the shear-modified barriers from Eq. (231) is related to the unperturbed barrier distribution  $\psi$  according to:

$$\psi_\lambda(F_\lambda) = \psi(F) \left[ 1 + e^{(F - F_{\lambda, \max})/k_B T} \right], \quad (233)$$

where  $F$  is understood as a function of  $F_\lambda$  via Eq.(231). Both the unperturbed and shear-modified barrier distributions (for a fragile substance near the glass transition) are shown in Fig.43 for a particular value of  $\lambda$ . We thus directly observe how facilitation modifies the barrier distribution. Presumably, one may use a similar approach to determine the barrier

distribution self-consistently and thus go beyond the simple approximations made to derive the barrier distributions in Eq. (191) and (192). To do so, one needs to better quantify the coupling between nearby reconfiguring regions. Some progress along these lines has been achieved recently in the context of glass rejuvenation [48, 49], as we saw in Subsection VIII B.

## B. Mechanical Strength

In the preceding Subsection, we used a purely kinetic argument to estimate the threshold value of the shear rate beyond which a glassy liquid will rupture. To develop a thermodynamic perspective on the mechanical strength of a *frozen* glass, we will employ the machinery developed earlier as part of the theory of ageing and of the crossover phenomena, from Sections VIII A and VII respectively. The relevance of the crossover becomes clear after one notes that on the verge of breakdown, the sample is near its mechanical stability limit implying that the reconfiguration barriers are low. This, in turn, means that one must include effects stemming from the reconfiguring regions being not fully compact. Wisitsorarak and Wolynes [47] essentially repeat the steps that led to the derivation of the free energy cost of reconfiguration near the crossover, Eq. (203), except now the driving force must also include two additional contributions:

$$F(N) = T \left[ s_c^{\text{perc}} - \left( s_c + \frac{\Delta\Phi}{T} + \kappa \frac{\sigma^2 a^3}{2\mu} \right) \right] N. \quad (234)$$

Indeed, as we have seen in our analysis of ageing in Subsection VIII A, the bulk driving force  $\Delta g$  for reconfiguration of a glass quenched to a temperature  $T < T_g$  exceeds the equilibrium configurational entropy at that temperature. By Eq. (217), together with  $T_1 = T_g$  and  $T_2 = T$ , we get  $\Delta\Phi = \Delta c_p(T_g) T_g \ln(T_g/T)$ . An additional contribution to the driving force is the free energy of the elastic stress that ends being released following the reconfiguration. In the simplest, spherical geometry, this elastic energy is equal to  $\kappa\sigma^2/2\mu$  per unit volume, where  $\sigma$  is the magnitude of stress,  $\kappa \equiv 3 - 6/(7 - 5\nu)$ ,  $\nu$  the Poisson ratio, and  $\mu$  the shear modulus. This yields the final term on the r.h.s. of Eq. (234).

As in the earlier analysis of the crossover, the free energy cost  $F(N)$  for reconfiguration, near the mechanical stability limit, is either exclusively uphill or downhill, depending on the sign of the expression in the square brackets in Eq. (234). The glass becomes unstable when the expression vanishes. This notion, together with some additional corrections, yields the following expression for the threshold value of the stress beyond which the glass will break catastrophically [47]:

$$\sigma_{\text{pred}}^* = \sqrt{\frac{2\mu k_B T}{\kappa a^3} \left( \left[ 3.20 \frac{T_K}{T} - 1.91 \right] - \frac{\Delta c_p(T_g) T_g}{k_B T} \ln \frac{T_g}{T_K} \right)} \quad (235)$$

As expected, the glass would be at its strongest at the (putative) Kauzmann temperature  $T_K$ . Indeed, if it were possible to equilibrate the liquid at  $T_K$ , this would correspond to the deepest valley in the free energy landscape of the system.

Predictions of the limiting strength, due to Eq. (235), are graphed in Fig. 44(a) against the shear modulus  $\mu$ , alongside the experimental values and a number of other notable types of limiting strength, see the legend. A direct comparison of the theoretically-predicted and experimental values of the limiting strength is performed graphically in Fig. 44(b). The agreement between theory and experiment is quite satisfactory considering that no adjustable parameters were used.

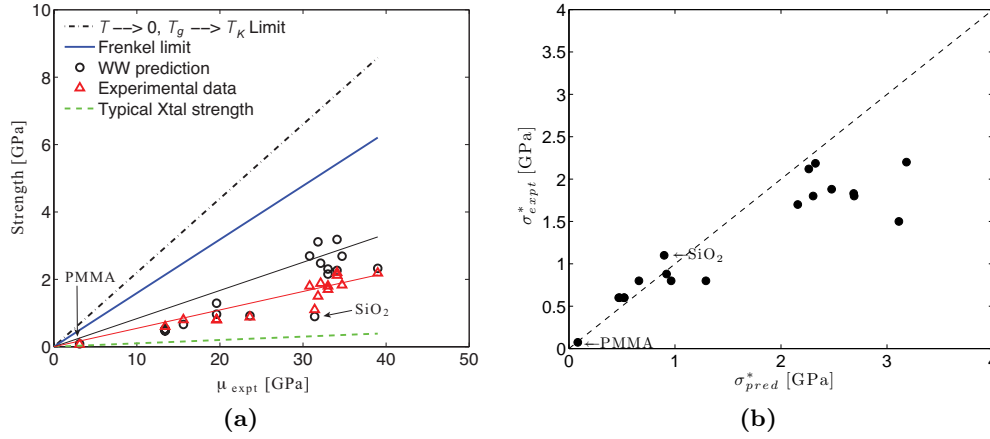


FIG. 44. (a) Predicted values of the limiting strength for several glasses, due to Wisitsorasak and Wolynes [47] (black circles), plotted vs. the shear modulus for select materials, alongside their experimental values (red triangles). The black and red lines are best linear fits through the corresponding sets. (b) Direct comparison of the theoretically-predicted and experimental values of the limiting strength, figure taken from Ref. [47].

## X. ULTRA-STABLE GLASSES

Because of the dramatic increase in the relaxation time with lowering temperature, there seems to be a natural limit to the depth one can reach in the free energy landscape of a liquid. The depth simply goes with the logarithm of the relaxation time times  $k_B T$ ; the relaxation time is limited by the duration of the experiment. It is quite rare that a controlled experiment lasts longer than a few hours or days, a notable exception provided by the famous tar pitch experiment in Australia [257]. Much, much longer *uncontrolled* experiments on glasses are also known, such as studies of fossil amber [258].

Given the intrinsic connection between the depth of the free energy minima and their multiplicity, see Eq. (154), there is a natural lower bound on the enthalpy of a glass. According to Eq. (95), the enthalpy of an equilibrated liquid at temperature  $T$  is:

$$h(T) = \Delta c_p(T_g^\circ) T_g^\circ \ln(T/T_g^\circ) \geq \Delta c_p(T_g^\circ) T_g^\circ \ln(T_K/T_g^\circ), \quad (236)$$

where we take as our reference temperature the conventional glass transition temperature  $T_g^\circ$ , say, on the time scale of 100 sec. The lower limit above is almost certainly an overestimate because most liquids will undergo some sort of partial ordering before the putative Kauzmann temperature could be reached, see Section XI and also below.

The lower the temperature at which the sample has been equilibrated, the deeper in the free energy landscape the liquid is. Consistent with this notion, the escape barrier from a state in a liquid equilibrated at temperature  $T_1$  to a state equilibrated at temperature  $T_2 > T_1$ , following a  $T_1 \rightarrow T_2$  temperature jump, is the higher the lower the temperature  $T_1$  is, see Eq. (223). In turn, this means that given the same speed of heating, a sample equilibrated at a lower temperature will melt at a higher temperature. The latter situation is in a loose way similar to the crystal-to-liquid transition, whereby a crystal made of molecules bonded by stronger forces will melt a higher temperature. Suppose two distinct polymorphs can be prepared at the same temperature, one of the polymorphs must then be metastable. The metastable polymorph will melt at a lower temperature than the stable one, because its free energy is higher than that of the stable polymorph, see Fig. 45(a). For the same reason, different faces melt at different temperatures because the bonding is generally differs in strength depending on the specific face [43, 259]. Note this is consistent

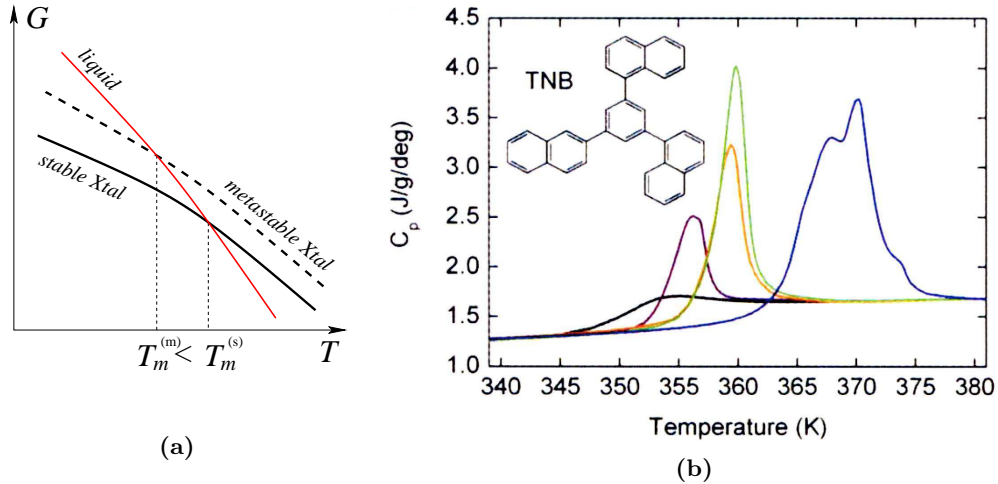


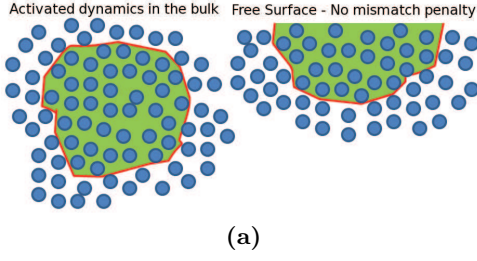
FIG. 45. **(a)** A schematic of temperature dependences of the Gibbs free energy of a stable polymorph (black solid line), metastable polymorph of the same substance (black dashed line) and the corresponding liquid (red line). The less stable polymorph will melt at a lower temperature,  $T_m^{(m)}$ , than the stable one,  $T_m^{(s)}$ . (Melting is kinetically preferable to the nucleation of the stable crystal, at least at  $T > T_m^{(m)}$ , because the barrier for surface melting is only a  $k_B T$  or so [65].) **(b)** Heat capacity,  $C_p$ , of TNB samples: vapour deposited directly into a DSC pan at 296 K at a rate of 5 nm/s (blue); ordinary glass produced by cooling the liquid at 40 K/min (black); ordinary glass annealed at 296 K for 174 days (violet), 328 K for 9 days (gold), and 328 K for 15 days (green). (Inset) Structure of TNB. Figure from Swallen et al. [260].

with the Lindemann criterion of melting [43, 259] since the vibrational displacement will be longest along the direction of weakest bonding; this longest displacement will satisfy the Lindemann criterion first as the crystal is heated. The corresponding face will thus be the first to melt.

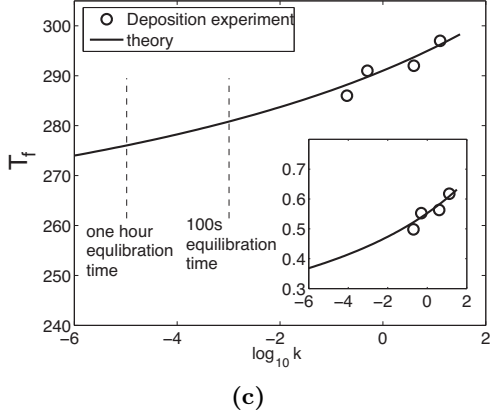
In a fascinating contrast with crystals, the typical bonding strength in glasses can be tuned *continuously*, simply by varying the speed of quenching. The slower the speed, the lower the glass temperature, the lower the enthalpy, the stronger the bonding, by Eq. (236). Another important distinction is that there is a substantial barrier for melting a glass—as determined by the driving force from Eq. (223)—and so the melting of glass is subject to kinetics as is the vitrification in the first place. In contrast, the barrier for the melting of a *periodic* crystal is very low, a  $k_B T$  or so, and the melting temperature of the crystal is largely determined by thermodynamics, not kinetics. To avoid confusion, we reiterate that glasses melt by gradual softening, not by sudden liquefaction, in contrast with periodic crystals.

Relatively recently, Ediger and coworkers [260–263] have generated glassy films by vapour deposition at a temperature significantly below the glass transition. These films melt at a significantly higher temperature than conventionally-produced bulk glasses made by thermally quenching a liquid at a generic rate, see Fig. 45(b). In this figure, the differential scanning calorimetry (DSC) curves other than the blue curve correspond to conventional glasses, some of which have also been subjected to additional thermal treatment. We clearly see that the lower the enthalpy of the sample is—as could be determined by integrating the heat capacity curves—the higher the temperature at which the sample will melt. The blue curve, which describes the vapour-deposited glass, clearly corresponds to a very stable glass. (It appears that the most stable samples are obtained when the substrate temperature is around 85% of the conventional  $T_g$ .) Note that the DSC peak corresponding to this sta-

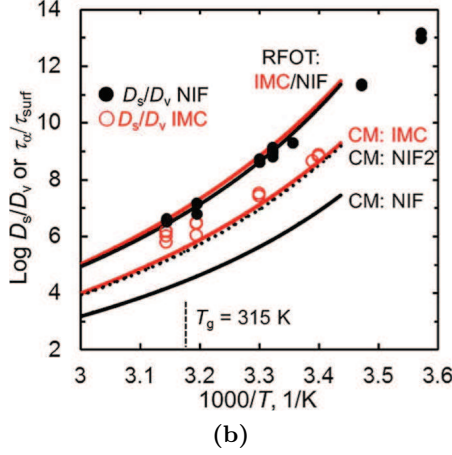




(a)



(c)



(b)

FIG. 46. (a) A schematic of a region reconfiguring near the surface of the sample. At the same curvature, both the volume and mismatch penalty are reduced resulting in a lowered reconfiguration barrier. (b) Experimental data [264] for surface mobility for two glasses plotted against theoretical predictions, including those by the RFOT-based argument [46]. Figure from Ref. [264]. (c) Fictive temperatures vs deposition rate for the glass former IMC. Data for the deposition experiment [265] are shown with symbols. The experimental fictive temperature was determined by intersecting the apparent  $T$ -dependences of the enthalpy, as determined by integrating  $\Delta c_p$  and the extrapolated enthalpy of the equilibrium liquid. The same data are shown in the inset plotted as  $s_c(T_f)/k_B$  per bead vs. deposition rate.

ble glass has a structure; this suggests the films are held together by distinct interactions that are relatively well separated in terms of energy. Consistent with these notions, later measurements [261, 262] confirmed that the packing in the stable samples is indeed quite anisotropic, whereby the planar portions of the constituent molecules seem to stack. Furthermore the direction of stacking could be either perpendicular or orthogonal to the film.

Stevenson and Wolynes [46] have put forth an argument as to why the *surface* of a glass—as it is being deposited—could become more stable than the bulk. The main idea is that at a fixed interface curvature, a reconfiguring region on the surface has a smaller contact area with its environment. Indeed, consider a roughly half-spherical region at the surface as in Fig. 46(a). A review of the argument leading to Eq. (168) indicates that there is no localisation penalty for molecules at the surface. In turn, owing to the absence of the mismatch penalty at the free surface, the overall nucleation profile from Eq. (162) is modified to account both for the reduction in the contact area of the region with its environment and the reduction in the volume. For a strictly half-spherical region, the nucleation profile is exactly a half of that for a full sphere, at the same value of the curvature [46]:

$$F(r) = 2\pi r^2 \sigma_0 (a/r)^{1/2} - (2\pi/3)(r/a)^3 T s_c. \quad (237)$$

Thus the reconfiguration of a typically-sized region near the surface is subject to a barrier

that is about a half of its value in the bulk:

$$F_{\text{surf}}^{\ddagger} = \frac{1}{2} F_{\text{bulk}}^{\ddagger}, \text{ when } r_{\text{surf}}^{\ddagger} = r_{\text{bulk}}^{\ddagger}. \quad (238)$$

Consequently, the relaxation time at the surface is about the square root of its value in the bulk [46]:

$$\tau_{\text{surf}} \approx \sqrt{\tau_0 \tau_{\text{bulk}}}, \quad (239)$$

where the bulk relaxation time  $\tau_{\text{bulk}}$  corresponds to the relaxation time  $\tau$  from Eq. (132) and  $\tau_0$  is the prefactor from the same equation. Brian and Yu [264] have tested the simple relation from Eq. (239) and found it agrees well with their data on surface mobility, see Fig. 46(b).

The argument above can be also turned around: Suppose one prepares a glass by surface deposition and controls the deposition rate so as to give the molecules as much time to rearrange—before they get covered by the next layer—as they would have in a *bulk* glass at the same temperature. By equations (238) and (154), the configurational entropy of the so deposited glass is about twice lower than in the bulk glass. In other words, the surface-deposited glass corresponds to a bulk glass equilibrated at a significantly lower temperature; one may thus say the surface glass has a significantly lower fictive temperature than what would be available to a bulk glass made by quenching. This observation immediately explains the remarkable stability of the surface glass in Fig. 45. Quantitatively, this notion can be expressed by relating the deposition rate  $k$  (of units length per unit time), the cooperative size  $\xi$ , and the relaxation time  $\tau$ :  $k = \xi/\tau$ . Combined with Eq. (170), this quantity can be directly related to the configurational entropy and the corresponding value of the fictive temperature [46]:

$$s_c(T_f) = \frac{32}{\ln(\xi/k\tau_0)}. \quad (240)$$

The thus predicted values of the fictive temperature vs. the deposition rate are plotted in Fig. 46(c), alongside the experimental values due to Kearns et al. [265]. The agreement between theory and experiment is notable, especially in view of the partial ordering that takes place in the ultrastable glasses. Indeed, it is not obvious that one would obtain quantitative results by extrapolating configurational entropy from a regime in which no apparent ordering takes place to a regime characterised by some ordering.

## XI. ULTIMATE FATE OF SUPERCOOLED LIQUIDS

Deeply supercooled liquids seem to be a great example of a self-fulfilled prophecy: Once they fail to crystallise below the fusion temperature, one can supercool them even more thus further diminishing the probability to crystallise. This is expected since the growth of the crystal nucleus is subject to viscous drag, which ordinarily becomes increasingly strong with lowering the temperature. Glycerol is an archetypal example of a system, in which crystallisation is suppressed for a seemingly indefinite period. Indeed, at normal conditions, glycerol is a supercooled liquid with a seemingly indefinite shelf-life, unless it becomes “infected” by crystallites. (According to an anecdote told by Onsager, a whole glycerol factory had to be shut down as a result of being infected by such crystallites [58].)

Yet it is not at all obvious that supercooled liquid should be harder to crystallise with lowering the temperature, because crystal nucleation and growth are subject to two competing factors. On the one hand, the viscous drag makes it difficult for an incipient crystallite to grow thus increasing the probability of its evaporation before it ever reaches the critical

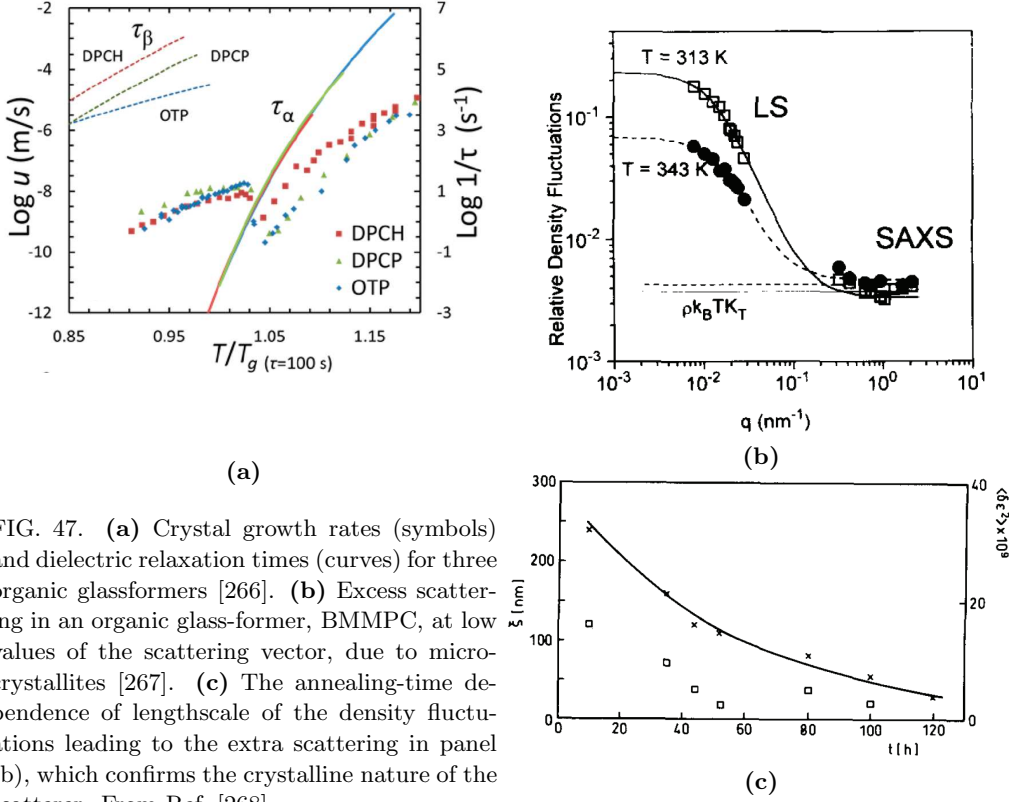


FIG. 47. (a) Crystal growth rates (symbols) and dielectric relaxation times (curves) for three organic glassformers [266]. (b) Excess scattering in an organic glass-former, BMMPC, at low values of the scattering vector, due to micro-crystallites [267]. (c) The annealing-time dependence of lengthscale of the density fluctuations leading to the extra scattering in panel (b), which confirms the crystalline nature of the scatterer. From Ref. [268].

size, as already mentioned. On the other hand, the ordinary nucleation theory tells us that the activation profile for nucleation is:

$$F_x(r) = 4\pi\sigma_x r^2 + (4\pi/3)\Delta g_x r^3, \quad (241)$$

where  $\Delta g_x < 0$  is the free energy difference between *equilibrated* crystal and liquid. Clearly, the equilibrium driving force,  $(-\Delta g_x)$ , increases while the critical nucleus size decreases upon cooling, see Fig. 45(a). In fact, if the liquid were uniform, it should presumably reach a mechanical stability limit at some temperature  $T < T_m$ , implying crystal nucleation is now a strictly downhill process, no matter how high the viscosity is! In line with the latter notions, the rate of crystal growth in certain organic liquids displays a re-entrant behaviour as a function of temperature, see Fig. 47(a).

One generally expects that the amount of crystallinity, if any, will depend on the history of the sample. And so, for instance, the crystallites' size and their growth in a glassy sample can be controlled to some degree by varying the sample's temperature and, hence, viscosity. Likewise, one can partially anneal out crystallites by warming the liquid to a sufficient extent. To give a household example of such a process, honey will begin to crystallise after prolonged storage but can be made visibly crystal-free by warming. Both the formation of crystallites and their melting in organic glassformers is systematically illustrated with results of Fischer et al. in Figs. 47(b) and (c).

Stevenson and Wolynes [50] have pointed out that the analysis of crystallisation in the landscape regime is complicated by the fact that the liquid may not be spatially uniform or equilibrated on the crystal-nucleation time. Qualitatively, if the critical nucleus for crystallisation significantly exceeds the cooperativity size  $\xi$ , crystal-nucleation occurs roughly as it would from the uniform-liquid state. In the opposite case, where the crystal nucleus is smaller than  $\xi$ , the crystal-nucleation would significantly speed up, compared with the

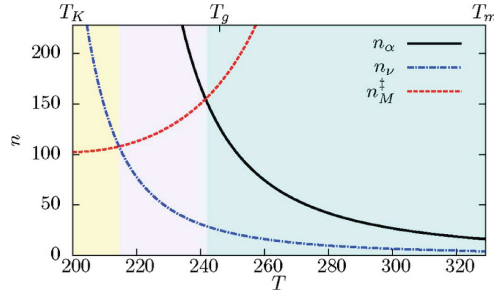


FIG. 48. Temperature dependence of the size  $n_\alpha$  of a typical structural reconfiguration; the transition state size  $n_M^\ddagger$  of classical crystal nucleation; and the number  $n_\nu$  of particles involved in nanocrystallisation. The latter size indicates the size of a nucleus stable against evaporation in an *individual* free energy minimum of the liquid. Within the shaded region on the right classical nucleation theory is valid. In the shaded region on the left direct nanocrystallisation can take place. Crystallisation in the centre region takes place through fluctuational, percolative nanocrystallisation. From Ref. [50].

uniform liquid. This is because an individual region is not configurationally equilibrated and is significantly higher in free energy (by  $Ts_c$  per particle) than the uniform liquid, see Eq. (115). Thus the driving force for crystallisation becomes greater than its value for the uniform-liquid-to-crystal transition. These notions are graphically summarised in Fig. 48(a). Thus SW have delineated distinct regimes in which activated reconfiguration between aperiodic structure kinetically competes with homogeneous crystallisation at high temperatures and nano-crystallisation at lower temperatures, see Ref. [50] for more detail. Regardless of system-specific peculiarities, it is predicted that nano-crystallisation will directly proceed at sufficiently low temperatures. This, in effect, resolves the Kauzmann paradox in that the putative ideal glass state would be always avoided owing to partial ordering.

## XII. QUANTUM ANOMALIES

So far, quantum mechanics has played no explicit role in our narrative even though the inter-particle interactions, including in particular a significant portion of the steric repulsion, are ultimately of quantum-chemical origin. It is, in fact, fair to say that the structural glass transition is an intrinsically classical phenomenon. Indeed the very long lifetime of glassy, metastable states is in contradiction with the Second Law and is predicated on the system's ignorance of the actual stable state. Such ignorance is guaranteed in classical mechanics since portions of the phase space separated by a barrier are entirely “unaware” of each other. Barrier crossing events are rare events that require activation. In contrast, the wavefunctions of the metastable and stable states have a non-zero overlap, even if small. When the overlap is sufficiently small, however, the “self-awareness” of glassy states as metastable configurations should not affect the dynamics within those states. Furthermore, quantum fluctuations in fact *augment* the glass transition temperature when sufficiently weak, by making the particles seem bigger than they are classically [269, 270]. Still, when the wave-function overlap between distinct minima becomes sufficiently large, the particles will eventually delocalise and the glass will readily “melt,” in accordance with expectation. In other words, the glass transition is suppressed by quantum fluctuations of sufficient magnitude, as any symmetry-lowering transition would be.

Some of the earliest quantum phenomena discussed in relation to amorphous materials were of electronic nature, such as Anderson's localisation [271] and Mott's variable range

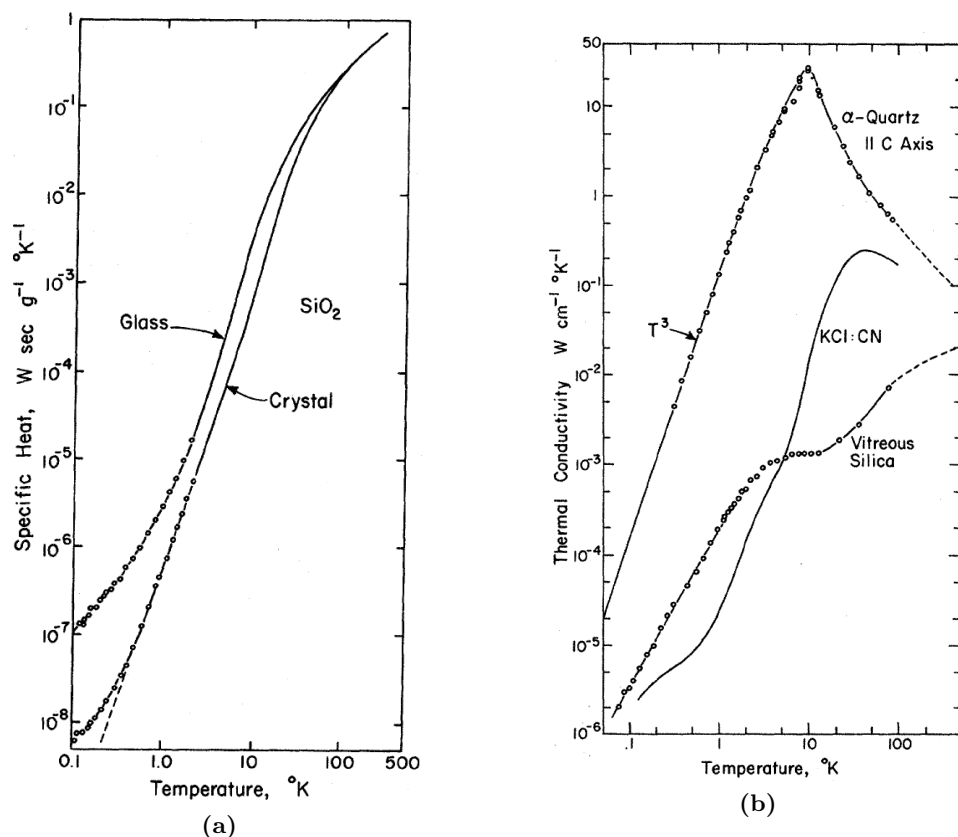


FIG. 49. (a) Heat capacity of amorphous vs. crystalline  $\text{SiO}_2$  [275] (b) Thermal conductivity of amorphous vs. crystalline  $\text{SiO}_2$ , samples' dimensions  $5 \times 5 \times 40$  mm [275].

hopping [272]. These fascinating phenomena are generic consequences of *static* disorder, largely regardless of the history of the sample, and would not be unique to glasses, as opposed to, for example, deposited amorphous films made of a poor glass-former. (The real story is more complicated in that *glassy* solids often exhibit stronger electron-phonon interactions [273, 274] and weaker scattering, owing to lack of dangling bonds.) Conversely, these electronic phenomena do not induce nuclear dynamics other than vibrational displacement.

In contrast, here we discuss quantum phenomena that are largely unique to glasses in that they rely on the existence of dynamics that connects the many distinct aperiodic states available to a sample made by quenching a liquid equilibrated below the crossover. We shall observe that the very same quantities computed in Section V, which set the length and time scales for the classical phenomena near the glass transition temperature, also determine the magnitude of excitations that operate down to sub-Kelvin temperatures and are entirely of quantum nature.

### A. Two-Level Systems and the Boson Peak

A number of low temperature anomalies observed in cryogenic glasses have certainly added to the mystique of glassy solids. Beginning from the definitive measurements by Zeller and Pohl [275] some four decades ago, it became clear that glasses are fundamentally different in their thermal properties from periodic solids, see Fig. 49(a) and (b). As already discussed, glassy liquids solidify in a gradual manner; they are aperiodic and vastly

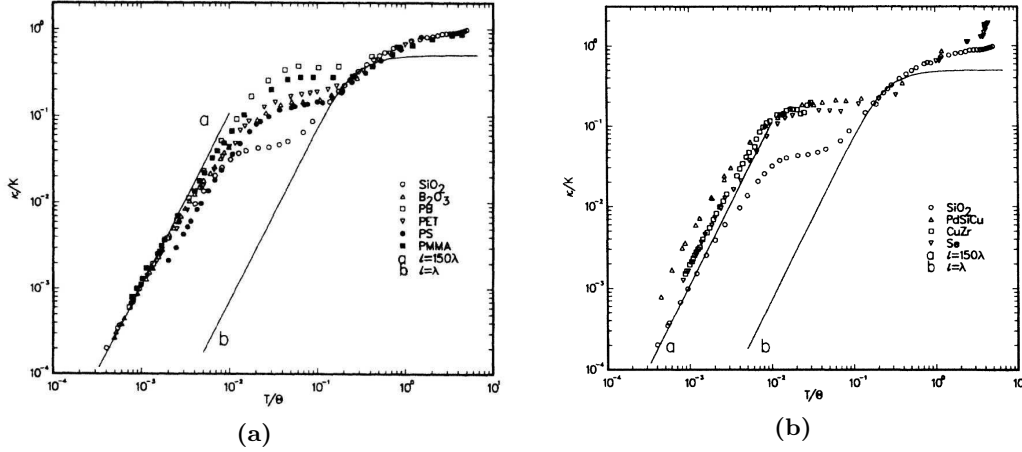


FIG. 50. **(a)** Scaled thermal conductivity ( $\kappa$ ) data for several amorphous materials. The horizontal axis is temperature in units the Debye temperature  $T_D$ . The vertical axis scale  $K \equiv \frac{k_B^3 T_D^2}{\pi \hbar c_s}$ . The value of  $T_D$  is somewhat uncertain, but its choice made in [276] is strongly supported by that it yields universality in the phonon localisation region. The solid lines are calculated using  $\kappa \simeq \frac{1}{3} \sum_{\omega} C_{\text{ph}}(\omega) l_{\text{mfp}}(\omega) c_s$  with  $l_{\text{mfp}}/\lambda = 150$  and  $l_{\text{mfp}}/\lambda = 1$  respectively. **(b)** Thermal conductivity of several metallic glasses plotted in the same fashion as in panel (a). The data for  $\text{SiO}_2$  are given for comparison. Both figures from Freeman and Anderson [276].

structurally-degenerate. Yet this circumstance does not prevent glasses from being macroscopically solid on very extended timescales so long as the temperature is sufficiently below  $T_g$ . Indeed the barrier for particle rearrangement in glasses is comparably high to or often higher than the barrier for mechanical failure in crystalline materials.

Given their macroscopic stability, one may reasonably expect that the thermal properties of glasses at sufficiently low temperatures would be identical to those of periodic crystals. This is because the wavelength of thermal phonons can be made arbitrarily greater than the correlation length characterising the structural inhomogeneity, if any, in frozen glasses. Contrary to this expectation, the heat capacity of cryogenic glasses is not cubic in temperature, but, instead, is approximately *linear* down to lowest measured temperatures and thus significantly exceeds the vibrational heat capacity, Fig. 49(a). (It is understood that equilibration could become increasingly sluggish at sub-Kelvin temperatures which may result in a transient low energy gap in the heat capacity.) The difference in phonon scattering between vitreous and crystalline samples is no less dramatic at these temperatures: While the phonon mean free path already exceeds the sample size in crystals—and so one should properly speak of heat *conductance*—it is of perfectly microscopic dimensions in glasses. In addition to the significantly reduced magnitude, the heat conductivity in glasses also has a distinct temperature dependence, approximately  $\propto T^2$ , Fig. 49(b), in contradistinction with the cubic law observed in crystals.

Shortly after Zeller and Pohl's discovery, Anderson, Halperin, and Varma [277], and Phillips [278] made an excellent circumstantial case that both the excess heat capacity and phonon scattering arise from the same microscopic entity. Clearly, the excess heat capacity cannot be due to static inhomogeneities, as already mentioned. Thus those workers concluded that cryogenic glasses must host small groups of atoms performing strongly anharmonic motions that result in local *resonances*; these can be approximated as two-level systems at low temperatures:  $E = -\frac{1}{2}(\epsilon\sigma_z + \Delta\sigma_x)$ . Expanding the diagonal component of the energy splitting in terms of the local deformation  $u$ ,  $\epsilon \approx \epsilon(u=0) + (\partial\epsilon/\partial u)u$  yields a

coupling to the sound waves:  $g \equiv -\frac{1}{2}(\partial\epsilon/\partial u)$ , thus yielding the TLS energy function:

$$E = -\frac{1}{2}(\epsilon\sigma_z + \Delta\sigma_x) + gu\sigma_z. \quad (242)$$

A flat density of states,  $n(E) = \bar{P} = \text{const}$ , approximately accounts for the  $T$ -dependence of *both* the heat capacity and conductivity [277–279]. Phonon-echo and single-molecule spectroscopy have directly confirmed the resonant nature of these mysterious excitations and even captured their becoming multi-level at increasing temperatures [280–282].

Already Zeller and Pohl noted the heat conductivity—a dimensional quantity—seemed only mildly system-dependent, a point that was forcefully brought home by Freeman and Anderson [276] some 15 years later, see Fig. 50(a). The latter authors have shown the ratio of the phonon mean-free path  $\lambda_{\text{mfp}}$  to the thermal phonon wavelength  $\lambda_{\text{th}}$  is near universally  $\approx 150$  for all tested, insulating vitreous substances, some polymeric. This ratio can be also expressed in terms of the parameters of the two level systems:

$$\frac{l_{\text{mfp}}}{\lambda_{\text{th}}} = \left( \frac{\bar{P}g^2}{\rho_m c_s^2} \right)^{-1} \simeq 150, \quad (243)$$

where  $\rho_m$  and  $c_s$  are the mass density and speed of sound respectively. One way to interpret the above figure is to say that the vibrational plain waves—or phonons—are reasonably well-defined, wave-like quasi-particles, despite the aperiodicity of the lattice. In addition to the low- $T$  regime in Fig. 50(a), which corresponds to the near universal line  $l_{\text{mfp}}/\lambda_{\text{th}} \simeq 150$ , there is also the regime on the higher temperature flank on Fig. 50(a), where this ratio is about one:  $l_{\text{mfp}}/\lambda_{\text{th}} \simeq 1$ . This regime is often referred to as the Ioffe-Regel regime [272, 283], whereby the phonon is no longer a well-defined quasi-particle. Instead, it is more appropriate to speak of energy transport in the solid as hopping of vibrational packets, a picture originally (and incorrectly) envisioned by Einstein for *crystalline* solids [284]. The intermediate regime  $1 < l_{\text{mfp}}/\lambda_{\text{th}} < 150$  is of considerable interest, too: This region corresponds with a significant rise in the heat capacity, Fig. 52(a), often called the heat-capacity “bump,” but also an increased rate of phonon scattering, which leads to a “plateau” in the heat conductivity,  $10^1 \lesssim T/\theta \lesssim 10^2$  in Fig. 50(a). One should not fail to notice that the plateau temperatures correspond to terahertz frequencies and thus match, frequency-wise, the Boson Peak excitations in Fig. 3.

Yu and Leggett [285] (YL) have stressed that there is little *à priori* reason for the ratio from Eq. (243) to be so consistent between different substances, considering that the density of states  $\bar{P}$  varies by at least two orders of magnitude. (The magnitude of the variation, while considerable, is still surprisingly small given the chemical variation among the tested materials.) YL also noted that the phonon-mediated interaction between two TLSs goes as  $(g^2/\rho_m c_s^2)r^{-3}$ —a fact we have already encountered at the end of Subsection IV D—consistent with Eq. (243) and the fact that  $\bar{P}$  has dimensions inverse energy-volume. Based on this realisation and noting the long-range character of the  $1/r^3$  interaction, YL proposed that the apparent density of states  $\bar{P}$  pertains to some renormalised excitations which span a large number of the local resonances. Thus this density of states could be a universal quotient of the inverse of the elemental interaction  $(g^2/\rho_m c_s^2)^{-1}$  irrespective of the precise nature of those local resonances. Showing why this quotient should be of order  $10^2$  has been difficult, but the “interaction” scenario is still being pursued [286–288]. To avoid confusion with the Bevezko-Lubchenko model [154, 155], we note that in the latter, the interaction is very strong, comparable to the glass transition temperature, Fig. 22(b), whereas the interaction between the *apparent* two-level systems is closer to sub-Kelvin energy scales [289], see also below.

Local resonances naturally arise in the RFOT scenario of the glass transition. Hereby the near universality of the ratio in Eq. (243) can be traced to the near universality in the cooperativity size  $\xi$ . To see this we first note that the activated reconfigurations in a

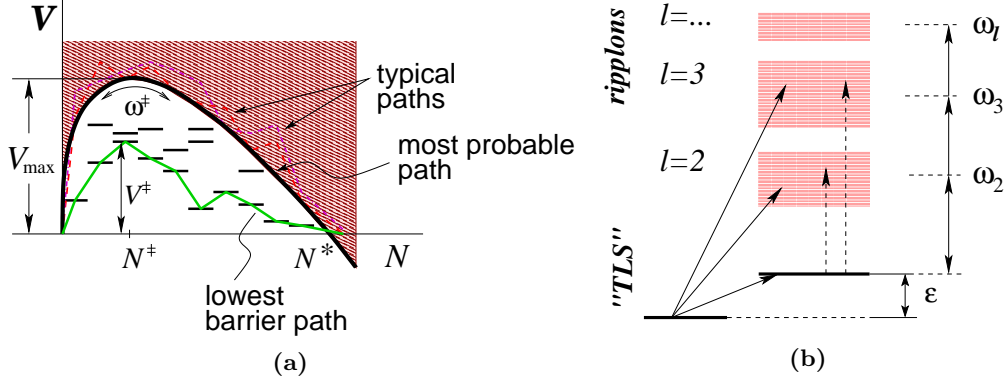


FIG. 51. (a) The black solid line shows the barrier along the most probable path. Thick horizontal lines at low energies and the shaded area at energies above the threshold represent energy levels available at size  $N$ . The red and purple line demonstrate generic paths, green line shows the actual (lowest barrier) path that would be followed in the thermally activated regime, where  $\hbar\omega^\ddagger < k_B T/2\pi$ . (b) Tunnelling to the alternative state at energy  $\epsilon$  can be accompanied by a distortion of the domain boundary and thus populating the vibrational states of the domain walls. All transitions exemplified by solid arrows involve tunnelling between the intrinsic states and are coupled linearly to the lattice distortion and contribute the strongest to the phonon scattering. The “vertical” transitions, denoted by the dashed arrows, are coupled to the higher order strain and contribute only to Rayleigh type scattering, which is much lower in strength than that due to the resonant transitions.

glassy liquid are perfectly reversible, so long as the surrounding matrix has not re-arranged during the waiting time for the reverse reconfiguration. Such reverse reconfigurations are thus unlikely to happen at high temperatures, as follows from the discussion of facilitation in Sections VI and IX. Now, Lubchenko and Wolynes [51] (LW) have shown that a certain fraction of the reconfigurations are essentially *zero-barrier*. These reconfigurations—and their reverses!—would be thus thermally active down to very low temperatures, while the rest, slower reconfigurations are frozen. These reversible reconfigurations underlie the structural resonances that give rise to the TLS and the excess phonon scattering. What is the distribution of the transition energy  $\Omega(E)$  for such reversible transitions? Setting aside the issue of the transition probability for a moment, we note that save some ageing, the frozen matrix itself and its excitations can thought of as pertaining exclusively to a *single* temperature scale. The latter is the fictive temperature, of course; in turn, it is approximately equal to the glass transition temperature  $T_g$ . Thus  $\partial \ln \Omega(E)/\partial E = 1/T_g$ . Setting the ground state energy at zero:  $\int_0^\infty dE \Omega(E) = 1$ , one gets  $\Omega(E) = \frac{1}{T_g} e^{E/k_B T_g}$ , per region that can reconfigure on some specified time scale. Note this exponential distribution can be explicitly obtained for spin glasses [290] and the random energy model [178].

To convince ourselves in the existence of low barrier reconfigurations, we may review the library construction in Fig. 23 and recognise that a typical activation profile gives the value of free energy at which the droplet+environment system is guaranteed to have a state, however the transition state for individual trajectories is *distributed*. We reiterate this notion in Fig. 51(a). In contrast with the equilibrium calculation in Subsection V A, the energies of both the initial and transition state are randomly distributed variables, as the surrounding matrix is now frozen and so one can no longer define a typical, equilibrated initial state. As a result, the barrier distribution is exponential—similarly to that of the classical density of states—but with a softer growth pattern, viz.,  $e^{V^\ddagger/\sqrt{2}k_B T_g}$ . Consequently, the barrier for rearranging a region of size  $\xi$  turns out to be lower than the typical barrier for irreversible reconfigurations at  $T_g$  [23, 51], i.e.,  $\approx 26k_B T_g$ . Though lower, this barrier is still much much



higher than what could be tunnelled through, however. Conversely, the chances that a region of size  $\xi$  will have a zero reconfiguration barrier,  $e^{-26k_B T_g / \sqrt{2}k_B T_g} \sim 10^{-8}$ , are small, even if not astronomically small. LW go further and consider the set of trajectories available to regions *larger* than  $\xi$ . To a region of size  $N > N^*$ , there are  $e^{s_c(N-N^*)/k_B}$  more states available. And so given  $s_c(T_g) = 0.82$ , at  $(N - N^*) = 22$ —only a 10% increase relative to  $N^*(T_g)$ —one *can* in fact find a trajectory with a zero barrier, since  $e^{s_c(N-N^*)/k_B} \sim 10^8$ . Importantly, alternative configurations are kinetically accessible only to regions larger than  $N^*(T_g)$ . The energy of such a larger region is below that of the typically reconfiguring region at  $T_g$ , implying only the negative tail of the distribution  $\Omega(E) = (1/T_g)e^{E/k_B T_g}$  is kinetically accessible, by *tunnelling*. That the barrier is zero makes the question of the tunnelling mass moot. Still, LW [51] point out the tunnelling coordinate is surprisingly low mass, in apparent similarity to the domain-wall solution in the Su-Schrieffer-Heeger hamiltonian [291]. (This similarity will be prominent in Subsection XII B.) We thus conclude that the density of states of the resonances that would thermally active at very low temperature is [22, 23, 51]:

$$n(\epsilon) \simeq \frac{1}{T_g \xi^3} e^{-|\epsilon|/k_B T_g}. \quad (244)$$

The resulting density of low energy excitations,  $\epsilon \ll k_B T_g$ , is thus

$$\bar{P} = 1/T_g \xi^3. \quad (245)$$

Interestingly, it is determined by the characteristics of the solid that were set at the temperature of preparation, which is two orders of magnitude greater than the ambient, cryogenic temperature! The generic value of  $\bar{P}$  is about  $10^{45} \text{ J}^{-1} \text{ m}^{-3}$ , consistent with observation [292]. It is easy to see that the TLS density of states should decrease with lowering of the glass transition temperature and, hence, of the rate of quench during vitrification. Indeed, by Eqs. (160) and (165), we obtain  $\bar{P} \propto s_c^2$  and  $\bar{P} \propto s_c^2/T$  respectively. Either quantity is an increasing function of temperature, because  $s_c \propto (T - T_K)$ . We thus conclude that for a material in the landscape regime, the density of states of the TLS should be the lower the more stable the glass is. Generically, this means that denser glasses have fewer two-level systems.

Let us return to a previous notion that near the crossover, the free energy cost of particle localisation is comparable to that due to elastic deformation of the newly formed elastic continuum. The latter free energy is fixed by the equipartition theorem:  $\langle |gu| \rangle \simeq \rho_m c_s^2 a^3 \langle u^2 \rangle \simeq k_B T_{\text{cr}}$ , where  $\rho_m$  is the mass density. (This simple estimate is consistent with a more detailed argument [51].) Thus we may estimate the TLS-phonon coupling in Eq. (242):

$$g \simeq \sqrt{\rho_m c_s^2 a^3 k_B T_g}. \quad (246)$$

Eqs. (245) and (246) immediately yield that the mysterious universality in the phonon scattering, as expressed in the ratio from Eq. (243) stems from the near universality of the cooperative size near the preparation temperature of the sample:

$$\frac{l_{\text{mfp}}}{\lambda_{\text{th}}} = \left( \frac{\bar{P} g^2}{\rho_m c_s^2} \right)^{-1} \simeq \left( \frac{\xi(T_g)}{a} \right)^3 \simeq 10^2. \quad (247)$$

According to the prediction above, the slower the quench used to prepare the glass, the less intense phonon scattering will be at cryogenic temperatures. This is consistent with our earlier statement that glasses residing in deeper free energy minima are bonded more strongly. Conversely, glasses made by quicker quenches should exhibit more phonon scattering. The latter notion, however, applies only so long as the material remains in the landscape regime. For instance, we have seen that amorphous films prepared by vapour deposition on a cold

substrate, likely reside in relatively high energy states whereby structural reconfigurations, if any, would involve bond breaking. Consistent with this expectation, amorphous silicon films show a significantly lower density of the two-level systems, according to recent measurements of internal friction by Liu et al. [293]. These workers have shown that by optimising the stability of such films—through varying the deposition rate and temperature—one can further reduce the amount of internal friction and the density of states of the TLS. [294] (The internal friction  $Q^{-1}$  is equal to the quantity in Eq. (247) times  $\pi/2$ .) We just saw that a similar trend is expected in *quenched* glasses.

Another instructive example is provided by metallic glasses. According to Fig. 50(b), the phonon scattering in the latter is similar to insulating glasses but is weaker by a half-order of magnitude or so. This strongly suggests that, while possibly present, the cooperative rearrangements typical of the landscape regime are not as abundant in (the rapidly quenched) metallic glasses as in their insulating counterparts, which were made by leisurely cooling. This is consistent with our earlier remarks in Subsection IV C that metallic glasses made by rapid quenching may not be as deep in the landscape regime as insulating glasses. Yet another interesting example is the ultrastable glasses of indomethacine. These do not seem to exhibit the two-level systems within the measured temperature interval and the sensitivity of the experiment [295]. According to the estimates of the configurational entropy in ultrastable glasses, due to Stevenson and Wolynes [50], and Eq. (171), the TLS density of states should be a half-order of magnitude lower in such ultrastable glasses compared with those made by traditional quenching. It will be interesting to see if these fascinating materials do in fact exhibit the structural resonances at sufficiently low temperatures. It is, in principle, possible that the local ordering in the deposited glassy films gives rise to new physics.

To obtain the basic estimates above, we did not have to discuss the detailed distribution of the tunnelling amplitude  $\Delta$  of the TLS. This is because the distribution of the tunnelling barriers is determined by a classical energy scale,  $\sim k_B T_g$ , which is much greater than the thermal energy at the cryogenic temperatures in question. This results in a nearly flat distribution of the barriers  $p(V^\ddagger) \approx \text{const}$ , which leads to  $p(\ln \Delta) \approx \text{const}$  and, consequently,  $p(\Delta) \propto 1/\Delta$ . Semi-classical corrections to this simple result can be obtained [23], which modify somewhat the simple inverse-linear probability distribution:  $p(\Delta) \propto 1/\Delta^{1+c}$ , where  $c \simeq \hbar\omega^\ddagger/\sqrt{2}k_B T_g$  and  $\omega^\ddagger$  is the typical under-barrier frequency, see Fig. 51(a). Simple estimates [23] show that the frequency  $\omega^\ddagger$  scales with the Debye frequency  $\omega_D$ , resulting in the numerical value of  $c \simeq 0.1$ . The resulting correction to the  $\Delta$  distribution partially accounts for apparent deviations of the temperature dependences of the heat capacity and conductivity from the simple linear and quadratic laws respectively.

At sufficiently high temperatures, the low-energy, TLS approximation becomes inadequate and one must confront the question of the full, multi-level structure of the internal resonances. The transition to such multilevel behaviour is expected to occur at a temperature  $T' \simeq \hbar\omega^\ddagger/2\pi$  [51, 296], even ignoring damping. In the lowest order approximation, the higher excited states can be imagined as the lowest excited state dressed with vibrations of the domain wall that circumscribes the reconfiguring region [22]. Indeed, the region itself is only defined within the zero-point vibrations of the particles comprising its boundary. Another way to look the vibrations of the domain walls is that they are Goldstone particles that emerge when the mosaic of the entropic droplets forms.

This multi-level structure of a tunnelling centre with added domain wall vibrations is illustrated in Fig. 51(b). Given the size of the region,  $(\xi/a) \simeq 6 \Rightarrow 2\pi(r^*/a) \simeq 20$ , and the lowest wavelength  $\simeq 2a$  for such vibrational excitations, we obtain that harmonics order 2 through 10 or so can be excited. (The zeroth harmonic corresponds to the uniform dilation, while the first harmonic corresponds with the structural transition itself.) Thus the basic

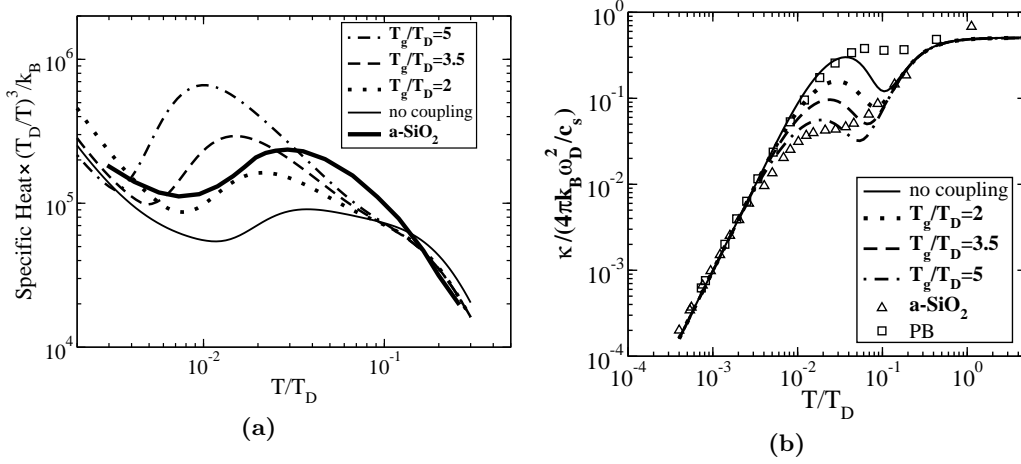


FIG. 52. **(a)** The bump in the amorphous heat capacity, divided by  $T^3$ , as follows from the derived TLS + ripplon density of states illustrated in Fig. 51(b), according to Refs. [22] and [23]. With the exception of the thin curve, the theoretical curves account for the shift in the ripplon frequency due to interaction with phonons. The amount of shift is determined by the ratio  $T_D/T_g$  of the Debye and glass transition temperatures. The thick solid line is experimental data for a-SiO<sub>2</sub> from [297]. The experimental curve, originally given in J/gK<sup>4</sup>, was brought to our scale by being multiplied by  $\hbar^3 \rho c_s^3 (6\pi^2)(\xi/a)^3 / k_B^4$ , where we used  $\omega_D = (c_s/a)(6\pi^2)^{1/3}$ ,  $(\xi/a)^3 = 200$ ,  $\rho = 2.2\text{g/cm}^3$ ,  $c_s = 4100\text{m/sec}$  and  $T_D = 342\text{K}$  [276]. (The Debye contribution was included in the estimate of the total specific heat). **(b)** Low temperature heat conductivity predicted in Refs. [22] and [23]. The “no coupling” case neglects phonon coupling effects on the ripplon spectrum, as in panel (a). The (scaled) experimental data are taken from [298] for a-SiO<sub>2</sub> ( $k_B T_g / \hbar \omega_D \simeq 4.4$ ) and [276] for polybutadiene ( $k_B T_g / \hbar \omega_D \simeq 2.5$ ). The empirical universal lower  $T$  ratio  $l_{\text{mfp}}/l \simeq 150$  [276], is used explicitly here to superimpose theoretical predictions on the experiment.

frequency scale  $\omega_{\text{BP}}$  for these quasi-harmonic modes is given by the expression:

$$\omega_{\text{BP}} \simeq \frac{a}{\xi} \omega_D, \quad (248)$$

where  $\omega_D$  stands for the Debye frequency. (The actual predicted scaling with  $a/\xi$  is  $(a/\xi)^{5/4}$  [22, 23] which would be hard to distinguish from the linear law in Eq. (248).) The identification of the frequency  $\omega_{\text{BP}}$  with the Boson peak is explained immediately below.

The vibrations of the domain wall share many characteristics with regular vibrational degrees of freedom such as the linear dependence of their energy on the temperature. Still, these vibrational modes are distinct from regular vibrational excitations on top of a unique ground state in that they would not be activated in the absence of the underlying anharmonic reconfiguration. To emphasise this distinction, LW have called these compound excitations “riplons.” Because the excitation density of the riplons is tied to the TLS density of states, while exhibiting a similar coupling strength to the phonons, it is straightforward to estimate the contribution of the riplons to both the heat capacity and phonon scattering. The resulting predictions for these quantities are shown in Fig. 52(a) and (b). The agreement with experiment is satisfactory given that no adjustable parameters are used and that damping of ripplon modes is ignored. Such damping can be included in the treatment and results in much better agreement with experiment [22, 23].

Lubchenko and Wolynes [170] have pointed out the identification of the riplons with the modes responsible for the *high*-temperature Boson peak from Fig. 3 is internally consistent. In the Yoffe-Regel regime, vibrational energy is being transferred by hopping of localised vibrations. The heat conductivity is thus given by the standard kinetic theory expression:  $\kappa = (3N_a k_B / a^3) D$ , where  $N_a$  is the number of atoms per volume  $a^3$  and  $D$  is the diffusion

constant for hopping of localised vibrations. The length of the hop is determined by the lattice spacing  $a$ , while the hop's waiting time is determined by the vibrational lifetime, i.e.  $\tau_{\text{vibr}}$ . The resulting diffusion constant is  $D \simeq a^2/6\tau_{\text{vibr}}$ , so that the heat conductivity:

$$\kappa \simeq \frac{k_B}{a\tau_{\text{vibr}}}(N_a/2). \quad (249)$$

Using  $a = 3\text{\AA}$ ,  $\tau_{\text{vibr}} = 1$  psec, and  $N_a = 3$  yields  $\kappa \simeq 0.1$  W/m·K, in agreement with the typical experimental value of the conductivity near  $T_g$  [276]. In view of Eq. (249) and the slow variation with temperature of the thermal conductivity above the Debye temperature, [276] the vibrational relaxation time should indeed exhibit little temperature dependence well below  $T_g$ . As a result, the corresponding peak in dielectric spectra should exhibit little temperature dependence, as though a set of resonances intrinsic to the lattice were responsible for the peak. Further, we recall Freeman and Anderson's empirical observation [276] that  $\kappa$ 's for several different materials tend to saturate at a value numerically close to  $(k_B c_s/a^2)(4\pi)^{1/3}(3N_a)^{2/3}$ . Combining this observation with Eq. (249), we get  $\tau_{\text{vibr}}^{-1} \simeq (c_s/a)2(4\pi/3N_a)^{1/3}$ , i.e. a universal fraction of the Debye frequency. As temperature is lowered, vibrational transfer should become less overdamped, but so should the low-barrier tunnelling motions discussed above. We thus expect that the motions that give rise to the high- $T$  Boson peak will be mixed with the vibrations of the domain walls, when both are present.

The relative unimportance of interaction between the structural resonances is a key feature of the present microscopic picture that distinguishes it from strong-interaction scenarios [286–288]. The weakness of the interaction results from the low concentration of thermally active resonances, as already mentioned. Still, each resonance is a multi-level system with a rich structure. Transitions within an individual resonance are coupled to transitions within the other resonances, via phonon exchange. This sort of off-diagonal coupling between local resonances lowers the energy [299] and is the mechanism of, for instance, the dispersion interactions or the venerable Casimir effect. Lubchenko and Wolynes [23] (LW) have pointed out that since the number of thermally active resonances in low temperature glasses grows with temperature, so will the total amount of phonon-mediated attraction between spatially separated portions of the sample. Depending on the amount of the local anharmonicity of the lattice, this heating-induced attraction may thus result in a negative thermal expansivity! Negative thermal expansivity is, in fact, observed in low temperature glasses [300]. The magnitude of the “Casimir” effect in glasses depends sensitively on the number of levels within an individual resonance. The results of LW analysis, which explicitly included the ripplon states, are in quantitative agreement with observation thus providing additional support for the RFOT-based microscopic picture of the resonances depicted in Fig. 51(b).

As pointed out in the beginning of this Section, structural *degeneracy* is the key to the presently discussed glassy anomalies, as opposed to effects of aperiodicity in a fully stable lattice per se. We must be mindful that the vibrational response of stable aperiodic lattices generally includes non-affine displacements [301], which *also* violate the Saint-Venant compatibility condition (110) [302]. These modes, which stem from a distribution in local elastic response [303–305], have been proposed as the cause of the Boson Peak, requiring however that the lattice be near its mechanical stability limit [21, 304, 306]. In the absence of such marginal stability, purely elastic scattering seems too weak to account for the apparent magnitude of phonon scattering at Boson Peak frequencies [23, 307, 308]. While the lack of periodicity in glasses undoubtedly contributes to the excess phonon scattering, the presently discussed structural resonances, which are inherently and strongly anharmonic processes, account *quantitatively* for the apparent magnitude of the heat capacity and phonon scattering in a (logarithmically) broad temperature range that covers both the two-level system

and Boson peak dominated regimes. The reader is referred to the detailed discussion of the combined distribution of the TLS parameters  $\epsilon$  and  $\Delta$  from Eq. (242) by Lubchenko and Wolynes [23]. In this treatment, the deviations of both the heat capacity and conductivity from strict linear and quadratic temperature-dependences, respectively, are expected. While the deviation is in the correct direction, its magnitude is somewhat below the observed value.

We note that only a relatively small number of regions host a zero-barrier mode at cryogenic temperatures:  $\xi^3 \int_0^T d\epsilon n(\epsilon) \simeq T/T_g \ll 1$ . This number, however, would be of the order one near  $T_g$  thus seemingly implying that the glass would catastrophically liquefy upon approaching the glass transition from below. This does not happen, of course. In reality, the zero-barrier modes become increasingly dampened with increasing temperature. This damping stems from the interaction of each individual bead movement along the trajectory in Fig. 51(a) with the phonons. Quantitative estimation of this damping does not appear to be straightforward. Empirically, however, the phonons are entirely dampened by the high- $T$  end of the plateau, and so should be elemental tunnelling motions, as the two modes are completely hybridised by that point. Another way of saying that the individual bead motions are dampened to the fullest extent is that each bead is subject to the regular viscous drag from the liquid. Under these circumstances, the calculation for the reconfiguration rate from Section V applies.

## B. The midgap electronic states

The cryogenic anomalies in glasses we have just discussed were a part of a thriving field of research on amorphous materials in the 1970s. Much of this effort seems to have been driven by potential applications in renewable energy. For instance, amorphous silicon was regarded to be a promising candidate material for photovoltaic applications. Another family of amorphous semiconductors was also studied, namely, the so called chalcogenide alloys, which contain “chalcogens,” i.e., elements from group XVI (S, Se, Te) and, often, “pnictogens,” i.e., elements from group XV (P, As, Sb, Bi) and also elements from group XIV (Si, Ge). Archetypal representatives of this group of compounds are  $\text{As}_2\text{S}_3$  and  $\text{As}_2\text{Se}_3$ ; both are good glassformers. More recently, chalcogenides have gained prominence in the context of applications in opto-electronics [3–9] and are often called “phase-change materials,” since their optical and electric properties can be readily “switched” [309] by converting the material between its crystalline and amorphous form.

The chalcogenides were first brought into prominence by the Kolomiets lab, including their remarkable property of being insensitive to doping [272, 310]. This is in contrast with traditional semiconductors, whose conductance can be manipulated by adding elements that prefer to bond to fewer or more atoms than the host species. Note that the prevailing view of amorphous insulators seems that they are not too different from their crystalline counterparts. Within the Anderson localisation paradigm [271, 311], these aperiodic materials can still convey electricity within continuous *mobility* bands made of overlapping orbitals. In addition, there are exponential (Urbach) tails of localised states extending away from the mobility bands, which may serve as efficient traps for charge carriers [273, 274]. Since the tails decay exponentially quickly, one may still speak of relatively well-defined mobility *gaps*.

While the ability of an equilibrated amorphous lattice to accommodate a broad range of bonding preferences of individual atoms is perhaps not too surprising, the apparent strict pinning of the Fermi level in amorphous chalcogenides does beg for explanation. What is even more puzzling, these materials cannot be doped extraneously yet, at the same time, they seem to possess a robust, *intrinsic* number of defect-like, midgap states. The latter states become apparent upon irradiation of an amorphous chalcogenide with high intensity

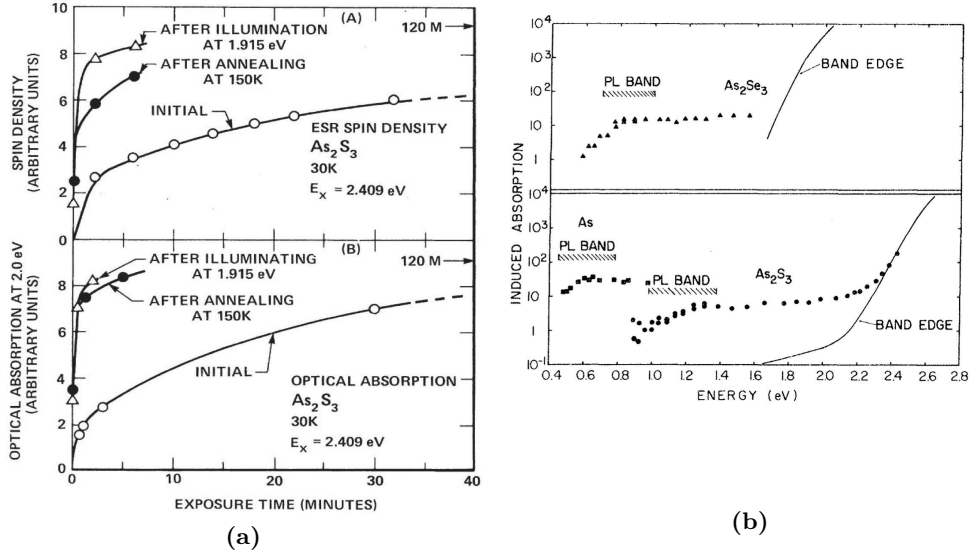


FIG. 53. (a) Time-dependence of photoinduced (a) ESR signal and (b) midgap absorption in amorphous  $\text{As}_2\text{S}_3$  [312]. (b) Midgap absorption in amorphous  $\text{As}_2\text{S}_3$  and  $\text{As}_2\text{Se}_3$  [313].

light at gap frequencies, see Fig. 53. Subsequently, the material begins to absorb light at energies extending to or even below the middle of the forbidden gap. At the same time, a population of unpaired spins emerges whose number and time dependence match those of the midgap light-absorbers. This number seems to saturate at  $\sim 10^{20} \text{ cm}^{-3}$  or one per several hundred atoms, nearly universally. None of these anomalies are seen in pristine samples prior to irradiation, thus implying there are no “dangling bonds.” In contrast, amorphous silicon or germanium films always host substantial numbers of unpaired spins hosted on such dangling bonds [272].

In 1975, Anderson [314, 315] proposed the so-called negative- $U$  model that captures the salient features of these mysterious midgap states. By the model’s premise, there is effective *attraction* between electrons on the same site, which can be formally implemented using the Hubbard model with a negative  $U$ . The mechanism of the effective attraction is similar to that giving rise to conventional superconductivity—i.e., through vibrational modes of the solid—except the electronic orbitals are *not* extended:

$$\mathcal{H} = \epsilon(n_{\uparrow} + n_{\downarrow}) - g(n_{\uparrow} + n_{\downarrow} - 1)q + \frac{kq^2}{2} + U[(n_{\uparrow} - 1/2)(n_{\downarrow} - 1/2) + 1/4], \quad (250)$$

where we have coupled the orbital to a single, harmonic configurational coordinate  $q$  and the electronic energies are measured relative to the Fermi energy of the undistorted lattice, which we set at zero. (Hamiltonian (250) is similar to the one used in Ref.[314], but modified so that the configurational variable  $q$  is unperturbed in the neutral, half-occupied state.) As can be readily seen—after integrating out the configurational coordinate—a sufficiently strong electron-phonon coupling leads to an effective on-site attraction between two electrons (holes) occupying the orbital:

$$U/2 - g^2/2k = U_{\text{eff}} < 0. \quad (251)$$

The on-site energy and phonon-driven stabilisation are generally distributed. Despite the distribution, the Fermi level will be strictly pinned, even if one attempts to dope the materials. This is because the orbital is empty, when  $2\epsilon + U_{\text{eff}} > 0$ , or doubly occupied, when

$2\epsilon + U_{\text{eff}} < 0$ . Further, optical excitations are significantly faster than nuclear dynamics. Thus a filled orbital is not optically active in the midgap range when filled but *will* give rise to midgap absorption when half-filled. In this picture of phonon-driven electron pairing, the same lattice effects give rise to the mobility gap, see also [316]. This is an unwelcome feature—though probably not damning—since the amorphous and crystalline chalcogenides are very much alike in terms of the gap size and detailed bonding patterns, thus implying a similar, *chemical* origin of the forbidden gap. It seems difficult to link these detailed chemical interactions and the simple electron-phonon hamiltonian in Eq. (250). Likewise, it is difficult to see why the concentration of the negative- $U$  centres would be, nearly universally, at one per several hundred atoms. Despite these potential issues, the model is quite elegant in its simplicity and has inspired much further work [317, 318] on identifying specific structural defects, in fiducial reference structures or simulated systems, that could be responsible for both the generic disorder-induced subgap states and negative- $U$  like centres [317–323]. While several of these detailed assignments are roughly consistent with the shapes of ESR spectra in specific compounds [324] they do not self-consistently prescribe how the defects combine to form an actual lattice or address the apparent near universal density of midgap states in many distinct materials and stoichiometries. Conversely, it is puzzling that supercooled melts equilibrated on one hour times should carry a large density of midgap electronic states that are very energetically costly yet do not incur dangling bonds.

More recently, Zhugayevych and Lubchenko [53] took up the notion from the library construction, Subsection V A, that each structural reconfiguration is a set of dynamically connected configurations. Two dynamically connected configurations differ only by the position of one rigid molecular unit, or “bead.” This statement can be made even stronger by noticing that consecutive bead movements must be also nearby in space and thus form a quasi-one dimensional chain in space. If such a chain were broken into two, those two chains would have to be considered as distinct reconfigurations if the gap between the chains is sufficiently large. Indeed, the elastic interaction between two such movements decays as  $1/r^3$  with distance, implying reconfigurations of distinct regions do not interact significantly. This picture can be refined to account for the facilitation effects discussed in Subsection VI A, but in any event, we will see shortly that even if a chain *is* broken into several, shorter chains, the main conclusions are not modified.

One may write down the simplest one-electron Hamiltonian that directly couples the electron density matrix to the mutual displacements of the beads that eventually can reconfigure to a rearrange a region:

$$\begin{aligned} \mathcal{H} = \sum_n \sum_{s=\pm 1/2} & \left[ t(x_n, x_{n+1})(c_{n,s}^\dagger c_{n+1,s} + c_{n+1,s}^\dagger c_{n,s}) + (-1)^n \epsilon_n c_{n,s}^\dagger c_{n,s} \right] \\ & + \mathcal{H}_{\text{lat}}(\{x_n\}), \end{aligned} \quad (252)$$

where one ordinarily assumes that the lattice-mediated bead-bead interaction  $\mathcal{H}_{\text{lat}}(\{x_n\})$  depends quadratically on the their mutual distance. The hopping matrix element  $t(x_n, x_{n+1})$  depends exponentially on the distance  $|x_n - x_{n+1}|$ , but a linear approximation already yields satisfactory accuracy. Eq. (252) is a generalisation of the Su-Schrieffer-Heeger [325] Hamiltonian that incorporates spatial variation in electronegativity  $\epsilon_n = \epsilon \neq 0$  [326]. If the latter is not too large and the electron count is not too different from half-filling, the energy function (252) corresponds to a one-dimensional metal. The latter are known to be Peierls-unstable toward partial dimerization. Hereby, each dimer is held together by a two-centre covalent bond while the dimers attract via a much weaker, closed-shell interaction. This interaction is often called “secondary” [327–330] or “donor-acceptor” [331]. The resulting bond-alternation pattern along the chain leads to the formation of an insulating gap. There are two ways for the chain to dimerize, call them state 1 and 2, see Fig. 54(a). (If the electronegativity variation is sufficiently strong, the chain instead becomes an ionic insulator

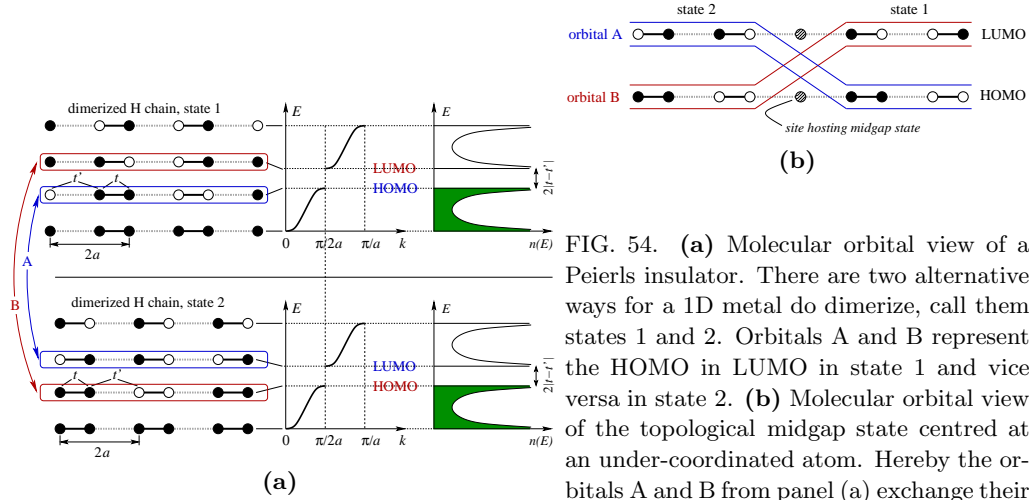


FIG. 54. **(a)** Molecular orbital view of a Peierls insulator. There are two alternative ways for a 1D metal to dimerize, call them states 1 and 2. Orbitals A and B represent the HOMO in LUMO in state 1 and vice versa in state 2. **(b)** Molecular orbital view of the topological midgap state centred at an under-coordinated atom. Hereby the orbitals A and B from panel (a) exchange their HOMO-LUMO identities at the malcoordinated atom. The effective gap vanishes and results in a mid-gap state, at that atom.

with a gap largely determined by the electronegativity differential  $\epsilon$  [326].)

But what happens if the very same chain happens to dimerize inhomogeneously, so that different portions of the chain happen to settle in distinct states? The atom at the interface between the two states is either over-coordinated or under-coordinated. Heeger and coworkers [291, 325] have shown, in the context of trans-polyacetylene, that there appears a midgap state centred on such a malcoordinated atom. The origin of this midgap state is topological and can be traced back to a rather general setup, in which a fermionic degree of freedom is coupled to a classical degree of freedom which is subject to a bistable potential [332]. There is a heuristic way to see the emergence of the midgap state using simple notions of the molecular orbital theory, as we illustrate in Fig. 54. According to panel (a), if the two orbitals at the edge of the forbidden gap of a Peierls insulator—call them A and B—are HOMO and LUMO in state 1, then they switch their roles in state 2. In panel (b), we observe that at the (undercoordinated) atom at the boundary between states 1 and 2, the molecular terms corresponding to orbitals A and B, respectively, must cross in the middle of the gap, implying there is midgap state at zero energy, which is centred on the undercoordinated atom. This molecular orbital-based picture demonstrates that not only will the midgap state be in the middle of the gap—given the electron-hole symmetry—but also that the orbitals from the valence and conduction band contribute in equal measure to the wavefunction of the midgap state. The state is thus robust with respect to effects of electron-electron interactions, among others.

This robustness is of topological origin: First of all, the malcoordination cannot be removed by elastic deformation, thus automatically violating the Saint-Venant compatibility condition (110). Another topological signature of the malcoordination is explicitly seen using a continuum limit of the Hamiltonian exhibited in Eq. (252), viz.,  $\mathcal{H} = -iv\sigma_3\partial_x + \Delta(x)\sigma_1 + \epsilon(x)\sigma_2$  [326, 333]. Here,  $\sigma_i$  are the Pauli matrices, while  $-iv$ ,  $\Delta(x)$  and  $\epsilon(x)$  correspond, respectively, to the kinetic energy, local one-particle gap and variation in electronegativity. The local gap  $\Delta(x)$  is space dependent and, in fact, switches sign at the defect, thus corresponding to a rotation of a vector  $(\Delta, \epsilon)$ . (This space-dependent gap is the energy difference between A and B orbitals in Fig. 54(b).) The orientation angle of this vector is the topological phase associated with the defect; it follows a solitonic profile across the interface. This notion shows that in addition to being robust with respect to local chemistry, the defects are stable against mutual annihilation unless they travel along



exactly the same chain. Indeed, the phases of defects travelling along different paths can not cancel.

The midgap states are remarkable in several ways: First of all, they exhibit a charge-spin relation opposite from that expected for a regular fermion: A neutral defect is half-filled and thus has spin 1/2; a charged state is paramagnetic. From a chemist's viewpoint, a neutral defect is merely a free radical solvated in a solid matrix. Last but not least, the wave-function of the midgap state is surprisingly extended. Indeed, a simple estimate shows that a generic bound state at  $\sim 1\text{eV}$  below a continuum should be of atomic dimensions. In contrast, both the wavefunction and the solitonic deformation pattern of the 1D lattice are about 10 lattice spacings across, for a semiconducting material [53]. (In trans-polyacetylene, this extent is as large as 20 lattice spacings because of the low effective mass of the electron in this material.) Thus, the malcoordination is evenly distributed over a considerable distance. Note that the bond length at the centre of the malcoordination is about midway between that of the long and short bond, also implying an intermediate bond strength.

In the ZL scenario, the effective attraction between two electrons/holes occupying the midgap state, if any, is not directly tied to the magnitude of the gap. Instead, it is a relatively subtle effect that stems from the attraction between a charge and a neutral radical embedded in a dielectric medium. While one expects such an attraction when the radical-plus-matrix system is sufficiently polarisable, its presence is not a given. We will return to this point shortly. In the most significant contrast with Anderson's phenomenological negative- $U$  model and the subsequent ultralocal defect views [317–323], the midgap states intrinsically stem from the structural degeneracy of the lattice and are topologically stable. The concentration of the midgap states is determined by the concentration of the domain walls near the glass transition, an *equilibrium* quantity:

$$n_{\text{DW}}(T_g) \simeq 1/\xi(T_g)^3 \simeq 10^{20}\text{cm}^{-3}, \quad (253)$$

consistent with observation. For the ZL [53] scenario to work, at least two basic requirements must be fulfilled by the material: (a) the bonds along the chain should not be saturated, and (b) the insulating gap should not be too large, since in this case the chain is an ionic insulator, as opposed to a Peierls insulator. Only one family of known glassformers seems to satisfy these restrictions, namely, the chalcogenides. Already this can be used to argue circumstantially for the presence of the midgap states in these materials.

It turns out that in the specific case of chalcogenide glasses, the specific atomic motifs leading to the midgap states can be directly identified based on a relatively simple chemical yet constructive picture. As the first step in their argument, Zhugayevych and Lubchenko [29] (ZL) argue that these materials are symmetry broken and distorted versions of much simpler, “parent” structures defined on the simple cubic lattice. This idea builds on the work of Burdett and coworkers on the structure of solid arsenic and electronically similar compounds [334, 335]. Similarly, the crystal of  $\text{As}_2\text{Se}_3$  can be thought of as a distorted version of the parent structure in Fig. 55(a), in which some of the vertices are occupied by vacancies. Each link in the parent structure corresponds with a covalent bond in the actual, distorted structure, whereas a gap will give rise to a secondary bond. The actual, distorted structure is much more complicated than its parent, see Fig. 55(b). The cause of the symmetry breaking in these 3D structures can no longer be traced with confidence to the Peierls instability, especially in view of the significant  $sp$ -mixing in these compounds [336], see, however, Ref. [337]. Still, the very fact of symmetry breaking between two adjacent covalent and secondary bonds that are nearly co-linear is documented on thousands of compounds [329].

Much as the crystal of  $\text{As}_2\text{Se}_3$  can be thought of as a distorted version of the parent structure in Fig. 55(a), chalcogenide glasses can also be thought of as being distorted versions of parent structures in which atoms and vacancies are placed aperiodically. In either case, a pnictogen (chalcogen) forms three (two) covalent bonds with its nearest neighbours and

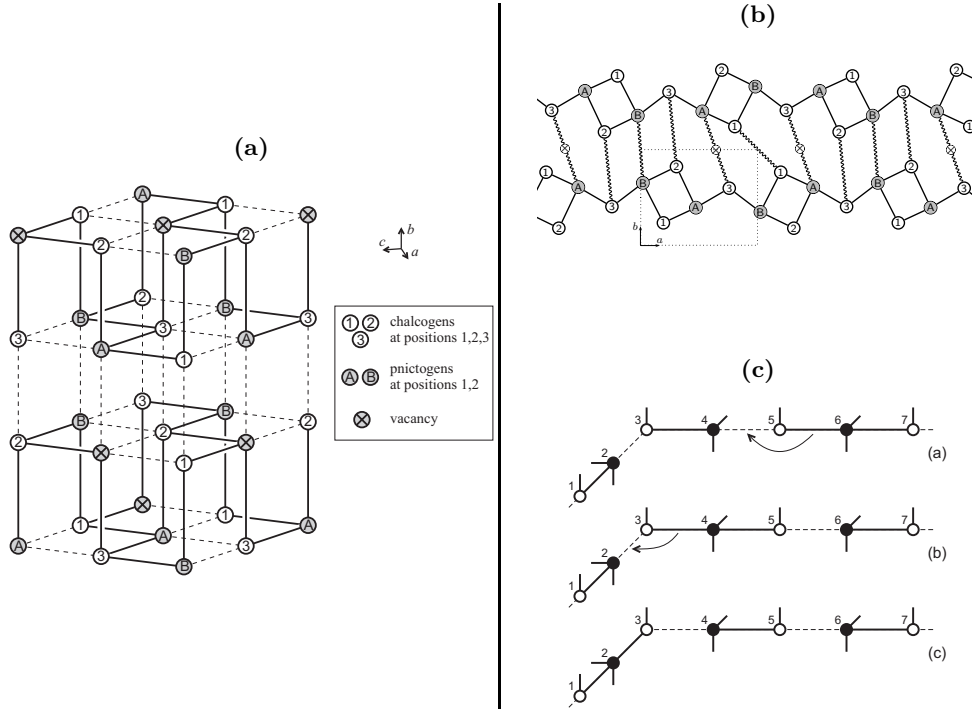


FIG. 55. **(a)** A parent structure for  $Pn_2Ch_3$  crystal ( $Pn=As$ ,  $Ch=Se$ ,  $S$ ) [29]. The bond placement represents a particular symmetry breaking pattern. **(b)** Side view of the actual  $As_2Se_3$  structure. The wavy lines indicate inter-layer nearest neighbours in the parent structure, except the A-3 link, which is through a vacancy. The lengths of the links are only partially indicative of the actual bond length because the bonds are not parallel to the projection plane. From Ref. [29]. **(c)** Illustration of the motion of an overcoordination defect by bond-switching along a linear chain (from atom 6 in (a) to atom 4 in (b)) or making a turn (from atom 4 in (b) to atom 2 in (c)). From Ref. [54].

a few secondary bonds [327] with next nearest neighbours. The covalent bonds must be approximately orthogonal. The above notion directly traces the thermodynamic stability of glasses to the same interactions that underlie the stability of the crystal. This commonality between periodic and aperiodic solids has been a recurring theme in this article. In contrast with the crystal, however, the bonding in the glass is typically somewhat weaker, consistent with its lower density (4.57 vs. 4.81-5.01 g/cm<sup>3</sup> for crystalline and amorphous  $As_2Se_3$  respectively). More importantly, the entropy stemming from the two alternative ways to perfectly dimerize the chains in the parent structure scales with the sample's *area* and, hence, is only sub-thermodynamic. Defects in the alternation pattern must be present to account for the excess liquid entropy of a glassy chalcogenide alloy. Such malcoordination defects are automatically supplied by the domain walls of the mosaic! Consistent with the mobility of the domain walls, the malcoordination motifs can move and make turns by switching bonds, very much like in the Grotthuss mechanism of bond switching in water, see Fig. 55(c). This is an explicit demonstration of how a reconfiguration takes place without breaking bonds. In addition, these observations enable one to fix the bead count at, approximately, one bead per arsenic, consistent with its value implied by the RFOT theory [54]. We remind that the calorimetric bead count from Eq. (96) does not work very well in the chalcogenides. Thus, we should expect that deciding on the identity of the effective ultraviolet cutoff of the theory is more complicated than counting the number of degrees of freedom frozen-in at the liquid-to-crystal transition and may involve system-specific microscopic considerations.

Thus in addition to being aperiodic, a parent structure for chalcogenide glass must also

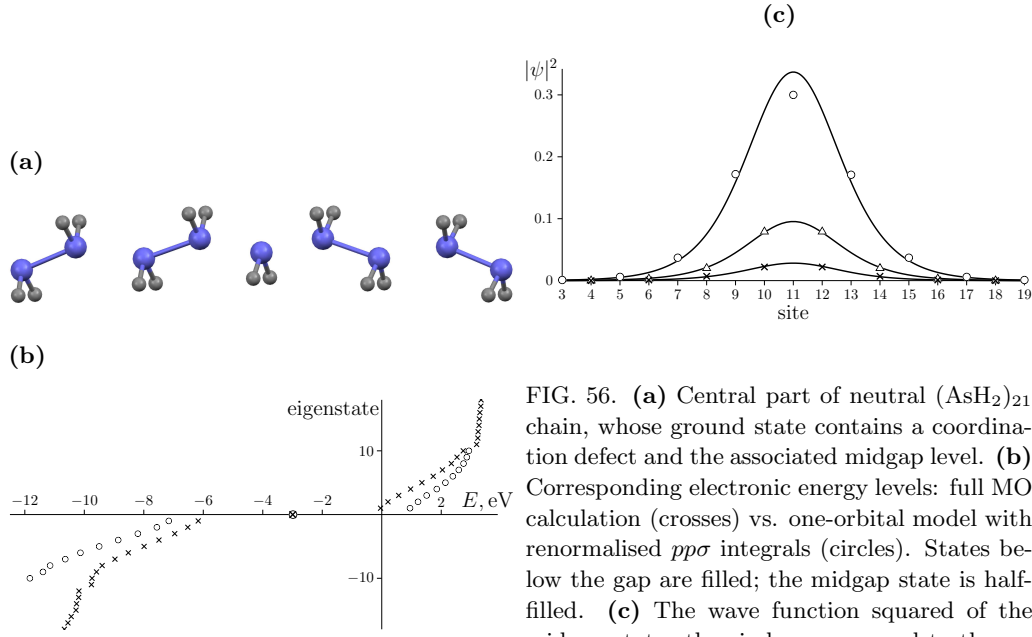
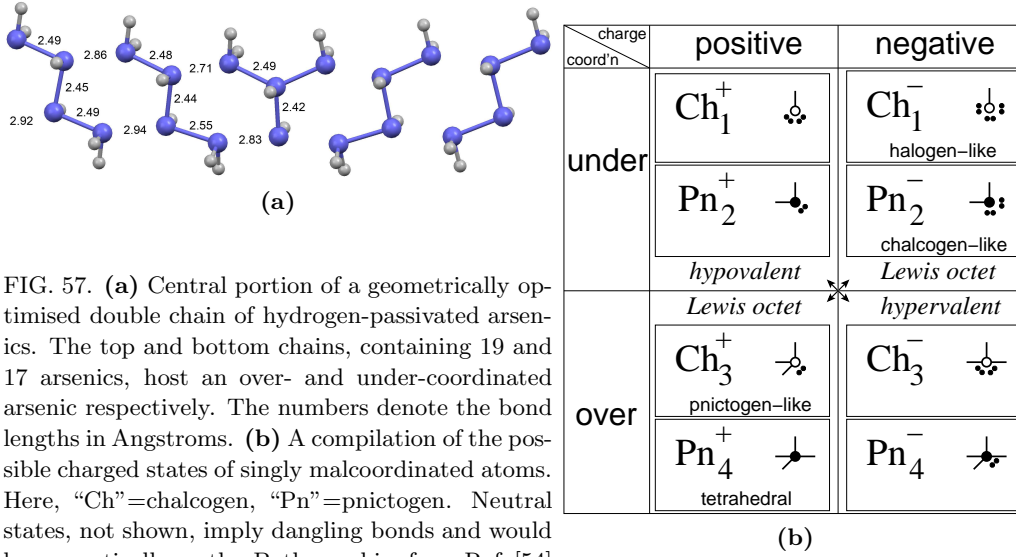


FIG. 56. **(a)** Central part of neutral  $(\text{AsH}_2)_{21}$  chain, whose ground state contains a coordination defect and the associated midgap level. **(b)** Corresponding electronic energy levels: full MO calculation (crosses) vs. one-orbital model with renormalised  $pp\sigma$  integrals (circles). States below the gap are filled; the midgap state is half-filled. **(c)** The wave function squared of the midgap state: the circles correspond to the arsenics'  $p_z$  atomic orbitals (AO) (total contribution 73%), triangles As  $s$ -AO's (21%), crosses – the rest of AO's (6%). Both figures from Ref. [54].

contain under(over)-coordinated atoms. On a pnictogen, for instance, such malcoordination corresponds to two colinear secondary (covalent) bonds, along any of the three principal axes. In actual distorted structures, the malcoordination is difficult to detect because it is distributed over a large region, consistent with the general difficulty in defining coordination in aperiodic lattices. When  $sp$ -mixing is relatively weak, the distorted cubic lattice can be presented as a collection of long stretches of distorted one-dimensional chains. The rest of the lattice, to a good approximation, renormalises the parameters of the chain, viz., the on-site energies and hopping integrals [29, 54]. Using these notions of quasi-one dimensionality, a concrete example of a malcoordination pattern can be obtained with the help of an actual 1D chain of  $pp\sigma$ -bonded molecules, such as the hydrogen-passivated arsenics in Fig. 56. As expected, a neutral chain hosts an unpaired electron in its non-bonding orbital. The latter orbital is indeed quite delocalized.

It is interesting to note that interacting malcoordinated defects can produce tetrahedral bonding patterns; the latter are not typical of the crystalline chalcogenide alloys, in which the bonding is primarily distorted-octahedral, see Fig. 57(a). It has been suggested that such tetrahedral patterns emerge following the glass transition in phase-change materials [4].

As already mentioned, a half-filled defect is essentially a free radical embedded in a dielectric medium and would be expected to be stabilised by adding a charge, given sufficient polarisability. Such stabilisation is imperative in order that the malcoordinated atom be charged and ESR-inactive in its ground state. Consistent with these notions, heteroatomic chalcogenides, which exhibit spatial variation in electronegativity, are better glassformers than elemental arsenic, for instance. The issue of the precise interaction between a radical and a charge is, generally, a subtle quantum-chemical problem. Still there is an important limit in which this question can be resolved using a very old chemical approximation, namely the Lewis octet rule. In the ultra-local limit, the charged states of chalcogens and pnictogens can be easily visualised as in Fig. 57(b). According to this graphical table, there are several charged configurations that exactly complete the Lewis octet and thus are predicted to be



stable. There are also two sets of configurations that should be formally designated as hypo- or hypervalent. The double arrows in the table indicate configurations that would be mutually attractive and form a stable pair like that shown in Fig. 57(a), in which a pair  $\text{Pn}_4^+ \text{Pn}_2^-$  is shown. The ultralocal limit, although ultimately being an oversimplification, is also instructive in that it allows one to connect the present discussion with early, phenomenological proposals on specific chemical motifs responsible for the midgap states [317, 318].

To summarise, the presence of the midgap states helps rationalise a number of electronic anomalies in amorphous chalcogenides [320] in a unified fashion. Perhaps the most important of these are the observation of a light-induced paramagnetic signal and midgap absorption of light. The outcome of the analysis [53] of the simple Hamiltonian (250) is also consistent with the apparent existence of two distinct types of photoluminescence and their fatigue in the chalcogenides [338–340]. The RFOT-based framework predicts a near universal density of the midgap states; this density is intrinsic and originates from the inherent density of cooperatively rearranging regions in an equilibrated supercooled liquid. The present microscopic picture and the much earlier, phenomenological negative- $U$  model [314, 315] share the property of pinning the Fermi level close to the middle of the gap thus explaining why conventional doping of chalcogenides is inefficient [272, 310]. Although the states are not very close to the band edge, there is no subgap absorption because of the Franck-Condon effect: The optical excitation is faster than the atomic movements, implying the energy needed to excite the electron from a filled level also includes the work needed to deform the lattice to the configuration it had when the level is half-filled to when it becomes completely filled. When half-filled, the states *will* absorb light at subgap frequencies [53].

Finally, the extent of the midgap states in chalcogenides scales inversely proportionally with the gap [53, 291, 333]. In view of the effective attraction between electrons, one expects that at high enough pressure, the midgap orbitals will overlap leading to superconductivity [53]. Chalcogenides are known to become superconducting at high pressure [341]. It will be interesting to see whether this very quantum phenomenon originates in things glassy.

### XIII. SUMMARY AND CONNECTION WITH JAMMED AND OTHER TYPES OF APERIODIC SOLIDS

In an informal remark dating from 1995, P. W. Anderson writes [342]: “The deepest and most interesting unsolved problem in solid state theory is probably the theory of the glass and the glass transition. This could be the next breakthrough in the coming decade.” It is probably fair to say that the problem of the structural glass transition has been as interesting and challenging as it has been controversial. So much so that it found a way into mass media some thirteen years after Anderson’s remark was published [343].

The reader has undoubtedly noticed that the present author feels significantly more secure about the current status of the theory of the glass transition than what the readers of the New York Times might infer from several less-than-optimistic views expressed in Ref. [343]. Although the RFOT theory uses approximations, the physical picture of the structural glass transition presented by it is constructive and quantitative. It uses well-established concepts of the classical density functional theory (DFT) complemented by more recent insight about systems with relatively complicated free energy landscapes; hereby the distinct free energy minima correspond to long-lived, but not infinitely-lived states. Although it is often difficult to treat finite-lifetime states using methods developed in *equilibrium* thermodynamics, such methods become quantitative (and physically transparent) given sufficient time scale separation between motions of individual particles and the progress coordinate that describes the escape from the long-lived states. Many examples of successful quantitative descriptions of such long-lived states exist, such as the transition state theory [199, 200, 296, 344], and, in particular, as applied to nucleation phenomena. The RFOT description takes advantage of the accuracy of the transition state theory to determine the distribution of the relaxation rates and cooperativity sizes in glassy liquids, without using adjustable parameters; in turn this allows one to predict the glass transition temperature (on a given timescale) using experimentally determined values of a specific quantity, viz., the excess liquid entropy. This quantity is defined and measured without reference to the glass transition itself. It should not be held against the theory that it cannot (yet) predict the configurational entropy for actual compounds, but only for model substances. Much the same way, we do not hold against existing theories of liquid-to-crystal transition that they cannot determine the melting point for actual compounds, but only can predict melting points for model substances with known interactions.

We have seen that the complicated free energy landscape of a glassy liquid begins to form when a uniform liquid undergoes a breaking of the translational symmetry, upon which the equilibrium density profile is no longer flat but consists of disparate, narrow peaks; the locations of the peaks form an aperiodic lattice. The breaking of the symmetry is driven by steric effects, as can be shown using independent arguments from the classical density functional theory, the mode-coupling theory, and a symmetry-breaking perspective afforded by the Landau-Ginzburg expansion. The density-driven symmetry breaking is entirely analogous to that during a density driven transition from the uniform liquid to a periodic crystal, although somewhat less so when the crystal structure is very open and mostly determined by directional bonding. In contrast with the periodic crystallisation, the peaks in the aperiodic structure are not entirely stationary but move about in an intermittent, cooperative fashion; if watched for a sufficiently long time, the liquid density profile becomes uniform again. These motions correspond to transitions between distinct metastable free energy minima and, hence, are driven by the complexity of the free energy landscape. For this special mechanism to work, the number of free energy minima must scale exponentially with the region size; the log-number per particle is called the configurational entropy  $s_c > 0$ .

This vast structural degeneracy introduces new physics in the problem, along with new length and time scales. It is entropically unfavourable for a glassy system to reside in

any given free energy minimum forever. The system thus undergoes local transitions to alternative metastable states. In the mean-field limit, it is possible to think of the liquid as a mosaic of regions, each of which is occupied by a structure corresponding to one of the mean-field free energy minima. The interfaces between the mosaic cells are made up of configurations corresponding to the barrier in the bulk free energy separating the minima. In finite dimensions, the picture is no longer as simple, but the liquid can still be thought of as a mosaic of regions characterised by relatively low free energy density separated by regions at relatively high free energy density. Each stable region can be thought of as being trapped in a state produced by *negative* free energy fluctuations, from a relatively high free energy state typical of the liquid that just begins to enter the landscape regime. Not every negative fluctuation would be long-lived, however, but only such that *also* happens to coincide with a transition to a specific free energy minimum. This is something that would be impossible in a landscape-free system that has a sub-thermodynamic number of alternative minima. Matching the magnitude of the stabilisation due to the fluctuation with the entropic stabilisation due to the complexity of the landscape,  $\delta G = Ts_c N$ , yields the size  $N^*$  of the region that was stabilised by the fluctuation. This size is finite because the fluctuation size scales sublinearly with  $N$ :  $\delta G = \gamma\sqrt{N}$ . (Note the equation  $\gamma\sqrt{N} = Ts_c N$  has no finite solutions when  $s_c$  is strictly zero.) Conversely,  $N^*$  is the region size that must be reconfigured (in equilibrium) for the liquid to escape the free energy minimum it is currently trapped in. It is the latter perspective that is worked out in the microscopic picture presented here. It is shown that the escape from the current minimum can be thought of as an activated, nucleation-like event driven by the multiplicity of the free energy minima,  $-Ts_c N$ , but is subject to a mismatch penalty between the initial and final states. If one takes the stabilised state as the free energy reference, the mismatch penalty to flip a region of size  $N$  is the typical magnitude of the free energy fluctuation:  $\gamma\sqrt{N}$ , Eq. (153). The resulting escape barrier is simply  $F^\ddagger = \gamma^2/4s_c T$ . This formalism yields many quantitative predictions, including, in particular, the  $\alpha$ -relaxation barrier and the cooperativity length and those predictions can directly be extended to non-equilibrium situations, such as ageing. A great deal of these predictions have to do with the local *fluctuations* in the structural degeneracy, which are directly reflected in the heat capacity jump at the glass transition. Hereby the intrinsic connections are revealed between the deviations from the Arrhenius temperature dependence of  $\alpha$ -relaxation, relaxations' exponentiality, and the fluctuation dissipation theorem.

Although transitions to both periodic and aperiodic crystal are discontinuous—the restoring force in response to finite wavelength deformation becomes finite via a discrete jump—the onset of measured rigidity in glassy liquid is gradual. This is because the spatial extent and lifetime of the long-lived structures increase continuously with lowering temperature and/or increasing pressure. The material becomes macroscopically rigid, if quenched sufficiently below the glass transition temperature  $T_g$ . This is because the barrier for activated transitions, which is about  $35 \dots 39 k_B T_g$ , becomes very large compared with the ambient temperature, not because the structure represents a unique energy minimum. (In fact, glasses are vastly structurally degenerate, in contradistinction with periodic crystals.) In this way, the rigidity of glasses and periodic crystals are subtly different. Still, relics of the structural reconfigurations that give rise to liquid flow above the glass transition survive down to very low, sub-Kelvin temperatures. These relics can be counted and turn out to fully account for the mysterious structural resonances people have phenomenologically associated with the so called two-level systems. The physical boundaries of the reconfigurations—or domain walls—are interesting objects in themselves: On the one hand, their vibrations quantitatively account for the famous Boson peak. (These vibrations can be thought of as the Goldstone modes that emerge when the mosaic forms.) On the other hand, the domain walls can host very special electronic states under certain circumstances that are physically

realised in amorphous chalcogenide alloys. The latter alloys have come back into prominence owing to their potential as phase-change memory materials.

As just said, the emergence of the landscape is the result of a discontinuous transition and, in fact, could be thought of an avoided critical point, see Fig. 7. In the absence of strongly-directional bonding, the criticality is avoided in *equilibrium* owing to steric effects, which stabilise locally dense structures. This can be seen using already a Landau-Ginzburg expansion and, quantitatively, the classical DFT. A quantitative criterion of the proximity to the critical point is the ratio of the volumetric particle size  $a$  and the magnitude  $d_L$  of the vibrational displacement near the mechanical stability limit of the aperiodic solid. In the case of aperiodic solids it is exactly the inverse of the venerable Lindemann ratio. By Eq. (83), the  $(a/d_L)$  ratio scales linearly with the dimensionality of space, up to a logarithmic correction and factor of order 1. In 3D, both experiment and calculation yield, nearly universally,  $(a/d_L) \simeq 10^1$  for a solid in equilibrium with the corresponding uniform liquid, be the solid periodic or aperiodic. For the liquid-to-solid transition to be continuous, this ratio would have to be close to  $10^0$ . The  $(a/d_L)$  ratio reappears under several guises during the analysis, because its square corresponds with the elastic modulus of the substance in terms of  $k_B T$ , by equipartition:  $(a/d_L)^2 \simeq K a^3 / k_B T$ . ( $K$  is the bulk modulus.) We have seen that this ratio corresponds with the excess relaxation time in a liquid compared to the corresponding solid. This mismatch is behind the kinetic catastrophe of the mode-coupling theory. The  $(a/d_L)^2$  ratio also enters in the expression for the escape barrier  $F^\ddagger$  since, approximately,  $\delta G^2/N \equiv \gamma^2 \propto K$ . Appropriately, the activated reconfigurations do not involve breaking of individual bonds; in fact  $d_L \simeq a/10$  is comparable to the typical vibrational magnitude. Despite the near harmonic nature of the motions of individual atoms, the overall reconfiguration event is strongly anharmonic, see Fig. 25(a). Specific microscopic realisations of such chemically-mild local motions have been identified. For instance, a covalent bond in glassy chalcogenides can gradually weaken into a secondary and, then, a van der Waals bond, before finally rupturing [29, 54]. This is quite similar to the Grotthuss mechanism of bond switching in water. Another often-cited example is the rotations of the  $\text{SiO}_{4/2}$  tetrahedra in glassy silica, during which covalent bonds are not broken but only distorted following a reconfiguration event. Yet another way to look at this chemically-interesting aspect of the landscape regime is provided by very very old samples of amber, which exhibit the cryogenic two-level systems and Boson peak despite the significant amount of cross-linking that took place over  $10^8$  years ago [345].

The  $(d_L/a)$  ratio may thus be legitimately thought of as the small parameter of the theory, non-withstanding the subtlety associated with the fact that this small parameter is not fixed upfront but is self-generated as a result of a *discontinuous* transition. Consistent with the lack of critical-like fluctuations, the correlation length for fluctuations in glassy liquids, has been shown to be comparable to the molecular length scale [32]. As a result, the cooperativity can be argued to be somewhat trivial, viz., due to ordinary Gaussian fluctuations. (A case for sub-dominant fluctuations stemming from wandering of the domain walls has been made recently [209].)

In contrast with substances in the landscape regime, amorphous films made of a poor glass-former that favours open structures, such as silicon or water at normal pressure, would rearrange by *bond-breaking*. Accordingly, energy quantities reflecting bond strength—as opposed to bond elasticity—would determine the barrier. (Note bond strength and elasticity are correlated in actual materials [105], because the atomic size varies relatively little across the periodic table and so the depth of a bounding potential must correlate with its curvature at the bottom.) Materials with open structures largely avoid entering the landscape regime because of the relative unimportance of the steric effects and thus are “unaware” of the aforementioned criticality in the first place. The bond directionality could be so strong that the liquid could expand upon freezing. Even in supercooled silicon, coordination decreases

with cooling [346]. *Amorphous* films made of such directionally bonding particles are even more open than the crystal and exhibit dangling bonds. In such films, which can be made by rapid quench or by sputtering on a cold substrate, steric effects are even less important than in corresponding crystals. In a way, one can think of such amorphous films as very cross-linked gels or vulcanised rubbers. Although generally aperiodic, these materials may be in the landscape regime only to a marginal extent. The steric interactions set the nearest neighbour distance but not the coordination pattern itself; as a result the films reconfigure predominantly by bond breaking. These notions are consistent with the apparent scarcity of cryogenic excitations in silicon and germanium films [210, 293, 294]. The latter excitations are predicted to be intrinsic (and quantum!) features of landscape systems. To summarise, materials that favour open structures avoid the landscape regime by either crystallising or forming gel-like aperiodic structures. While such aperiodic open structures may share some properties with glasses made by quenching an equilibrated liquid, these properties are expected to be quite system-specific, in contrast with glasses, whose key microscopic properties are set by the cooperativity length at the glass transition and the glass transition temperature itself.

To avoid confusion we note that materials with very directional bonding may be poor glassformers at ordinary pressures but could be vitrified more readily following pressurisation [138–141], which would make steric repulsion more prominent. This is not a general rule, however. For instance, elemental calcium, which is close-packed at normal pressure, becomes simple-cubic at sufficiently high pressures, supposedly due to a density-induced hybridisation of electronic orbitals. In any event, it is requisite that an open structure undergo a pressure-induced phase transition into a phase with higher coordination *before* it can enter the landscape regime; the barrier for such a transition is largely energetic because bond breaking must take place. Polymers seem to be a mixed case in that while exhibiting extremely anisotropic bonding in one direction, they can usually pack quite well in the other two dimensions. Indeed, polymers exhibit a broad distribution of glassiness vs. local ordering. Many polymers do exhibit the cryogenic two-level excitations [276], see Fig. 50(a).

In the opposite limit of completely isotropic interactions—as could be realised, for instance, in Lennard-Jones liquids—steric effects contribute prominently to the free energy, near melting, and so the aperiodic-crystal phase would seem to be easily accessible from the uniform liquid phase. However, the nucleation barrier for *periodic* crystallisation is very low in such systems because monodisperse spheres line up in close-packed structures very readily. Thus isotropically-interacting, monodisperse particles avoid vitrification when quenched not too rapidly, owing to *periodic* crystallisation, similarly to silicon. Yet in contrast with silicon, crystallisation in rigid systems is induced by the very same forces that cause the RFOT transition to the landscape regime. To appreciate the distinction more clearly, we note that if forbidden to crystallise—by controlling local orientational order, for instance [347]—silicon would still fail to enter the landscape regime but, instead, form a gel-like film even if cooled leisurely. In contrast, hard spheres would undergo the RFOT transition and eventually vitrify under such circumstances; we saw this explicitly in Subsection IV A.

What should we think of an amorphous sample made of monodisperse spheres? Such structures can be readily made with colloids, because of particle-solvent friction, or by ultra-fast quenching on a computer. The resulting structure is caught in a relatively shallow, high altitude minimum and could catastrophically relax into a denser structure in the presence of thermal fluctuations. Conversely, at zero-temperature or infinite pressure such structures would become and, consequently, *jammed*. Consistent with these systems being far away from equilibrium, there is no longer one-to-one correspondence between density and pressure, at constant temperature. In a mean-field limit, the least one may do is to use a *triad* of intensive variables to describe the state of the system, such as pressure-density-temperature or pressure-coordination number-temperature, etc.



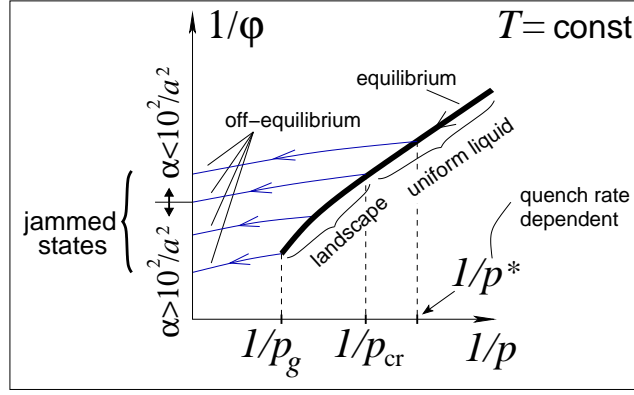


FIG. 58. The thick solid line shows the pressure dependence of the inverse filling fraction as resulting from a relatively (but not infinitely) slow quench. By varying the speed of quenching, one may control the density and pressure,  $p^*$ , at which the liquid is brought out of equilibrium, as shown by the thin solid lines. Apart from ageing, there is one-to-one correspondence between the state at which the system vitrified and the resulting jammed structure. Given a high enough quench rate, however, the uniform liquid can be brought out of equilibrium at a density *below* the density  $\rho_{cr}$ , at which the landscape regime sets in in equilibrium. Under these circumstances, there is no longer direct correspondence between the  $p = \infty$  jammed states and states equilibrated in a specific metastable free energy minimum. Roughly speaking, the jammed states will sample portions of the phase space characterised by a relatively small value of the force constant  $\alpha$  of the effective Einstein oscillator. These high enthalpy states are vestiges of the avoided critical point from Fig. 7. This is a non-meanfield effect, c.f. the mean-field analysis of Mari et al. [20], see also Ref. [170].

The jammed states could be thought of, generally, as corresponding to states near the spinodal in  $F(\alpha)$  in Fig. 13(a), but with the quantity  $\alpha^\dagger a^2 \simeq \alpha_0 a^2 \simeq (a/d_L)^2$  now distributed in a range  $10^0 \dots 10^2$ , as opposed to the equilibrium value of  $10^2$  or so. This correspondence can be seen using, as a starting point, results of the elegant mean-field analysis of Mari, Krzakala, and Kurchan [20]. By solving a liquid model defined on a Bethe tree, Mari et al. have explicitly shown that one may think of a jammed state as a liquid first equilibrated in the landscape regime and then rapidly compressed at constant temperature. According to this result, we may associate to each jammed state an *equilibrated* state and the corresponding values of  $\alpha^\dagger$  and  $\alpha_0$ , see Fig. 58. In the mean-field limit, the smallest possible value of  $\alpha$  is that at the density  $\rho_A$  at which the metastable minimum in  $F(\alpha)$  just begins to appear. In finite dimensions, the landscape regime sets in within a finite density interval centred at  $\rho_{cr} > \rho_A$ , as is reflected in Fig. 58. (The crossover is usually well separated from the sharply defined  $\rho_A$  [35].) Yet given a fast enough speed of compression, a liquid can be jammed starting also from a state *below*  $\rho_{cr}$ , since metastable structures already appear but quickly “melt” into the uniform liquid characterised by smaller values of  $\alpha$ . The faster the quench speed, the less stable the resulting structure will be. The important thing is, if the density at which the liquid fell out of equilibrium is below  $\rho_{cr}$ , one must associate the jammed structure not with a particular, equilibrium  $F(\alpha)$  but, instead, a set of location-specific  $F(\alpha)$ ’s, some of which are necessarily non-equilibrium. Because the system undergoes significant fluctuations toward the uniform liquid state, there will be many regions in which the typical value of  $\alpha$  would be significantly less than the equilibrium  $10^2/a^2$  and, in fact, as small as  $10^0/a^2$ . The latter value is pertinent to configurational equilibration in uniform liquids, which occurs by particles exchanging their positions. Alternatively said, that  $\alpha^\dagger a^2 \simeq \alpha_0 a^2$  could be as small as 1 signifies that particles could move a distance comparable to their size, after the liquid is unjammed, in a sort of a local avalanche. We have explicitly seen in Fig. 20(d) how small values of  $\alpha$  stem from fluctuations away from the landscape regime. Alternatively, one

may think of such fluctuations as arising from local reduction in dimensionality, according to Eq. (83).

The smallness of the effective  $\alpha$  is a key difference between a jammed and vitrified system. We reiterate that because the system is off-equilibrium, there is no intrinsic relation between the stiffness of the jammed system and the value of  $\alpha_0$  of the type from Eq. (30); the stiffness becomes infinitely high in the  $p \rightarrow \infty$  limit whereas  $\alpha_0$  remains finite. Said in simpler terms, the spacing between (vibrating) particles in contact, in a jammed structure, can be made arbitrarily small while the structure remains practically the same. The particle displacement upon unjamming, which is largely determined by the structure, is thus decoupled from the vibrational motions.

Now take the zero temperature limit. Because the system is confined to an *individual* free energy minimum at  $T = 0$ , before it escapes to a much lower enthalpy state, the correlations should be mean-field like. This implies, among other things, that the relaxation time should scale quadratically with the correlation length,  $\tau \propto \xi_A^2$ , as follows from the mean-field Onsager-Landau ansatz for the relaxation of the pertinent order parameter  $\phi$ :  $\dot{\phi} \propto -\delta F/\delta\phi$  and Eq. (3). Given the decoupling between thermal vibration and density, it is convenient to choose the filling fraction as the order parameter. Now, the scaling  $\xi_A \sim |\phi_A - \phi|^{-1/4}$  applies near a mean-field spinodal [348], where  $\phi_A$  is the location of the metastable minimum. Thus we obtain  $\tau \propto |\phi_A - \phi|^{-1/2}$ . This is consistent with the  $\omega^* \propto |\phi_A - \phi|^{1/2}$  scaling discussed in Refs. [19, 349], where  $\omega^*$  is the infra-red edge of stable harmonic modes, and also with recent unjamming simulations of soft spheres by Ikeda, Berthier, and Biroli [350], in the low temperature limit. Although reasonable, the above discussion is clearly qualitative and, certainly, is not a full-fledged field theory. Such a field theory would have to contain exponentially many order parameters and appears to be a complicated undertaking. Some progress toward obtaining such a field-theoretical description of the landscape regime in *finite* dimensions has been achieved recently with the help of replica techniques, see Refs. [209, 351] for instance.

In light of our earlier statements that the quantity  $\alpha_0 a^2$  reflects the sharpness of the first order transition from liquid to solid, we may conclude that, in fact, the lower density jammed states are vestiges of an avoided critical point. That the critical point is destroyed in equilibrium, means in thermodynamic terms that the critical fluctuations correspond to higher free energy states. (Sometimes, such high free energy states may still correspond to *conditional* equilibrium, such as the liquid-liquid separation in protein solutions mentioned in Subsection IV B.) We have argued in Subsection III A that the critical point is pushed down to zero temperature, which implies the solid formed as a result of the continuous transition would be only marginally stable. And indeed, jammed systems are effectively zero temperature. Long-range, critical correlations are destroyed by fluctuations in equilibrium, but would be present in jammed systems which are not allowed to equilibrate. In fact, we just saw that a diverging lengthscale appears during unjamming at low temperatures.

We thus conclude that there is a *continuum* of jammed states. The states from the more stable, higher density part of this continuum are generated by quenching a liquid starting at a density above  $\rho_{\text{cr}}$ , i.e., from a state that was fully equilibrated in the landscape regime. In other words, the starting structure is trapped in a relatively well-defined free energy minimum. The resulting jammed structure is hyperstatic. It appears that while being jammed, such hyperstatic structures could exhibit additional, replica-symmetry breaking transitions [352, 353] that are similar to the so called Gardner transitions in mean-field spin glasses [354]. It is quite possible that in finite dimensions, these additional symmetry-breaking transitions have to do with freezing out the residual string-like excitations that would be characteristic of the crossover to the landscape regime. In contrast, the lower density states from the continuum of jammed states can be traced to the very critical point that is avoided when the system undergoes an equilibrium, discontinuous transition to the

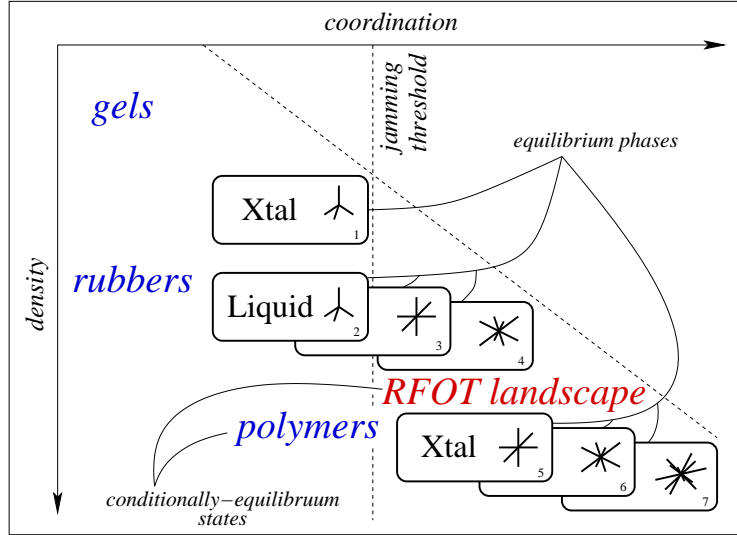


FIG. 59. Qualitative structural map of condensed matter phases, periodic and aperiodic, in terms of density and average coordination. Boxes 1 through 7 correspond to equilibrium phases. Box 1 could be exemplified by crystalline silicon. Boxes 2 through 4 represent uniform liquids in the order of increasing coordination/density. Boxes 5 through 7 represent crystals, also in the order of increasing coordination/density. The stick figures inside boxes are meant to depict coordination in a pictorial way and, obviously, do not cover all possible ways to arrange particles. Direct transitions between some equilibrium phases are allowed. For instance,  $1 \leftrightarrow 2$  pertains to water,  $1 \leftrightarrow 3$  to germanium. In the present scheme, colloidal suspensions and room-temperature ionic liquids would be classified as liquids in a pre-landscape regime, even if very viscous. Materials to the left of the “jamming threshold” line would have to undergo a discontinuous transition before they could be jammed let alone enter the landscape regime.

landscape regime. These relatively low-density structures are generated when the liquid falls out of equilibrium at a density below  $\rho_{cr}$  and are *hypostatic*. Because the crossover has a finite width, there is no sharp boundary between the hyperstatic and hypostatic regimes, which seems to be consistent with recent simulations of Morse and Corwin [355]. In any event, the outcome of a jamming experiment likely depends on the precise quenching protocol for *any* starting density, including the putative  $\rho_K$ . This is probably true even in meanfield, owing to the aforementioned Gardner transitions. Also in meanfield, the crossover is replaced by a sharply defined density  $\rho_A$ , implying one can unambiguously define an *isostatic* jammed structure, which then sharply demarcates the hyper- and hypostatic regimes. According to the above discussion, an amorphous sample made of isotropically-interacting particles would be similar to a quenched glass, the degree of similarity depending on the speed of quenching. The greater the similarity, the greater the number of the low-energy resonances that give rise to the two-level systems.

The above discussion also implies that given a fixed quenching rate, the glass-forming ability is optimised within a *window* of bonding directionality, the low and high extremes corresponding to relatively close-packed and open-structure crystal states respectively.

It is hoped that in addition to a systematic exposition of technical aspects of the RFOT theory of the glass transition, the present article has clarified the limits of applicability of the theory and succeeded, at least to some degree, to place the theory of glasses made by quenching liquids in a broader context of other amorphous materials prepared in a variety of ways. This broader context is graphically summarised in Fig. 59.

Anderson concluded his informal remark in Science by stating: “The solution of the prob-

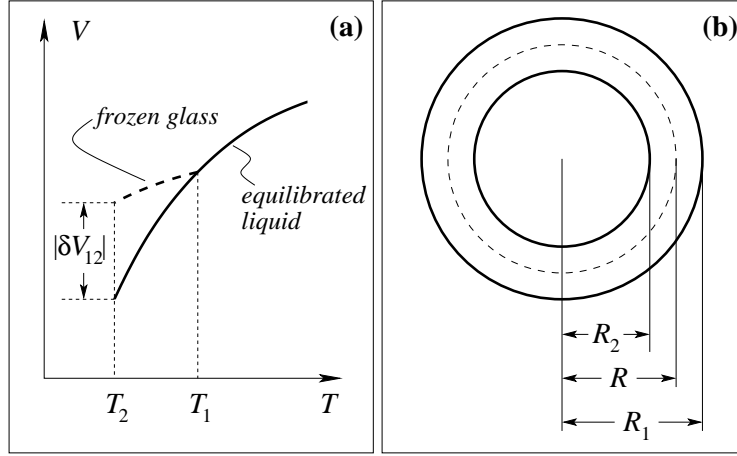


FIG. 60. **(a)** The temperature dependence of the volume of an equilibrated sample (solid line) and of a sample rapidly quenched from temperature  $T_1$  to temperature  $T_2$ . **(b)**: Illustration of the volume mismatch due to ageing. A spherical region of radius  $R_1$  of a sample rapidly quenched to temperature  $T_2$  from temperature  $T_1$  would be of radius  $R_2$  if fully equilibrated at the ambient pressure. To avoid rupture, both the chosen region and the environment must stretch, leading to a negative excess pressure. The boundary between the aged region and its environment is at radius  $R$ ,  $R_2 < R < R_1$ .

lem of spin glass in the late 1970s had broad implications in unexpected fields like neural networks, computer algorithms, evolution, and computational complexity. The solution of the more important and puzzling glass problem may also have a substantial intellectual spin-off. Whether it will help make better glass is questionable.” Better glass has definitely been made since 1995, such as the famous Gorilla Glass. It is fair to say that theoretical investigations had little to do with that progress. Still, in view of the complicated interplay between the glass transition and details of bonding in various glasses, such as the chalcogenides, there is hope that the theory will help make better glass by at least allowing one to narrow the scope of the search. Perhaps more importantly, it may help one make better *crystalline* solids by explaining how to avoid vitrification altogether.

*Acknowledgement.* The author gratefully acknowledges his collaborators Peter G. Wolynes, Andriy Zhugayevych, Pyotr Rabochiy, Dmytro Bevzenko, Jon Golden, and Ho Yin Chan. His work has been supported by the National Science Foundation (Grants CHE-0956127, MCB-0843726, and MCB-1244568), the Alfred P. Sloan Research Fellowship, the Welch Foundation Grant E-1765, the Arnold and Mabel Beckman Foundation Beckman Young Investigator Award, and the Donors of the Petroleum Research Fund of the American Chemical Society.

## Appendix A: Volume mismatch during ageing

As before, consider a prompt thermal quench from equilibrium at temperature  $T_1$  to a different temperature  $T_2$ , at ambient pressure. The volume mismatch between a sample equilibrated at  $T_2$  and the actual sample is the volume difference between a fully equilibrated sample and the one that is only vibrationally relaxed:

$$\delta V_{12} = \int_{T_1}^{T_2} V(\alpha_{\text{eq}} - \alpha_{\text{vibr}}) dT. \quad (\text{A1})$$

For concreteness, let us consider a downward  $T$ -jump:  $T_2 < T_1 \Rightarrow \delta V_{12} < 0$ , see illustration in Fig. 60(a). Suppose a spherical region is of radius  $R_1$  before it structurally relaxed, *at the ambient pressure and temperature*, and would be of radius  $R_2 < R_1$  after relaxation, if *also* at the ambient pressure and temperature. In view of the smallness of  $\delta V_{12}/V$  (usually not exceeding a few thousandth),  $\delta R/R \equiv (R_2 - R_1)/R \approx \delta V_{12}/3V$ , where  $R$  stands for the actual radius of the droplet upon reconfiguration. To avoid fracture, both the inner and outer regions must stretch ( $R_2 < R < R_1$ ), see Fig. 60(b), leading to an excess negative pressure  $p(r)$  throughout the sample. This pressure is constant within the reconfigured region; it decreases away from the region and vanishes strictly at the external boundary of the sample:  $p(\infty) = 0$ . The excess pressure can be straightforwardly related to the deformation using a solved problem from Chapter 7 of Ref. [85], assuming, for simplicity, isotropic elasticity and a (macroscopic) spherical sample. At the boundary of the reconfigured region,  $R - R_2 = -p(R)R_2/3K_{\text{in}}$  and  $R - R_1 = p(R)R_1/4\mu_{\text{out}}$  where  $K_{\text{in}}$  is the equilibrium bulk modulus at  $T_2$  and the *ambient* pressure, while  $\mu_{\text{out}}$  the shear modulus of an individual aperiodic state, also at  $T_2$  and ambient pressure. Excluding  $R$ , we find:

$$p(R) = \frac{\delta V_{12}}{V} \left( \frac{1}{K_{\text{in}}} + \frac{3}{4\mu_{\text{out}}} \right)^{-1}. \quad (\text{A2})$$

To estimate this excess pressure,  $p \sim (\delta V_{12}/V)\mu/2$ , we note that for a realistic quench,  $|\delta V_{12}/V| \lesssim 5 \cdot 10^{-3}$  [356], while the rule of thumb for elastic constants is  $\mu(T_{\text{cr}})a^3 \simeq 12k_B T_{\text{cr}}$ , see Eq. (208). And so, generically,  $\mu(T_g)a^3 \simeq 20k_B T_g$ , since  $T_g < T_{\text{cr}}$ , while  $\mu$  usually increases with lowering temperature. As a result, the excess pressure is comparable to but probably less than  $|\delta V_{12}/V|20k_B T/a^3$ . The latter does not exceed  $10^{-1}k_B T/a^3$ , which is greater than the atmospheric pressure by a couple of orders of magnitude, but is comparably less than the *kinetic* pressure. The latter is the relevant pressure reference here; its numerical value is about  $(k_B T/a^3)(a/d_L) \sim 10k_B T/a^3$  [37, 170], see Subsection V C.

The environmental deformation, as a function of the radius vector  $\mathbf{r}$ , is given by [85]

$$\mathbf{u}(\mathbf{r}) = (\mathbf{r}/r^3)p(R)R^3/4\mu_{\text{out}} \quad (r > R). \quad (\text{A3})$$

The resulting volume change of the sample is  $4\pi \times p(R)R^3/4\mu_{\text{out}}$ , yielding for the relative volume change of the whole sample:

$$\left. \frac{\delta V}{V} \right|_{\text{sample}} = \frac{\delta V_{12}}{V} \left( 1 + \frac{4\mu_{\text{out}}}{3K_{\text{in}}} \right)^{-1} \quad (\text{A4})$$

Note this total volume change takes place even as the environmental deformation from Eq. (A3) is pure shear:  $\nabla \mathbf{u} \equiv u_{ii} = 0$ .

Also of potential interest is the free energy excess due to the deformation of the environment, which can be estimated by integrating the standard expression for the free energy density over space, assuming again the isotropic elasticity and remembering that  $u_{ii} = 0$  for  $r > R$ :  $\int_R^\infty (\mu_{\text{out}} u_{ik}^2) 4\pi r^2 dr$ . This yields for the excess energy:

$$E_{\text{exc}} = \frac{\pi p(R)^2}{2\mu_{\text{out}}} R^3, \quad (\text{A5})$$

where  $p(R)$  is from Eq. (A2). Note this energy scales with the volume of the droplet. As expected, there would not be any excess pressure or stored energy, if the material around the nucleus could flow, in which case  $\mu_{\text{out}} = 0$  ( $p \propto \mu_{\text{out}}$  for  $\mu_{\text{out}} \rightarrow 0$ , by Eq. (A2)). Finally note that formulae (A2)-(A5) apply for a  $\delta V_{12}$  of either sign, i.e., for both downward and upward  $T$ -jumps. The physical difference between the two cases is that the excess pressure  $p$  will be negative and positive for downward and upward jumps respectively.

It is apparent from Eq. (A4) that, owing to the shear resistance of the sample, the relative volume change of the sample is always smaller than that of the reconfiguring (microscopic) sub-regions, since the r.h.s. of Eq. (A4) is less than  $\delta V_{12}/V$ , as long as  $\mu_{\text{out}} > 0$ . This would seemingly imply that the sample will never reach its equilibrium volume! There is no contradiction here, however. As the sample equilibrates, i.e., the ageing proceeds, the assumption of the mechanical stability is no longer valid. Hereby the material relaxes throughout, all stored excess energy from Eq. (A5) is released, as recently described in Ref. [47], while the shear modulus  $\mu_{\text{out}}$  that enters in Eq. (A4) effectively decreases and vanishes upon complete equilibration. Note that to achieve the latter, regions that originally relaxed at a non-zero excess pressure  $p$ , will also have to relax until they are in equilibrium at  $p = 0$ .

To quantify the significance of the volume-mismatch effect for the thermodynamics of ageing we first note the stabilisation of state 2 from Eq. (216), per particle, is approximately  $\delta\Delta g \simeq (Vp)/N = pa^3$ , where we have used the usual expression for the Gibbs energy increment:  $dG = -SdT + Vdp$ . Together with Eq. (A2), this yields

$$\delta\Delta g = \frac{\delta V_{12}}{V} \left( \frac{1}{K_{\text{in}}} + \frac{3}{4\mu_{\text{out}}} \right)^{-1} a^3. \quad (\text{A6})$$

We thus observe that *initial* ageing events always *overshoot* in the following sense: For downward  $T$ -jumps, the final state free energy is lower than the equilibrium free energy at the ambient pressure ( $\delta V_{12} < 0$ ) and vice versa for upward  $T$ -jumps ( $\delta V_{12} > 0$ ).

To get a quantitative sense of this overshoot, let us adopt  $\delta\Delta g \simeq (\delta V_{12}/V)\mu a^3/2$  for the sake of argument. As in the above estimate for the excess pressure, the stabilisation for the  $\delta V_{12}/V = -1 \dots 5 \cdot 10^{-3}$  range thus corresponds to  $\delta\Delta g \approx -0.01 \dots 0.05 k_B T$ . This stabilisation will be partially offset by the excess elastic energy stored in the environment, from Eq. (A5):  $E_{\text{exc}}/N \simeq (3/8)p^2 a^3/\mu_{\text{out}} \simeq +0.1 \cdot (\delta V_{12}/V)^2 \mu a^3$ , however the offset is second order in the volume mismatch and sub-dominant by several orders of magnitude to the main effect.

To quantify the effects of the overshoot caused by the volume-mismatch on the kinetics of ageing, we note the free energy difference  $\Delta g$  itself is about  $-0.9 k_B T$  at equilibrium just above the glass transition on 1 hr time scale, according to Eq. (164) and using 1 psec for the rate prefactor. For quenches below the glass transition:  $T_1 = T_g$ ,  $T_2 < T_1$ ,  $\Delta g$  is only weakly  $T$ -dependent and predicted to decrease somewhat by absolute value [40], see Eq. (217). Assuming for the sake of argument  $\Delta f = -0.8 k_B T$  (i.e., a relaxation time of  $10^5$  s) one gets, upon replacing  $\Delta g = -0.8 k_B T$  by  $\Delta g = -0.85 k_B T$ , a speed up by a factor of ten or so. Note that the thermal expansivity and the elastic moduli tend to anti-correlate [105], and so the combination  $\delta V_{12}\mu$ , for similar quench depths, should not vary wildly among different substances.

We have thus established that as regards thermodynamics and kinetics of ageing, the volume-mismatch effect is quantitatively, but not qualitatively significant. One possible exception is melting of ultrastable glasses, where the volume mismatch could exceed one percent [261], thus leading to a relatively large  $\delta\Delta g$ .

- 
- [1] I. Liritzis and C. Stevenson, *Obsidian and Ancient Manufactured Glasses*, University of New Mexico Press, Albuquerque, 2012.
  - [2] J. Schroers, *Physics Today* 66 (2013), pp. 32–37.
  - [3] S. Raoux, W. Wehlic, and D. Ielmini, *Chem. Rev.* 110 (2010), pp. 240–267.
  - [4] M. Wuttig and N. Yamada, *Nature Mat.* 6 (2007), pp. 824–832.
  - [5] D. Lencer, M. Salinga, B. Grabowski, T. Hickel, J. Neugebauer, and M. Wuttig, *Nature Mat.* 7 (2008), pp. 972–977.

- [6] A.V. Kolobov, P. Fons, A.I. Frenkel, A.L. Ankudinov, J. Tominaga, and T. Uruga, *Nature Mat.* 3 (2004), pp. 703–708.
- [7] C. Steimer, V. Coulet, W. Welnic, H. Dieker, R. Detemple, C. Bichara, B. Beuneu, J. Gaspard, and M. Wuttig, *Adv. Mat.* 20 (2008), pp. 4535–4540.
- [8] P. Hosseini, C.D. Wright, and H. Bhaskaran, *Nature* 511 (2014), pp. 206–211.
- [9] Y. Li, Y. Zhong, J. Zhang, L. Xu, Q. Wang, H. Sun, H. Tong, X. Cheng, and X. Miao, *Sci. Rep.* 4 (2014), p. 4906.
- [10] N.W. Ashcroft and N.D. Mermin, *Solid State Physics*, Harcourt Brace College Publishers, Fort Worth, 1976.
- [11] E. Leutheusser, *Phys. Rev. A* 29 (1984), p. 2765.
- [12] U. Bengtzelius, W. Götze, and A. Sjolander, *J. Phys. C: Solid State Physics* 17 (1984), pp. 5915–5934.
- [13] A.S. Keys, J.P. Garrahan, and D. Chandler, *Proc. Natl. Acad. Sci. U. S. A.* 110 (2013), pp. 4482–4487.
- [14] A.S. Keys, L.O. Hedges, J.P. Garrahan, S.C. Glotzer, and D. Chandler, *Phys. Rev. X* 1 (2011), p. 021013.
- [15] R.G. Palmer, D.L. Stein, E. Abrahams, and P.W. Anderson, *Phys. Rev. Lett.* 53 (1984), pp. 958–961.
- [16] G.H. Fredrickson and H.C. Andersen, *Phys. Rev. Lett.* 53 (1984), pp. 1244–1247.
- [17] A.S. Keys, A.R. Abate, S.C. Glotzer, and D.J. Durian, *Nature Physics* 3 (2007), pp. 260–264.
- [18] A.J. Liu and S.R. Nagel, *Nature* 395 (1998), pp. 21–22.
- [19] L.S. Silbert, A.J. Liu, and S.R. Nagel, *Phys. Rev. Lett.* 95 (2005), p. 098301.
- [20] R. Mari, F. Krzakala, and J. Kurchan, *Phys. Rev. Lett.* 103 (2009), p. 025701.
- [21] T.S. Grigera, V. Martin-Mayor, G. Parisi, and P. Verrocchio, *Nature* 422 (2003), pp. 289–292.
- [22] V. Lubchenko and P.G. Wolynes, *Proc. Natl. Acad. Sci. U. S. A.* 100 (2003), pp. 1515–1518.
- [23] V. Lubchenko and P.G. Wolynes, *Adv. Chem. Phys.* 136 (2007), pp. 95–206.
- [24] L. Onsager, *Phys. Rev.* 37 (1931), pp. 405–426.
- [25] L. Onsager, *Phys. Rev.* 38 (1931), pp. 2265–2279.
- [26] N. Goldenfeld, *Lectures on phase transitions and the renormalization group*, Addison-Wesley, Reading, MA, 1992.
- [27] V. Lubchenko and P.G. Wolynes, *Annu. Rev. Phys. Chem.* 58 (2007), pp. 235–266.
- [28] V. Lubchenko, *J. Phys. Chem. Lett.* 3 (2012), pp. 1–7.
- [29] A. Zhugayevych and V. Lubchenko, *J. Chem. Phys.* 133 (2010), p. 234503.
- [30] T.R. Kirkpatrick, D. Thirumalai, and P.G. Wolynes, *Phys. Rev. A* 40 (1989), pp. 1045–1054.
- [31] X. Xia and P.G. Wolynes, *Proc. Natl. Acad. Sci. U. S. A.* 97 (2000), pp. 2990–2994.
- [32] P. Rabochiy and V. Lubchenko, *J. Chem. Phys.* 138 (2013), 12A534.
- [33] P. Rabochiy, P.G. Wolynes, and V. Lubchenko, *J. Phys. Chem. B* 117 (2013), pp. 15204–15219.
- [34] V. Lubchenko and P. Rabochiy, *J. Phys. Chem. B* 118 (2014), pp. 13744–13759.
- [35] V. Lubchenko and P.G. Wolynes, *J. Chem. Phys.* 119 (2003), pp. 9088–9105.
- [36] J. Stevenson and P.G. Wolynes, *J. Phys. Chem. B* 109 (2005), pp. 15093–15097.
- [37] P. Rabochiy and V. Lubchenko, *J. Chem. Phys.* 136 (2012), p. 084504.
- [38] X. Xia and P.G. Wolynes, *Phys. Rev. Lett.* 86 (2001), pp. 5526–5529.
- [39] X. Xia and P.G. Wolynes, *J. Phys. Chem.* 105 (2001), pp. 6570–6573.
- [40] V. Lubchenko and P.G. Wolynes, *J. Chem. Phys.* 121 (2004), pp. 2852–2865.
- [41] J.D. Stevenson, J. Schmalian, and P.G. Wolynes, *Nature Physics* 2 (2006), pp. 268–274.
- [42] P. Rabochiy and V. Lubchenko, *J. Phys. Chem. B* 116 (2012), pp. 5729–5737.
- [43] V. Lubchenko, *J. Chem. Phys.* 126 (2007), p. 174503.
- [44] J.D. Stevenson and P.G. Wolynes, *Nature Physics* 6 (2010), pp. 62–68.
- [45] V. Lubchenko, *Proc. Natl. Acad. Sci. U. S. A.* 106 (2009), pp. 11506–11510.
- [46] J.D. Stevenson and P.G. Wolynes, *J. Chem. Phys.* 129 (2008), p. 234514.
- [47] A. Wisitsorarak and P.G. Wolynes, *Proc. Natl. Acad. Sci. U. S. A.* 109 (2012), pp. 16068–16072.
- [48] P.G. Wolynes, *Proc. Natl. Acad. Sci. U. S. A.* 106 (2009), pp. 1353–1358.
- [49] A. Wisitsorarak and P.G. Wolynes, *Phys. Rev. E* 88 (2013), p. 022308.
- [50] J.D. Stevenson and P.G. Wolynes, *J. Phys. Chem. A* 115 (2011), pp. 3713–3719.
- [51] V. Lubchenko and P.G. Wolynes, *Phys. Rev. Lett.* 87 (2001), p. 195901.

- [52] V. Lubchenko, R.J. Silbey, and P.G. Wolynes, *Mol. Phys.* 104 (2006), pp. 1325–1335.
- [53] A. Zhugayevych and V. Lubchenko, *J. Chem. Phys.* 132 (2010), p. 044508.
- [54] A. Zhugayevych and V. Lubchenko, *J. Chem. Phys.* 133 (2010), p. 234504.
- [55] L.D. Landau and E.M. Lifshitz, *Statistical Mechanics*, Pergamon Press, New York, 1980.
- [56] R.S. Berry, S.A. Rice, and J. Ross, *Physical Chemistry*, John Wiley & Sons, Hoboken, NJ, 1980.
- [57] W.M. Haynes (ed.), *CRC Handbook of Chemistry and Physics, 96th Edition*, CRC Press, Boca Raton, 2015.
- [58] O. Penrose, *J. Stat. Phys.* 78 (1995), pp. 267–283.
- [59] T. Hikima, Y. Adachi, M. Hanaya, and M. Oguni, *Phys. Rev. B* 52 (1995), pp. 3900–3908.
- [60] Y. Sun, H. Xi, S. Chen, M.D. Ediger, and L. Yu, *J. Phys. Chem. B* 112 (2008), pp. 5594–5601.
- [61] C.A. Angell, *Science* 267 (1995), pp. 1924–1935, Available at <http://www.jstor.org/stable/2886440>.
- [62] P. Lunkenheimer, M. Köhler, S. Kastner, and A. Loidl, *Dielectric spectroscopy of glassy dynamics*, in *Structural Glasses and Supercooled Liquids: Theory, Experiment, and Applications*, P.G. Wolynes and V. Lubchenko, eds., John Wiley & Sons, Hoboken, NJ (2012), pp. 115–149.
- [63] M. Born and K. Huang, *Dynamic Theory of Crystal Lattices*, Oxford, Clarendon Press, 1968.
- [64] N.F. Mott and R.W. Gurney, *Trans. Faraday Soc.* 35 (1939), pp. 364–368.
- [65] V. Lubchenko, *J. Phys. Chem. B* 110 (2006), pp. 18779–18786.
- [66] J. Daeges, H. Gleiter, and J. Perepezko, *Phys. Lett. A* 119 (1986), pp. 79 – 82.
- [67] J.H. Bilgram, *Phys. Rep.* 153 (1987), pp. 1–89.
- [68] S.R. Philpot, S. Yip, P.R. Okamoto, and D. Wolf, *Role of interfaces in melting and solid-state amorphization*, in *Materials Interfaces: Atomic-level Structure and Properties*, D. Wolf and S. Yip, eds., Springer, New York (1992), pp. 228–254.
- [69] A.P. Young, *Phase Diagrams of the Elements*, Lawrence Livermore Laboratory, University of California, Livermore, CA, 1975.
- [70] J.E. Lennard-Jones and A.F. Devonshire, *Proceedings of the Royal Society of London. Series A* 163 (1937), pp. 53–70.
- [71] J. Hirschfelder, D. Stevenson, and H. Eyring, *J. Chem. Phys.* 5 (1937), pp. 896–912.
- [72] W.G. Hoover and F.H. Ree, *J. Chem. Phys.* 49 (1968), pp. 3609–3617.
- [73] M. Fixman, *J. Chem. Phys.* 51 (1969), pp. 3270–3279.
- [74] J.D. Bernal, *Trans. Faraday Soc.* 33 (1937), pp. 27–40.
- [75] L. Landau, *Phys. Z. Sowjet.* 11 (1937), p. 26, English translation in "Collected Papers of Landau", 1965, Gordon and Breach.
- [76] L. Landau, *Phys. Z. Sowjet.* 11 (1937), p. 545, English translation in "Collected Papers of Landau", 1965, Gordon and Breach.
- [77] R.J. Baxter, *J. Chem. Phys.* 41 (1964), pp. 553–558.
- [78] J.P. Hansen and I.R. McDonald, *Theory of Simple Liquids*, Academic Press, New York, 1976.
- [79] R. Evans, *Adv. Phys.* 28 (1979), pp. 143–200.
- [80] P. Hohenberg and W. Kohn, *Phys. Rev.* 136 (1964), pp. B864–B871.
- [81] N.D. Mermin, *Phys. Rev.* 137 (1965), pp. A1441–A1443.
- [82] J.S. McCarley and N.W. Ashcroft, *Phys. Rev. E* 55 (1997), pp. 4990–5003.
- [83] D. Henderson and E.W. Grundke, *J. Chem. Phys.* 63 (1975), pp. 601–607.
- [84] S. Asakura and F. Oosawa, *J. Polymer Sci.* 33 (1958), pp. 183–193.
- [85] L.D. Landau and E.M. Lifshitz, *Theory of Elasticity*, Pergamon Press, 1986.
- [86] A.C. Eringen and D.G.B. Edelen, *Int. J. Engrg. Sci.* 10 (1972), p. 233.
- [87] I.A. Kunin, *Elastic Media with Microstructure*, Springer, New York, 1982.
- [88] K.C. Valanis, *Arch. Mech.* 52 (2000), pp. 817–838.
- [89] A.J.M. Yang, P.D. Fleming, and J.H. Gibbs, *J. Chem. Phys.* 64 (1976), pp. 3732–3747.
- [90] S. Alexander and J. McTague, *Phys. Rev. Lett.* 41 (1978), pp. 702–705.
- [91] P.W. Anderson, *Basic Notions of Condensed Matter Physics*, Benjamin Cummins, 1984.
- [92] T.C. Hales, *Notices Amer. Math. Soc.* 47 (2000), pp. 440–449.
- [93] S.A. Brazovskii, *JETP* 41 (1975), pp. 85–89.
- [94] S.A. Brazovskii and S.G. Dmitriev, *JETP* 42 (1975), pp. 497–502.
- [95] J. Fröhlich and T. Spencer, *Commun. Math. Phys.* 84 (1982), pp. 87–101.
- [96] P.W. Anderson and G. Yuval, *J. Phys. C* 4 (1971), pp. 607–620.



- [97] P.M. Chaikin and T.C. Lubensky, *Principles of Condensed Matter Physics*, Cambridge University Press, Cambridge, 2000.
- [98] M.I. McMahon and R.J. Nemes, Chem. Soc. Rev. 35 (2006), pp. 943–963.
- [99] H. Olijnyk and W. Holzapfel, Phys. Lett. A 100 (1984), pp. 191 – 194.
- [100] D. Legut, M. Friák, and M. Šob, Phys. Rev. Lett. 99 (2007), p. 016402.
- [101] S.M. Woodley and R. Catlow, Nature Materials 7 (2008), pp. 937 – 946.
- [102] J.G. Kirkwood and E. Monroe, The Journal of Chemical Physics 9 (1941), pp. 514–526.
- [103] V.N. Ryzhov and E.E. Tareeva, Theor. Mat. Phys. (USSR) 48 (1981), pp. 835–840.
- [104] S.A. Rice, C. Cerjan, and B. Bagchi, J. Chem. Phys. 82 (1985), pp. 3350–3359.
- [105] G. Grimvall and S. Sjödin, Phys. Scripta 10 (1974), p. 340.
- [106] M. Mézard and G. Parisi, Phys. Rev. Lett. 82 (1999), pp. 747–750.
- [107] F.A. Lindemann, Phys. Z. 11 (1910), pp. 609–612.
- [108] J.D. van der Waals, *Over de Continuïtet van der Gas- en Vloeistofoestand*, Ph.D. thesis, Univ. Leiden, 1873, english translation: *Phys. Mem.*, vol. 1, p. 333, 1890.
- [109] P. Weiss, J. Phys. Theor. Appl. 6 (1907), pp. 661–690.
- [110] D.M. McQuarrie, *Statistical Mechanics*, Harper-Collins, New York, 1973.
- [111] H.B. Callen, *Thermodynamics and an Introduction to Thermostatistics*, Wiley, Hoboken, NJ, 1985.
- [112] R. Lovett, C.Y. Mou, and F.P. Buff, J. Chem. Phys. 65 (1976), pp. 570–572.
- [113] A.D.J. Haymet and D.W. Oxtoby, J. Chem. Phys. 74 (1981), pp. 2559–2565.
- [114] L.D. Landau and E.M. Lifshitz, *Mechanics*, Pergamon Press, New York, 1976.
- [115] T.V. Ramakrishnan and M. Yussouff, Phys. Rev. B 19 (1979), pp. 2775–2794.
- [116] M.S. Wertheim, J. Chem. Phys. 65 (1976), pp. 2377–2381.
- [117] R. Lovett, J. Chem. Phys. 66 (1977), pp. 1225–1230.
- [118] J.K. Percus and G.J. Yevick, Phys. Rev. 110 (1958), pp. 1–13.
- [119] E. Thiele, J. Chem. Phys. 39 (1963), pp. 474–479.
- [120] M.S. Wertheim, Phys. Rev. Lett. 10 (1963), pp. 321–323.
- [121] W.L. Bragg and E.J. Williams, Proc. Roy. Soc. A145 (1934), pp. 699–730.
- [122] R. Feynman, *Statistical Mechanics: A Set Of Lectures*, Advanced Books Classics Series, Westview Press, Boulder, CO, 1998.
- [123] L. Onsager, Ann. N. Y. Acad. Sci. 51 (1949), pp. 627–659.
- [124] J.L. Lebowitz and J.K. Percus, J. Math. Phys. 4 (1963), pp. 116–123.
- [125] F.H. Stillinger, P.G. Debenedetti, and S. Sastry, J. Chem. Phys. 109 (1998), pp. 3983–3988.
- [126] L.S. Ornstein and F. Zernike, Proc. Acad. Sci. Amsterdam 17 (1914), pp. 793–806, reproduced in H. Frisch and J. L. Lebowitz, *The Equilibrium Theory of Classical Fluids*, Benjamin, 1964.
- [127] M.P. Allen and D.J. Tildesley, *Computer Simulation of Liquids*, Oxford University Press, USA, Oxford, 1989.
- [128] M. Dixon and P. Hutchinson, Mol. Phys. 33 (1977), pp. 1663–1670.
- [129] A.R. Denton and N.W. Ashcroft, Phys. Rev. A 39 (1989), p. 4701.
- [130] H. Lowen, J. Phys.: Condens. Matter 2 (1990), pp. 8477–8484.
- [131] J.L. Barrat, J.P. Hansen, G. Pastore, and E.M. Waisman, J. Chem. Phys. 86 (1987), pp. 6360–6365.
- [132] W.A. Curtin and N.W. Ashcroft, Phys. Rev. Lett. 56 (1986), pp. 2775–2778.
- [133] J.P. Hansen and L. Verlet, Phys. Rev. 184 (1969), pp. 151–161.
- [134] B.W.H. van Beest, G.J. Kramer, and R.A. van Santen, Phys. Rev. Lett. 64 (1990), pp. 1955–1958.
- [135] J.H. Magill, J. Chem. Phys. 47 (1967), pp. 2802–2807.
- [136] T.A. Albright, J.K. Burdett, and M.H. Whangbo, *Orbital Interactions in Chemistry*, Wiley, Hoboken, NJ, 2013.
- [137] G. Parisi and F. Zamponi, Rev. Mod. Phys. 82 (2010), pp. 789–845.
- [138] S.M. Sharma and S. Sikka, Prog. Mater. Sci. 40 (1996), pp. 1 – 77.
- [139] V.V. Brazhkin and A.G. Lyapun, J. Phys. Cond. Mat. 15 (2003), p. 6059.
- [140] E. Ponyatovsky and O. Barkalov, Mat. Sci. Rep. 8 (1992), pp. 147 – 191.
- [141] R.J. Hemley, A.P. Jephcoat, H.K. Mao, L.C. Ming, and M.H. Manghnani, Nature 334 (1988), pp. 52–54.
- [142] J.P. Stoessel and P.G. Wolynes, J. Chem. Phys. 80 (1984), pp. 4502–4512.

- [143] Y. Singh, J.P. Stoessel, and P.G. Wolynes, Phys. Rev. Lett. 54 (1985), pp. 1059–1062.
- [144] C. Bennett, J. Appl. Phys. 43 (1973), pp. 2727–2734.
- [145] M. Baus and J.L. Colot, J. Phys. C: Solid State Phys. 19 (1986), pp. L135–L139.
- [146] T.R. Kirkpatrick and P.G. Wolynes, Phys. Rev. A 35 (1987), pp. 3072–3080.
- [147] W. Kauzmann, Chem. Rev. 43 (1948), pp. 219–256.
- [148] M. Mézard and G. Parisi, J. Chem. Phys. 111 (1999), pp. 1076–1095.
- [149] M. Mézard and G. Parisi, *Glasses and Replicas*, in *Structural Glasses and Supercooled Liquids: Theory, Experiment, and Applications*, P.G. Wolynes and V. Lubchenko, eds., John Wiley & Sons, Hoboken, NJ (2012), pp. 151–191.
- [150] F. Mezei and M. Russina, J. Phys. Condens. Matter 11 (1999), p. A341.
- [151] F. Simon, Trans. Faraday Soc. 33 (1937), pp. 65–73.
- [152] M. Tatsumisago, B.L. Halfpap, J.L. Green, S.M. Lindsay, and C.A. Angell, Phys. Rev. Lett. 64 (1990), pp. 1549–1552.
- [153] R. Richert and C.A. Angell, J. Chem. Phys. 108 (1998), p. 9016.
- [154] D. Bevezko and V. Lubchenko, J. Phys. Chem. B 113 (2009), pp. 16337–16345.
- [155] D. Bevezko and V. Lubchenko, J. Chem. Phys. 141 (2014), p. 174502.
- [156] G. Adam and J.H. Gibbs, J. Chem. Phys. 43 (1965), pp. 139–146.
- [157] F. Smallenburg and F. Sciortino, Nature Physics 9 (2013), pp. 554 – 558.
- [158] R.W. Hall and P.G. Wolynes, Phys. Rev. Lett. 90 (2003), p. 085505.
- [159] P.R. ten Wolde and D. Frenkel, Science 277 (1997), pp. 1975–1978.
- [160] P.M. Duxbury, D.J. Jacobs, M.F. Thorpe, and C. Moukarzel, Phys. Rev. E 59 (1999), pp. 2084–2092.
- [161] J. Horbach and W. Kob, Phys. Rev. E 64 (2001), p. 041503.
- [162] W. Götze and L. Sjögren, Rep. Progr. Phys. 55 (1992), pp. 241–376.
- [163] J.O. Hirschfelder, C.F. Curtiss, and R.B. Bird, *Molecular theory of gases and liquids*, Wiley, 1964.
- [164] J. Wu and J. Cao, Phys. Rev. Lett. 95 (2005), p. 078301.
- [165] G. Biroli, J.P. Bouchaud, K. Miyazaki, and D.R. Reichman, Phys. Rev. Lett. 97 (2006), p. 195701.
- [166] S.M. Bhattacharyya, B. Bagchi, and P.G. Wolynes, Phys. Rev. E 72 (2005), p. 031509.
- [167] S.M. Bhattacharyya, B. Bagchi, and P.G. Wolynes, Proc. Natl. Acad. Sci. U. S. A. 105 (2008), pp. 16077–16082.
- [168] W. Götze, *Complex Dynamics of Glass-Forming Liquids: A Mode-Coupling Theory*, International Series of Monographs on Physics, OUP Oxford, 2008.
- [169] S.P. Das, Rev. Mod. Phys. 76 (2004), pp. 785–851.
- [170] V. Lubchenko and P.G. Wolynes, *Theories of Structural Glass Dynamics: Mosaics, Jamming, and All That*, in *Structural Glasses and Supercooled Liquids: Theory, Experiment, and Applications*, P.G. Wolynes and V. Lubchenko, eds., John Wiley & Sons (2012), pp. 341–379.
- [171] D. Sherrington and S. Kirkpatrick, Phys. Rev. Lett. 35 (1975), pp. 1792–1796.
- [172] M. Mézard, G. Parisi, and M. Virasoro, *Spin Glass Theory And Beyond*, World Scientific, 1987.
- [173] L. Onsager, J. Am. Chem. Soc. 58 (1936), pp. 1486–1493.
- [174] P.W. Anderson, *Lectures on Amorphous Systems*, in *Ill-condensed matter; Les Houches, Session XXXI*, R.B. at el., ed., North-Holland, Amsterdam (1979), p. 161.
- [175] D.J. Thouless, P.W. Anderson, and R.G. Palmer, Phil. Mag. 35 (1977), pp. 593–601.
- [176] M. Mézard and A. Montanari, *Information, Physics, and Computation*, Oxford University Press, 2009.
- [177] D.J. Gross and M. Mézard, Nucl. Phys. B 240 (1984), pp. 431–452.
- [178] B. Derrida, Phys. Rev. B 24 (1981), p. 2613.
- [179] T.R. Kirkpatrick and D. Thirumalai, Phys. Rev. Lett. 58 (1987), pp. 2091–2094.
- [180] T.R. Kirkpatrick and D. Thirumalai, Phys. Rev. B 36 (1987), pp. 5388–5397.
- [181] T.R. Kirkpatrick and P.G. Wolynes, Phys. Rev. B 36 (1987), pp. 8552–8564.
- [182] D.J. Gross, I. Kanter, and H. Sompolinsky, Phys. Rev. Lett. 55 (1985), pp. 304–307.
- [183] R.J. Baxter, *Exactly Solved Models in Statistical Mechanics*, Academic Press, London, 1982.
- [184] R.K.P. Zia and D.J. Wallace, J. Phys. A 8 (1975), pp. 1495–1507.
- [185] J.S. Langer, Rep. Prog. Phys. 77 (2014), p. 042501.

- [186] M. Tarzia and M.A. Moore, Phys. Rev. E 75 (2007), p. 031502.
- [187] J. Yeo and M.A. Moore, Phys. Rev. E 86 (2012), p. 052501.
- [188] J. Yeo and M.A. Moore, Phys. Rev. B 85 (2012), p. 100405.
- [189] M.C. Angelini and G. Biroli, Phys. Rev. B 90 (2014), p. 220201.
- [190] T. Takahashi and K. Hukushima, Phys. Rev. E 91 (2015), p. 020102.
- [191] M.P. Eastwood and P.G. Wolynes, Europhys. Lett. 60 (2002), pp. 587–593.
- [192] J.D. Stevenson, A.M. Walczak, R.W. Hall, and P.G. Wolynes, J. Chem. Phys. 129 (2008), 194505.
- [193] R. Monasson, Phys. Rev. Lett. 75 (1995), pp. 2847–2850.
- [194] J.S. Rowlinson and B. Widom, *Molecular Theory of Capillarity*, Clarendon Press, Oxford, 1982.
- [195] A.J. Bray, Adv. Phys. 43 (1994), pp. 357–459.
- [196] C. Teodosiu, *Elastic Models of Crystal Defects*, Springer, 1982.
- [197] M. Baus and R. Lovett, Phys. Rev. A 44 (1991), pp. 1211–1218.
- [198] L. Yan, G. Düring, and M. Wyart, Proc. Natl. Acad. Sci. U. S. A. 110 (2013), pp. 6307–6312.
- [199] H. Frauenfelder and P.G. Wolynes, Science 229 (1985), p. 337.
- [200] P. Hänggi, P. Talkner, and M. Borkovec, Rev. Mod. Phys. 62 (1990), pp. 251–341.
- [201] K. Trachenko, M.T. Dove, M.J. Harris, and V. Heine, J. Phys.: Condens. Matter 12 (2000), pp. 8041–8064.
- [202] J.P. Bouchaud and G. Biroli, J. Chem. Phys. 121 (2004), pp. 7347–7354.
- [203] H.W. Cahn and J.E. Hilliard, J. Chem. Phys. 28 (1958), pp. 258–267.
- [204] M. Dzero, J. Schmalian, and P.G. Wolynes, Phys. Rev. B 72 (2005), p. 100201(R).
- [205] S. Franz, J. Stat. Phys. (2005), p. P04001.
- [206] J. Villain, J. Phys. (Paris) 46 (1985), pp. 1843–1852.
- [207] F.W. Starr, J.F. Douglas, and S. Sastry, J. Chem. Phys. 138 (2013), p. 12A541.
- [208] P.G. Wolynes, Proc. Natl. Acad. Sci. U. S. A. 94 (1997), pp. 6170–6174.
- [209] G. Biroli and C. Cammarota, ArXiv e-prints, <http://adsabs.harvard.edu/abs/2014arXiv1411.4566B> (2014).
- [210] R.O. Pohl, X. Liu, and E. Thompson, Rev. Mod. Phys. 74 (2002), pp. 991–1013.
- [211] R. Hall and P. Wolynes, J. Chem. Phys. 86 (1987), pp. 2943–2948.
- [212] J.C. Dyre, N.B. Olsen, and T. Christensen, Phys. Rev. B 53 (1996), pp. 2171–2174.
- [213] J.C. Dyre and W.H. Wang, J. Chem. Phys. 136 (2012), 224108.
- [214] C. Klieber, T. Hecksher, T. Pezeril, D.H. Torchinsky, J.C. Dyre, and K.A. Nelson, J. Chem. Phys. 138 (2013), p. 12A544.
- [215] L.M. Wang and C.A. Angell, J. Chem. Phys. 118 (2003), pp. 10353–10355.
- [216] L. Berthier, G. Biroli, J.P. Bouchaud, L. Cipelletti, D. El Masri, D. L’Hôte, F. Ladieu, and M. Perino, Science 310 (2005), pp. 1797–1800.
- [217] S. Capaccioli, G. Ruocco, and F. Zamponi, J. Phys. Chem. B 112 (2008), pp. 10652–10658.
- [218] U. Tracht, M. Wilhelm, A. Heuer, H. Feng, K. Schmidt-Rohr, and H.W. Spiess, Phys. Rev. Lett. 81 (1998), pp. 2727–2730.
- [219] E.V. Russell and N.E. Israeloff, Nature 408 (2000), pp. 695–698.
- [220] M.T. Cicerone and M.D. Ediger, J. Chem. Phys. 104 (1996), pp. 7210–7218.
- [221] S. Ashtekar, G. Scott, J. Lyding, and M. Gruebele, J. Phys. Chem. Lett. 1 (2010), pp. 1941–1945.
- [222] P.G. Wolynes, J. Res. Inst. Stand. Technol. 102 (1997), pp. 187–194.
- [223] E. Flenner, H. Staley, and G. Szamel, Phys. Rev. Lett. 112 (2014), p. 097801.
- [224] G. Biroli, S. Karmakar, and I. Procaccia, Phys. Rev. Lett. 111 (2013), p. 165701.
- [225] G.M. Hocky, T.E. Markland, and D.R. Reichman, Phys. Rev. Lett. 108 (2012), p. 225506.
- [226] A. Wisitsorasak and P.G. Wolynes, J. Phys. Chem. B 118 (2014), pp. 7835–7847.
- [227] C. Cammarota, G. Gradenigo, and G. Biroli, Phys. Rev. Lett. 111 (2013), p. 107801.
- [228] A. Malins, S.R. Williams, J. Eggers, and C.P. Royall, J. Chem. Phys. 139 (2013), p. 234506.
- [229] C.P. Royall and S.R. Williams, Phys. Rep. 560 (2015), pp. 1–75.
- [230] K. Zhang, W.W. Smith, M. Wang, Y. Liu, J. Schroers, M.D. Shattuck, and C.S. O’Hern, Phys. Rev. E 90 (2014), p. 032311.
- [231] H. Tanaka, T. Kawasaki, H. Shintani, and K. Watanabe, Nature Materials 9 (2010), pp. 324 – 331.

- [232] A. Hirata, L.J. Kang, T. Fujita, B. Klumov, K. Matsue, M. Kotani, A.R. Yavari, and M.W. Chen, *Science* 341 (2013), pp. 376–379.
- [233] S. Sachdev and D.R. Nelson, *Phys. Rev. B* 32 (1985), pp. 1480–1502.
- [234] C. Cammarota and G. Biroli, *Europhys. Lett.* 98 (2012), p. 36005.
- [235] P.K. Dixon and S.R. Nagel, *Phys. Rev. Lett.* 61 (1988), p. 341.
- [236] M.P. Eastwood, T. Chitra, J.M. Jumper, K. Palmo, A.C. Pan, and D.E. Shaw, *J. Phys. Chem. B* 117 (2013), pp. 12898–12907.
- [237] R. Richert, *Supercooled liquid dynamics: Advances and challenges*, in *Structural Glasses and Supercooled Liquids: Theory, Experiment, and Applications*, P.G. Wolynes and V. Lubchenko, eds., John Wiley & Sons, Hoboken, NJ (2012), pp. 1–30.
- [238] F.S. Howell, R.A. Bose, P.B. Macedo, and C.T. Moynihan, *J. Phys. Chem.* 78 (1974), p. 639.
- [239] F. Stickel, E.W. Fischer, and R. Richert, *J. Chem. Phys.* 104 (1996), pp. 2043–2055.
- [240] Y. Gebremichael, M. Vogel, and S.C. Glotzer, *J. Chem. Phys.* 120 (2004), pp. 4415–4427.
- [241] R.W. Hall and P.G. Wolynes, *J. Phys. Chem. B* 112 (2008), pp. 301–312.
- [242] R. Casalini and C.M. Roland, *Phys. Rev. Lett.* 92 (2004), p. 245702.
- [243] R. Casalini and C.M. Roland, *Phys. Rev. E* 72 (2005), p. 031503.
- [244] D.W.V. Krevelen, *Properties of Polymers*, Elsevier, New York, 1990.
- [245] J. Wiedersich, T. Blochowicz, S. Benkhof, A. Kudlik, N.V. Surovtsev, C. Tschirwitz, V.N. Novikov, and E. Rössler, *Journal of Physics: Condensed Matter* 11 (1999), p. A147.
- [246] A.Q. Tool, *J. Am. Ceram. Soc.* 29 (1946), pp. 240–253.
- [247] O.S. Narayanaswamy, *J. Am. Ceram. Soc.* 54 (1971), pp. 491–498.
- [248] C.T. Moynihan, A.J. Easteal, M.A. Debolt, and J. Tucker, *J. Am. Ceram. Soc.* 59 (1976), pp. 12–16.
- [249] P.K. Gupta and C.T. Moynihan, *J. Chem. Phys.* 65 (1976), pp. 4136–4140.
- [250] A. Alegría, E. Guericca-Echvarría, L. Goitandía, I. Tellería, and J. Colmenero, *Macromol.* 28 (1995), pp. 1516–1527.
- [251] S.F. Swallen, K. Windsor, R.J. McMahon, M.D. Ediger, and T.E. Mates, *J. Phys. Chem. B* 114 (2010), pp. 2635–2643.
- [252] A. Sepúlveda, S.F. Swallen, L.A. Kopff, R.J. McMahon, and M.D. Ediger, *J. Chem. Phys.* 137 (2012), 204508.
- [253] A. Kolmogoroff, I. Petrovsky, and N. Piscounoff, Moscow University, *Bull. Math.* 1 (1937), pp. 1–25, translated and reprinted in P. Pelce, *Dynamics of Curved Fronts* (Academic Press, San Diego, 1988).
- [254] R.A. Fisher, *Ann. Eugenics* 7 (1937), pp. 353–369.
- [255] B. Derrida and H. Spohn, *J. Stat. Phys.* 51 (1988), pp. 817–840.
- [256] S.L. Webb and D.B. Dingwell, *Phys. Chem. Minerals* 17 (1990), pp. 125–132.
- [257] <http://www.nature.com/news/world-s-slowest-moving-drop-caught-on-camera-at-last-1.13418>.
- [258] J. Zhao, S.L. Simon, and G.B. McKenna, *Nat. Commun.* 4 (2013), p. 1783.
- [259] L. Valenta, *Czech. J. Phys.* 6 (1996), pp. 607–619.
- [260] S.F. Swallen, K.L. Kearns, M.K. Mapes, Y.S. Kim, R.J. McMahon, M.D. Ediger, T. Wu, L. Yu, and S. Satija, *Science* 315 (2007), pp. 353–356.
- [261] S.S. Dalal and M.D. Ediger, *J. Phys. Chem. Lett.* 3 (2012), pp. 1229–1233.
- [262] S.S. Dalal, Z. Fakhraai, and M.D. Ediger, *J. Phys. Chem. B* 117 (2013), pp. 15415–15425.
- [263] A. Sepúlveda, M. Tyllinski, A. Guiseppi-Elie, R. Richert, and M.D. Ediger, *Phys. Rev. Lett.* 113 (2014), p. 045901.
- [264] C.W. Brian and L. Yu, *J. Phys. Chem. A* 117 (2013), pp. 13303–13309.
- [265] K.L. Kearns, S.F. Swallen, M.D. Ediger, T. Wu, Y. Sun, and L. Yu, *J. Phys. Chem. B* 112 (2008), pp. 4934–4942.
- [266] C.T. Powell, K. Paeng, Z. Chen, R. Richert, L. Yu, and M.D. Ediger, *J. Phys. Chem. B* 118 (2014), pp. 8203–8209.
- [267] E. Fischer, *Physica A: Statistical Mechanics and its Applications* 201 (1993), pp. 183 – 206.
- [268] E. Fischer, G. Meier, T. Rabenau, A. Patkowski, W. Steffen, and W. Thönnies, *J. Non-Cryst. Sol.* 131-133 (1991), pp. 134–138.
- [269] H. Westfahl, J. Schmalian, and P.G. Wolynes, *Phys. Rev. B* 68 (2003), p. 134203.
- [270] T.E. Markland, J.A. Morrone, B.J. Berne, K. Miyazaki, E. Rabani, and D.R. Reichman,

- Nature Physics 7 (2011), pp. 134–137.
- [271] P.W. Anderson, Phys. Rev. 109 (1958), pp. 1492–1505.
  - [272] N.F. Mott, *Conduction in Non-crystalline Materials*, Clarendon Press, Oxford, 1993.
  - [273] D. Emin, Comments Solid State Phys. 11 (1983), pp. 35–46.
  - [274] D. Emin, Comments Solid State Phys. 11 (1983), pp. 59–72.
  - [275] R.C. Zeller and R.O. Pohl, Phys. Rev. B 4 (1971), pp. 2029–2041.
  - [276] J.J. Freeman and A.C. Anderson, Phys. Rev. B 34 (1986), pp. 5684–5690.
  - [277] P.W. Anderson, B.I. Halperin, and C.M. Varma, Philos. Mag. 25 (1972), pp. 1–9.
  - [278] W.A. Phillips, J. Low Temp. Phys. 7 (1972), pp. 351–360.
  - [279] W.A. Phillips (ed.), *Amorphous Solids: Low-Temperature Properties*, Springer-Verlag, Berlin, Heidelberg, New York, 1981.
  - [280] B. Golding and J.E. Graebner, Phys. Rev. Lett. 37 (1976), pp. 852–855.
  - [281] A.M. Boiron, P. Tamarat, B. Lounis, R. Brown, and M. Orrit, Chem. Phys. 247 (1999), pp. 119–132.
  - [282] M. Bauer and L. Kador, J. Chem. Phys. 118 (2003), pp. 9069–9072.
  - [283] N.F. Mott, *Metal-Insulator Transitions*, Taylor and Francis, London, 1990.
  - [284] A. Einstein, Ann. Phys. 35 (1911), pp. 679–694.
  - [285] C.C. Yu and A.J. Leggett, Comments Cond. Mat. Phys. 14 (1988), pp. 231–251.
  - [286] A.L. Burin and Y. Kagan, Sov. Phys. JETP 82 (1996), pp. 159–171.
  - [287] A.J. Leggett and D.C. Vural, J. Phys. Chem. B 117 (2013), pp. 12966–12971.
  - [288] P. Esquinazi (ed.), *Tunneling Systems in Amorphous and Crystalline Solids*, Springer-Verlag, Heidelberg, 1998.
  - [289] P. Neu, D.R. Reichman, and R.J. Silbey, Phys. Rev. B 56 (1997), pp. 5250–5260.
  - [290] M. Mézard, G. Parisi, and M.A. Virasoro, J. Physique Lett. 46 (1985), pp. 217–222.
  - [291] A.J. Heeger, S. Kivelson, J.R. Schrieffer, and W.P. Su, Rev. Mod. Phys. 60 (1988), pp. 781–850.
  - [292] J.F. Berret and M. Meissner, Z. Phys. B 70 (1988), pp. 65–72.
  - [293] X. Liu, D.R. Queen, T.H. Metcalf, J.E. Karel, and F. Hellman, Phys. Rev. Lett. 113 (2014), p. 025503.
  - [294] D.R. Queen, X. Liu, J. Karel, H.C. Jacks, T.H. Metcalf, and F. Hellman, J. Non-Cryst. Sol. 426 (2015), pp. 19–24.
  - [295] T. Pérez-Castañeda, C. Rodríguez-Tinoco, J. Rodríguez-Viejo, and M.A. Ramos, Proc. Natl. Acad. Sci. U. S. A. 111 (2014), pp. 11275–11280.
  - [296] P.G. Wolynes, Phys. Rev. Lett. 47 (1981), pp. 968–971.
  - [297] R.O. Pohl, in *Amorphous Solids: Low-Temperature Properties*, W.A. Phillips, ed., Springer-Verlag, Berlin, Heidelberg, New York (1981).
  - [298] T.L. Smith, Ph.D. thesis, University of Illinois, 1974.
  - [299] L.D. Landau and E.M. Lifshitz, *Quantum Mechanics*, Pergamon Press, 1981.
  - [300] D.A. Ackerman, A.C. Anderson, E.J. Cotts, J.N. Dobbs, W.M. MacDonald, and F.J. Walker, Phys. Rev. B 29 (1984), pp. 966–975.
  - [301] F. Léonforte, A. Tanguy, J.P. Wittmer, and J.L. Barrat, Phys. Rev. Lett. 97 (2006), p. 055501.
  - [302] A. Paul, S. Sengupta, and M. Rao, J. Phys.: Condens. Matter 26 (2014), p. 015007.
  - [303] H. Wagner, D. Bedorf, S. Kchemann, M. Schwabe, Z. Bo, W. Arnold, and K. Samwer, Nature Materials 10 (2011), pp. 439 – 442.
  - [304] H. Mizuno, S. Mossa, and J.L. Barrat, Europhys. Lett. 104 (2013), p. 56001.
  - [305] S.G. Mayr, Phys. Rev. B 79 (2009), p. 060201.
  - [306] W. Schirmacher, Europhys. Lett. 73 (2006), pp. 892–898.
  - [307] A.C. Anderson, in *Amorphous Solids: Low-Temperature Properties*, W.A. Phillips, ed., Springer-Verlag, Berlin, Heidelberg, New York (1981).
  - [308] Y.P. Joshi, Phys. Stat. Sol. (b) 95 (1979), p. 317.
  - [309] S.R. Ovshinsky, Phys. Rev. Lett. 21 (1968), pp. 1450–1453.
  - [310] B.T. Kolomiets, J. Phys. (Paris) C4 42 (1981), pp. 887–897.
  - [311] P.W. Anderson, Rev. Mod. Phys. 50 (1978), pp. 191–201.
  - [312] D.K. Biegelsen and R.A. Street, Phys. Rev. Lett. 44 (1980), pp. 803–806.
  - [313] S.G. Bishop, U. Strom, and P.C. Taylor, Phys. Rev. B 15 (1977), pp. 2278–2294.
  - [314] P.W. Anderson, Phys. Rev. Lett. 34 (1975), pp. 953–955.

- [315] P.W. Anderson, J. Phys. (Paris) C4 (1976), pp. 339–342.
- [316] P.W. Anderson, Nat. Phys. Sci. 235 (1972), pp. 163–165.
- [317] M. Kastner, D. Adler, and H. Fritzsche, Phys. Rev. Lett. 37 (1976), p. 1504.
- [318] R.A. Street and N.F. Mott, Phys. Rev. Lett. 35 (1975), pp. 1293–1296.
- [319] D. Vanderbilt and J.D. Joannopoulos, Phys. Rev. B 23 (1981), pp. 2596–2606.
- [320] K. Shimakawa, A. Kolobov, and S.R. Elliott, Adv. Phys. 44 (1995), pp. 475–588.
- [321] J. Li and D.A. Drabold, Phys. Rev. Lett. 85 (2000), pp. 2785–2788.
- [322] S.I. Simdyankin, S.R. Elliott, Z. Hajnal, T.A. Niehaus, and T. Frauenheim, Phys. Rev. B 69 (2004), p. 144202.
- [323] S.A. Dembovsky and E.A. Chechetkina, J. Optoelectronics Adv. Mat. 3 (2001), pp. 3–18.
- [324] J. Hautala, W.D. Ohlsen, and P.C. Taylor, Phys. Rev. B 38 (1988), pp. 11048–11060.
- [325] W.P. Su, J.R. Schrieffer, and A.J. Heeger, Phys. Rev. B 22 (1980), pp. 2099–2111.
- [326] M.J. Rice and E.J. Mele, Phys. Rev. Lett. 49 (1982), pp. 1455–1459.
- [327] N. Alcock, Adv. Inorg. Chem. Radiochem. 15 (1972), pp. 1–58.
- [328] P. Pykkö, Chem. Rev. 97 (1997), pp. 597–636.
- [329] G.A. Landrum and R. Hoffmann, Angew. Chem. Int. Ed. 37 (1998), pp. 1887–1890.
- [330] G.A. Papoian and R. Hoffmann, Angew. Chem. Int. Ed. 39 (2000), pp. 2408–2448.
- [331] H.A. Bent, Chem. Rev. 68 (1968), pp. 587–648.
- [332] R. Jackiw and C. Rebbi, Phys. Rev. D 13 (1976), pp. 3398–3409.
- [333] H. Takayama, Y.R. Lin-Liu, and K. Maki, Phys. Rev. B 21 (1980), pp. 2388–2393.
- [334] J.K. Burdett and T.J. McLarnan, J. Chem. Phys. 75 (1981), pp. 5764–5773.
- [335] J.K. Burdett, P. Haaland, and T.J. McLarnan, J. Chem. Phys. 75 (1981), pp. 5774–5781.
- [336] D. Seo and R. Hoffmann, J. Sol. State Chem. 147 (1999), pp. 26–36.
- [337] S. Shang, Y. Wang, H. Zhang, and Z.K. Liu, Phys. Rev. B 76 (2007), p. 052301.
- [338] T. Tada and T. Ninomiya, Sol. St. Comm. 71 (1989), pp. 247–251.
- [339] T. Tada and T. Ninomiya, J. Non-Cryst. Sol. 114 (1989), pp. 88–90.
- [340] T. Tada and T. Ninomiya, J. Non-Cryst. Sol. 137&138 (1989), pp. 997–1000.
- [341] N. Sakai and H. Fritzsche, Phys. Rev. B 15 (1977), pp. 973–978.
- [342] P. Anderson, Science 267 (1995), p. 1615.
- [343] <http://www.nytimes.com/2008/07/29/science/29glass.html?pagewanted=1&r=1&ei=5087&em&en=ee7d66b6da266795&ex=1217476800>.
- [344] H.A. Kramers, Physica (Utrecht) 7 (1940), pp. 284–304.
- [345] T. Pérez-Castañeda, R.J. Jiménez-Riobóo, and M.A. Ramos, Phys. Rev. Lett. 112 (2014), p. 165901.
- [346] N. Jakse, L. Hennet, D.L. Price, S. Krishnan, T. Key, E. Artacho, B. Glorieux, A. Pasturel, and M.L. Saboungi, Appl. Phys. Lett. 83 (2003), pp. 4734–4736.
- [347] Y. Zhou and S. Milner, Soft Matter 11 (2015), pp. 2700–2705.
- [348] C. Billotet and K. Binder, Z. Phys. B 32 (1978), pp. 195–213.
- [349] A.J. Liu, S.R. Nagel, W. van Saarloos, and M. Wyart, *The jamming scenario - an introduction and outlook*, in *Dynamical Heterogeneities in Glasses, Colloids, and Granular Media*, L. Berthier, G. Biroli, J.P. Bouchaud, L. Cipelletti, and W. van Saarloos, eds., Oxford University Press, Oxford (2011), pp. 1–44.
- [350] A. Ikeda, L. Berthier, and G. Biroli, J. Chem. Phys. 138 (2013), p. 12A507.
- [351] M. Dzero, J. Schmalian, and P.G. Wolynes, *Glassiness in Uniformly Frustrated Systems*, in *Structural Glasses and Supercooled Liquids: Theory, Experiment, and Applications*, P.G. Wolynes and V. Lubchenko, eds., John Wiley & Sons (2012), pp. 341–379.
- [352] P. Charbonneau, Y. Jin, G. Parisi, C. Rainone, B. Seoane, and F. Zamponi, Phys. Rev. E 92 (2015), p. 012316.
- [353] J. Kurchan, G. Parisi, P. Urbani, and F. Zamponi, J. Phys. Chem. B 117 (2013), pp. 12979–12994.
- [354] E. Gardner, Nuclear Physics B 257 (1985), pp. 747 – 765.
- [355] P. Morse and E. Corwin, 2015. unpublished.
- [356] A.J. Kovacs, J.M. Hutchinson, and J.J. Aklonis, *Isobaric volume and enthalpy recovery of glasses (I) A critical survey of recent phenomenological approaches*, in *The Structure of Non-Crystalline Materials*, P.H. Gaskell, ed., Taylor and Francis, Oxford (1977), pp. 153–163.

This figure "cR.jpg" is available in "jpg" format from:

<http://arxiv.org/ps/1511.05998v1>